

UNIVERSITY OF  
CAMBRIDGE

---

UNDERSTANDING TOUGHNESS AND DUCTILITY  
IN NOVEL STEELS WITH MIXED MICROSTRUCTURES

---

*by*

LUCY CHANDRA DEVI FIELDING



JESUS COLLEGE

This thesis is submitted for the degree of Doctor of Philosophy

*June 2014*

*Cambridge, United Kingdom*



## ABSTRACT

---

The purpose of the work presented in this thesis was to explore and understand the mechanisms governing toughness, ductility and ballistic performance in a class of nanostructured carbide-free bainite-austenite steels, sometimes known as ‘superbainite’. The mechanical properties of these alloys have been extensively reported, but their interpretation is not clear. The thesis begins with an introduction to both the relevant nanostructures and some of the difficulties involved in explaining observed properties, alongside a summary of the role of mixed-microstructures in alloy development.

An overview of the debate regarding the mechanism of bainite formation is presented in Chapter 2, in the form of a literature survey encompassing the period of explicit recognition of the bainite microstructure. Of note is the role played by the displacive theory of formation in the development of the alloy structures investigated in this thesis.

A characterisation of a commonly available bainitic alloy forms the basis for Chapter 4. Observations confirm the nanoscale nature of the structure, although additional phases are found to be present, namely: cementite and martensite. This is explained as resulting from relatively low alloying additions and chemical segregation effects, which are modelled using thermodynamic and kinetic approaches.

Chapters 5 and 6 contain a comprehensive study of the response of this alloy to the stress concentration present at the notch root of a Charpy impact sample. The work provides evidence of notch root embrittlement due to stress-induced martensite transformation. Results from synchrotron and laboratory X-ray experiments in particular reveal that machining, as well as applied stress, can initiate the austenite-martensite transformation, and methods to mitigate this effect

are suggested.

An innovative approach is harnessed in Chapter 7, in order to identify experimentally the volume fraction at which three-dimensional connectivity ('percolation') of austenite is lost in a superbainitic steel. Hydrogen thermal desorption techniques are applied to this problem, inspired by the tendency of such alloys to undergo tensile failure with limited or zero necking. The striking result sheds light on the importance of austenite morphology in restricting the diffusion of hydrogen into a mixed structure.

The final set of experimental work is directed towards understanding the damage mechanisms that occur during projectile penetration of a coarser bainitic armour-plate alloy. The formation of adiabatic shear bands is found to be a dominant factor governing the ballistic failure of the plate. The sheared material undergoes severe high-temperature deformation, but does not change phase upon cooling, leading to the proposal of certain methods that could be implemented to improve ballistic resistance of the steel.

The totality of the research presented herein is summarised in Chapter 9, which draws attention to new areas of interest that have arisen from the current work, proposing several future directions of investigation. The broader issue of understanding, common to all studies performed thus far, is that of the causes, effects, and extent, of stress-induced transformation to martensite experienced by the retained austenite that is a key feature of superbainite and similar steels.

## DECLARATION

---

This thesis:

- is my own work and contains nothing that is the outcome of work done in collaboration with others, except where specifically indicated in the text;
- is not substantially the same as any that I have submitted for a degree or diploma or other qualification at any other university; and
- does not exceed the prescribed limit of 60,000 words.

Aspects of this work have been published in the literature as follows:

- CHAPTER 2 has been published as: **L.C.D. Fielding**, “The Bainite Controversy”, *Materials Science and Technology*, 9 (2013) 383-399.
- CHAPTER 7 has been published as: **L.C.D. Fielding**, E.J. Song, D.K. Han, H.K.D.H. Bhadeshia, D.-W. Suh, “Hydrogen diffusion and the percolation of austenite in nanostructured bainitic steel”, *Proceedings of the Royal Society A*, 470 (2014) 20140108.
- CHAPTER 8 has been published as: **L.C.D. Fielding** and H.K.D.H. Bhadeshia, “Shear-band structure in ballistically tested bainitic steels”, *Materials Science and Technology*, 30 (2014) 812-817.

L.C.D. Fielding  
Cambridge, May 2014



## ACKNOWLEDGEMENTS

---

I would like to express my overwhelming gratitude to my supervisor, Professor Harry Bhadeshia, for his support, guidance, advice, enthusiasm and mockery during my research — and most of all, for his constant reassurance that “these are just technical problems. Don’t bother me with technical problems”, which ultimately drove me to become a more competent and self-reliant scientist.

Alongside Harry, I must thank my industrial supervisors: Peter Morris, Andrew Rose and Andrew Smith, for many constructive meetings and discussions about my work. I am grateful to Tata Steel UK for financial support, and to the many scientists and technicians there who supplied me with material, helped with experiments, and gave feedback on my research: Sally Parker, Farooq Mohammed, David Wilcox, James Silvester, Andy Howe and all the people at the annual Academia Symposium.

The work presented in this thesis could not have been completed without the input of many scientific collaborators. In particular, I must acknowledge Eun Ju Song, Do-Kyeong Han and Professor Dong-Woo Suh, of the Graduate Institute of Ferrous Technology, without whom the hydrogen work would not have been possible. I also wish to thank the students at GIFT who gave me such a warm welcome during my time there, and I acknowledge the financial support of the Worshipful Company of Ironmongers.

To my synchrotron team, I wish to express my sincere thanks: Joanna Walsh, Steven Van Boxel, Matthew Blackmur, Prakash Srirangam Venkata and Bernard Ennis — their contributions helped to make the experiment a success. Additionally, thanks go to the staff on the I15 beamline at DLS: Heribert Wilhelm, Annette, Dominic — and especially to the Experimental Hall Co-ordinators who fixed the detector shield at 2am. I wish to credit Peter Lee and Philip Withers

for their invaluable advice during the project, and for providing access to the computing and microscope facilities at the University of Manchester.

I would like to extend further thanks to everyone in the Department of Materials Science who provided assistance and advice to me. To Professors Lindsay Greer and Mark Blamire for the provision of laboratory facilities; to David Nicol and Jon Barnard, for helping with TEM and FIB work; to Mary Vickers and Andrew Moss, for advice and guidance with X-ray work; to Simon Griggs for assistance with SEM; to Frank Clarke for help with metallography; to Kevin Roberts for his help with furnaces; to Blanka Szost for teaching me how to use the Thermec; to Andrew Rayment for assisting with mechanical testing; to Howard Stone for advice on beamline proposals; to Jakub Rydel for help with MatCalc; to Tony Cheetham, Pedro Rivera and Vasant Kumar for feedback and discussion of my first year work; and exceptional thanks to Ken, Paul and everyone else in the workshop who performed small miracles in order to get my samples prepared.

Additional thanks go to Simon Redfern and Giulio Lampronti at the Department of Earth Sciences, and Alistair Ross at the Department of Engineering, for carrying out some of my X-ray and machining work, respectively.

I am unendingly grateful to the members of PT Group, both past and present, who made my experience at Cambridge an exceptional one. Special mentions for Aseel, who taught me how to use a grinding wheel in my first week; Ashwin, for showing me how to etch a sample; and Mathew, for being a constant source of aid, advice and amusement. To everyone else: Arijit, Yan, Steve, David, Hala, Chris, Ed, James, Tim, Subhankar, Wil, Hector, Ivan, Hojo, Toru, Lin Sun, Guo Lei, Wendy, Joachim, Neel, Mandla, Rashid and Amir — thank you all for your friendship, your antagonism, your accusations of espionage, and the many discussions in the office, not one of which had anything to do with metallurgy. I am particularly indebted to Pat Wilson, who was a great source of practical support, and to both Anne and Anita for their limitless patience and cheer.

The achievements herein would not have been possible without the contribution of the people throughout my life who helped to ignite my interest in science. Accordingly, I must thank the teachers at Kennedy School and Casterton School, and the professors and supervisors of Jesus College, Cambridge, for helping me

get this far, in particular: Annette Stabb, Paul Hamblin, Andy Bell, Jim Howard, Maurice Martin, Tony Thomas, Tim Wilkinson and Geoff Parks.

Finally I would like to thank all my friends and family for their love, support and companionship, especially Richard Ingham, Fiona Llewellyn-Beard, Becky Jeffers, James Rickenbach, Steph Jones, Sarah Barrington, Lucy Osborne, Poul Alexander and Jonathan Crass. My special gratitude goes to Michael Probyn, for all our adventures; to Tom Grimble, for being there for me every day; to Daniel Wilkins, for always being ridiculous; and most of all to Kelly Mullens, for her friendship over the past twenty-five years. Thanks to Paul, Jo, Bethany and Tamsin, for all the great trips to Somerset; to my brother Kyran for his support; and to my sister Brenna, for encouraging me to apply for this project in the first place. Lastly, to my parents, Sarla and Richard: thank you for raising me to be a scientist. I could have turned out a lot worse.



# CONTENTS

---

<b>1</b>	<b>Introduction</b>	<b>21</b>
<b>2</b>	<b>Review: The Bainite Controversy</b>	<b>25</b>
2.1	Introduction . . . . .	25
2.2	The origin of the two theories . . . . .	29
2.3	A thermo-kinetic explanation . . . . .	31
2.3.1	Comparisons with martensite and pearlite . . . . .	35
2.4	Growth rate and surface relief . . . . .	37
2.5	A crystallographic approach . . . . .	39
2.6	Mechanism-based-theory . . . . .	43
2.7	Experimentally-based criticisms . . . . .	44
2.8	Surface relief revisited . . . . .	50
2.9	Further support for a diffusional mechanism . . . . .	51
2.10	Validation of the displacive theory . . . . .	53
2.10.1	The design of new bainitic alloys . . . . .	56
2.11	Conclusions . . . . .	59
<b>3</b>	<b>Experimental Methods</b>	<b>63</b>
3.1	Materials . . . . .	63
3.2	Sample preparation . . . . .	64
3.3	Microstructural observations . . . . .	65
3.3.1	Optical microscopy . . . . .	65
3.3.2	Scanning electron microscopy . . . . .	65
3.3.3	Transmission electron microscopy . . . . .	65
3.4	Metallurgical experiments . . . . .	66
3.4.1	Heat treatments . . . . .	66
3.4.2	Thermodynamic calculations . . . . .	66
3.4.3	Dilatometry . . . . .	67

3.5	Mechanical testing . . . . .	68
3.5.1	Hardness testing . . . . .	68
3.5.2	Bend tests . . . . .	69
3.5.3	Charpy tests . . . . .	70
3.6	X-ray diffraction . . . . .	70
3.6.1	Common errors in X-ray diffractometry . . . . .	71
3.6.2	Rietveld refinement . . . . .	72
<b>4</b>	<b>Characterisation of Fast-Transforming Nanostructured Bainite</b>	<b>77</b>
4.1	Introduction . . . . .	77
4.2	Experimental methods . . . . .	79
4.2.1	Determination of martensite-start temperature . . . . .	79
4.2.2	Estimation of bainite-start temperature . . . . .	79
4.2.3	Estimation of prior austenite grain size . . . . .	80
4.2.4	Determination of final volume fraction of bainite . . . . .	80
4.2.5	Thermodynamic calculations . . . . .	81
4.2.6	Neural network . . . . .	81
4.3	Results and discussion . . . . .	82
4.3.1	Dilatometry . . . . .	82
4.3.2	Optical microscopy . . . . .	93
4.3.3	Transmission electron microscopy . . . . .	98
4.3.4	Scanning electron microscopy . . . . .	103
4.3.5	X-ray diffraction . . . . .	107
4.3.6	Thermodynamic and kinetic modelling . . . . .	110
4.4	Conclusions . . . . .	117
<b>5</b>	<b>Resolving Toughness Anomalies in Nanostructured Bainite</b>	<b>119</b>
5.1	Introduction . . . . .	119
5.2	Experimental methods . . . . .	120
5.2.1	Microhardness testing . . . . .	121
5.3	Results and discussion . . . . .	121
5.3.1	Mechanical tests . . . . .	121
5.3.2	Fractography . . . . .	123
5.3.3	X-ray diffraction . . . . .	124
5.3.4	Microhardness . . . . .	130
5.4	Conclusions . . . . .	132

<b>6</b>	<b>Toughness Anomalies in Nanostructured Bainite: A Synchrotron Study</b>	<b>135</b>
6.1	Introduction . . . . .	135
6.2	Experimental methods . . . . .	136
6.2.1	Synchrotron experiments . . . . .	136
6.3	Results and discussion . . . . .	141
6.3.1	Austenite lattice . . . . .	145
6.3.2	Ferrite lattice . . . . .	151
6.4	Conclusions . . . . .	155
<b>7</b>	<b>Austenite Percolation in Nanostructured Bainite</b>	<b>157</b>
7.1	Introduction . . . . .	157
7.1.1	Collaboration . . . . .	158
7.2	Experimental methods . . . . .	159
7.3	Results and discussion . . . . .	162
7.3.1	TEM characterisation . . . . .	162
7.3.2	Thermal desorption analysis . . . . .	167
7.3.3	“Calibration” experiments . . . . .	169
7.3.4	Role of retained austenite . . . . .	170
7.3.5	Permeation experiments . . . . .	174
7.3.6	Decomposition of retained austenite . . . . .	178
7.4	Conclusions . . . . .	181
<b>8</b>	<b>Shear-band Structure in Ballistically-Tested Bainitic Steels</b>	<b>183</b>
8.1	Introduction . . . . .	183
8.2	Experimental methods . . . . .	184
8.2.1	Convergent beam electron diffraction . . . . .	186
8.3	Results and discussion . . . . .	186
8.3.1	Metallography . . . . .	186
8.3.2	Transmission electron microscopy . . . . .	190
8.4	Conclusions . . . . .	202
<b>9</b>	<b>General Conclusions and Future Work</b>	<b>203</b>
9.1	Scope for future work . . . . .	205
	<b>Bibliography</b>	<b>233</b>

<b>A</b>	<b>Appendix</b>	<b>235</b>
A.1	Laboratory X-ray analysis of Charpy notch . . . . .	235
A.2	Tetragonality of ferrite . . . . .	236
A.3	Effects of machining upon Charpy tests . . . . .	237
A.4	Thermodynamics of oxidation . . . . .	239





---

# NOMENCLATURE

---

$\alpha'$	Martensite
$\alpha$	Ferrite
$\alpha_b$	Bainitic ferrite
$\gamma$	Austenite
$\Delta$	Error minimisation function
$\Delta G$	Gibbs free energy change
$\Delta S$	Entropy change
$\Delta U$	Strain energy of transformation
$\epsilon_{\text{offset}}$	Offset strain used to calculate $M_S$
$\sigma$	Standard deviation
$\theta$	Cementite
$\phi$	Azimuthal angle around diffraction ring
$\psi$	Ratio of fluxes of hydrogen through ferrite and austenite
$a$	Unit cell lattice parameter
$Ac_3$	The temperature separating the $\alpha + \gamma$ and $\gamma$ phase fields during heating
$Ae_3$	The equilibrium temperature separating the $\alpha + \gamma$ and $\gamma$ phase fields
$b$	Fitting parameter used in the Koistinen-Marburger equation
$B_S$	Bainite-start temperature
$c$	Tetragonal unit cell lattice parameter
$C_\gamma$	Austenite carbon content
$D_\alpha$	Diffusion coefficient of hydrogen in ferrite

$D_\gamma$	Diffusion coefficient of hydrogen in austenite
$D_l$	Apparent time-lag diffusion coefficient
$D_b$	Apparent break-through diffusion coefficient
$J_\alpha$	Hydrogen flux through ferrite
$J_\gamma$	Hydrogen flux through austenite
$J_{np}$	Hydrogen flux through a non-percolating structure
$J_{os}$	Hydrogen flux through an open structure
$J_p$	Hydrogen flux through a percolating structure
$K_{1C}$	Fracture toughness in mode 1 loading
$M_S$	Martensite-start temperature
$p$	Partial pressure
$P$	Permeability
$R_{wp}$	Weighted-profile $R$ -value (a minimisation parameter)
$R_{exp}$	Expected $R$ -value (minimum possible value of $R_{wp}$ )
$\dot{T}$	Heating rate in $^\circ\text{C h}^{-1}$
$T_{aus}$	Austenitisation temperature
$T_0$	The temperature at which bainitic ferrite and austenite of identical composition have identical free energy
$T'_0$	A modification of $T_0$ that accounts for stored strain energy in the surrounding austenite
$T_q$	Quenching temperature
$V_{\alpha_b}$	Volume fraction of bainitic ferrite
$V_\gamma$	Volume fraction of austenite
$w_i$	Weighting factor of reflection line $i$ in the error minimisation function
$x_\alpha$	Atomic concentration of hydrogen in ferrite
$x_\gamma$	Atomic concentration of hydrogen in austenite
$\bar{X}$	Average carbon content of alloy
$y_i$	Intensity of reflection line $i$

AFM	Atomic force microscope
BCC	Body-centred cubic
CBED	Convergent-beam electron diffraction
CCT	Continuous cooling transformation
EBS	Electron back-scattered diffraction
EDX	Energy-dispersive X-ray
FWHM	Full width half maximum
HTM	Sample heat-treated before machining
MHT	Sample machined before heat-treatment
MTT	Microstructural transition temperature
SAD	Selected-area diffraction
SDLE	Solute-drag-like effect
SEM	Scanning electron microscope
STM	Scanning tunneling microscope
TDA	Thermal desorption analysis
TEM	Transmission electron microscope
TRIP	Transformation-induced plasticity
TTT	Time-temperature-transformation
TWIP	Twinning-induced plasticity
UTS	Ultimate tensile strength



*Ray, pretend for a moment that I don't know anything about metallurgy, engineering, or physics, and just tell me what the hell is going on.*

Dr Peter Venkman, *Ghostbusters*

# CHAPTER 1

---

## INTRODUCTION

---

Despite the arguably superior, density-correlated properties of materials such as aluminium, titanium and carbon fibre composites, advanced steels remain the material of choice due to their comparatively low cost and versatility [1–3]. The creation of such high-performance alloys has been made possible by a deeper understanding of how the morphology and behaviour of the microstructure is able to influence the mechanical properties. Steels in particular offer a diverse range of properties thanks in part to the many phase transformations that can be achieved with the appropriate use of heat treatment and alloying. A particular goal of metallurgists is to improve combinations of mechanical properties — a challenging task that requires compromises to be overcome with new principles [4, 5].

For a long time, few ferrous alloys were able to compete with the strength-toughness combinations generated in martensitic steels. Following the formal identification of bainite in 1930 [6], much effort was directed towards developing this ‘new’ structure into viable applications [7, 8]. It was recognised that the ability to refine the bainite ‘sheaf’ could produce steels with property combinations comparable to those in martensitic alloys, although this would not be realised for many decades [9].

Further key advances accompanied the discovery that silicon suppresses cementite precipitation in steels. The coarse, brittle cementite particles in bainite were replaced with carbon-enriched retained austenite films, further expanding the potential of these alloys [10, 11]. The stability of this retained austenite is exploited

in bainitic alloys such as TRIP (TRansformation-Induced Plasticity) steels, which derive ductility from a stress-induced transformation to martensite [12]. It has been recently revealed that the majority of the ductility in these steels comes from the composite (mixed-microstructure) nature of the material [13]. The presence of retained austenite films and the composite behaviour of mixed-microstructure steels are also advantageous for toughness. The fine distribution of interfaces and varying crystal structures are effective obstacles to crack propagation [14, 15]. Conversely, blocks (as opposed to films) of retained austenite are unstable and prone to stress- or strain-induced martensitic transformation, generating large brittle regions [14, 15].

Mixed-microstructure alloys such as these have experienced a resurgence in metallurgical research. They are not a new phenomenon by any means — many early ferrous alloys necessarily comprised mixed-microstructures as a result of continuous cooling manufacturing processes. However, modern expertise in alloying and heat treatment enables the generation of such microstructures to be controlled to a much greater degree than was previously possible. Indeed, it has been found that alloys containing an appropriate mixture of phases can sometimes improve upon the properties of single-phase steels [16]. These include dual phase alloys consisting of bainite-martensite microstructures [17–20], bainite-ferrite microstructures [21], martensite-austenite microstructures and bainite-austenite microstructures [22, 23]. The combined properties of such steels are now capable of matching, or even surpassing, those produced in martensitic alloys.

Alongside this progress in manufacturing new alloys has come the formulation of detailed thermodynamic and kinetic theories: important tools in alloy design [24–27]. These theories have been used to design a nanoscaled, mixed-structure bainitic alloy known as ‘superbainite’. This steel consists of exceptionally thin platelets of bainitic ferrite separated by films of retained austenite, a structure produced by heat treatment alone [22, 23, 28] — yet one that results in an interfacial area per unit volume that is greater than that associated with the majority of severe plastic deformation experiments [29]. This gives the bulk material high strength and hardness, and reasonable toughness and ductility [30–33].

With this class of alloys, as with all types of steel, it is crucial to build an understanding of the mechanisms that govern the properties. In particular, the

ductility and impact toughness of superbainite are lower than expected, which is problematic when structural integrity is crucial [23, 34, 35]. It has been shown that both the ductility and the impact toughness may be improved by austempering the alloy at a higher temperature, although this will reduce the strength [36–38]. There are also additional complications. Other factors — such as the behaviour and composition of retained austenite under stress and strain; the work-hardening rate and the ‘composite effect’ — come into play [39–41]. A small number of speculative theories has been proposed to account for the mechanical properties observed in these alloys, accompanied by some supporting evidence [35, 40, 42–44].

The aim of this work was therefore to investigate the phenomena that are thought to influence toughness and ductility in these and similar mixed-microstructure steels. The focus is on understanding how this highly refined two-phase microstructure responds to loading conditions characteristic of various standard mechanical tests. Using novel approaches, it has been possible to obtain experimental evidence in support of existing theories that purport to explain the mechanical behaviour of the alloys in question.



*I shall not today attempt to further define the kinds of material I understand to be embraced within that shorthand description; and perhaps I could never succeed in intelligibly doing so. But I know it when I see it.*

Justice Potter Stewart, *Jacobellis v. Ohio*

## CHAPTER 2

---

# LITERATURE REVIEW: THE BAINITE CONTROVERSY

---

## 2.1 Introduction

The value of a scientific theory lies both in its ability to explain our observations and in its usefulness as a predictive tool. A theory of phase transformations is no different in this regard, enabling us on the one hand to account for observed microstructural features and, on the other, to design new microstructures according to our own requirements.

Metallurgy is a strongly practical subject, driven by the development of new alloys with improved properties. The bainitic microstructure has become widely used in industrial applications and as technology evolves, greater demands are placed upon materials. It is thus essential to develop a quantitative understanding of the kinetics of the bainite transformation, so that new alloys may be designed to meet high performance industry standards. More ambitiously, one could create steels with better-than-expected properties, opening up the potential for new applications.

The progress towards a quantitative theory of the bainite transformation has been controversial, however, with opinion divided as to whether the mechanism is diffusion-controlled or displacive and diffusionless. This review is intended to chart the development of the two theories — from their initial conception to the quantitative models as they exist today.

To begin with, it is important to highlight that there have been many attempts to produce an exact definition of bainite, based upon microstructural or kinetic features. However, it has been difficult to settle on a generally accepted definition [45–47]. The various definitions can be inconsistent with each other, so a phase may be called bainite in terms of one definition but not another [45–49]. Although this is relatively inconsequential when simply describing a structure, problems arise when the definition is used to link the structure to a specific mechanism. Over time, some less familiar forms of bainite have been described: these include granular bainite [50], columnar bainite [51] and inverse bainite [52]. These terms have value in communicating the appearance of a microstructure. However, it is misleading to imagine that the morphologies share similar, ‘bainitic’, mechanisms of transformation, since they do not [9].

Granular bainite is the most ‘accurate’ term of the three, commonly used to describe the (partly) bainitic microstructure obtained from a continuous cooling process. The appearance is of a coarse ferrite matrix containing islands of martensite and austenite [50, 53], although in reality the ferrite region is made up of bainitic ferrite sheaves separated by thin regions of austenite [54]. The granular appearance is due to the gradual transformation that occurs during continuous cooling, resulting in the formation of coarse sheaves of bainite. On an optical scale, it looks different from ‘ordinary’ bainite; in the electron microscope, the two structures are similar [55]. Inverse bainite forms in hyper-eutectoid steel, with cementite precipitating first and ferrite forming consequentially on the precipitated cementite plates [52, 56]. However, little evidence has been provided to support the assertion that this structure is bainitic, and the mechanism of transformation is not well understood [9]. Columnar bainite is another structure associated with hypereutectoid compositions. The morphology is of a nonlamellar arrangement of cementite and ferrite in the shape of “an irregular and slightly elongated colony”, however, the mechanism of formation is reconstructive [57]. It has been asserted that to call these latter two structures “bainite” is a misnomer due to their different mechanisms of transformation [9, 57, 58] although according to the generalised microstructural definition [6, 59], the description is accurate.

In order to avoid confusion, it is helpful to identify some of the agreed-upon, and notable, features of the bainite transformation, for which any theory must

provide an explanation:

## Upper and lower bainite

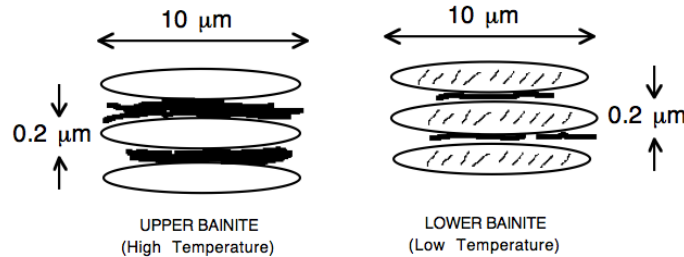


**Figure 2.1:** The microstructural features of upper and lower bainite (from Bhadeshia [9]). The dimensions are approximate and dependent upon factors such as transformation temperature and composition.

Bainite manifests as two distinctly different forms: upper bainite and lower bainite [60]. Upper bainite exhibits a characteristic lath shape, comprised of ferrite subunits of matching crystallographic orientation arranged in units called ‘sheaves’. The subunits themselves are separated by carbide precipitates, and can be of either plate or lath morphology.

The subunits in lower bainite tend to be coarser than those in upper bainite, but the two morphologies are similar as far as microstructure and crystallography are concerned. However, in lower bainite, the individual ferrite subunits also contain a fine distribution of carbide particles in addition to the inter-platelet carbides.

Figure 2.1 illustrates the essential differences between the two microstructures, and micrographs of upper and lower bainite subunits are shown in Figure 2.2. Upper bainite forms at higher temperatures (550-400°C) than lower bainite (400-250°C) in the same steel. The transition is also determined to an extent by the carbon content of the steel [55]. Mixtures of upper and lower bainite may be obtained by isothermal transformation.

## The bainite-start temperature

It can be demonstrated for many steels that there is a temperature  $B_S$  above which no bainite will form [62]. In some steels this corresponds to the bay in the

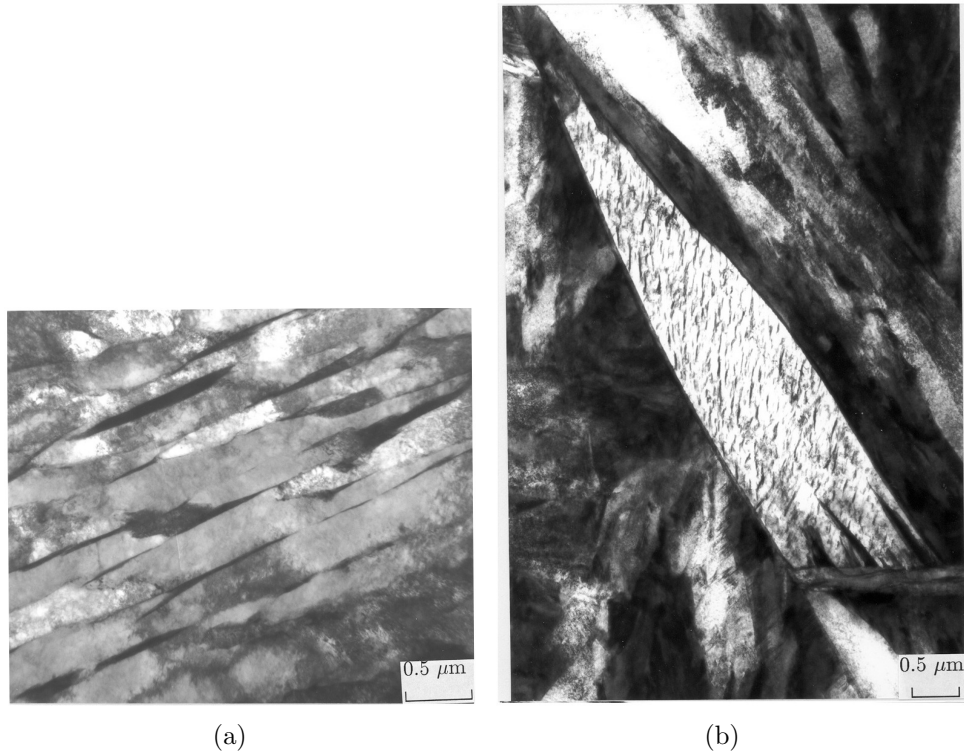


**Figure 2.2:** Transmission electron micrographs of (a) upper bainite subunits in a 0.095C-1.63Si-1.99Mn-1.97Cr wt% steel and (b) lower bainite subunits in a 0.46C-2.10Si-2.15Mn wt% steel. Image (b) shows carbide precipitation within the subunits themselves. From Chang and Bhadeshia [61].

TTT diagram between the overlapping curves of pearlite and bainite [63]. This temperature is well below that at which pro-eutectoid ferrite formation becomes thermodynamically possible.

### The incomplete-reaction phenomenon

As the transformation temperature is reduced below  $B_S$ , the fraction of austenite that transforms to bainite is progressively increased [64]. However, during isothermal transformation, a limit is reached beyond which austenite will no longer transform to bainite, despite a significant quantity remaining untransformed. The reaction is said to be ‘incomplete’ since it is halted before the austenite achieves the equilibrium composition. The extent of the incomplete transformation in a given steel is composition-dependent: higher carbon contents will reduce the degree of transformation at a given temperature [65], although the phenomenon is difficult to detect in plain carbon steels.

## 2.2 The origin of the two theories

The nature of the bainite transformation has been a subject of controversy ever since the bainitic microstructure was identified by Davenport and Bain in 1930 [6]. Figure 2.3 is a reproduction of the ‘dark-etched, acicular microstructure’ they observed. It was suggested that such a phase transformation “would occur just a little in advance of the carbide precipitation”, *via* a process akin to that of the martensite transformation.

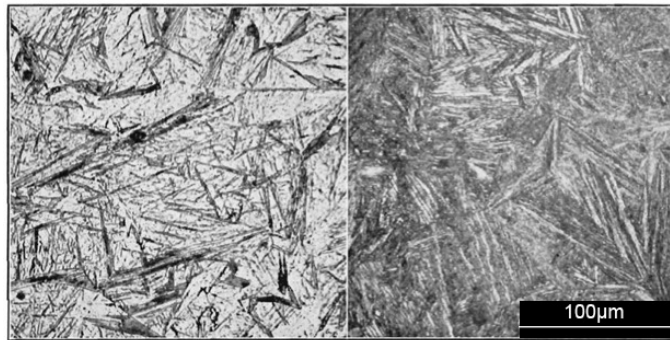


**Figure 2.3:** The original micrographs of ‘martensite-troostite’ taken from the work of Davenport and Bain [6]

The theory of a displacive mechanism of bainite formation had been proposed in 1926 by Hultgren [66] to explain observations of what he described as “needles of troostite” (but which was characteristic of a bainitic microstructure, troostite being the name then given to all fine mixtures of ferrite and cementite). First referred to as ‘martensite-troostite’ in the 1930 paper due to morphological similarities to martensite (see Figure 2.4), bainite has maintained an association with the martensitic microstructure. Some have suggested that this initial case of mistaken identity influenced early theories of bainite formation [67, 68]. It is certainly true that some subsequent work expressed as a fact the assumption that bainite forms with a supersaturation of carbon [69–71]. One early example is the mechanism described by Vilella [72] as the rapid growth of flat plates of ‘quasi-martensite’ — supersaturated ferrite — which subsequently reject the excess carbon into the surrounding austenite at a rate dependent on the transformation temperature. This entire process was thought to last only a few millionths of a second. Vilella’s work built upon the ideas of Davenport and Bain to form the beginnings of a diffusionless, displacive theory of transformation.

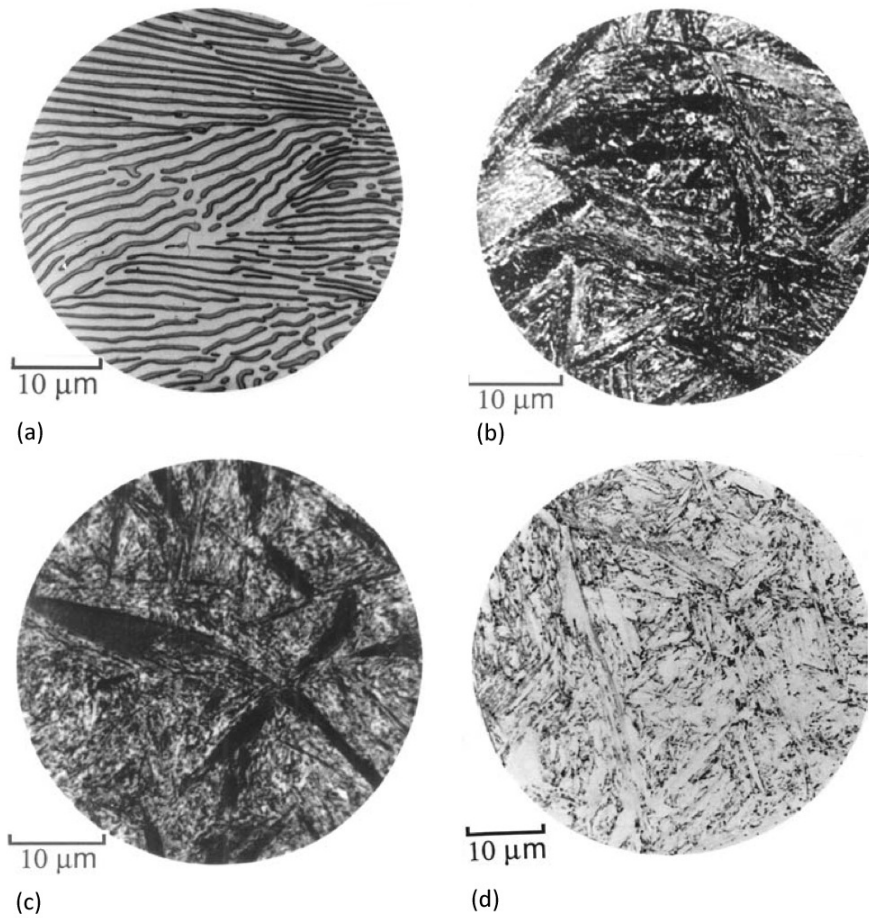


**Figure 2.4:** Micrographs of structures in a eutectoid steel taken by Vilella [73] and reproduced in Bhadeshia [9]: (a) Pearlite; (b) bainite formed at 290°C (c) bainite formed at 180°C; (d) martensite. Note the similarities between the bainite and martensite morphologies.

Robertson also made a direct observation of the bainite microstructure prior to the 1930 paper, but failed to identify it as a new structure [59]. At the time, interest was focused on ‘intermediate microstructures’. Named martensite, troostite and sorbite, these microstructures were thought to form sequentially as transitional stages of the austenite-pearlite transformation. Robertson’s detailed study of the relationship between these microstructures and cooling rate provided him with several micrographs of dark-etched acicular structures that he struggled to identify. He compared the bainite to pearlite, suggesting that the “complete change in the crystallography of the structures” was due to pearlite being nucle-

ated by carbides, and bainite being nucleated by ferrite. He remained convinced that the growth of the Widmanstätten-like structures was limited by carbon diffusion. Much work to follow agreed with this hypothesis and many felt that a diffusion-controlled transformation was the correct explanation [60, 67, 74, 75].

The classification of bainite into two forms — upper and lower bainite — provided an opportunity for a theory incorporating two different mechanisms of transformation. Indeed, it was suggested that upper bainite formed *via* a diffusion-controlled process, while lower bainite was formed *via* lattice shearing [60]. Similar theories would be put forward for many years to come, and will be discussed later.

## 2.3 A thermo-kinetic explanation

Hultgren approached the problem of a displacive *versus* a reconstructive mechanism by considering the shape of TTT-diagrams of various steels. The presence of two distinct C-curves suggested that two different transformation mechanisms were at work [74]. In the cases of alloy steels there was a clear break in the zero-line, which was interpreted as evidence of a change in transformation mechanism, although Hultgren did not believe the bainitic mechanism was diffusionless. However, his measurement of the alloy content of pearlitic cementite indicated that it had a higher alloy content than bainitic cementite (in the same steel), which shared the composition of the austenite. This is consistent with a diffusionless mechanism of transformation and led Hultgren to theorise that substitutional alloying elements do not participate in the bainite reaction.

One year earlier, in 1946, Zener had undertaken an analysis of the decomposition of austenite in which he assumed a diffusionless mechanism of bainite formation [71]. He arranged various alloying elements in order of their effectiveness in retarding the bainite transformation, and noted that this order was identical for both bainitic and martensitic transformations, implying that the two were “closely related”. He saw that certain alloying elements were more effective at retarding the pearlite transformation than the bainite and martensite transformations. The ability to do this seemed to correlate to the carbide-forming tendency of these elements. Indeed, it was well-known that in high alloy steels the bainite reaction remained rapid even when the pearlite transformation was very slow [76].

This built upon work done by Davenport to elucidate the effect of alloying elements upon isothermal transformation curves [77]. He too had documented the severity of the retardation to be linked to carbide-forming tendency, although he also wrote that “in many instances these curves [are] so individual that it is very difficult indeed to summarize the trends except in a quite general way.” Chromium, molybdenum and vanadium were strongest at limiting predominantly the pearlite transformation, while combinations of these and other elements were found to have more complex effects. Cobalt, meanwhile, had the opposite effect: it accelerated the decomposition of austenite.

Zener’s conclusion was that the alloying elements concentrated at nucleation sites, producing alloy carbides during pearlite formation. The subsequent segregation of the substitutional alloying elements slowed the transformation. However, the effect of these elements on bainite and martensite was not believed to be related to nucleation, but rather to the free energy available for the transformation. The elements would affect the free energy of the system during pearlitic transformation as well, of course, but the dominant effect here was due to segregation. At the lower temperatures of bainite and martensite transformation, substitutional solutes are kinetically immobile, and so they cannot segregate to form alloy carbides. Their dominant effect was to alter the driving force for the phase transformations. Later, experimental work by Hultgren [74] and Murakami and Imai [78], as well as others, would support this theory.

Zener used the idea of free energy to explain the growth of bainite, by quantifying a  $T_0$  temperature — the temperature at which austenite and ferrite of the same composition have the same free energy. Zener expressed the change in free energy of the system as a sum of three factors:

$$\Delta G = -\Delta G_{Fe^{\alpha\gamma}} + C\Delta G_{C^{\gamma\alpha}} - CT\Delta S_{C^{\gamma\alpha}} \quad (2.1)$$

where

$-\Delta G_{Fe^{\alpha\gamma}}$  = the change in free energy of one mole of pure iron in the austenite phase compared to the ferrite phase;

$\Delta G_{C^{\gamma\alpha}}$  = the change in free energy of one mole of carbon in the ferrite phase compared to the austenite phase (similar expressions may be included for other

alloying elements, if present);

$\Delta S_{C\gamma\alpha}$  = the excess of entropy of one mole of carbon when dissolved in austenite (this factor is negligible if the transformation proceeds quickly compared with the rate of carbon diffusion);

$C$  = the molar fraction of carbon in the original austenite. The final ferrite retains this carbon concentration.

By setting  $\Delta G$  equal to zero, it is possible to solve equation 2.1 for the austenitic carbon concentration in terms of the critical temperature. It is this line, plotted on an equilibrium phase diagram, that became known as the  $T_0$  line. If one considers a steel of a given carbon content, the  $T_0$  line represents a maximum possible temperature for the bainite transformation: a  $B_S$  temperature. Similarly, for a fixed transformation temperature, the  $T_0$  line limits the degree of transformation.

The limiting influence of the  $T_0$  temperature on the bainite transformation was an important idea that had also been explored by Wever and Lange [79]. A consideration of the free energy of the system and of the equilibrium phase diagram serves to illustrate the key features of the theory (Figures 2.5 and 2.6).

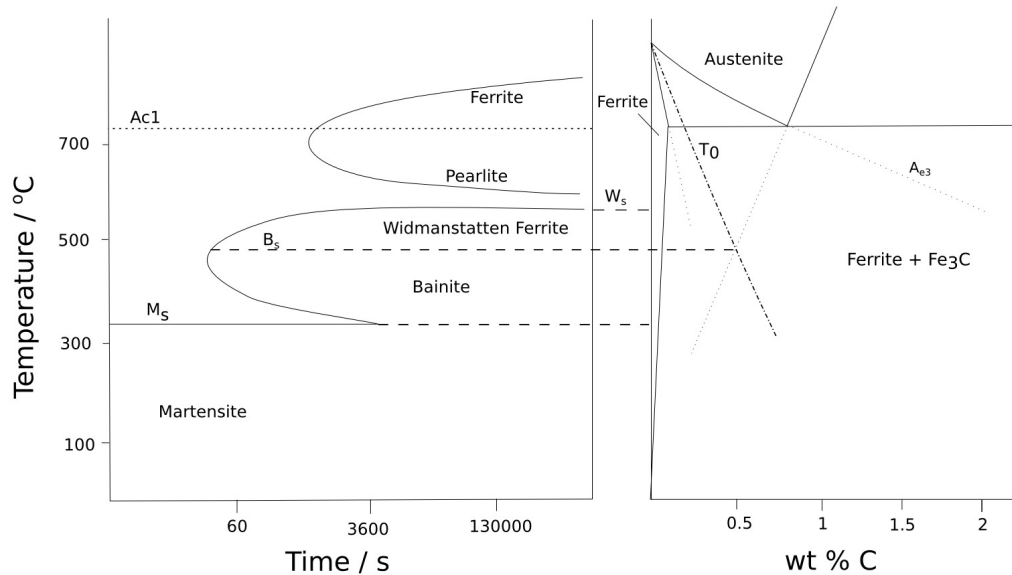


**Figure 2.5:** A sketch showing how the  $T_0$  line determines the bainite start temperature, and how this is related to the phase diagram and corresponding TTT diagram.

During isothermal transformation, a subunit of bainite — supersaturated with

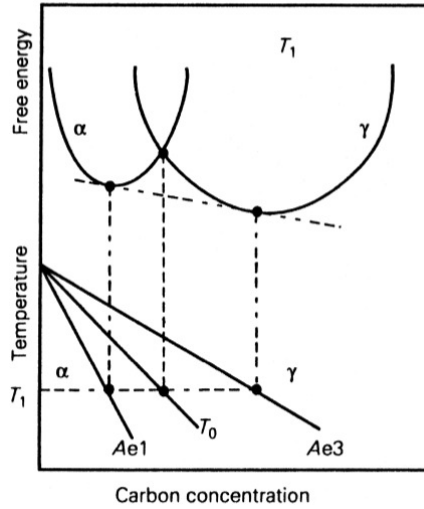


**Figure 2.6:** Illustration of the  $T_0$  line on an Fe-C phase diagram, from Bhadeshia [9]

carbon — grows from austenite. The excess carbon is subsequently rejected into the surrounding austenite, increasing its carbon content (assuming that carbides are not formed by precipitation). The next subunit of bainite must then nucleate and grow from carbon-enriched austenite, for which there is a slightly lower driving force. From Figure 2.6, it can be seen that, as the carbon content of the austenite continues to increase, the free energy available for transformation to bainitic ferrite will fall until it reaches zero at the  $T_0$  line, and no more austenite will transform. It was suggested that this was responsible for the incomplete transformation phenomenon. In the case of carbide precipitation, carbide film formation around the bainite subunits was thought to prematurely halt the transformation. That this occurs before the austenite reaches an equilibrium composition marked by the  $Ae_3$  line is indicative of a diffusionless, displacive transformation.

Experimental results using 3% chromium steels agreed with the predictions of this theory [71] and were consistent with Davenport's observations. Zener was able to account for the anomalous behaviour of cobalt by noting that the quantity  $\Delta G_{C\gamma\alpha}$  would be negative, rather than positive as it was for most alloying elements. The addition of cobalt would therefore increase the driving force for austenite decomposition.

As a result of his work, Zener claimed that a diffusionless mechanism of bainite formation could explain the incomplete transformation phenomenon, the  $B_S$

temperature, the variation in microstructure between upper and lower bainite and the effects of alloying elements. However, several researchers disagreed with the implication that the controversy had been settled. Troiano claimed that the bainite reaction was “time dependent and in this respect completely dissimilar to the martensite reaction” (although since martensite formation is a first order transformation it is also time dependent) [80]. Meanwhile, Klier insisted that the assumption of a diffusionless mechanism was due to a misunderstanding of the data presented in 1944 [64], instead claiming “incontrovertible evidence that a fluctuation of carbon concentration precedes the formation of bainite”. His theory stated that these fluctuations would produce regions of low- and high-carbon austenite, so that austenite enrichment took place prior to the bainite reaction, *via* diffusion.

### 2.3.1 Comparisons with martensite and pearlite

As discussed in Section 2.2, the bainite microstructure was confused with martensite at the time of its discovery. When faced with a new decomposition product, it is understandable that the first step is to attempt to link it and place it relative to known morphologies. This was an approach taken by both schools of thought, with diffusive theories attempting to link bainite and pearlite together.

Interestingly, Zener also undertook a free energy analysis of the martensite transformation in his 1946 work, deriving an expression similar to equation 2.1:

$$\Delta G = \Delta G_{Fe^{\alpha\gamma}} + C\Delta G_{C^{\gamma\alpha}} + \Delta U \quad (2.2)$$

Here, in the case of rapid transformation, the entropy term is neglected and replaced with  $\Delta U$ , representing the strain energy of the transformation. Once again, the  $\Delta G$  term can be set to zero and thenceforth it is possible to relate a given carbon content to a critical temperature: the  $M_S$  temperature.

However, Zener stopped short of assuming that bainite was also formed via a shear transformation, like martensite. He chose to distinguish the martensite and bainite phases by the residual strains and stresses associated with the former, since he believed that bainite formation was not accompanied by strain [81]. According to him, it was only the alloying elements that did not diffuse during the

bainite transformation. The process still required “the transfer of iron atoms from equilibrium positions on the austenite side of an interface to new equilibrium positions on the bainite side of the interface”, but Zener was vague as to how this occurred. In some ways, Klier and Lyman took an opposite view to that of Zener. Although they proposed that carbon diffusion produced inhomogeneities in the austenite composition, they believed that the low-carbon regions would transform to supersaturated ferrite via a martensitic shear mechanism [64].

Hultgren, meanwhile, considered analogies with both martensite and pearlite. His work led him to develop separate hypotheses for bainite formation in alloy and plain carbon steels [74].

In an alloy steel (as in all steels), martensite is formed without diffusion and inherits its composition from the austenite. Hultgren postulated a form of BCC iron that would, at intermediate temperatures (i.e. those at which bainite formed), inherit the *substitutional* alloy content from the austenite, while the carbon was still free to diffuse at a reasonable rate [74]. He named this metastable state ‘paraequilibrium’ and the ferrite ‘paraferrite’. The growth of paraferrite would eventually be accompanied by the formation of ‘paracementite’ (also inheriting its substitutional solute composition from the parent austenite). He compared this to pearlite, formed in alloy steels via diffusion of all elements — a state he named ‘ortho-equilibrium’. Both morphologies, he suggested, underwent diffusion-controlled growth, becoming finer at lower transformation temperatures.

Hultgren extended his theory to the case of very low or zero carbon content alloys, in which martensite and paraferrite would be the same thing [74]. Troiano pointed out that this seemed unlikely since paraequilibrium transformation appeared to exclude the possibility of homogeneous shear that was characteristic of martensite [82]. Transformation curves as determined by Lyman and Troiano for 3% chromium steels seemed “to offer no chance of [the bainite and martensite curves] extrapolating to the same temperature at zero carbon content” [65, 82].

Where plain carbon steels were concerned, Hultgren took note of the theories of Robertson [59] and Mehl, which were based upon orientation observations of pearlitic and bainitic ferrite. Hultgren classified propearlitic ferrite, bainitic ferrite and martensite as sharing a single orientation of ferrite relative to the

austenite. He named this the primary orientation, to distinguish it from the orientation of pearlitic ferrite (which he called the secondary orientation) [83]. He also distinguished the orientations of pearlitic cementite and bainitic cementite with similar terms. Pearlitic cementite was of a primary orientation while bainitic cementite was of a secondary orientation [84].

Pearlite formation would begin with cementite nucleation and growth, followed eventually by the nucleation and growth of an adjoining ferrite particle. The presence of pearlitic cementite would encourage the ferrite to grow in its less-preferred (secondary) orientation. In contrast, bainite would nucleate with a particle of ferrite in the primary orientation, which would result in cementite precipitating and growing in its secondary orientation. This theory implied that bainite was an ‘inverse’ sort of pearlite. The different transformation temperatures of pearlite and bainite were thought to affect the relative power of ferrite and cementite to influence the other’s orientation. The possibility that this process could also occur in alloy steels was not ruled out. Some criticism of his ideas came from Dubé and Alexander [85] who believed that the ‘orientation power’ of ferrite and cementite should be independent of transition temperature.

## 2.4 Growth rate and surface relief

Ko and Cottrell, in their 1952 work, approached the problem from a different angle, using hot stage microscopy to observe the growth of bainite in a range of alloy steels [86]. They found that the growth rate was slow compared with that of some martensitic transformations, and observed that bainite formation was a continuous, rather than an incremental, process. This indicated a diffusion-driven transformation. However, in the same study, they recorded a surface relief similar to that of martensite, and found that bainite plates did not cross austenite grain or twin boundaries. Both of these factors pointed towards a displacive transformation. Furthermore, the surface relief was indicative of strain, demonstrating Zener’s earlier assumption to be incorrect.

In order to circumvent these contradictory observations, they proposed a new type of transformation to describe both bainite and martensite transformations. Named ‘coherent transformation’, it allowed for shear transformations subject to the kinetic limitations of carbon diffusion into the parent austenite. They

suggested that at temperatures below  $B_S$ , there exists a driving force for decomposition of austenite into supersaturated ferrite, in terms of the free energy change of the system. However, additional driving force is needed to accommodate the increase in volumetric and shear strain energies incurred during martensite formation: this is therefore only possible at large undercoolings (i.e. below  $M_S$ ). At intermediate temperatures, this strain energy could be reduced by lowering the carbon content of the supersaturated ferrite (either by carbide precipitation or diffusion), altering the energy balance and favouring transformation to an alternative product: bainite.

This placed bainite on a continuum with martensite, and also neatly explained the existence of upper and lower bainite (in upper bainite, carbon is removed predominantly by diffusion; in lower bainite, by precipitation). The presence of carbide-forming alloying elements was thought to ‘anchor’ clusters of carbon atoms, reducing their mobility and thus slowing the growth of bainite. Within this framework, the distinction between bainite and martensite moved from being based upon strain to being based upon the presence or absence of carbon diffusion.

Ko and Cottrell’s growth rate measurements were later confirmed by other publications [87, 88] and seemed to point conclusively towards a diffusion-controlled transformation. Zener’s equation governing diffusion-controlled edgewise growth of a plate was modified by Hillert, who applied it to Widmanstätten ferrite and bainite [52]. After some further refinements [67, 89, 90] and comparison with experimental data [91, 92] it seemed that the measured growth rates were slightly lower than those predicted by carbon diffusion, allowing ferrite of both types to grow at a rate low enough to avoid supersaturation of carbon.

Meanwhile, those supporting the diffusionless paradigm concentrated on the surface relief evidence. Confusingly, further studies revealed that Widmanstätten ferrite (thought to form *via* diffusion) also produced a surface relief [93]. Many attempts were made to reconcile or explain away the conflicting results.

In particular, Oblak and Hehemann, in 1967, examined the structures of Widmanstätten ferrite and bainite more closely [94]. Their electron micrographs revealed that Widmanstätten ferrite formed as single crystals, while upper bainite plates consisted of much smaller subunits. They concluded that there was no

evidence that Widmanstätten ferrite and bainite formed via the same mechanism. This meant that the presence of a surface relief could not be used as evidence of a diffusionless mechanism. Although this seemed to deal a blow to the diffusionless theory, the authors proposed a mechanism of bainite formation whereby the individual subunits grew rapidly via a diffusionless, displacive transformation. The growth rate of bainite was limited not by diffusion, as had been believed, but by the rate of nucleation of these subunits. The shape and size of the subunits was restricted by the displacement strain accumulated during growth. In this way, a plate-like sheaf of bainite could be “formed by the sympathetic nucleation of successive subunits” (Figure 2.7).

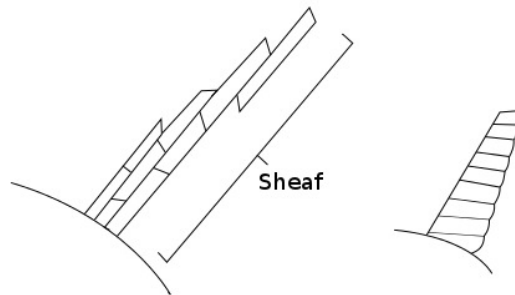


**Figure 2.7:** Sketches of two possible structures formed by the repeated nucleation and growth of subunits as postulated by Oblak and Hehemann [94].

## 2.5 A crystallographic approach

The discovery of uniformly-distributed  $\epsilon$ -carbides [10, 94, 95] (which had never been observed to precipitate from austenite) in lower bainite was consistent with the belief that bainitic ferrite forms in a supersaturated state. Using dilatometric techniques, Deliry measured the amount of  $\epsilon$ -carbide in lower bainite and found it equivalent to the total carbon content of the steel [95]. These observations indicated that a displacive mechanism was at work, although they did not exclude the possibility that the shear mechanism was diffusion-controlled.

The method of carbide formation in upper bainite was less clear. The presence of a large quantity of carbon-enriched austenite suggested a diffusional mecha-

nism [94], but crystallographic evidence [96, 97] seemed to point towards carbide precipitation from carbon-enriched austenite following a displacive, diffusionless transformation. Whether this precipitation takes place during or after the bainite transformation, however, was a puzzle that was to remain unsolved.

The general understanding followed Christian [98], who accepted that lower bainite formed from ferrite supersaturated with carbon but upper bainite did not. It was therefore suggested that “the crystallography of upper bainite should match that of low-carbon martensite while that of lower bainite should match the crystallography of martensite (in the same alloy)”.

Following from Ko and Cottrell’s surface relief observations, further work had characterised the bainite shape change as approximately an invariant-plane strain (Figure 2.8), similar to that associated with martensitic transformation [99]. Furthermore, evidence showed that the austenite and ferrite were related by a Kurdjumov-Sachs relationship in both bainite and martensite [97, 100]. This led Srinivasan and Wayman, in 1968, to undertake a phenomenological analysis of the lower bainite transformation [101].

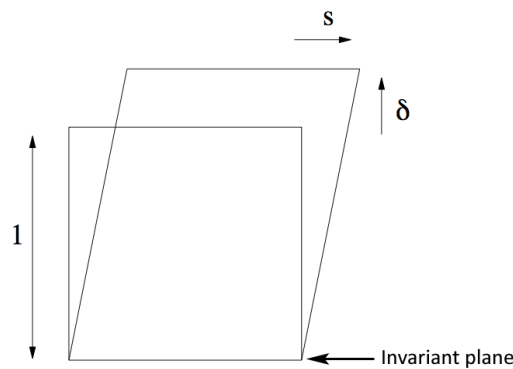


**Figure 2.8:** Schematic of an invariant-plane strain. The invariant plane is the habit plane and the displacement consists of a dilatational component ( $\delta$ ) and a shear component ( $s$ ), producing a homogeneous distortion.

Alongside this, they carried out TEM and X-ray work, hoping to measure crystallographic parameters (habit plane and specific variant of the austenite-ferrite orientation relationship) for comparison with their theoretical work [101, 102]. They found that, while martensite often exhibited internal twinning, there was no evidence that it occurred during the bainite transformation. The orientation

relationship of the carbides in bainite pointed towards the presence of slip planes predicted by the theory to be operative during formation, which supported the conclusion that bainite formed *via* shear and stepwise growth. Moreover, the discovery that bainite forms as platelets in three dimensions bolstered the case for a displacive transformation, since one would expect a parallel arrangement of plates from a diffusive process. Overall, their practical and theoretical work agreed well, and seemed to indicate a shear transformation mechanism for lower bainite.

These results were questioned by Kinsman and Aaronson (in a debate with Hehemann) [46], who argued that the agreement between observed crystallography and phenomenological theory was only possible by assuming a contraction of the ferrite lattice during transformation — something they did not accept was correct. Srinivasan and Wayman, along with Edwards and Kennon [103] found no similarity between the orientation relationships and habit planes of lower bainite and martensite. Kinsman and Aaronson therefore concluded that “neither upper nor lower bainite forms by a martensitic mechanism”. Instead, they promoted a growth mechanism involving the propagation of ledges controlled by a diffusive process [104]. The principle was validated by the work of Laird and Aaronson on aluminium alloys [105, 106], so it became a question of whether it was also applicable in ferrous alloys.

Nemoto’s 1974 work [107] confirmed the results of Kinsman and Aaronson, who had used thermionic emission microscopy to show that bainite growth was continuous and did not occur in steps [46]. However, his results also revealed the formation of dislocations in and around the bainite, characteristic of a plastic relaxation accompanying a displacive shape change. Hehemann, meanwhile, argued that the lack of twinning in bainite was responsible for the variation in habit plane, and did not rule out a displacive mechanism [46]. Although the data were specific to lower bainite, Hehemann believed the conclusions could be applied to upper bainite also. Referring back to Ko and Cottrell [86], he insisted that “the question of the continuity of the growth process is independent of the growth mechanism”: slow continuous growth rates could equally support a shear mechanism controlled by carbon diffusion.

Although bainite was often compared with martensite, the similarities between

bainitic ferrite and Widmanstätten ferrite were also especially strong, leading some to argue that there should not be a distinction between the two [68, 86]. Others attempted to demonstrate how the two phases could achieve such a similar appearance *via* different transformation mechanisms [25, 108–111].

There was much evidence to suggest that the surface relief of Widmanstätten ferrite corresponds to an invariant-plane strain with a large shear component [108]. Questions arose as to whether a ledge mechanism as proposed by Aaronson could produce such surface relief [108]. Instead it was found that the observed surface relief was in good agreement with the predictions of the Bowles-Mackenzie crystallographic theory [99], suggesting that Widmanstätten ferrite grew with a displacive mechanism. It certainly seemed that the presence of an invariant-plane strain was at odds with a diffusional or massive transformation [112, 113]. However, Aaronson *et al.* demonstrated that it was thermodynamically impossible for Widmanstätten ferrite to form *via* a shear mechanism [109]. McDougall disagreed with this analysis, pointing out a flaw in their assumption that the ferrite would be elastically accommodated [110]. He asserted that plastic relaxation would relieve the elastic strain energy under transformation conditions, thus overcoming the thermodynamic barrier.

In 1980, Bhadeshia interpreted the Widmanstätten crystallography as indicative of back-to-back displacive growth of mutually accommodating ferrite plates [111]. He went on to develop a kinetic theory of nucleation and growth, whereby both Widmanstätten ferrite and bainitic ferrite underwent carbon partitioning at nucleation, but only bainitic ferrite grew without diffusion, instead rejecting carbon into the austenite after the transformation was complete [25]. This implied that, at nucleation, the two forms were identical, and the formation of bainite was dependent upon the availability of a sufficient driving force to sustain supersaturation during growth. Although the bainitic ferrite would appear virtually identical to Widmanstätten ferrite, the stored energy of bainite was expected to be significantly higher. The equilibrium carbon content of the bainite nucleus, in contrast to the supersaturated martensite nucleus, was thought to explain the differences in crystallography between those two microstructures.

## 2.6 A mechanism-based theory for bainite nucleation and growth

The crystallographic incongruities having been tackled, the problem returned to one of carbon diffusion. Bhadeshia and Edmonds argued strongly for the diffusionless case [114, 115]. Their electron micrographs of a silicon steel revealed lenticular subunits separated by retained austenite of the same crystallographic orientation. The observation of subunit growth even when carbide formation was suppressed implied that the subunits could not be compared with ledges, since they were individually isolated by carbon-enriched austenite films. The addition of silicon was an important step, since it allowed the study of the austenite-ferrite transformation without the interference of carbide precipitation.

The size of each subunit was limited by a frictional stress associated with the plastic accommodation of the shape deformation, such that constant nucleation of new subunits was required to propagate a sheaf [114]. This growth occurred *via* sympathetic nucleation at the tips of fully formed subunits. It was shown that this was energetically more favourable than nucleation adjacent to the subunits; by nucleating at the tips, the new subunits could avoid the carbon-enriched regions formed by diffusion from complete subunits [115]. The total volume fraction of bainite formed was limited by the  $T'_0$  line.

The  $T'_0$  line is a modification of the  $T_0$  line that includes the strain energy of the bainite transformation. It was first proposed by Le Houillier *et al.* [116] and represents the point at which the free energies of austenite and ferrite of the same composition are equal, once this strain energy has been incorporated into the calculation. The value of the strain energy was calculated to be  $400 \text{ J mol}^{-1}$  [25]. The difference between  $T_0$  and  $T'_0$  was considered to be negligible by some [117], and certain subsequent papers continued to refer to  $T_0$ , neglecting strain energy. This approach would later be criticised by Hillert, whose own calculations pointed to a significant difference between  $T_0$  and  $T'_0$  [118].

Although the work of Bhadeshia and Edmonds did not account for carbide precipitation, it was emphasised that it was a process in direct competition with carbon rejection into residual austenite. If this were the case, it would explain

why the incomplete transformation phenomenon was difficult to detect in plain carbon steels, where precipitation processes dominate. In alloy steels, the suppression of cementite, and kinetic barriers to the formation of alloy carbides (even those thermodynamically more stable than cementite, e.g.  $\text{Cr}_{23}\text{C}_6$ ) minimise the presence of precipitation, so incomplete transformation is readily observed.

This and other work [26] was consolidated into a mechanism-based theory for the bainite reaction [119]. It was able to reproduce the effects of various alloying elements (Ni, Si, Mn, Cr) on the shape of TTT curves and transformation kinetics. However, the authors themselves noted that the predictive ability of their theory was somewhat limited by an inability to account for “secondary effects” of these elements. Nevertheless, it was a good starting point and would continue to be improved over the following years [24, 120–123].

## 2.7 Experimentally-based criticisms

Since the 1950s, there had accumulated a great deal of experimental evidence showing ‘solute-induced diffusional drag on grain boundary motion’ (‘solute drag’) [124–128]. The original work of Lücke and Detert [129] had postulated that grain boundaries represented low energy regions for impurity atoms. These atoms would therefore segregate and diffuse in the boundary, exerting a dragging force on the grain boundary as it continued to grow. However, despite much development of the accompanying quantitative theory it still could not be generalised to any interphase interface [130]. Some variations of this theory required segregation of alloying elements to the transformation interface. This idea was used to reconcile a diffusional transformation with observed incongruities in the kinetic measurements of the bainite transformation, for example: the incomplete transformation phenomenon [45, 46, 131].

The solute-drag concept was not the only diffusion-controlled model that had been applied to the bainite transformation. The local equilibrium model [132] assumed a constant partial molar free energy among elements across the austenite-ferrite interface. This requires both the alloy and carbon atoms to partition during transformation. In the case of highly-supersaturated phases, the local equilibrium model also demands a narrow concentration spike for alloy elements in the interfacial austenite, in order that the alloy concentration at the interface

match the equilibrium value [75].

Paraequilibrium transformation, in contrast, requires only partial supersaturation and no redistribution of substitutional alloying elements across the transformation interface (as first suggested by Hultgren [74]). Carbon partitions during transformation to maintain a constant partial molar free energy across the interface, while the X atoms, with a much lower diffusivity than carbon, do not. In the case of ferrite, the model implies that growth is controlled by carbon diffusing across the interface, in accordance with equilibrium conditions, whereas the atomic X:Fe ratio is constant across the interface and remains so for the duration of the transformation.

These theories were reviewed carefully by Bhadeshia and Waugh [26, 133], who used atom-probe imaging to examine the distribution of various elements across a bainitic ferrite-austenite interface. They found no evidence of a compositional spike of alloy elements, nor did they detect (substitutional) solute segregation, in direct contradiction to the theories of local equilibrium and solute drag. On the contrary: it has been demonstrated that there is no difference between the substitutional alloy element content of bainite and that of the parent austenite [134–136].

They also undertook a thermodynamic analysis of the incomplete transformation phenomenon, assuming a paraequilibrium mechanism. The calculated levels of carbon supersaturation in the ferrite during growth were too high to be physically feasible, indicating that the paraequilibrium hypothesis may also be invalid [26].

Most exciting, however, was the use of hot-stage microscopy to observe the growth of individual subunits of bainite [133]. The measured growth rate under these conditions at 380°C was  $75 \mu\text{m s}^{-1}$  — about three times faster than the maximum growth rate allowed by diffusion of carbon, as calculated using Trivedi's theory [90, 137]. This seemed to put paid to the idea that the bainite transformation was diffusion-controlled, and provided direct evidence for Oblak and Hehemann's theory. However, the work has been criticised as being merely 'preliminary', with no subsequent follow-up or further work being published [68]. Many instead pointed to the larger body of work showing lower growth rates.



Hillert combined his diffusionless model with the work of Ohmori and Maki [140] and Steven and Haynes [141] on Fe-C alloys. He first validated the model using  $M_S$  data (Figure 2.9(a)): he took a value of  $600 \text{ J mol}^{-1}$  for the driving force [142] and assumed a diffusionless, adiabatic transformation, achieving quite good agreement with experimental  $M_S$  values taken from Ohmori and Maki. By comparing  $B_S$  data with the calculated  $T_0$  line (Figure 2.9(b)), he showed that the  $B_S$  data bore no relation to the  $T_0$  line. Although the data for  $B_S$  are not very extensive in this case, these results indicated that neither  $T_0$  nor  $T'_0$  corresponds to  $B_S$  as the diffusionless theory predicted.

However, a study of the transition of upper bainite to lower bainite in plain carbon steels of 0.2-1.8 wt% C [143] revealed a link between the microstructural transition temperature (MTT — the point where upper bainite is replaced by lower bainite) and  $T_0$  [143, Figure 5]. The work revealed that the MTT line was shifted relative to the  $T_0$  line; this difference was taken to represent the non-chemical free energy for displacive growth of lower bainite, although the authors do not go into detail.

Of further interest was the finding that, below 0.35 wt% C, no lower bainite formed at all. This was significant since it agreed with the predictions of models that balanced the decarburisation by diffusion of supersaturated ferrite against cementite precipitation kinetics [144]. Ferrite is assumed to grow in the supersaturated state, and the excess carbon is subsequently rejected into austenite. Upper bainite is expected to predominate at lower carbon contents, whereas at higher carbon contents some carbon may also precipitate within the ferrite sheaves themselves, forming lower bainite.

Curiously, although the authors contended that “the bainitic transformation is essentially martensitic”, Figure 5 in [143] clearly shows that upper bainite was observed to form above the  $T_0$  curve: something precluded by the displacive theory. The lower bainite transformation, on the other hand, is restricted both by the  $T_0$  curve and by a maximum temperature ( $350^\circ\text{C}$ ) at lower carbon contents (in agreement with the presumption that upper bainite will dominate at these compositions). However, in an earlier paper [145] the same hypereutectoid data is presented and indicates that no upper bainite was observed, which *is* in accordance with the displacive theory. It is likely that the authors have neglected to label the pearlite region in their later paper.

The authors also highlighted the morphological similarities between martensite and bainite and used morphological features to distinguish upper and lower bainite. Martensite morphology undergoes a composition-dependent change: from needle- or plate-like (high C%) to feather- or lath-like (lower C%). Oka and Okamoto accordingly classified their bainitic microstructures as either ‘feathery’ (upper bainite) or ‘needle’ (lower bainite). They noted that the constant MTT corresponded to the  $M_S$  at which the martensite also undergoes a morphological transition.

The predictions of the displacive model were consistent with the results of other experimental work. Srinivasan and Wayman [146] had found that upper bainite did not form at all in a Fe-7.9 Cr-1.1 C wt% alloy. Conversely, no lower bainite phase was found in high purity Fe-C alloys with a carbon concentration below 0.4 wt% [147]. The model also explained the occurrence of intragranularly nucleated upper bainite — but never lower bainite — in welds. The typically low carbon content of weld metals would be expected to favour the formation of upper bainite over lower bainite. This had been confirmed in 1989 when Sugden and Bhadeshia achieved intragranular lower bainite (‘lower acicular ferrite’) by deliberately increasing the carbon content of such alloys [148].

In 1990, the International Conference on the Bainite Transformation provided a platform for research on the incomplete reaction phenomenon. In a series of papers, several workers presented evidence disputing that the incomplete reaction phenomenon (“transformation stasis”) was a general characteristic of all bainitic transformations [149–151]. They adapted the solute drag idea to explain why the bainite transformation apparently stopped in certain alloy steels — and did not seem to be inhibited at all in others. The solute-drag-like effect (SDLE) described how certain alloying elements (typically Mo, Mn, Cr) segregate to an austenite-ferrite interface and alter the carbon concentration gradient in austenite, thereby slowing the rate of ferrite growth [149]. Of five alloying elements studied (Ni, Cu, Si, Mn, Mo), only steels containing Mn or Mo showed signs of incomplete reaction [150, 151]. Since only Mn and Mo are able to significantly lower the activity of carbon, Reynolds *et al.* [150] concluded that “incomplete transformation is a manifestation of the SDLE.”

It may, however, be premature to infer that these observations are not in accordance with a displacive theory. In several of the experiments, carbide precipitation was not suppressed and secondary reaction products were present, which would affect the carbon concentration of the austenite and possibly prevent any incomplete reaction occurring. The authors chose to use a microstructural definition to identify bainite: “nonlamellar...ferrite” or “any nonlamellar eutectoid decomposition product”, which does not provide for a distinction between bainite, Widmanstätten ferrite and proeutectoid ferrite.

The work by Reynolds *et al.* also served to highlight a strong similarity between the displacive and diffusional theories [150]. The authors suggest that bainitic ferrite consists of ‘sheaves’, which themselves grow *via* ‘sympathetic nucleation’ of smaller ferrite crystals: a process which seems similar, if not identical to, autocatalytic nucleation. In the diffusional case, the growth of these individual crystals is limited by the SDLE; in the displacive case, subunit growth is halted by plastic deformation in the adjoining austenite. Reynolds *et al.* explain:

“When carbide precipitation does not occur, the formation of ferrite is necessarily accompanied by carbon enrichment of the austenite adjacent to the ferrite crystals. The higher carbon concentration in this austenite lowers the driving force for sympathetic nucleation of ferrite, and transformation stasis results when sympathetic nucleation ceases [151]. Stasis ends when carbide precipitation restores ferrite growth by relieving the SDLE and by locally increasing the supersaturation for ferrite growth.”

Another interesting piece of evidence in favour of the diffusional theory came from Spanos, who carried out extensive TEM work and examined that of others, concluding that the crystallographic evidence was inconsistent with the displacive model [152]. He observed that cementite in lower bainite (in a 0.6 C-4.02 Mn-2.02 Si wt% alloy) showed good atomic matching with both the ferrite and the austenite phases, and this was supported by similar observations from other researchers [102, 153]. Following also the work of Shackleton and Kelly [97], Spanos concluded that such a three-phase crystallographic correspondence was indicative that cementite precipitated from the austenite. However, the conclusions reached in this work claimed that these observations could be explained “equally well” by a diffusive theory rather than flatly contradicting the displacive theory. Crystal-

lographic matching between all three phases is not always present [115] and there are several variables in the work by Spanos whose effects are unknown.

The evidence presented in support of a diffusional theory was certainly compelling, but not conclusive — although the same could still be said of the displacive theory. By the mid-1990s, however, the displacive theory of the bainite transformation had become sufficiently developed to enable its implementation in the design of new steels [154, 155]. This by no means guaranteed that it was correct, but certainly it proved its usefulness.

## 2.8 Surface relief revisited

In 1996, Swallow and Bhadeshia revisited the issue of surface relief [156]. Since Ko and Cottrell, many attempts had been made to quantify experimentally and theoretically the invariant-plane strain [102, 115, 157, 158]. It was not until 1982 that a value for the shear component of the strain was determined that agreed with the theory [159]. Swallow and Bhadeshia confirmed that this value was approximately equal to 0.26. The existence of such a large shear component pointed towards a deformation involving the co-ordinated movement of atoms, which required a coherent, glissile interface.

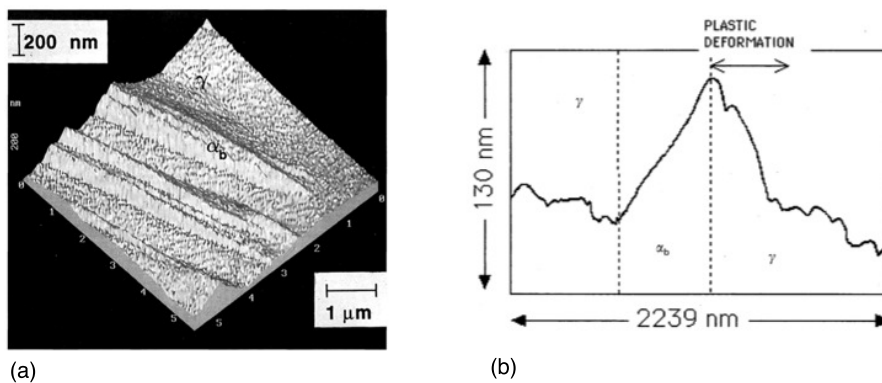


**Figure 2.10:** (a) Atomic force microscope image of several bainite subunits, showing plastic accommodation in the adjoining austenite (dark patches). (b) Atomic force microscope scan across a bainite subunit, showing similar plastic deformation. From Swallow and Bhadeshia [156].

Atomic force measurements revealed plastic deformation in the austenite adjacent to the bainitic ferrite subunits (Figure 2.10). This does not usually occur in martensite, which tends to be accommodated elastically. The higher temperature of the bainite transformation lowers the yield strength of the austenite, producing plastic behaviour. This is a crucial point: the deformation of the austenite prematurely halts subunit growth before they impinge on an obstacle. As a result, a new subunit of bainite must nucleate to propagate the transformation further, forming the characteristic sheaf morphology.

A further piece of evidence in support of the displacive paradigm was presented in 1999. It was shown that heavy deformation of austenite retards its subsequent decomposition into bainite [160]. In a reconstructive process, such deformation always leads to an accelerated transformation. This is because the generated defects act as additional nucleation sites, providing extra driving force, and are then eliminated by the growth of the new phase. During a displacive transformation the defects are inherited by the new phase. It was found that, in the case of bainite, the transformation rate initially increases, but then falls. This was thought to be impossible for a reconstructive process [160], and provided a compelling argument in favour of a displacive transformation.

## 2.9 Further support for a diffusional mechanism

Despite the evidence to the contrary, there was still much support for a diffusion-controlled bainitic transformation *via* a ledge mechanism [161–165]. The work of Nemoto [107] was held up in contradiction to the work of Bhadeshia and it was maintained that the majority of experimental work showed interface velocities corresponding to diffusion-control [161].

The STM and AFM observations of Fang [166], which revealed a ‘tent-like’ bainite surface relief on a sub-unit scale (Figure 2.11) — as opposed to that of the invariant-plane strain seen by Swallow and Bhadeshia — were taken as evidence of a diffusive, ledgewise process. Subunits of this type were expected to form *via* such a mechanism, which had previously been shown to be favourable under certain conditions: higher carbon contents and lower transformation temperatures [167].

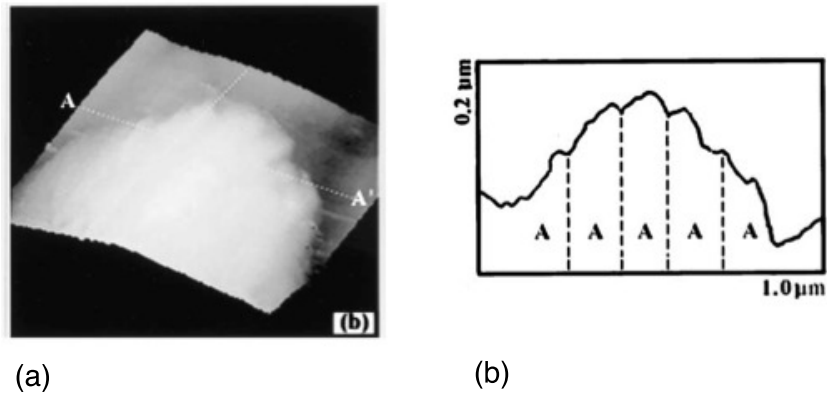


**Figure 2.11:** (a) Atomic force microscope image of a bainite subunit. (b) Atomic force microscope scan across the subunit AA', showing a tent-like surface relief. From Fang [166].

Hillert insisted that there was no clear experimental evidence of either the supersaturation of newly-formed bainitic ferrite or the high growth velocities characteristic of martensitic transformations [161]. He and others continued to favour an alternative framework, within which bainite and Widmanstätten ferrite comprised a continuous spectrum of acicular ferrite [52, 118], as evidenced by the continuous smooth gradation of growth rate and critical carbon content between the two forms [67]. Several workers proposed kinetic models based upon these ideas — among them Quidort and Bréchet [168]. It has been noted that the weakness of such models lies in the adoption of the solute-drag effect in order to explain certain aspects of the kinetics [138, 169, 170]. Mo segregation is also invoked, yet high-resolution analysis supports Bhadeshia's previous result that no segregation of alloying elements occurs at the transformation interface [135, 171]. While the work of Humphreys *et al.* seemed to contradict this, the transformations that they studied occur at temperatures at which substitutional solutes would be mobile, and the transformation product appears to be proeutectoid ferrite rather than bainite [172].

In 2004, Hillert *et al.* modelled the thermodynamics of diffusion-controlled growth of acicular ferrite [118]. They examined the Fe-C-Si system (2.01 wt% Si used to eliminate carbides), extrapolating growth rate data to zero to plot the critical limit for acicular ferrite growth (Figure 2.12). Agreement with experimental results was good and the analysis was extended to examine the effects of other

alloying elements: Mn, Cr, Mo and Ni. When compared with Bhadeshia’s approach [115], based upon the  $T'_0$  curve (also in Figure 2.12), it seemed clear that the diffusional model gave better agreement with the experimental data. However, the authors noted that Bhadeshia used a different thermodynamic database to calculate  $T'_0$  — one which gives different results compared with those presented by Hillert.

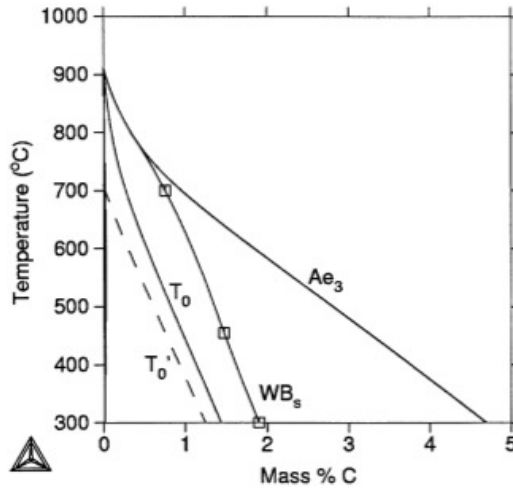


**Figure 2.12:** Predicted  $B_S$  according to Hillert [118]. Here it is designated  $WB_S$  as it represents the limit above which acicular ferrite cannot grow. This work considers bainite part of a continuous spectrum of acicular ferrite, along with Widmanstätten ferrite. The square symbols indicate experimental data and show bainite growth above the  $T_0$  limit.

Hillert’s method was able to predict the growth limits in Fe-C alloys as well as the effects of austenite-stabilising elements. The analysis indicated that the thermodynamic effects of these elements (Ni and Mn) “would be much weaker [than they observed experimentally] if ferrite is assumed to inherit the carbon content of the parent austenite”. The limitations of the diffusional approach, meanwhile, lay in its inability to accurately predict the effects of Cr and Mo, once again relying on solute-drag to explain the discrepancies.

## 2.10 Validation of the displacive theory

The work and ideas behind the displacive mechanism were soon consolidated into a rigorous kinetic theory [24]. Classical nucleation theory was not adequate

to describe the nucleation mechanisms involved in the bainite transformation [25]. With refinement to allow for the distinction between grain-boundary nucleation and autocatalytic nucleation, the theory was “able to generate accurate predictions of isothermal and continuous cooling transformation curves” [24]. In addition, the displacive theory continued to be applied successfully to steel design [22, 23, 30].

With the availability of more sophisticated imaging and characterization techniques, evidence in support of the displacive mechanism increased markedly. One remarkable piece of work employed acoustic emission measurements to record the formation of bainite and martensite, demonstrating that both transformations generated peaks in the acoustic data, as expected from a displacive mechanism [173]. X-ray analysis confirmed that the bainite transformation was limited by the  $T'_0$  curve, and that the retained austenite was enriched in carbon to a degree predicted by the curve [9, 31, 136]. Atom maps verified that no segregation of substitutional solutes occurred during transformation in high-C high-Si alloys and, for the first time, revealed the presence of Cottrell atmospheres in bainitic ferrite [136]. This confirmed Bhadeshia’s earlier prediction that Cottrell atmospheres at the transformation interfaces would hinder the bainite transformation [115], which explained the increased size of subunits at lower carbon contents.

It had been known for some time, as a result of X-ray analysis [30, 31, 174], atom probe analysis [26, 135, 171] and convergent beam electron diffraction analysis [175], that the carbon content of bainitic ferrite following transformation remained higher than predicted by paraequilibrium (i.e. allowing for only the carbon to partition after the transformation). This was accounted for by the trapping of large amounts of carbon at dislocations around the ferrite-austenite interface [136]. Additionally, recent work has supplied evidence of the tetragonal nature of bainitic ferrite in these alloys, which entails greater carbon solubility in the lattice [176]. Cottrell atmospheres also provided a possible explanation as to why  $\epsilon$ -carbide is not always detected as a precursor to cementite precipitation in lower bainite. The  $\epsilon$ -carbide is thought to be the first stage in cementite precipitation sequence in lower bainite [177], but is sometimes missed out in the case of high-carbon, high-silicon steels (despite the fact that silicon is expected to favour the formation of  $\epsilon$ -carbide) [114, 136]. Caballero was able to explain this phenomenon by demonstrating that the carbon is instead “tied up at the

dislocations.”

Synchrotron X-ray studies revealed the nonuniform stresses generated by the displacive transformation and were able to demonstrate that “the austenite remains homogeneous prior to the bainite transformation, and that the reaction remains thermodynamically incomplete” [178]: that is, there is no carbon rejection into the austenite before transformation, and the reaction does not go to completion as expected from the phase diagram. The observed change in the austenite lattice parameter prior to transformation was consistent with carbon partitioning between austenite and bainitic ferrite during nucleation, and provided strong evidence in support of ferrite supersaturation [178]. Although Babu *et al.* additionally reported that the austenite diffraction peak underwent splitting prior to bainite transformation [179], later work failed to replicate these results [178, 180].

Borgenstam and Hillert continued to argue in favour of diffusion-controlled growth, choosing to pursue a metallographic argument [68]. They showed that the ‘overlapping’ of lower bainitic subunits observed by Oblak and Hehemann [94] is analogous to the way sub-colonies overlap in ledeburite. Because ledeburite forms gradually *via* carbon diffusion and ledge propagation, the inference was that bainite must undergo a similar transformation to achieve the ‘overlapping’ morphology.

The authors also pointed out that the lamellar appearance of ferrite and cementite in lower bainite subunits resembled pearlite, and was indicative of cooperative growth. They provided micrographs purporting to show carbide-free sections of ferrite inside a bainite plate, and claimed that these sections were the regions from which the rest of the structure had originally formed. Finally, they compared upper bainite to Widmanstätten ferrite and concluded, based on observations of surface relief and plate morphology, that bainitic ferrite and Widmanstätten ferrite are identical. Among the conclusions in this work, the authors stated that

“it seems that one should now abandon the idea about bainitic ferrite being supersaturated when first formed.”

However, soon afterwards, atom probe tomography revealed for the first time the supersaturation of and subsequent carbon rejection from bainitic ferrite in the

earliest stages of transformation of a high carbon, high silicon nanocrystalline steel [181]. Later work confirmed these results and also provided additional evidence of plastic relaxation due to the shape change accompanying the bainite transformation [182].

### 2.10.1 The design of new bainitic alloys

Part of the value of a theory of the bainite transformation lies in its predictive ability. Currently, a significant distinction between the diffusive and displacive theories is that only the latter has been applied to alloy design.

An early area of interest was rail steels. Historically, rail steels have been pearlitic, however, the presence of brittle carbides makes them vulnerable to fracture [155]. A demand for high-strength, wear-resistant rails led many to consider a bainitic alternative, although early attempts produced alloys that did not perform as well as the conventional steels [183]. The challenge was to develop a carbide-free steel consisting of bainitic ferrite and retained austenite; the difficulty was that suppressing cementite precipitation produced regions of blocky austenite that would transform to martensite under stress. By alloying appropriately, it is possible to alter the  $T'_0$  curve to encourage the bainite reaction to go further to completion, eliminating the blocky austenite. The bainitic alloys produced by this method outperformed pearlitic premium rail in both wear resistance and rolling contact fatigue life [155, 183].

A more recent innovation involved the design of carbide-free bainitic alloys for defence applications. The aim was to use the displacive theory to design alloys with “unprecedented combinations of strength and toughness in bulk samples” [22]. Upon testing, these alloys were found to display the then highest ever combination of strength and toughness seen in bainitic steel (1600 MPa, 130 MPa m<sup>1/2</sup>) [23]. Development of this concept has led to the production of a range of high-strength bainitic steels with a nanoscaled structure [30, 31, 33, 35, 174, 184]. The properties exhibited by these steels match, and in some cases, exceed, those of other high-performance classes of steels, including TRIP-assisted steels, quenched and tempered martensitic steels, dual phase steels and maraging steels [35, 36, 184] (see Figure 2.13). The theory has also been used to modify the kinetics of the transformation in order to achieve more rapid transformation times [185, 186],

and to enable transformation at lower temperatures [174]. Currently, however, the necessarily high carbon contents of these alloys precludes them from applications where weldability is important, limiting their scope.

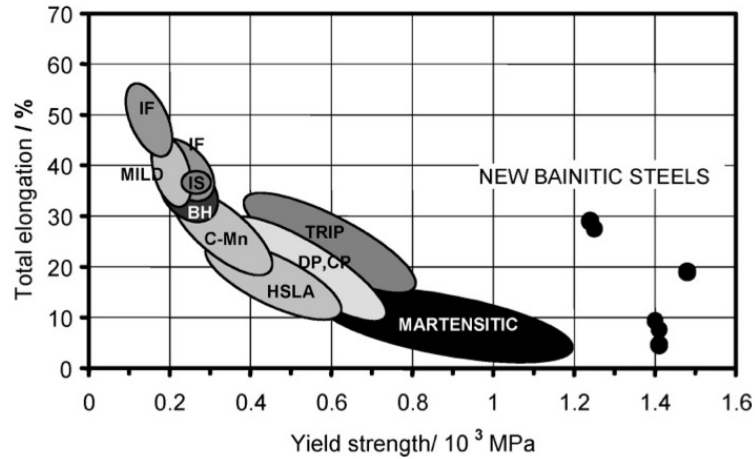


**Figure 2.13:** A comparison of elongation and strength of nanostructured bainite and conventional steels including: interstitial free (IF); carbon-manganese (CMn), bake hardenable (BH); isotropic (IS); dual phase (DP); complex phase (CP) [36]

The displacive theory has been used to design new alloys for a range of potential applications: aerospace; pipelines [187, 188]; bearings [189] — with promising results. Many of these areas are traditionally the preserve of quenched and tempered martensitic steels (favoured for their combined strength and toughness).

Casting a wider net, it is possible to find many other alloys which, while not specifically designed using a quantitative theory for bainite transformation, do owe their existence to the search for a more complete understanding of the bainite transformation. In the 1950s, for example, Irvine and Pickering worked on the development of low-carbon bainitic steels by applying their knowledge of hardenability to study the behaviour of a range of low-carbon alloys under various conditions of composition and heat treatment [7]. Their ‘Fortiweld’ steels have been described as the origin for all ultra-low-carbon bainitic steels in use today [190].

TRIP steels, a more familiar class of alloys, were first developed back in the 1960s as part of an effort to better study the mechanism of bainite transformation [12].

In this application, the retained austenite resulting from the incomplete bainite transformation is crucial to achieving the mechanical properties. An adaptation of the carbide-free bainite structure led to the creation of TRIP-assisted steels, which rely on the composite nature of a mixed bainite-austenite-allotriomorphic ferrite microstructure to enhance their ductility [13]. The principle has recently been further expanded to produce TWIP steels, which claim greater elongation than TRIP and TRIP-assisted steels, and which have found applications in impact-absorbing vehicle structures [191].

## 2.11 Conclusions

The bainite controversy has persisted for eighty years. Described as “one of the [most] intensely discussed phenomena in steels” [138], it draws attention to the unusual and fascinating features of the bainitic microstructure.

The opposing theories of diffusion-driven transformation and diffusionless transformation both claim evidence in their favour. The problem, as both sides agree, is that “direct experimental evidence for either theory is difficult to obtain. Therefore, one is left with indirect evidence” [168]. Often the same evidence can be interpreted in the context of both mechanisms [46, 86] and for the undecided, it can be a challenge to establish which is the more convincing interpretation.

### Summary Of The Theories

#### Diffusive

Bainite both nucleates and grows *via* a reconstructive mechanism. The growth rate is greater in the edgewise direction: lengthening of subunits dominates over thickening. This results in the formation and propagation of ledges. Cementite and ferrite grow simultaneously and cooperatively. Supporting evidence includes the metallographic similarities between bainite and other structures known to form *via* diffusion [68]; high resolution measurements of slow and continuous growth rates [46, 107]; and AFM measurements of a subunit showing a surface relief characteristic of a ledge mechanism.

The quantitative diffusive theory is able to calculate the limits of growth of both Widmanstätten ferrite and bainitic ferrite (in terms of a critical carbon content of austenite) [118]. It can also predict with reasonable accuracy the growth kinetics of bainite [162, 168, 169]. A limitation of the theory is an inability to account quantitatively for the effects of carbide-forming alloy elements, although it is thought that solute-drag may provide an explanation.

#### Displacive

A subunit of bainitic ferrite nucleates with carbon partitioning, and grows displacively until growth is halted by plastic relaxation in the adjacent austenite.

Carbon is then rejected from the supersaturated ferrite by diffusion and precipitation into the austenite (forming upper bainite) and may also precipitate within the subunit (forming lower bainite). New subunits nucleate and grow on the tips of old subunits. Where carbide precipitation is suppressed, bainite growth is limited by the  $T'_0$  curve resulting in incomplete transformation.

This theory is supported by measurements showing surface relief and plastic relaxation in the austenite [107, 156, 182]; measurements of high subunit growth rates [133]; X-ray measurements showing that retained austenite contents match the  $T'_0$  curve [9, 31, 182]; synchrotron studies showing carbon partitioning during nucleation [178]; and high resolution atom probe measurements of the carbon supersaturation in bainitic ferrite during transformation [181, 182].

The displacive theory explains why it is possible in high carbon steels to avoid the formation of upper bainite, and in low carbon steels to avoid forming lower bainite [144]. It accounts for a lack of partitioning of substitutional solutes and explains why Widmanstätten ferrite does not always form in steels, and why some steels only transform to martensite [25]. In its quantitative form, it is able to predict the shapes of TTT and CCT curves with reasonable accuracy [24]. It has been used to design many new bainitic alloys with excellent properties [22, 23, 155, 187, 189].

## The Definitions of Bainite

It has become clear through the course of this review that a major challenge for researchers in this area is the conflict between the three main definitions of bainite. The generalised microstructural definition states that bainite is a nonlamellar eutectoid decomposition product [6, 59]. It has also been stated more specifically as describing “the product of the diffusional, noncooperative, competitive ledge-wise growth of two precipitate phases formed during eutectoid decomposition, with the minority phase appearing in nonlamellar form” [192]. The surface relief definition describes bainite as a plate-shaped product that produces an invariant plane strain surface relief as formed by shear [86, 102]. The overall reaction kinetics definition incorporates the existence of an upper limiting temperature well below the eutectoid temperature ( $B_S$ ) and an incomplete reaction phenomenon, and considers bainite to have a separate C-curve on a TTT diagram [69, 79].

These three definitions cannot simultaneously be true. One definition excludes the possibility of carbide-free bainite. Two of the definitions include a stated mechanism of formation as part of the definition! It is then straightforward to dismiss any bainite-like structure that does *not* form *via* the expected mechanism as ‘not bainite’. When faced with a huge quantity of literature on the subject of the bainite transformation, a lack of definitional consistency only serves to confuse the matter further. Indeed, a great deal of effort has gone into attempting to resolve this problem [192]. It is not trivial. It is, however, apparent that until a general consensus is reached as to the definition of bainite, it is unlikely that a similar consensus will be reached with regard to the mechanism of transformation.



*Always be wary of any helpful item that weighs less than its operating manual.*

Terry Pratchett, *Jingo*

## CHAPTER 3

---

# EXPERIMENTAL METHODS

---

This section provides an overview of the common experimental techniques used in this work, except where the use of a technique is specific to a particular chapter.

### 3.1 Materials

The alloys studied in this work are listed in Table 3.1. Four of them, A–D, are superbainitic, whereas Alloys F and G are conventional carbide-free bainitic alloys. Of the superbainitic variety, Alloy A comprises a revised composition aimed at reducing the total alloy content and accelerating the bainite transformation. It contains less than half the typical amount of silicon usually added to achieve a carbide-free structure. The reduced manganese content lowers the thermal stability of the retained austenite, increasing transformation rates. Alloys B and C contain cobalt and aluminium additions, which also promote faster transformation. Alloy D does not contain these solutes and hence takes longer to transform. Alloy E is a dual-phase steel consisting of a coarse mixture of austenite and ferrite. It is relevant because the austenite grains are isolated from each other by a ferrite matrix, making it useful when studying the influence of austenite morphology on mechanical properties in Chapter 7. The compositions of Alloys F and G were originally devised with gun barrel applications in mind, and the design requirements and final alloy design are explained in the original work [22, 23].

Alloys A–C were produced as steel ingots, hot-rolled to narrow slab (40 mm thickness in the case of Alloys B and C) and finally to narrow coil (in the case of Alloy A) [40, 193]. Alloy A was then provided as uncoiled plate. Alloy D was man-

ufactured as a vacuum melt, followed by electro-slag remelting and rolling into cylinders of 0.2 m diameter. Details of production for Alloys E–G are described in Chapters 7 and 8 respectively.

	C	Si	Mn	Ni	Cr	Mo	Co	V
Alloy A	0.82	0.71	1.30	0.02	0.9	0.2	-	-
Alloy B	0.79	1.56	1.98	-	1.01	0.24	1.51	-
Alloy C	0.83	1.57	1.98	-	1.02	0.24	1.54	-
Alloy D	0.80	1.51	2.03	1.05	0.22	0.38	-	-
Alloy E	0.11	-	6.17	-	-	-	-	-
Alloy F	0.305	1.42	2.09	0.03	1.32	0.24	-	0.10
Alloy G	0.295	1.46	0.02	3.54	1.42	0.25	-	0.10
	Al	Cu	Nb	Sn	Ti	N	P	S
Alloy A	0.033	0.02	-	0.004	-	0.007	0.01	0.003
Alloy B	1.01	-	-	-	-	-	0.002	0.002
Alloy C	-	-	-	-	-	-	-	-
Alloy D	0.57	-	-	-	-	-	0.006	0.006
Alloy E	0.98	-	-	-	-	-	-	-
Alloy F	0.015	0.009	0.002	0.001	0.0016	0.001	0.002	0.0018
Alloy G	0.011	0.009	0.001	0.001	0.001	0.001	0.002	0.0014

**Table 3.1:** Chemical compositions of alloys studied, wt%.

## 3.2 Sample preparation

Sample sections were prepared for analysis by hot-mounting in conductive bakelite and grinding using silicon carbide emery papers (800-grade to 2500-grade), followed by polishing with 4000-grade silicon carbide paper and finally with 0.06  $\mu\text{m}$  colloidal silica on a polishing cloth. Between grinding stages, the samples were cleaned and rinsed, and surface quality was checked between all stages using an optical microscope. After polishing, the samples were cleaned with ethanol. Samples were etched using a solution of 2% nital (2% nitric acid, 98% methanol). Unmounted sections were prepared in a similar fashion. The mounted sections were used for optical analysis, scanning electron microscopy and hardness testing. The unmounted sections were used for X-ray analysis.

Thin foil samples for transmission electron microscopy were prepared from discs of 3 mm diameter (and 0.3 mm thickness), cut using spark erosion techniques. They were ground down to  $\sim 50 \mu\text{m}$  thickness and then thinned at  $7.5^\circ\text{C}$  using a twin jet electropolisher set to a voltage of 26 V. The electrolyte consisted of 15% perchloric acid and 85% ethanol by volume.

### **3.3 Microstructural observations**

#### **3.3.1 Optical microscopy**

The majority of the optical microscopy was performed using a Zeiss Axiotech optical microscope with attached QImaging MicroPublisher 3.3 RTV camera. The magnification ranged from 50–500. A Leica Microsystems DM2500M microscope with attached DFC295 camera was also used. Leica Application Suite software, ImagePro Plus imaging software and Adobe Photoshop CS image editing software were used to make minor digital enhancements (cropping, addition of scale bars, brightness and contrast adjustments).

#### **3.3.2 Scanning electron microscopy**

Scanning electron microscopy (specifically, imaging and energy-dispersive X-ray (EDX) analysis) was carried out using a JEOL 5800LV microscope.

#### **3.3.3 Transmission electron microscopy**

Imaging and electron diffraction were performed on a JEOL 200CX transmission electron microscope. In particular, measurement of the scale of bainitic microstructures was done using transmission electron micrographs. The apparent bainite plate thickness was measured normal to the plate length and stereological corrections were applied to determine the true thickness [194]. A Helios Focused Ion Beam Workstation was used to prepare thin sections taken from shear bands in the ballistic alloys studied in Chapter 8.

## 3.4 Metallurgical experiments

### 3.4.1 Heat treatments

Superbainitic alloys are isothermally transformed from the austenitic state at temperatures in the range 200-400°C. In the case of Alloy A, an appropriate austenitisation temperature was selected with the aid of equilibrium phase diagrams calculated using MTDATA (Figure 3.1) [195, 196], to ensure complete dissolution of cementite. For Alloys B-D, and for later work on Alloy A, the austenitisation temperature was chosen based on the conventional industrial heat treatment. In the cases of Alloys F and G, the material underwent a continuous cooling process, described in detail in Chapter 8.

Samples were austenitised for 1 h, followed by isothermal hold in a Carbolite box oven and finally water quenching to room temperature. In these latter cases, it is not possible to control the cooling rates of the alloy. To avoid oxidation during austenitisation, an argon tube-furnace was used. The furnace is repeatedly evacuated and flushed with argon prior to heat treatment, so austenitisation can then take place in an inert atmosphere. Table 3.2 gives details of typical heat treatment schedules for each alloy. Details of homogenisation, which was carried out for the work in Chapter 5, are also provided. Additional heat treatments — described in Chapter 4 — were carried out in a dilatometer.

### 3.4.2 Thermodynamic calculations

The National Physical Laboratory's Metallurgical and Thermodynamic Data Bank (MTDATA) program [195, 196] was used to calculate phase equilibria for Alloy A in Chapters 4 and 5. By calculating and minimising the Gibbs free energy of a system (defined by the user), it can estimate the composition and mass fractions of the phases present.

The reliability of the results depends on the available data for the various subsystems involved in the calculation. MTDATA is able to predict any system thermodynamically, and forms the basis of kinetic modelling. In some cases, ThermoCalc software was also used to perform thermodynamic calculations. However,

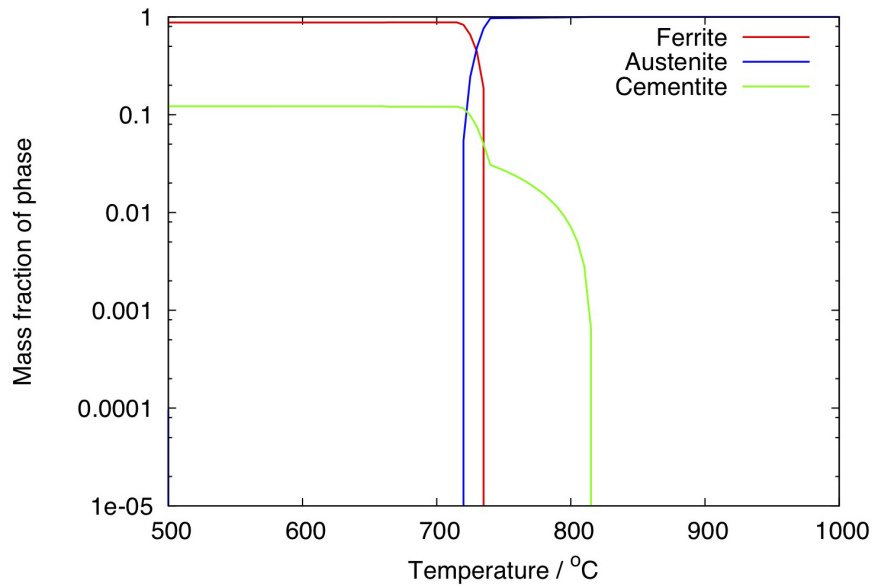


**Figure 3.1:** Equilibrium phases of Alloy A calculated using MTDATA v.4.73 with the TCFE v.5 database. This calculation was performed allowing ferrite, austenite and cementite phases to exist.

the results from MTDATA (used, for example, to predict the  $A_{e3}$  temperature) matched more closely the experimental results from the superbainitic alloys in question, and so this program was used in preference [197]. In ThermoCalc, the TCFE v.6 database was used; in MTDATA, the TCFE v.1 database was used (equivalent to TCFE v.5 in ThermoCalc).

### 3.4.3 Dilatometry

Cylindrical samples of diameter 8 mm and length 12 mm were machined from Alloy A, perpendicular to the plate rolling direction for heat treatment in the *Thermecmaster Z* thermomechanical simulator. This apparatus can be used to impose various heat treatment schedules, during which the load, strain and temperature data are recorded. Dilatometry is a valuable tool in the analysis of phase transformations. Temperature changes, phase changes and the dissolution or precipitation of alloying elements and their compounds (typically cementite) all lead to a change in the lattice parameter of iron. These effects induce a macroscopic volume change in the sample. The specimen diameter is then recorded to an accuracy of 5  $\mu\text{m}$ , while an R-type thermocouple attached to the sample tracks the temperature. This enables phase transformations to be accurately monitored

Alloy	Homogenisation	Austenitisation	Austempering
Alloy A	None	930°C for 1 h	200°C for 96 h 250°C for 16 h 300°C for 8 h
Alloy B	1200°C for 2 days	900°C for 30 minutes	200°C for 96 h 250°C for 16 h
Alloy C	1200°C for 2 days	900°C for 30 minutes	200°C for 96 h 250°C for 16 h
Alloy D	None	850°C for 1 h	200°C for 168 h
Alloy F	1200°C for 2 days	1200–905°C	Air cooled to 25°C.
Alloy G	1200°C for 2 days	1200–905°C	Air cooled to 25°C.

**Table 3.2:** Heat treatments used in this work. Details of the heat treatment for Alloy E can be found in Chapter 7.

in real time.

The dilatometry experiments in Chapter 7 were performed using a Dilatronic III dilatometer, with a calibrated S-type thermocouple. Samples 3 mm in diameter were cut from tempered specimens and analysed in the dilatometer.

## 3.5 Mechanical testing

### 3.5.1 Hardness testing

Hardness was measured using Vickers hardness testing equipment with a 30 kg load. This system has the advantage that the hardness value is independent both of the size of the indenter and the test force used (for loads greater than 0.2 kg) [198]. A wide range of test forces available means the Vickers test is suitable for virtually all metallic materials. A pyramid indenter is pressed into the surface of the material with a constant test force. The diagonal lengths of the square indent made are measured optically and converted into a hardness value using

the following formula:

$$HV \simeq \frac{0.1891F}{d^2}$$

where  $F$  is the test load in N and  $d$  is the diagonal measurement in mm. Tables are usually provided to facilitate the calculation. As with all indenter hardness tests, the area around each indentation will be work-hardened. It is therefore important to maintain a suitable distance between indents when doing repeat measurements on a sample; a distance of at least  $2.5d$  is recommended. Five repeat measurements were taken for each sample, which were then averaged.

Errors in hardness measurement, where stated, were calculated to be the statistical standard error:  $\frac{\sigma}{\sqrt{N}}$ , where  $N$  is the total number of measurements made.

### 3.5.2 Bend tests

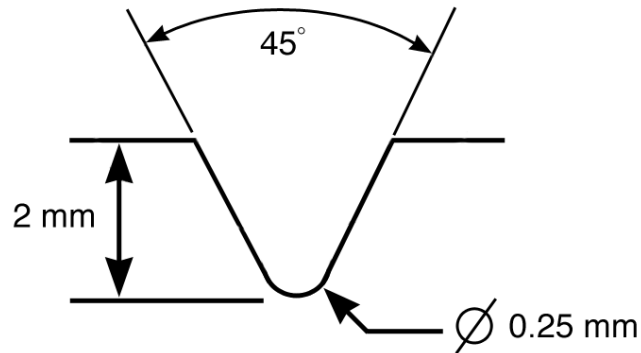


**Figure 3.2:** Sketch showing detail of the notch geometry of a standard Charpy impact energy test specimen.

Sub-size Charpy specimens measuring  $10 \text{ mm} \times 7.5 \text{ mm} \times 55 \text{ mm}$  were prepared from Alloy A plate according to the EN 10045-1 standard. A sketch of the notch geometry is provided in Figure 3.2. The specimens were heat treated as blanks before being sent for final machining. Because of the presence of strong banding in the sample, the Charpy specimens were oriented with the notch in the rolling direction, as illustrated by specimen C in Figure 3.3. These samples were subject to three-point-bend tests, carried out over a gauge length of 40 mm using an Instron Mayes 100 kN servo hydraulic machine, at a strain rate of  $8.4 \times 10^{-3} \text{ s}^{-1}$ .

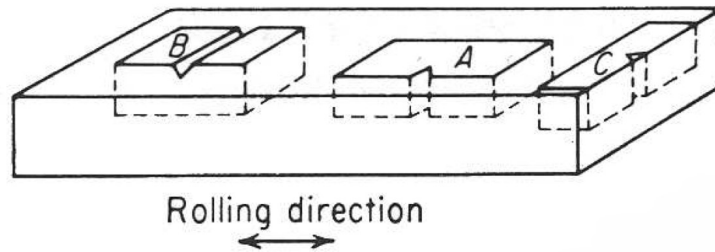


**Figure 3.3:** Sketch showing various orientations of Charpy samples machined from rolled plate. (A) and (B) are in the longitudinal orientation; (C) is in the transverse orientation. Sketch adapted from Dieter [199].

### 3.5.3 Charpy tests

Charpy specimens measuring  $10\text{ mm} \times 10\text{ mm} \times 55\text{ mm}$  were prepared from Alloys B and C according to the EN 10045-1 standard. The specimens were heat treated as blanks before being sent for final machining. Sub-size specimens measuring  $10\text{ mm} \times 7.5\text{ mm} \times 55\text{ mm}$  were prepared from Alloy A plate, machined in both the longitudinal and transverse directions (corresponding to specimens A and C in Figure 3.3). Charpy impact tests were carried out over a gauge length of 40 mm using a Zwick 50 J Charpy impact tester.

## 3.6 X-ray diffraction

X-ray diffraction was performed using Philips PW1820 and PW150 vertical diffractometers operated at 40 kV and 40 mA, with unfiltered  $\text{Cu-K}\alpha_1$  radiation and optics as described in Table 3.3. The machine operated in continuous scanning mode, scanning an angular range of  $2\theta = 40\text{--}140^\circ$ , with a step size of  $0.05^\circ$  and collection times ranging from 3 s to 28 s at each step.

Small samples were mounted on a silicon wafer, in order to prevent reflections from the aluminium specimen holder.

Peak positions and phases were identified using Bruker TOPAS v.4.2 software (v.5 used for automatic refinement of synchrotron data), and peak fitting was done using Philips ProFit software. Quantitative phase analysis was performed using Rietveld refinement. The retained austenite volume fraction was calculated using integrated intensities of the  $\{111\}$ ,  $\{200\}$ ,  $\{220\}$  and  $\{311\}$  austenite peaks

Filter	None
Divergence slit	1°
Anti-scatter slit	1°
Receiving slit	Fixed, 0.3 mm
Soller slits	Before & after specimen
Monochromators	Secondary, graphite

**Table 3.3:** Diffractometer optics

and the  $\{110\}$ ,  $\{002\}$ ,  $\{112\}$  and  $\{022\}$  ferrite peaks. By using multiple peaks, the influence of texture effects upon the refinement results is minimised [200].

Retained austenite carbon content was calculated from the measured lattice parameters as described by Dyson and Holmes [201], while bainitic ferrite carbon content was determined from equations derived by Bhadeshia *et al.* [202]. The former method is regularly used to analyse X-ray data taken from superbainitic steels [28, 44, 178, 203]. However, the compositions of these alloys often fall outside of the original composition range considered by Dyson and Holmes. In particular, the high carbon contents exceed the applicable range of 0.004-0.126 wt%. More recent studies by Peet, Garcia-Mateo *et al.* and Caballero *et al.* showed a good level of agreement between the austenite carbon content determined from the Dyson and Holmes equation, and from atom probe measurements, validating the use of this approach in the analysis of nanostructured steels [44, 136, 204].

### 3.6.1 Common errors in X-ray diffractometry

Common sources of error when carrying out X-ray analysis include the following:

- Instrument misalignment
- Specimen displacement
- Zero-shift
- Flat specimen
- Transparency

Figure 3.4 shows the relative magnitudes of these errors. The most significant with respect to lattice parameter measurement originate from specimen displace-

ment and zero-shift errors. It is possible to take these into account during refinement, and this was done during the refinement of spectra in this thesis.

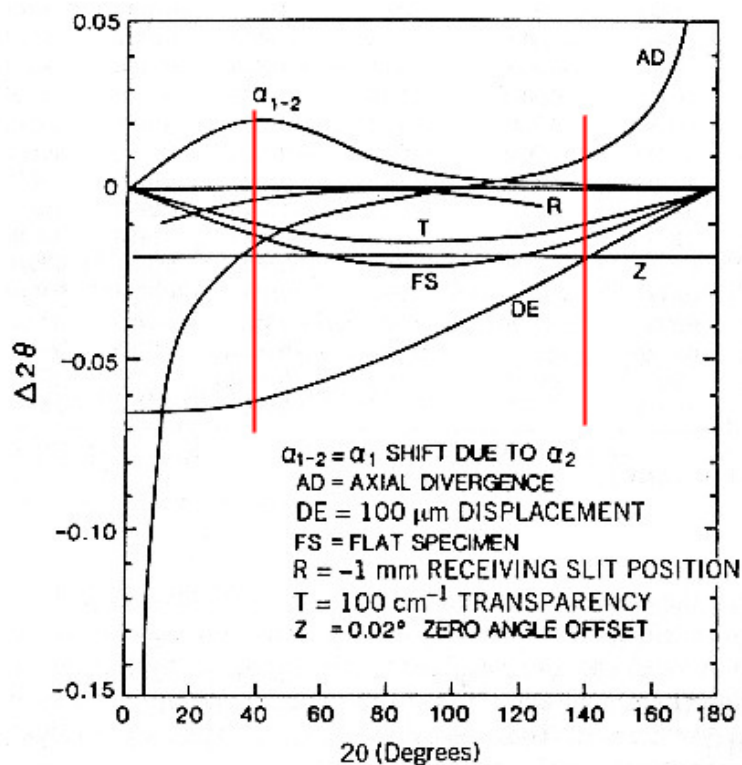


**Figure 3.4:** Common sources of error leading to peak shifts in X-ray diffraction spectra. The flat specimen error was assessed by constantly illuminating 13 mm of the specimen length [205]. The red bars indicate the angular range used in this work.

### 3.6.2 Rietveld refinement

Rietveld refinement is a commonly-used method for fitting peak shapes to an X-ray spectrum in order to perform quantitative phase analysis. When provided with information about the crystal structures present (such as lattice parameter, space group, site occupancy, temperature factors) and about the diffraction set-up (such as X-ray wavelength, Lorentz-Polarisation factor, width of slits) it is possible to calculate a spectrum that is then compared with the X-ray data. By adjusting the crystallographic variables the model can be modified to minimise the difference between the observed and calculated spectra, *via* an iterative least-

squares refinement process. The function to be minimised may be expressed as:

$$\Delta = \sum_i w_i [y_i(obs) - y_i(calc)]^2 \quad (3.1)$$

where  $y_i(obs)$  and  $y_i(calc)$  are the observed and calculated intensities respectively and  $w_i$  is a weighting factor applied to each reflection.

The refinable parameters in Rietveld analysis include: background; scale factors; zero-shift error; lattice parameters; profile parameters; peak shape parameters; asymmetry parameters; preferred orientation parameters; isotropic temperature factor. Because of the iterative nature of the process, the refinement must be carried out in a particular sequential manner. Additionally, some of these variables may be modelled in different ways (such as peak shape, profile parameters and preferred orientation) and it is important to select an appropriate model in each case. Below are some details and comments on the choice and refinement of variables in this work, much of which is based on the recommendations of McCusker *et al.* [206].

**Background:** Polynomial functions of the order 8 or 9 were found to model the background well and were used in preference to background subtraction.

**Lattice parameters:** Lattice parameters were permitted to vary freely except when modelling ferrite as a tetragonal structure. In this case, limitations were imposed on the lattice parameter to ensure that  $a < c$ .

**Peak shapes:** It was found that the best fit was given by using a pseudo-Voigt peak shape, which is a linear combination of Lorentzian and Gaussian shape components.

**Profile parameters:** There are five refinable profile parameters (U, V, W, X, Y) for the pseudo-Voigt case, which describe the full width half maximum (FWHM) for Gaussian and Lorentzian peak shapes as a function of  $\theta$  (equations 3.2 and 3.3 respectively) [206]:

$$FWHM^2 = U \tan^2 \theta + V \tan \theta + W \quad (3.2)$$

$$FWHM = X \tan \theta + \frac{Y}{\cos \theta} \quad (3.3)$$

Care was taken to ensure that no profile parameter was given a negative value.

**Preferred orientation:** Preferred orientation effects were accounted for using spherical harmonics of order 6 or below. It is important to use the minimum number of coefficients possible since this parameter can significantly influence the intensity calculation, which may result in negative intensity calculations and large errors.

**Isotropic temperature factor:** This accounts for the thermal vibration of atoms about their equilibrium positions, which can influence the intensity of the diffraction lines. It must be carefully controlled if refined, since it can often be a sink for other fitting errors. Refinement of this parameter was carried out last and was limited to a range of 0.1-0.5.

### Quality of refinement

There are various methods of assessing the quality of the fit of the calculated pattern to the observed data. In this work, the key parameter used was the weighted profile R value, defined as:

$$R_{\text{wp}} = \left( \frac{\sum_i w_i [y_i(\text{obs}) - y_i(\text{calc})]^2}{\sum_i w_i [y_i(\text{obs})]^2} \right)^{\frac{1}{2}} \quad (3.4)$$

Typically,  $R_{\text{wp}}$  values of 10 or below are considered ‘excellent’ for the purposes of refinement, however, it is appropriate to also examine the statistically expected R value,  $R_{\text{exp}}$ :

$$R_{\text{exp}} = \left( \frac{(N - P)}{\sum_i^N w_i y_i(\text{obs})^2} \right)^{\frac{1}{2}} \quad (3.5)$$

where  $N$  is the number of observations and  $P$  is the number of parameters.

As the fit improves,  $R_{\text{wp}}$  should approach  $R_{\text{exp}}$  and neither should be too large (this usually occurs due to insufficient data collection times). In conjunction with inspecting  $R$  values, the calculated spectra were compared visually with the observed data, to assess whether the fit was reasonable at all points. However, the analysis of the synchrotron data was automated, due to the large number of spectra, and in this case the  $R_{\text{wp}}$  values for each spectrum were plotted to allow an overall assessment of the quality of the refinement.

TOPAS is able to automatically calculate errors corresponding to each refine-

able parameter, and they are accordingly reported alongside X-ray data in this thesis. In each case, the error refers to  $\pm 1\sigma$  (the estimated standard deviation) from the mean, as calculated during the least-squares approach described above.



*To perceive is to suffer.*

Aristotle

## CHAPTER 4

---

# CHARACTERISATION OF FAST-TRANSFORMING NANOSTRUCTURED BAINITE

---

### 4.1 Introduction

A notable feature of superbainitic steels is the relatively low temperature at which they are transformed (typically 200-300°C). Calculations have shown that it is theoretically possible to progressively lower the bainite-start temperature ( $B_S$ ) of these alloys *via* addition of carbon [35]. Low transformation temperatures are advantageous, generating finer microstructures and allowing a greater fraction of bainitic ferrite to form [14, 15, 122]. From an industrial perspective, cooler furnaces represent lower energy-costs — in part because there is no need to protect the steel against oxidation. However, this can result in excessively long transformation times of several weeks [204]. It is therefore useful to develop alloys with improved low-temperature kinetics.

Garcia-Mateo *et al.* used cobalt and aluminium to increase the free energy change of the austenite–ferrite transformation, without compromising the hardenability of the steel [185]. A reduction of 20% in the transformation time at 200°C was achieved with the addition of cobalt, and a reduction of 60% when aluminium is also included [204]. These reductions are quoted relative to the transformation time of a conventional superbainitic alloy. Specific compositions are given in Ta-

ble 4.1 (Alloys 1-3).

	C	Si	Mn	Ni	Cr	Mo	Co	V	Al	Ref.
Alloy 1	0.98	1.46	1.89	-	1.26	0.26	-	0.09	-	[185]
Alloy 2	0.83	1.57	1.98	-	1.02	0.24	1.51	-	-	[185]
Alloy 3	0.78	1.49	1.95	-	0.97	0.24	1.60	-	0.99	[185]
Alloy 4	1.15	2.15	-	-	0.58	0.25	1.58	-	0.89	[207]

**Table 4.1:** Chemical compositions of superbainitic alloys with accelerated kinetics, given in wt%.

Meanwhile, Amel-Farzad *et al.* developed an alloy with zero manganese content, increasing carbon additions to 1.15 wt% so as to improve the mechanical properties without causing embrittlement (Alloy 4 in Table 4.1) [207]. By removing manganese, it is possible to counteract the effects that added carbon will have on the  $B_S$  and  $M_S$  temperatures. Additionally, the removal of manganese shifts the  $T'_0$  and  $Ae_3$  curves to the right, which increases the degree of bainite transformation possible. The new alloy was found to undergo accelerated transformation to bainite, achieving a hardness of 700 HV30 after treatment at 200°C for 8 days.

Similarly, Huang *et al.* carried out an extensive study of 729 alloy combinations to evaluate how individual alloying additions interact in terms of producing nanostructured steels. They revealed that “manganese reduction appears to be the most effective means to accelerate bainite formation at low temperatures” [208]. In this case, chromium rather than carbon was used to compensate for the removal of manganese.

Manganese has been known for decades to reduce the rate of transformation. One commercial form of the low temperature bainite has been available with a low manganese content well before the studies reported in [207, 208], for the specific reason of faster kinetics [193]. This chapter is devoted to the microstructural characterisation and dilatometric analysis of this low-manganese, low-silicon fast-transforming nanostructured steel (Alloy A in Table 3.1), with a view to later understanding how the structure influences impact and tensile properties. In particular, it was important to assess whether this reduction in alloy content produces a structure that can still be defined as ‘superbainite’: a mixture of carbide-free

austenite and bainitic ferrite measured on the scale of tens of nanometres.

## 4.2 Experimental methods

All dilatometry presented in this chapter was performed on a *Thermecmaster Z* dilatometer, the details of which are in Section 3.4.3. Heat treatments for transmission electron microscopy specimens were carried out in furnaces; all other treatments were carried out in the dilatometer.

Austenitisation temperatures were selected on the basis of calculated equilibrium phase fractions. Figure 4.1a shows the results of the original calculations, performed using the TCFE v.4 database. An austenitisation temperature of 800°C was therefore chosen initially. Subsequent calculations with the TCFE v.5 database indicate that there may still be undissolved carbides at this temperature, albeit at small volume fractions (Figure 4.1b). However, microstructural and dilatometric observations suggest that any carbides present in the structure have precipitated during formation of bainite. Key heat treatments were repeated at an austenitisation temperature of 930°C, corresponding to the conditions used to produce the commercial alloy. Except where indicated, all dilatometry and optical results were taken from samples austenitised at 800°C. Specimens used for transmission electron microscopy were austenitised at 930°C.

### 4.2.1 Determination of martensite-start temperature

For comparison with models predicted using thermodynamic information from MTDATA, the martensite-start temperature ( $M_S$ ) of Alloy A was measured experimentally using the dilatometer. The samples were austenitised for 15 min and subsequently quenched at a rate of 30°C s<sup>-1</sup> to a temperature of 30°C. In order to pinpoint  $M_S$  reproducibly, the offset method was used, with a strain of  $\epsilon_{\text{offset}} = 1.126 \times 10^{-4}$  [209]. This value corresponds to the transformation strain due to the formation of 1 vol% of martensite.

### 4.2.2 Estimation of bainite-start temperature

An attempt was made to measure  $B_S$  following the method of Pak *et al.* [210]. The maximum strain at each isothermal transformation temperature is estimated from dilation curves, and  $B_S$  is determined by extrapolating this data to find the

temperature at which the transformation strain is zero. However, this method assumes that no other phase transformation interrupts the formation of bainite, which was later found not to be the case for this alloy. Therefore,  $B_S$  was determined experimentally by transforming the alloy at progressively higher temperatures, and checking whether the dilatometry curve exhibited the sigmoidal shape indicative of bainitic transformation. Using this approach, it was possible to pinpoint  $B_S$  to within  $5^\circ\text{C}$ .

### 4.2.3 Estimation of prior austenite grain size

Austenite grain sizes were measured using the thermal groove technique described by Andrés *et al.* [211]. Polished samples were austenitised in vacuum for 30 min before being quenched to  $40^\circ\text{C}$  at a rate of  $30^\circ\text{C s}^{-1}$ . This temperature was chosen to encourage a significant but not excessive quantity of martensite to form, so that the degree of surface relief did not obscure the thermally-etched grain boundaries. Optical micrographs of the resulting structures were digitally enhanced (brightness/contrast) and the grain size determined by the linear intercept method [212].

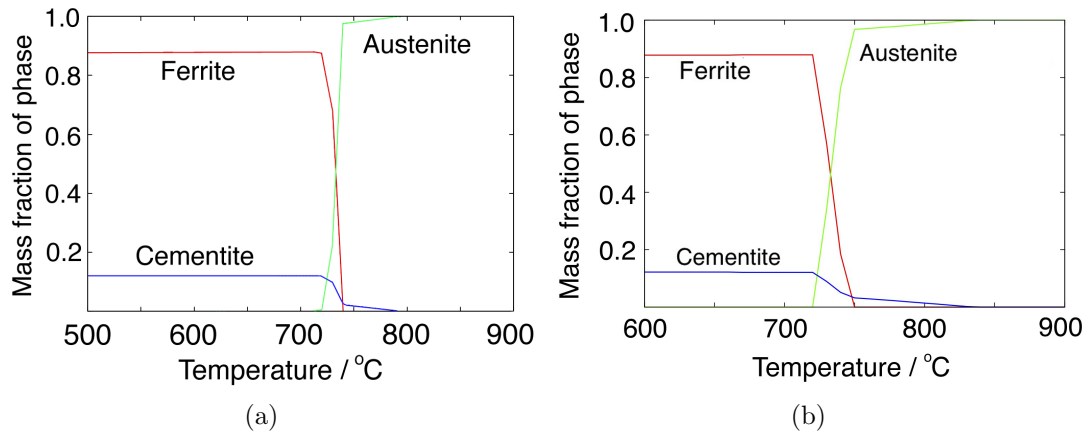


**Figure 4.1:** Equilibrium phases calculated using MTDATA v.4.73, with (a) TCFE v.4 database; (b) TCFE v.5 database.

### 4.2.4 Determination of final volume fraction of bainite

In order to understand the kinetics of Alloy A, it is useful to relate the degree of transformation (as measured from dilatometry curves) to the volume fraction of bainite formed. This was done using the method of Bhadeshia *et al.* [202]. It

is necessary to measure the thermal expansion coefficients of the austenite and bainitic ferrite of the alloy. A specimen was austenitised in the dilatometer at 1200°C and subsequently cooled to 800°C at a rate of 1°Cs<sup>-1</sup>; the expansion coefficient for austenite was then measured from a graph of strain *versus* time. For bainitic ferrite, the sample was tempered at 650°C for 30 min, cooled to room temperature at 5°Cs<sup>-1</sup> and reheated to 650°C at a rate of 1°Cs<sup>-1</sup>, and the expansion coefficient was measured from the dilatometry graph. Although some cementite is present at these temperatures, it is in a quantity small enough to be negligible when approximating the ferrite thermal expansion coefficient.

#### 4.2.5 Thermodynamic calculations

TTT<sup>1</sup> diagrams were calculated using the MUCG83 model [213]. The fundamental calculations that are applied in this program can be found detailed elsewhere [214]. Over time the original program has been modified to extend the temperature range over which it can be applied, and to increase the number of alloying elements for which it accounts. A second model, MTTTDATA, was also used to perform the same calculations [215]. This is based on the same principle as MUCG83, however it draws its thermodynamic information from MTDATA. In general, it was found that the two programs gave consistent results.

Calculations of the  $\gamma/(\gamma + \theta)$  curve for Alloy A were performed using MatCalc software v.5.51 with corresponding MatCalc Fe database v.0.017 [216]. MatCalc was chosen because it contains built-in routines for direct calculation of this type of phase boundary.

As a reliability check, calculations of the  $T'_0$  curve and equilibrium phase fractions for Alloy A were performed in both MatCalc and MTDATA. The results agreed well.

#### 4.2.6 Neural network

A neural network approach was used to calculate the  $M_S$  of retained austenite at various (high) carbon contents. The published literature contains many equations for calculating  $M_S$ , based upon composition [141, 217, 218]. However, these are predominantly straightforward linear regression models that account only for

---

<sup>1</sup>Time-temperature-transformation

chemical composition within a limited range, and were found to be unsuitable for the present work. There now exist more advanced models for calculating  $M_S$  — based upon thermodynamic principles rather than empirical relationships [219, 220] — but these can still be limited in terms of the composition range and the variables accounted for. A thorough critique of these approaches can be found in Sourmail *et al.* [221].

In contrast, it has been shown that neural networks are successful in predicting  $M_S$ , because they encompass more complex interactions between variables [222–224]. The theory and construction of neural networks is described in detail in the literature [223, 225–228]. Briefly, they represent an advanced form of regression analysis. Whereas conventional (i.e. linear) regression methods are limited to expressing linear or pseudo-linear relationships (and these relationships must be chosen before performing the analysis), neural networks introduce additional flexibility to model data. Each input to the model is multiplied by a random weighting factor, such that the sum of the resulting products (plus a constant) is the argument of a hyperbolic tangent, giving a nonlinear output. Additional nonlinearity is achieved by combining multiple hyperbolic functions in the output. The weightings are then varied by the network to obtain a best-fit output.

Because it is important to avoid over- or under-fitting the model, it is best to ‘train’ the neural network on one half of a dataset, and to test its predictive abilities on the second half. Equally, care must be taken to include all key input variables. For these reasons, the neural network developed by Sourmail and Garcia-Mateo was used [221, 229], since the model has been thoroughly tested and validated on a wide range of steel compositions, and found to be successful in predicting  $M_S$ . Details of the databases, input variables, training procedure and accuracy of output can be found in the original work.

## 4.3 Results and discussion

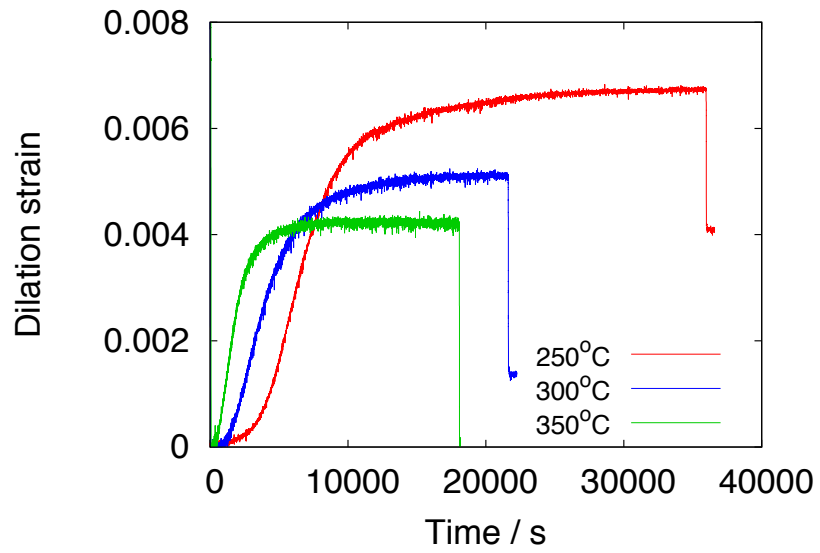
### 4.3.1 Dilatometry

Figure 4.2 shows typical dilatometry curves for various isothermal transformation temperatures. All display the asymptotic S-shape characteristic of bainitic

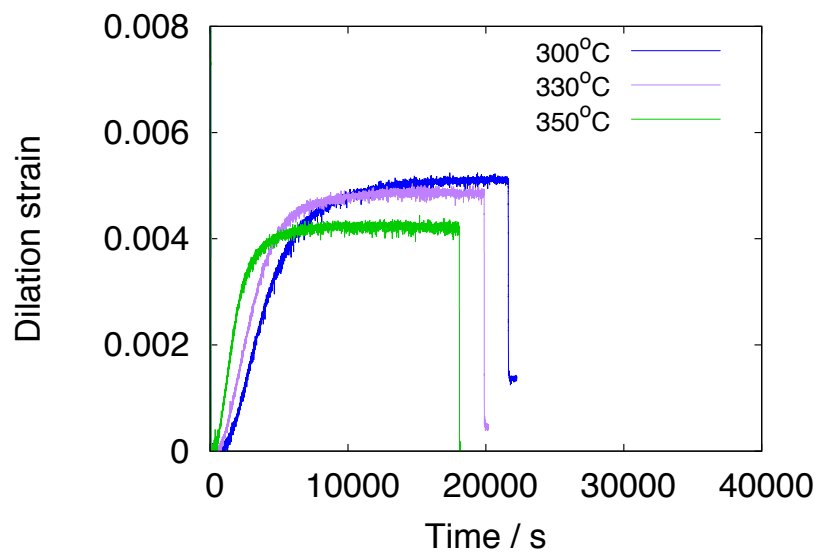
transformation. They show progressively faster transformation and lower volume fractions of bainitic ferrite (i.e. a lower maximum transformation strain) at higher transformation temperatures, as expected.

Above a temperature of 350°C, the shapes of the curves change (Figure 4.3). Rather than tending asymptotically to a maximum limiting strain, the dilation curves increase linearly with time and no ‘transformation-finish’ point is obvious over the time scale of the experiment. Cementite may be precipitating from the retained austenite or bainitic ferrite, thus allowing the bainite transformation to continue unabated. This is a reasonable assumption given the low silicon and aluminium content of the alloy [208], and in fact there is evidence of cementite precipitation occurring even in nanostructured steels with higher silicon additions [180]. In the case of samples austenitised at 800°C, the linear increase may represent the growth of pre-existing cementite precipitates.

Figure 4.4 shows the dilatometry curves of samples transformed at 300°C and 275°C, and austenitised at two different temperatures. In this case, the austenitisation temperature has an impact on the kinetics but not on the extent of transformation. At a lower austenitisation temperature the austenite grain size is smaller, increasing the density of nucleation sites for sheaves of bainitic ferrite and accelerating the transformation. That there is no effect on the final volume fraction of bainitic ferrite is a result of the transformation being limited by the  $T'_0$  curve in both cases. This implies that any cementite precipitation is minimal, since significant removal of carbon from solution would allow the transformation to progress further than when precipitation is inhibited. Although there is a discrepancy between the dilation achieved at 275°C, this is probably because the sample austenitised at 930°C has not yet levelled off as a function of time.



(a)



(b)

**Figure 4.2:** Dilatometry curves obtained at various transformation temperatures.

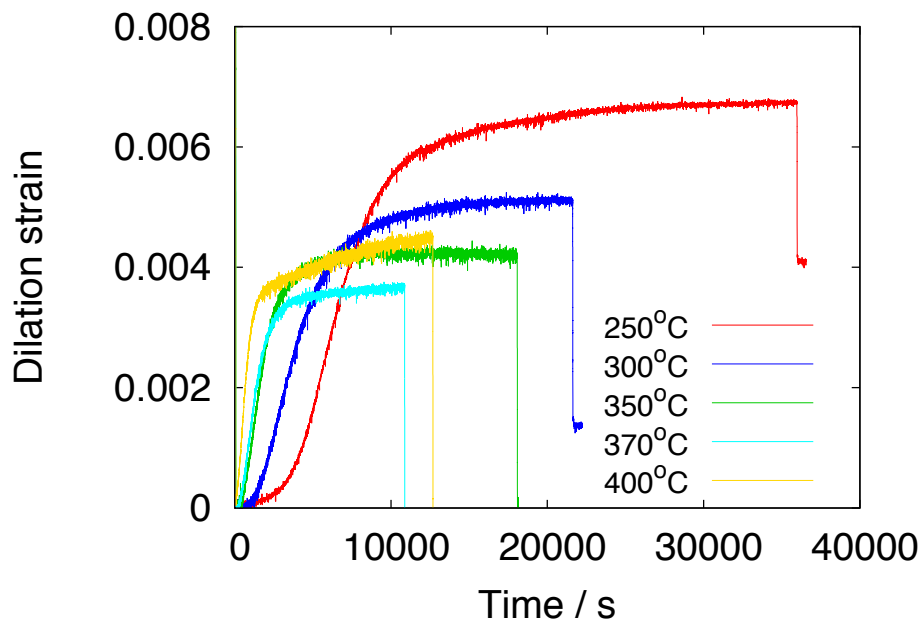
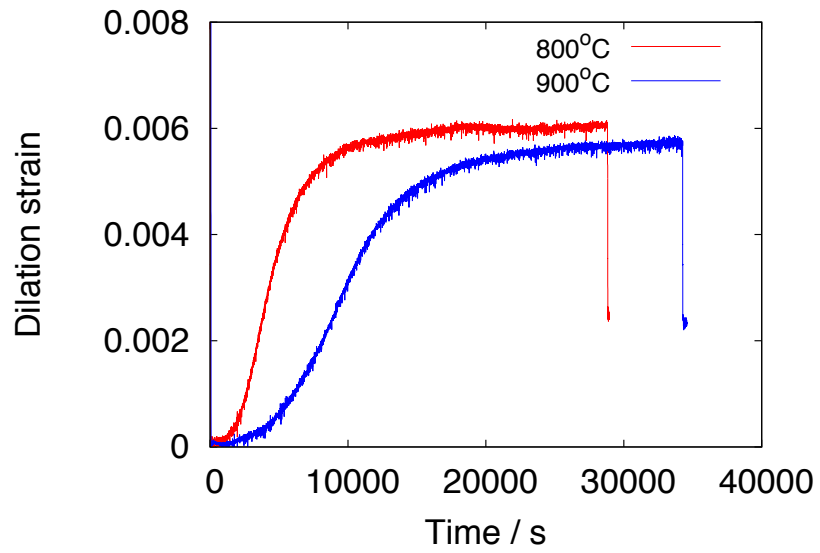
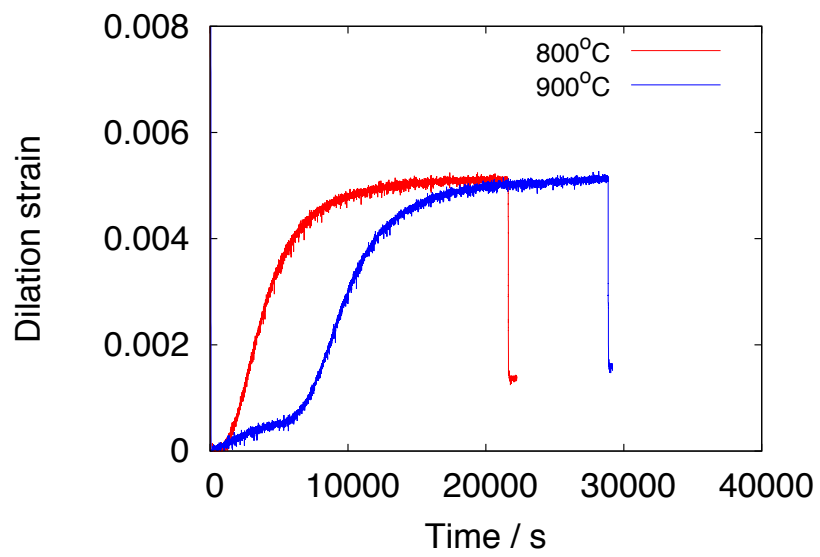


**Figure 4.3:** Comparison of dilatometry curves obtained at different isothermal transformation temperatures.



(a)



(b)

**Figure 4.4:** Comparison of dilatometry curves obtained at different austenitisation temperatures, and subsequently transformed at (a) 275°C; (b) 300°C.

Dilatometry data were converted into volume fraction data using the method of Bhadeshia *et al.* [202]. Figure 4.5 shows the results. Notably, the final volume fraction of bainitic ferrite formed, as predicted in Figure 4.5, does not match the measurements from quantitative X-ray phase analysis (Table 4.2 and Section 4.3.5), which revealed a high volume fraction of bainitic ferrite present in samples transformed at all three temperatures — around 0.9 in each case. This seems unusually high; comparable values in Alloy B and Alloy C are  $\sim 0.6$ – $0.8$ , and it is expected that transformation temperature should have a greater impact on final phase fractions than was observed in this case.

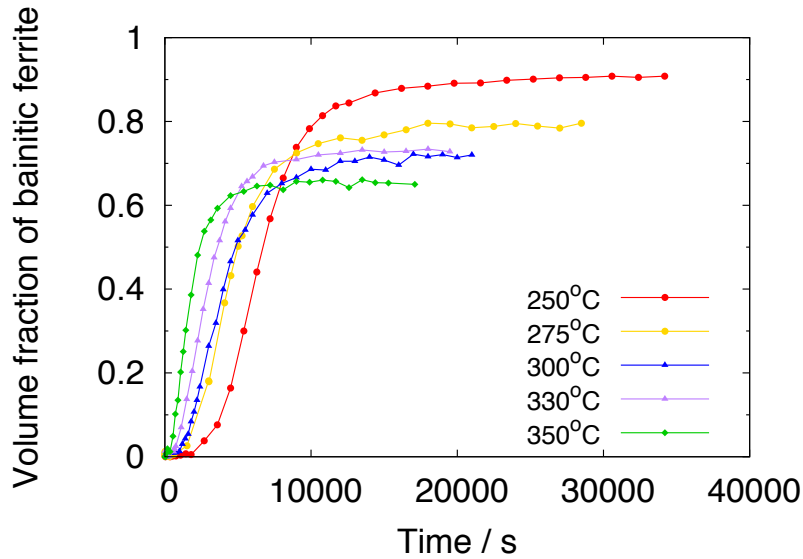


**Figure 4.5:** Quantity of bainitic ferrite formed at various isothermal transformation temperatures, as calculated from the dilatometry data. Error bars are excluded for clarity.

This discrepancy may be due to the formation of martensite during the final water quench, since it is difficult to distinguish from bainitic ferrite using laboratory X-ray equipment. Note also that the disagreement increases with transformation temperature. This is consistent with theory, as residual austenite formed at lower transformation temperatures is expected to have a higher carbon content and hence is stabilised more effectively against martensite transformation. Thus, it is reasonable to conclude that there may be martensite present in the samples transformed at 275°C and above. The dilatometry calculations should be treated with caution, however, since they are sensitive to lattice parameter values. This is

illustrated in Figure 4.6, which includes error bars derived from small variations in the lattice parameter input values. The error is large because the relevant equations incorporate the difference in the cube of the austenite and ferrite lattice parameters. Independent verification of these conclusions is therefore needed.

$T / ^\circ\text{C}$	$V_{\alpha_b}$ (X-ray)	$V_{\alpha_b}$ (Dilatometry)	Discrepancy (%)
250	$0.93 \pm 0.05$	$0.91 \pm 0.16$	1.94
275	$0.94 \pm 0.04$	$0.80 \pm 0.20$	15.3
300	$0.95 \pm 0.07$	$0.72 \pm 0.18$	24.2
330	$0.92 \pm 0.04$	$0.73 \pm 0.15$	21.7
350	$0.93 \pm 0.05$	$0.65 \pm 0.25$	30.0

**Table 4.2:** Comparison of volume fraction of bainitic ferrite in samples as calculated *via* dilatometry and X-ray methods.  $T$  represents the isothermal transformation temperature. Percentage discrepancies are calculated relative to the average X-ray results.

A calculation of the  $M_S$  of the residual austenite in each case shows that it is possible for some martensitic transformation to take place during quenching. Figure 4.7 shows the variation of  $M_S$  with austenite carbon content, as determined from a neural network and the method of Ghosh and Olson (with ordering) [219, 221]. The difference in results is likely due to the fact that the thermodynamic model does not account for certain factors – grain size and precipitation effects, for example, are not included. The limitations of the latter when compared with a neural network are discussed in detail by Sourmail *et al.* [221]. The neural network predictions are likely more reliable in this case.

Even with significant carbon enrichment, the residual austenite in this alloy is not completely stabilised against martensite transformation. Furthermore, it is possible to estimate what fraction will transform to martensite, given  $M_S$  and a quench temperature, using the Koistinen-Marburger equation [230]:

$$(1 - V_\gamma) = \exp(-b(M_S - T_q)) \quad (4.1)$$

where  $b = 1.1 \times 10^{-2}$ .

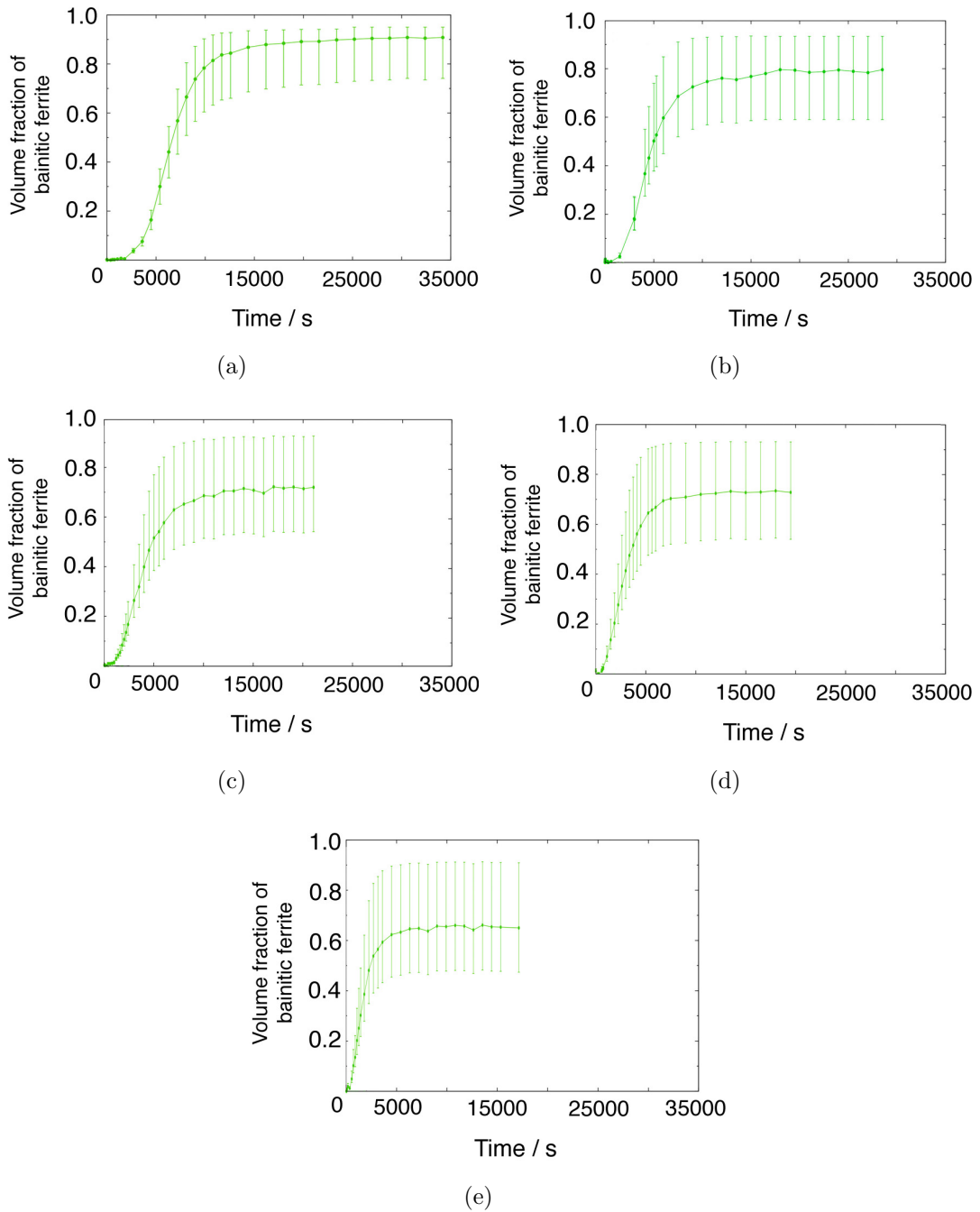


**Figure 4.6:** Volume fraction data calculated from dilatometry curves, for samples isothermally transformed at (a) 250°C; (b) 275°C; (c) 300°C; (d) 330°C; (e) 350°C. Error bars represent a variation of 0.25% in the lattice parameter input data. This is an arbitrary value chosen to illustrate the sensitivity of the calculation to changes in this variable, and is of comparable order of magnitude to the accuracy of lattice parameter calculations performed using X-ray methods.

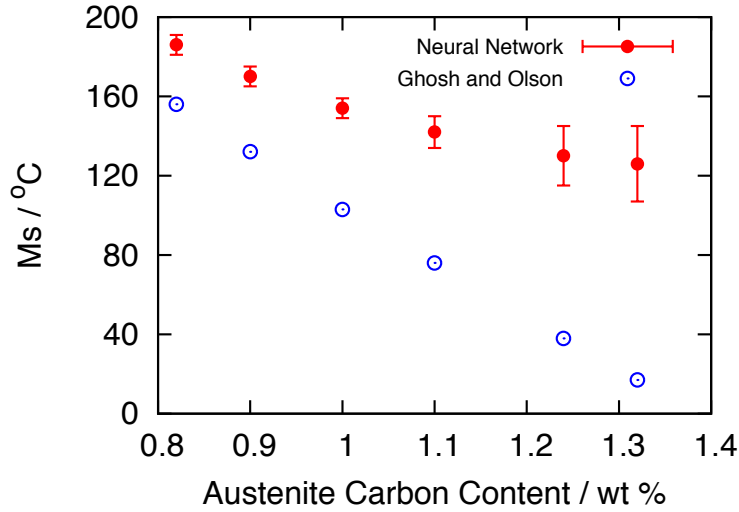


**Figure 4.7:** Results of calculations showing the influence of austenite carbon content on  $M_S$ .

The data in Table 4.2 suggest that upwards of 75% of the residual austenite should transform to martensite after quenching from the isothermal hold, in order for the X-ray and dilatometry results to match. A rough application of equation 4.1 to the current dataset (Table 4.3) indicates that this is feasible given the  $M_S$  values predicted in Figure 4.7.

Care must be taken when interpreting this result, since the Koistinen-Marburger equation is an empirical relation, in which the fitting constant  $b$  should be chosen based on experimental data from the steel in question, rather than estimated for use as a predictive tool. Table 4.3 illustrates the importance of choosing  $b$  appropriately; in the third column,  $V_\gamma$  is calculated using  $b = 0.004$ , used to fit experimental data from 300M steel, which consists of a mixed microstructure of bainite and retained austenite [231].

The hypothesis can be further explored by plotting the cooling curves for the transformed samples. By comparing the cooling curve to the thermal expansion coefficient, it is possible to detect whether any phase changes occur during cooling from the isothermal transformation temperature.

The thermal expansion coefficients in Table 4.4 have been estimated from measurements taken in the dilatometer. When the ferrite thermal expansion coeffi-

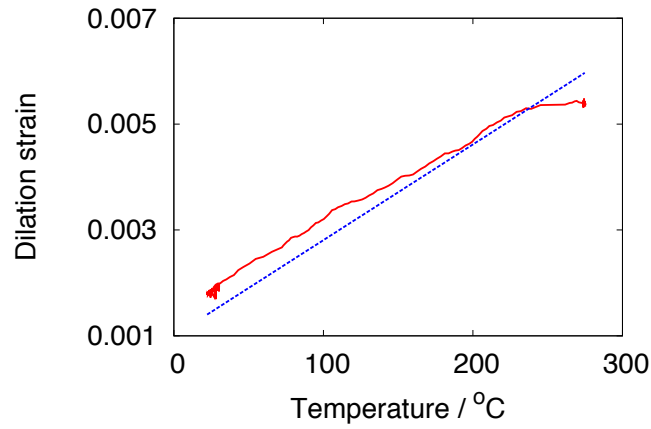
$M_S$	$V_\gamma$ [230]	$V_\gamma$ [231]
190	0.84	0.48
170	0.80	0.44
150	0.75	0.39
140	0.72	0.37
130	0.69	0.34
120	0.65	0.32
100	0.56	0.26
70	0.39	0.16
40	0.15	0.06

**Table 4.3:** Volume fraction of residual austenite expected to transform to martensite for a given  $M_S$ , as calculated using the Koistinen-Marburger equation. Columns 2 and 3 are calculated using values of  $b$  taken from the original work by Koistinen and Marburger, and from a later paper by Khan and Bhadeshia, respectively.

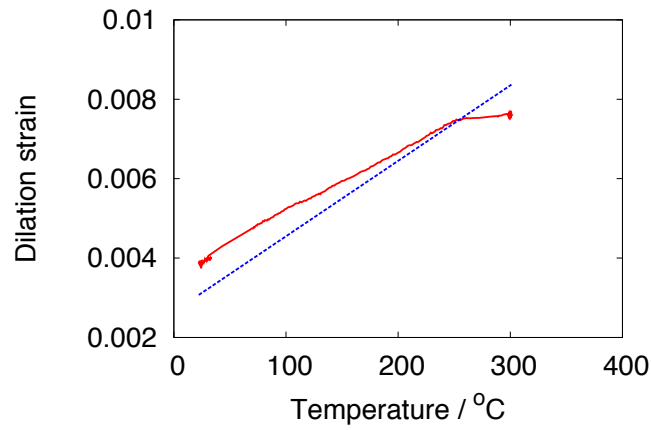
cient was measured, both ferrite and cementite were present, but the latter was assumed to be present in a negligible quantity. In order to estimate the thermal expansion coefficient for the alloy overall, the coefficients for individual phases were combined in a weighted manner according to the volume fraction measurements taken from the dilatometry data. The cooling curves and corresponding thermal expansion curves are shown in Figure 4.8. That the cooling curves stray from their expected path is indicative of other, expansive, phase transformations taking place.

Phase	Expansion coefficient / $^{\circ}\text{C}^{-1}$
Austenite	$2.8 \times 10^{-5}$
Ferrite	$1.5 \times 10^{-5}$

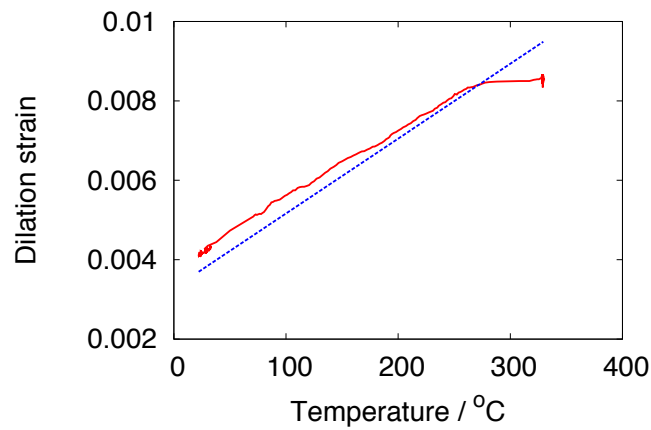
**Table 4.4:** Thermal expansion coefficients of austenite and bainitic ferrite as calculated from dilatometry measurements.



(a)



(b)



(c)

**Figure 4.8:** Cooling curves for three of the samples: (a) 275°C; (b) 300°C; (c) 330°C. Thermal expansion coefficients are calculated using the phase proportions predicted from the dilatometric curves. Estimated thermal contraction curves are shown in blue; measured cooling curves are shown in red.

### 4.3.2 Optical microscopy

Under optical magnifications, the samples transformed at 250°C and 275°C display a bainitic structure of fine scale (Figure 4.9). Lighter regions of retained austenite can also be seen, and these become more numerous with increased transformation temperature (Figure 4.10).

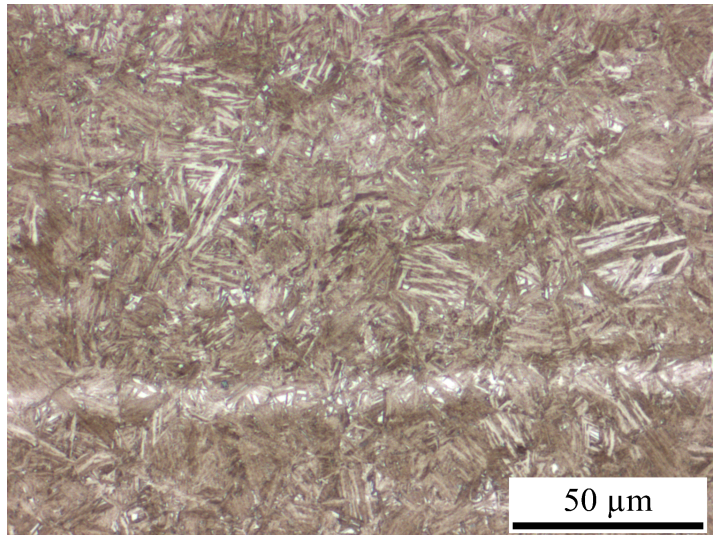
Of particular interest is the presence of banding, as in Figure 4.11 (and also visible in Figure 4.9), which is indicative of segregation. The samples were machined perpendicular to the rolling direction so banding due to rolling is expected to show up in this orientation. The banding grows more distinct with increasing transformation temperature. Measurements of the banding showed a weak inverse relationship between band thickness and transformation temperature. However, this may not be significant owing to the large variation in band thickness, and the difficulty of making accurate measurements, particularly in samples transformed at lower temperatures. This alloy contains manganese — an austenite stabiliser that is known to partition during solidification — and it is likely that the lighter bands are Mn-rich regions, and the darker bands Mn-poor regions.

Figure 4.12 is a micrograph of a specimen quenched to 30°C from 800°C and shows a martensitic structure. The variation in colour arises from the differential etching of the structure. Hardness measurements of 855 HV confirm the presence of martensite, while X-ray phase analysis indicates that there is about 5 vol% austenite present.

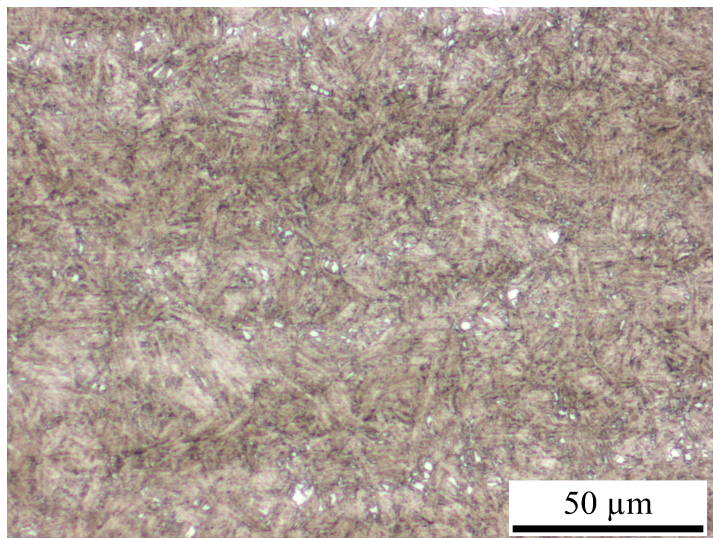
$T_{\text{aus}} / ^\circ\text{C}$	Grain size / $\mu\text{m}$
800	$5.6 \pm 0.1$
930	$16.7 \pm 0.3$

**Table 4.5:** Prior austenite grain sizes measured for two different austenitisation temperatures.

Micrographs of prior austenite grains are presented in Figure 4.13, showing the thermally-etched grains and some surface relief from martensite formation. Measured grain sizes are listed in Table 4.5. The grain size is reduced by two thirds when  $T_{\text{aus}}$  is lowered from 930°C to 800°C. This is expected to result in increased kinetics, as is observed in the dilatometer.



(a)



(b)

**Figure 4.9:** Micrographs of samples isothermally transformed at (a) 250°C; (b) 275°C. Note the banding, typical of chemical segregation effects, present in (a).

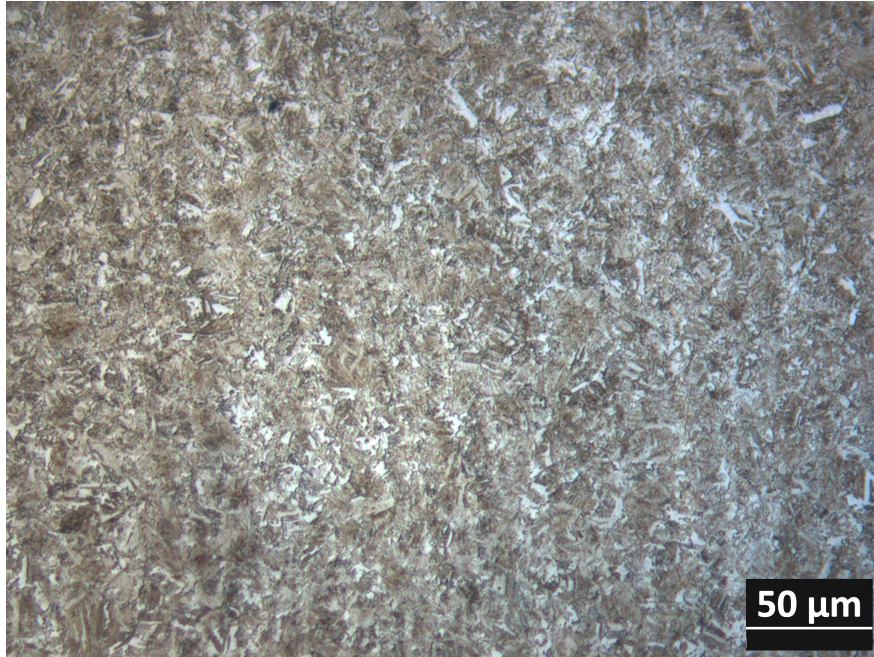


**Figure 4.10:** Micrograph of sample isothermally transformed at 300°C, in which lighter areas are visible.

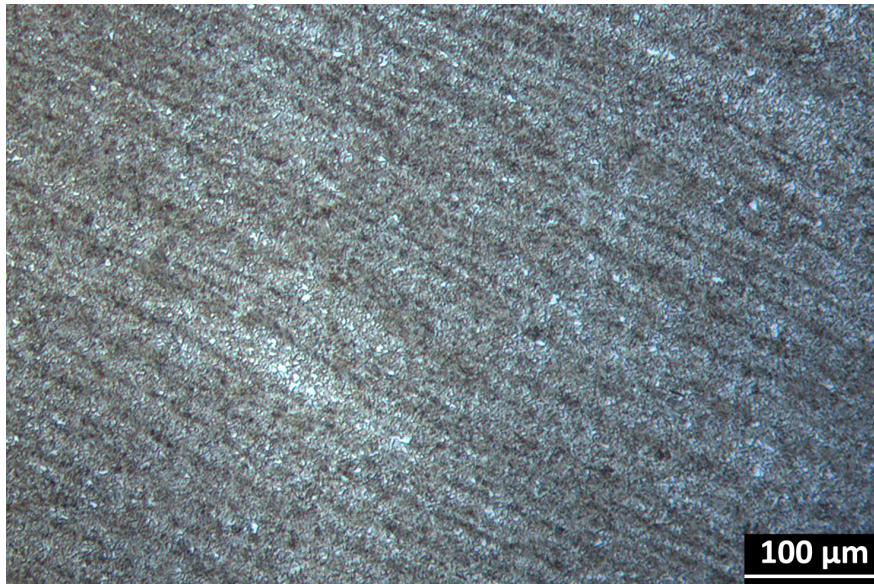


**Figure 4.11:** Micrograph of sample isothermally transformed at 330°C, in which banding due to segregation is visible.

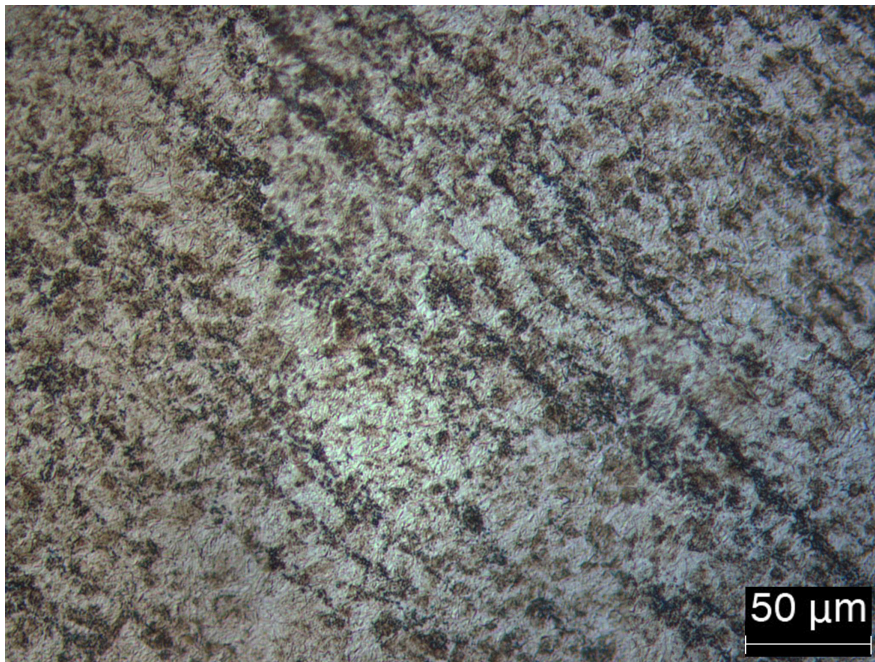
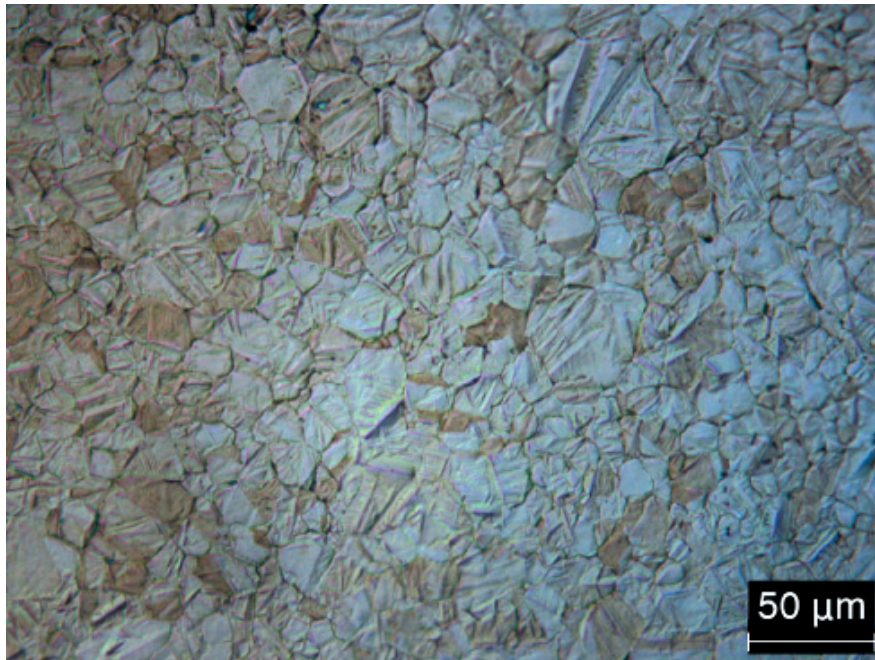
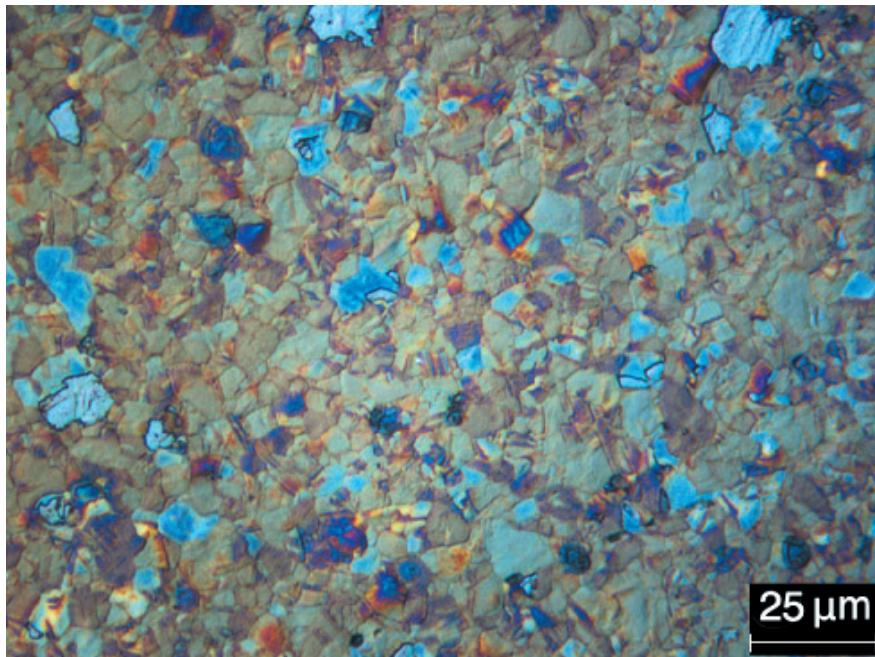


**Figure 4.12:** Micrograph of sample quenched to 30°C from 800°C.



(a)



(b)

**Figure 4.13:** Micrographs of samples thermally etched at austenitisation temperatures of (a) 930°C and (b) 800°C.

### 4.3.3 Transmission electron microscopy

Alloy A was characterised in detail using transmission electron microscopy (TEM). This technique provides sufficient resolution to measure the scale of the structure. Because of the variation in apparent bainite plate thickness in TEM images it was necessary to take a large number of measurements — over 800 — and to apply appropriate stereological corrections as described by Chang and Bhadeshia [194]. The results are shown in Table 4.6, with Alloys B and C (typical superbainitic steels) for comparison.

Isothermal transformation temperature / °C	Hardness / HV30	Mean plate thickness / nm	Alloy B plate thickness / nm	Alloy C plate thickness / nm
200	$693 \pm 4$	$57 \pm 3$	45	38
250	$637 \pm 3$	$83 \pm 3$	41	38
300	$555 \pm 2$	$87 \pm 3$	52	106

**Table 4.6:** Bainite plate thickness and corresponding hardness in Alloy A. Equivalent measurements from Garcia-Mateo *et al.* [185] are also provided for comparison. All thicknesses are expressed as true thicknesses.

While the structure of Alloy A is well within the nanoscale range, it is coarser than the other superbainitic alloys. This may be due to the reduced quantity of alloying additions in the former, which would reduce the solid solution strengthening of the parent austenite and result in coarser plates [122].

Electron diffraction analysis (Figure 4.14) revealed that cementite precipitation had occurred during transformation at all three temperatures. In several cases it was possible to identify the ferrite-cementite orientation relationship as the Bagaryatskii orientation relationship [9]. This is commonly known as the ‘tempering’ orientation relationship — found in tempered martensite — and is indicative that the cementite has precipitated from the bainitic ferrite rather than from the austenite. In these samples, cementite was only ever identified alongside ferrite. However, little if any austenite was observed at all using this method — one example is provided in Figure 4.15 — so the possibility of cementite precipitation from austenite should not be excluded.

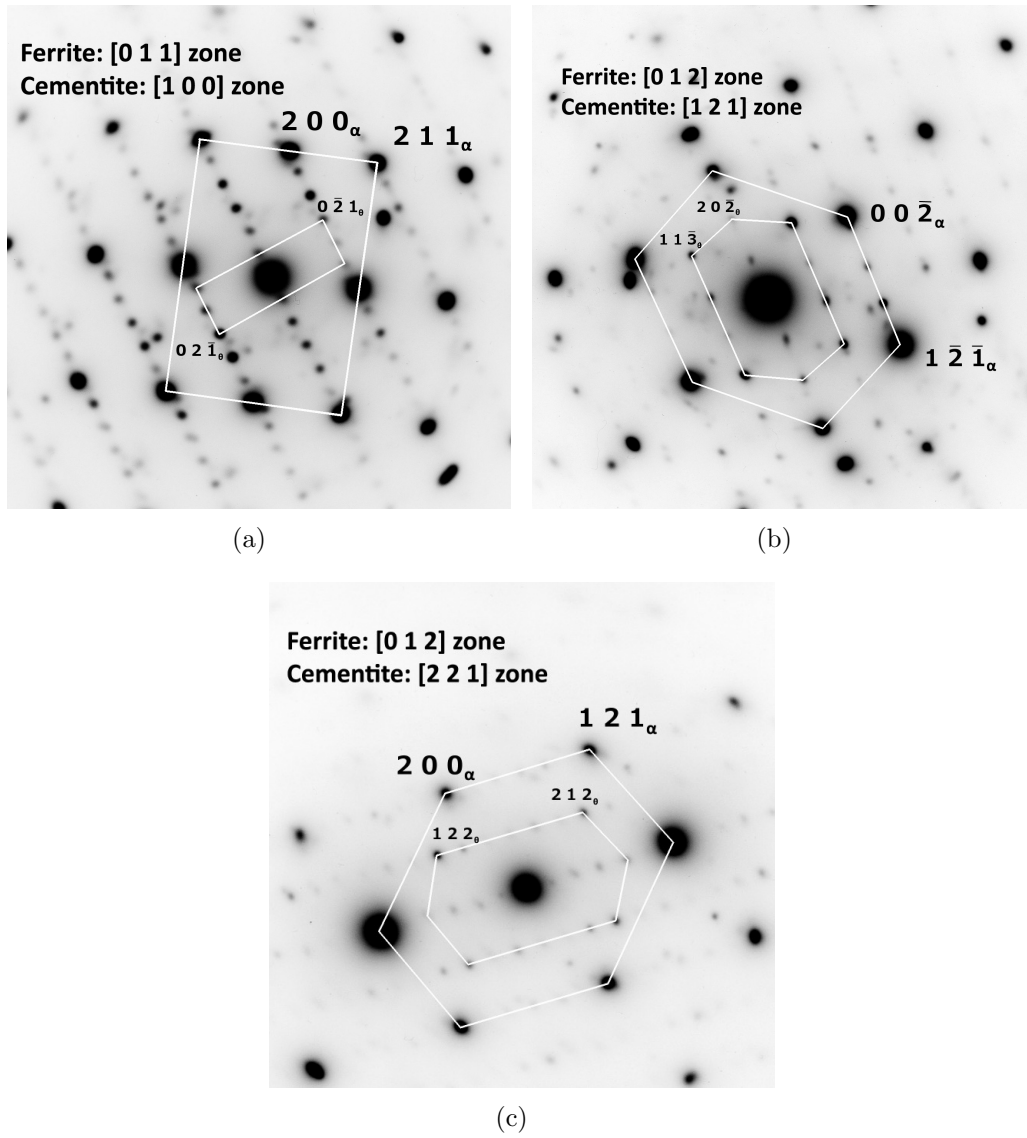


**Figure 4.14:** Electron diffraction micrographs showing the presence of cementite in Alloy A transformed at (a) 200°C; (b) 250°C; (c) 300°C. Image (a) shows the Bagaryatskii orientation relationship.

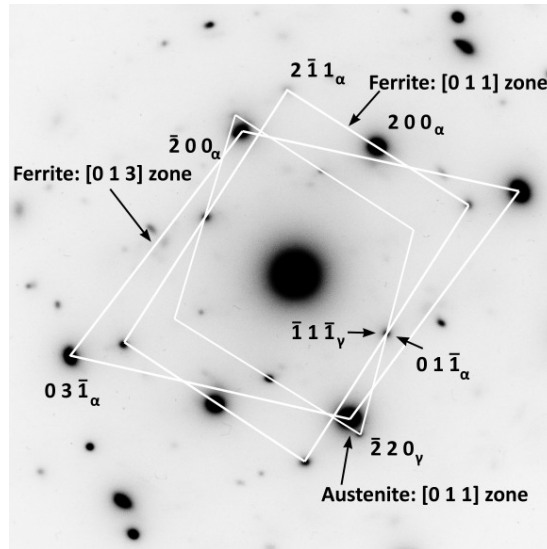


**Figure 4.15:** Electron diffraction micrograph showing austenite and ferrite in Alloy A transformed at 250°C. The  $\{111\}_\gamma$  and  $\{011\}_\alpha$  planes — both closest-packed directions — are parallel, as is expected from  $\alpha_b/\gamma$  orientation relationships [9].

The images in Figure 4.16 are representative of the transformed structure of Alloy A, showing its fine bainitic nature. Notably, however, Figure 4.16c shows that, when transformed at 300°C, the structure does contain regions of coarser bainitic ferrite. Meanwhile, Figure 4.17 shows examples of cementite precipitation within a bainite plate. This result contradicts the claims of Rose *et al.* who state that carbides, while present in this steel, do not form in the bainitic laths [193]. The precipitates are consistently positioned at an angle of  $\sim 60^\circ$  to the plate, reminiscent of a tempered martensite structure. In fact, the mechanism of carbide precipitation in lower bainite is documented in the literature as having many similarities to the tempering of martensite [232]. Martensite itself was present in the sample transformed at 300°C (Figure 4.18), which supports the speculation that this is the reason for a mismatch between the X-ray and dilatometric phase data. Note also the presence of ‘midribs’ along the centre of the plates in Figure 4.17. This feature is sometimes found in high-carbon ( $> 1$  wt%) steels transformed at low ( $< 250^\circ\text{C}$ ) temperatures, and is thought to be a thin plate of martensite that stimulates the formation of the surrounding lower bainite [9, 233].

These results are of note as they suggest that it may not be appropriate to refer to this new alloy as ‘superbainite’, since the structure is not carbide-free, as a consequence of reducing the silicon content. On the other hand, Sourmail *et al.*

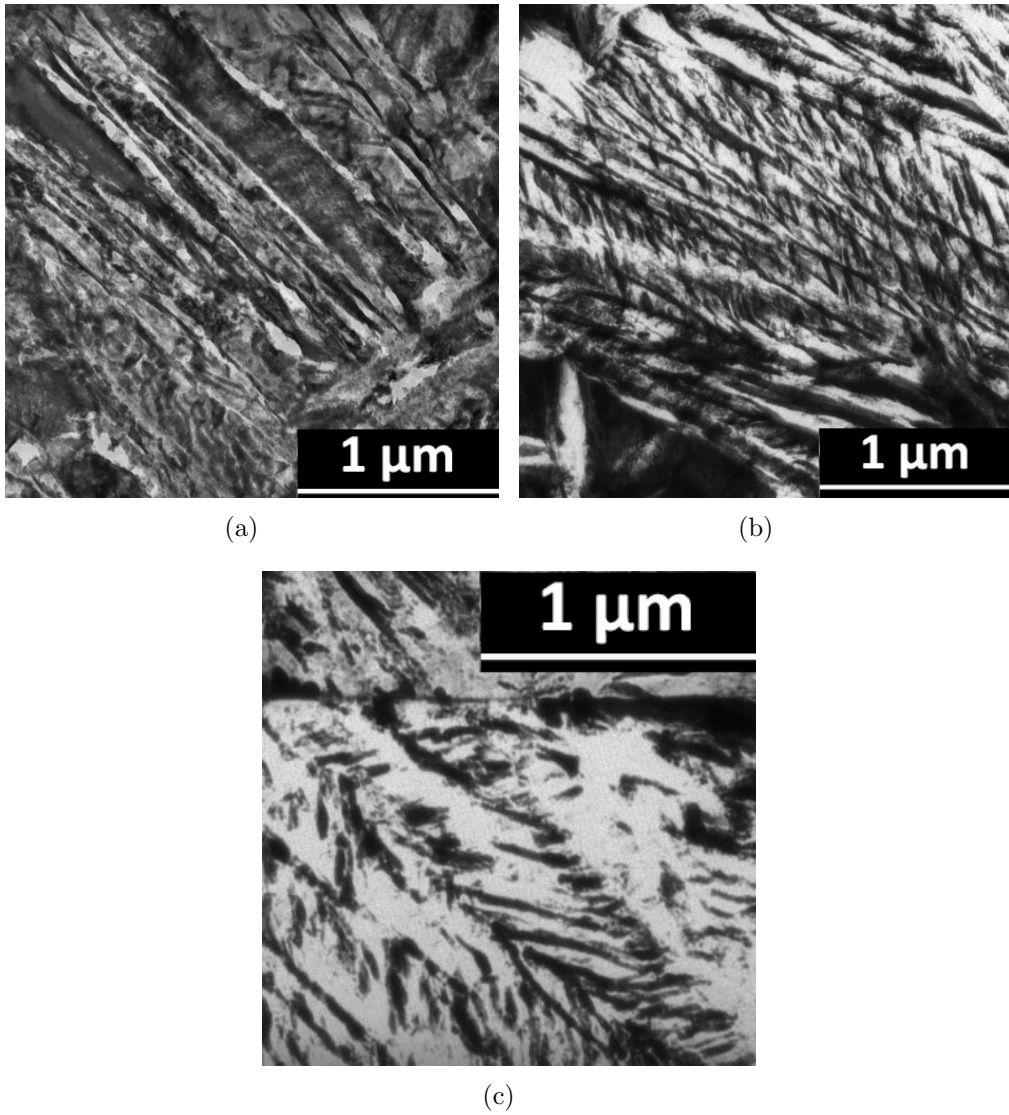


**Figure 4.16:** Transmission electron micrographs showing the structure of Alloy A after transformation at (a) 200°C; (b) 250°C; (c) 300°C.

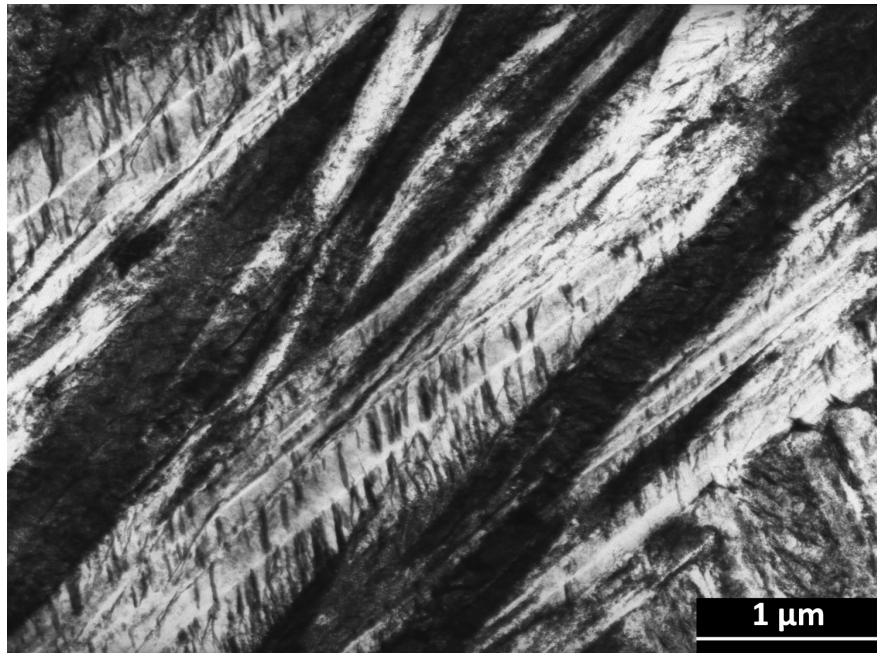


**Figure 4.17:** Transmission electron micrograph of Alloy A transformed at 200°C showing significant cementite precipitation within bainitic ferrite.



**Figure 4.18:** Transmission electron micrograph of Alloy A transformed at 300°C showing a region of martensite. Note the thin, faint twins.

have recently highlighted that, given the increasing evidence of cementite precipitation in other nanostructured steels, the original classification of superbainite as being carbide-free should perhaps be reconsidered [234].

#### 4.3.4 Scanning electron microscopy

Scanning electron microscopy was used to investigate possible segregation effects. A sample with pronounced banding (transformed at 330°C) underwent energy-dispersive X-ray analysis to quantify the segregation, however, the results are inconclusive.

The microscope was used in backscatter mode to identify the bands *via* atomic contrast. Since the atomic weights of manganese and iron are similar, this was difficult to achieve. Four points were selected for analysis, labelled 1–4 on Figure 4.19. Points 1 and 4 lie in what are thought to be high-manganese regions, and points 2 and 3 lie in low-manganese regions. The results of the spectral analysis are given in Tables 4.7 and 4.8. The data is expressed in ratios to account for the fact that carbon content cannot be measured using this method (although individual concentrations are also shown for comparison). Overall, the data do not definitively point to segregation. Regions of high manganese have been identified, but no corresponding regions of low manganese. This does not necessarily contradict the observations of banding, but could merely indicate that a greater number of points needs to be examined, and over a wider area. In fact, this type of analysis has been known to overestimate the manganese content in similar circumstances [235, 236], and so it may be necessary to calibrate the equipment against a sample of known composition to check whether this is a factor in the present case.

In order to identify any regions of low manganese, a linescan was carried out across several of the bands as shown in Figure 4.20. However, this also failed to pinpoint any areas of obvious segregation. Figure 4.21 shows the element map obtained for manganese. There is some variation in the levels of manganese detected across the line X-X' but the data is simply not of sufficient resolution to justify this being a real effect. The linescan was carried out at a relatively low magnification; it would be preferable to focus on a segregation boundary and analyse the manganese concentration across it. However, the location of the

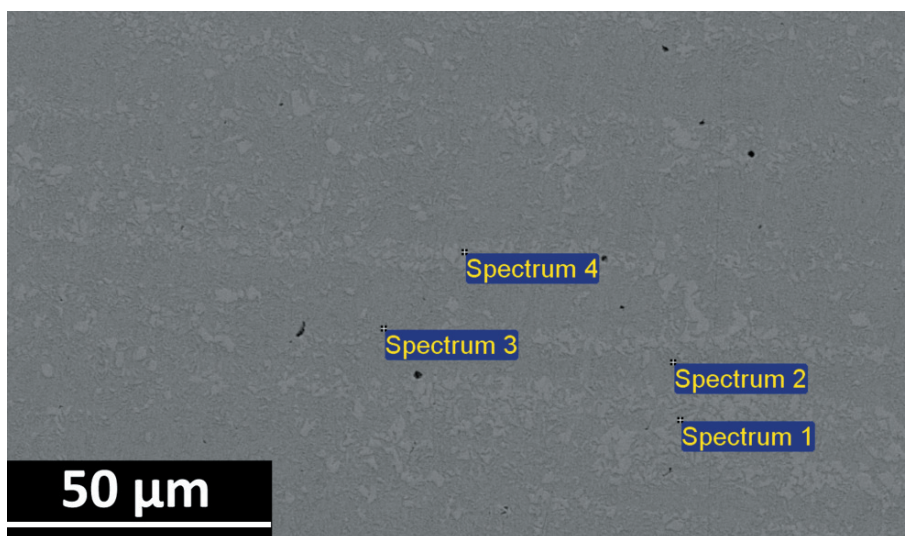


**Figure 4.19:** SEM backscatter image of sample transformed at 330°C. Points 1–4 indicate locations where spectra were taken.

boundaries is not precisely known; the only guide is the visible banding. Higher magnifications or longer dwell times would produce a more accurate map of manganese concentration and this is something that should be considered for future work. It is likely that point analysis is necessary to get statistically meaningful results.

Spectrum	Si	Cr	Mn	Fe
1	$0.74 \pm 0.07$	$1.07 \pm 0.11$	<b><math>1.46 \pm 0.16</math></b>	$92.52 \pm 0.31$
2	$0.70 \pm 0.07$	$0.77 \pm 0.10$	<b><math>1.30 \pm 0.15</math></b>	$91.97 \pm 0.32$
3	$0.72 \pm 0.07$	$0.93 \pm 0.10$	<b><math>1.61 \pm 0.15</math></b>	$91.46 \pm 0.32$
4	$0.83 \pm 0.07$	$1.06 \pm 0.10$	<b><math>1.58 \pm 0.16</math></b>	$89.75 \pm 0.33$
Bulk	0.71	0.90	<b>1.30</b>	95.96

**Table 4.7:** Results of spectral analysis. All values in wt%.

Spectrum	Si:Fe	Cr:Fe	Mn:Fe
1	$8.00 \pm 0.78 \times 10^{-3}$	$1.16 \pm 0.12 \times 10^{-2}$	<b><math>1.58 \pm 0.18 \times 10^{-2}</math></b>
2	$7.61 \pm 0.79 \times 10^{-3}$	$8.37 \pm 0.11 \times 10^{-3}$	<b><math>1.41 \pm 0.17 \times 10^{-2}</math></b>
3	$7.87 \pm 0.79 \times 10^{-3}$	$1.01 \pm 0.11 \times 10^{-2}$	<b><math>1.76 \pm 0.17 \times 10^{-2}</math></b>
4	$9.24 \pm 0.81 \times 10^{-3}$	$1.18 \pm 0.12 \times 10^{-2}$	<b><math>1.76 \pm 0.19 \times 10^{-2}</math></b>
Bulk	$7.43 \times 10^{-3}$	$9.37 \times 10^{-3}$	<b><math>1.35 \times 10^{-2}</math></b>

**Table 4.8:** Results of spectral analysis expressed as ratios of weight concentrations.

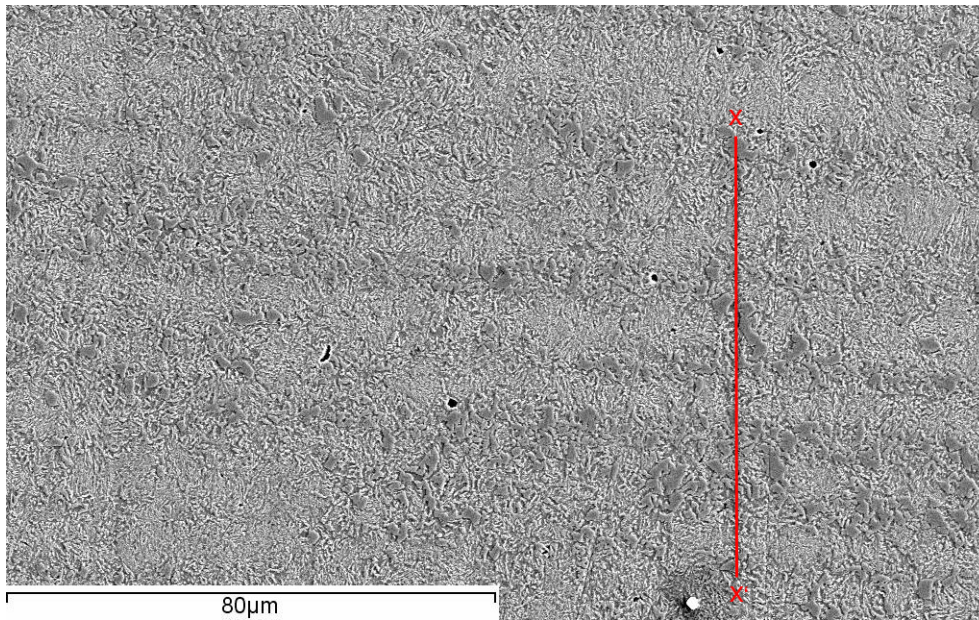


**Figure 4.20:** Scanning electron micrograph showing location of linescan.

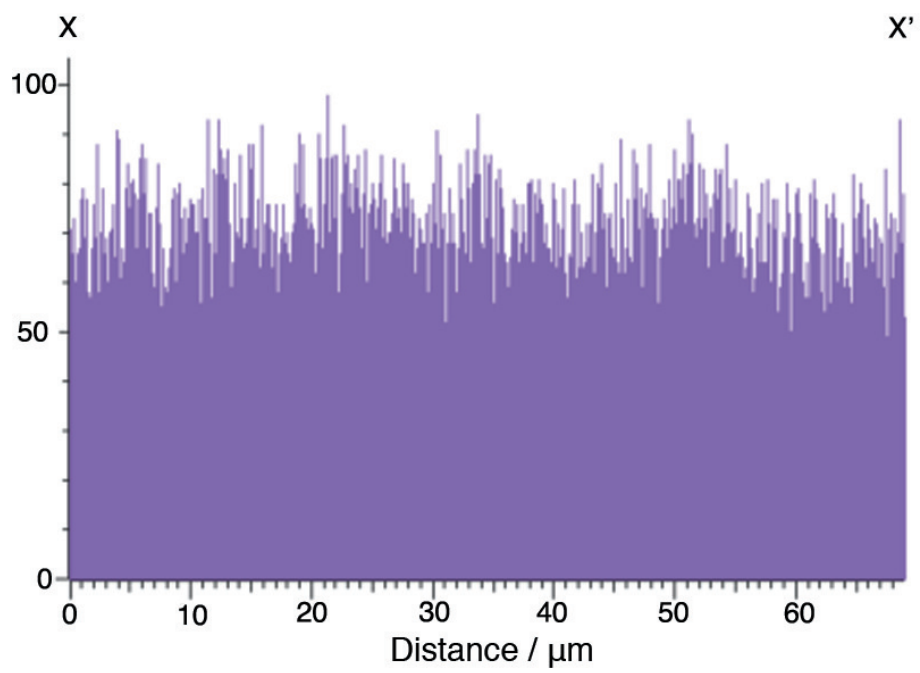


**Figure 4.21:** Manganese linescan spectrum along line XX' in Figure 4.20.

Examination of the data in Tables 4.7 and 4.8 identifies chromium as an alternative candidate for segregation. This element has been found to undergo segregation in carbide-free ausferritic steels [237], while Rose *et al.* report that chromium segregation in the present alloy influenced the etching behaviour (producing visible bands) but did not alter the structure of the steel [193].

### 4.3.5 X-ray diffraction

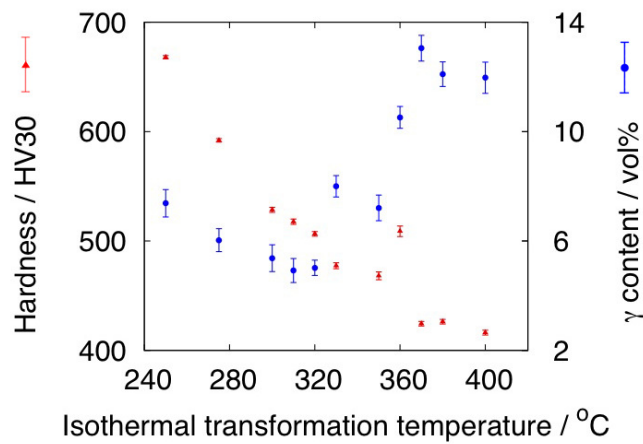


**Figure 4.22:** Retained austenite content and hardness of samples transformed isothermally.

X-ray analysis was used to quantify the volume fraction of retained austenite and the carbon contents of both the retained austenite and bainitic ferrite. Figures 4.22 and 4.23 contain the results of the analysis.

The retained austenite content is at a minimum at a transformation temperature of 310°C. At lower transformation temperatures, the partitioning of carbon into retained austenite and the subdividing of the retained austenite by bainitic ferrite plates both lead to increased stability: it is difficult for the austenite to decompose. Conversely, at higher transformation temperatures, the austenite is less stable and more prone to decomposition. However, the quantity of retained austenite initially present is higher at these temperatures. Subsequently, there is still a large amount of retained austenite present after this decomposition has taken place. The lower stability of the retained austenite at higher transformation temperatures is reflected in the carbon content data given in Figure 4.23,

which shows a fall in the retained austenite carbon content with increased transformation temperature.

The hardness data presented in Figure 4.22 conform to the expected trend. Increased hardness values at lower transformation temperatures are indicative of a greater volume fraction of bainitic ferrite. The retained austenite is also harder due to its higher carbon content [238].

Figure 4.23 contains data on the carbon content of both bainitic ferrite and retained austenite, and illustrates how the carbon is partitioned between the two phases at various transformation temperatures. The transformation stops roughly at the  $T_0$  curve, as expected, although the austenite carbon content does stray beyond the  $T_0$  line. This can occur when films of austenite become trapped between growing sheaves of ferrite, all of which reject excess carbon into the adjacent austenite film, raising its carbon content above that expected from the theory. That the data exceeds the  $T'_0$  limit reflects the fact that the assumption of purely elastic accommodation of the shear strains in the adjacent austenite, is questionable.

The effects of manganese segregation on the  $T'_0$  and  $Ae_3$  curves are also shown in Figure 4.23, but are not particularly significant. A similar set of calculations was performed for chromium segregation, however, there was no discernible change to the  $T'_0$  curve.

Given that cementite was found during TEM characterisation of the alloy, it is relevant to look for corroboration of this from the X-ray results. The cementite is thought to be present in small quantities only, so it is not likely to appear on a short ( $\sim 2$  h) scan of the full 40-140° spectrum. Podder and Bhadeshia were able to identify cementite using X-ray methods by performing long-duration ( $\sim 12$  h) scans in the range 36-52° [239]. Using this approach, it was possible to confirm the presence of cementite in a sample transformed at 400°C (Figure 4.24), but not in samples transformed below this temperature, due to the small volume fractions involved.

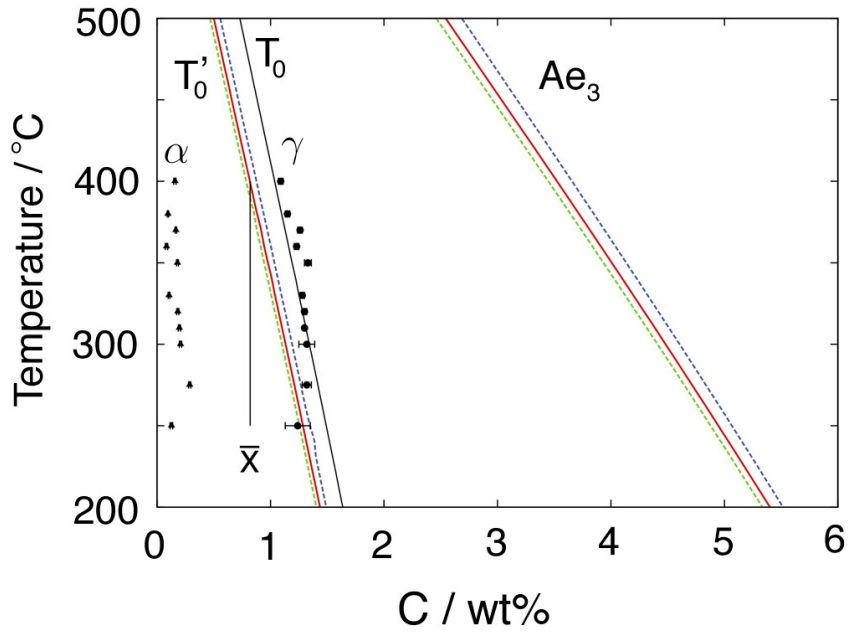


**Figure 4.23:**  $T_0$ ,  $T'_0$  and  $Ae_3$  curves calculated using MTDATA v.4.73 and the TCFE v.5 database, with experimental X-ray results showing the carbon content of bainitic ferrite and retained austenite. Also shown are the  $T'_0$  and  $Ae_3$  curves for a high ( $\sim 1.7$  wt%) Mn content (green) and low ( $\sim 0.6$  wt%) Mn content (blue). The overall carbon content of the alloy is given by  $\bar{X}$ .

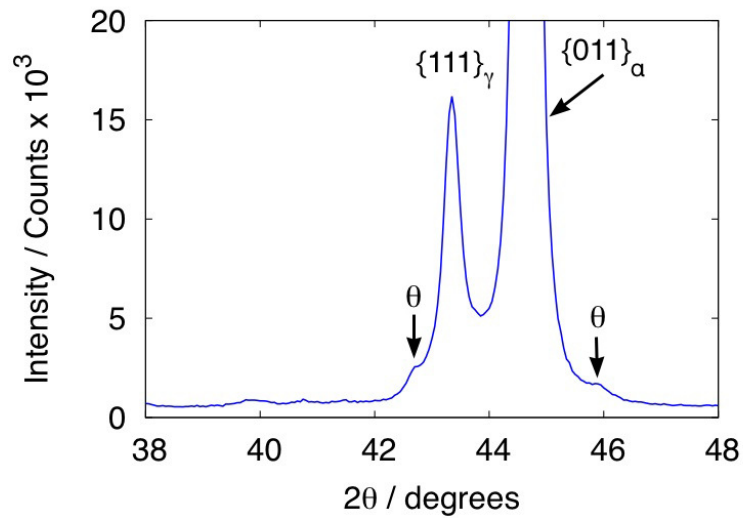


**Figure 4.24:** Cementite reflections observed in Alloy A transformed at  $400^\circ\text{C}$  for 3 h.

Using high-resolution X-ray techniques, it may even be possible to resolve any martensite and ferrite peaks generated from these structures. The spectra obtained in this work are of insufficient quality to isolate the two phases, especially considering that martensite may only be present in small amounts. An alternative analysis was considered wherein a single tetragonal model is used to fit the ferrite peaks, and the  $c/a$  ratio is calculated. In theory, small quantities of martensite will cause an increase in this tetragonality, so that a qualitative comparison of martensite content may be made between samples. However, this approach is not appropriate here, since a change in transformation temperature will also affect the carbon supersaturation, and hence  $c/a$  ratio, of the bainitic ferrite [240]. An increase in tetragonality due to the formation of martensite may well be undetectable over the larger, corresponding decrease due to a higher transformation temperature. Indeed, this is broadly what is observed in the present case, although the errors are too large for the conclusion to be certain (Table 4.9).

T / °C	$c/a$
200	$1.0077 \pm 0.001$
275	$1.0067 \pm 0.002$
300	$1.0059 \pm 0.002$

**Table 4.9:** Measured  $c/a$  ratio of Alloy A samples transformed at various temperatures.

### 4.3.6 Thermodynamic and kinetic modelling

Figure 4.25a illustrates the thermodynamic conditions required for cementite to precipitate from austenite in a bainitic alloy: the constitution point of the alloy must lie within the shaded region in this diagram. A paraequilibrium calculation was performed to find the locus of the  $\gamma/(\gamma + \theta)$  phase boundary in Alloy A (Figure 4.25b), assuming paraequilibrium for all phases. Although all observations of cementite in this work indicate that it has precipitated from bainitic ferrite, these results imply that cementite precipitation from austenite may also occur. The curve is indicative of the limited capacity of this alloy to suppress cementite formation: austenite is unstable to this transformation below  $\sim 650^\circ\text{C}$ , a relatively high temperature.

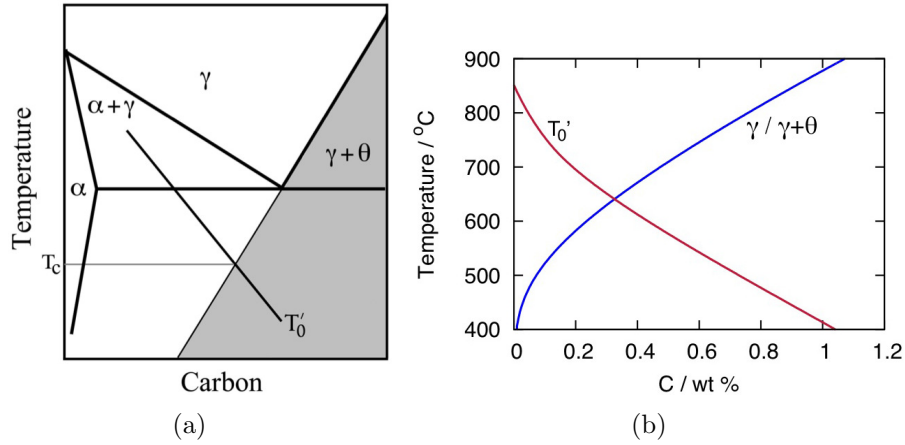


**Figure 4.25:** (a) Thermodynamic condition for cementite precipitation from austenite in a bainitic alloy, taken from Bhadeshia [9]. (b) Equivalent plot of  $T_0'$  and paraequilibrium  $\gamma/(\gamma + \theta)$  curve for Alloy A.

The TTT curve for Alloy A is shown in Figure 4.26. This was compared with data obtained from the isothermal heat treatments. Also shown in Figure 4.26 are the experimentally-measured transformation start and finish times, measured from the dilatometry curves using an offset method. The experimental and predicted curves agree weakly, although the  $M_S$  values do correlate better (Table 4.10).  $M_S$  and  $B_S$  were estimated as described in Sections 4.2.1 and 4.2.2, illustrated in further detail in Figures 4.27 and 4.28.

	$M_S / ^\circ\text{C}$	$B_S / ^\circ\text{C}$
Experimental	145	$\sim 455$
Calculated	118	313

**Table 4.10:** Calculated and experimental values of  $M_S$  and  $B_S$ .

The samples used to find  $B_S$  experimentally were examined in the optical microscope (Figure 4.29). However, neither structure appears bainitic, even at high magnifications. Figures 4.29a,b could be interpreted as showing a mixture of ferrite and pearlite, rather than the expected retained austenite, bainitic ferrite and cementite structure. Note, however, that there is a stark difference between Figures 4.29a and c, with the former mostly consisting of light-etching regions and the latter predominantly dark-etching regions. These darker regions could well be

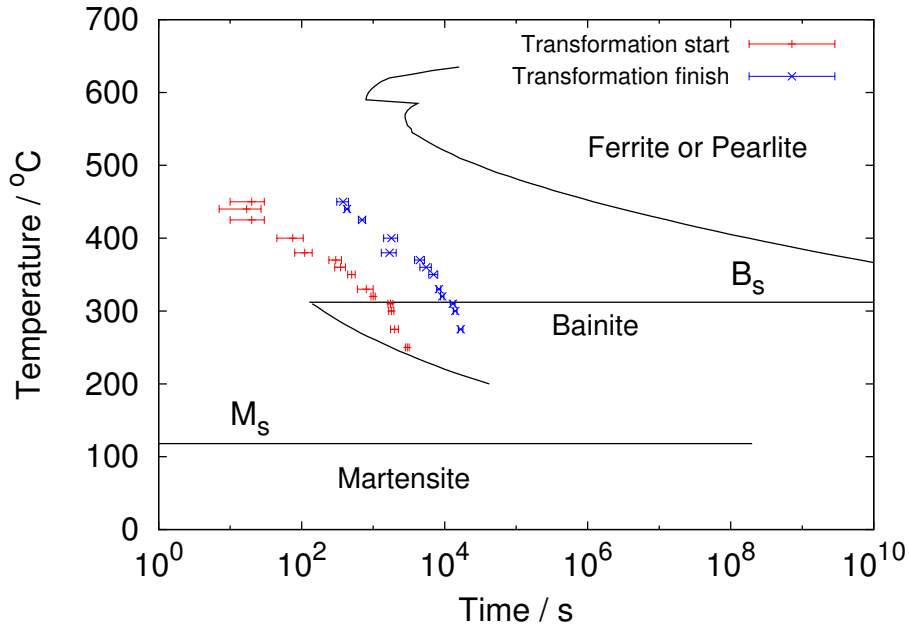


**Figure 4.26:** TTT diagram of Alloy A, calculated using MUCG83 [213].

fine pearlite, the lamellar structure being indistinguishable at the optical magnifications available. Both optical and dilatometric evidence indicate that a distinct change in transformation occurs between 450°C and 460°C. Transmission electron microscopy would provide additional detail about the two microstructures to assist in the interpretation of the optical micrographs.

There is significant disagreement between the measured and calculated values for  $B_S$  (Table 4.10). Manganese can have a strong influence on  $B_S$  and it is worth re-calculating the TTT diagram to take this into account, as has been done in Figure 4.30. It was hoped that the results from the SEM would provide more quantitative information on the manganese segregation, to aid this calculation. Nevertheless, a ‘high-Mn’ band has been plotted on the TTT diagram based on the average of the data obtained from the SEM (1.5 wt% Mn). This value is subject to an error of 0.14 percentage points. The ‘low-Mn’ band was calculated using a value of 1.1 wt%, so that the mean of the high and low values equates to the manganese content of the bulk alloy. Figure 4.31 shows the corresponding TTT diagram with chromium segregation taken into account. According to these calculations, chromium segregation has only minor effects on the thermodynamics of the alloy. The results shown in Figure 4.30 suggest that manganese segrega-

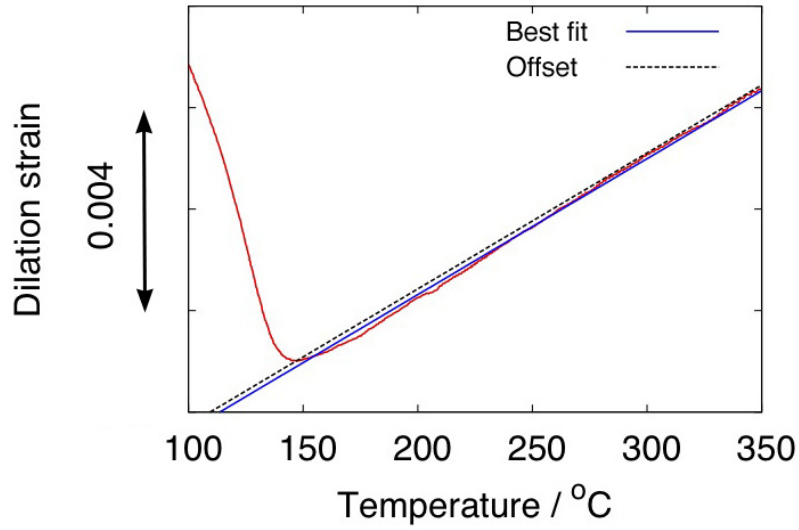


**Figure 4.27:** Offset method used to find  $M_S$ , with  $\epsilon_{\text{offset}} = 1.126 \times 10^{-4}$ .

tion may be at least partly responsible for the high transformation temperatures observed, although the agreement is still poor. It is possible that, in reality, the C-curves for this alloy overlap somewhat, such that it is not possible to identify a distinct  $B_S$  experimentally. The absence of a ‘bay’ in the experimental data supports this hypothesis.

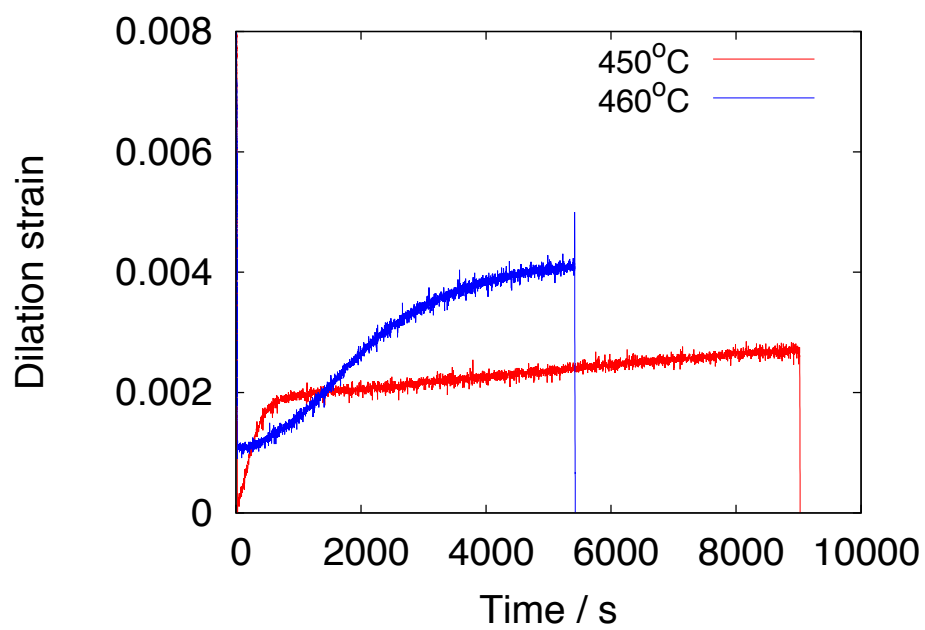
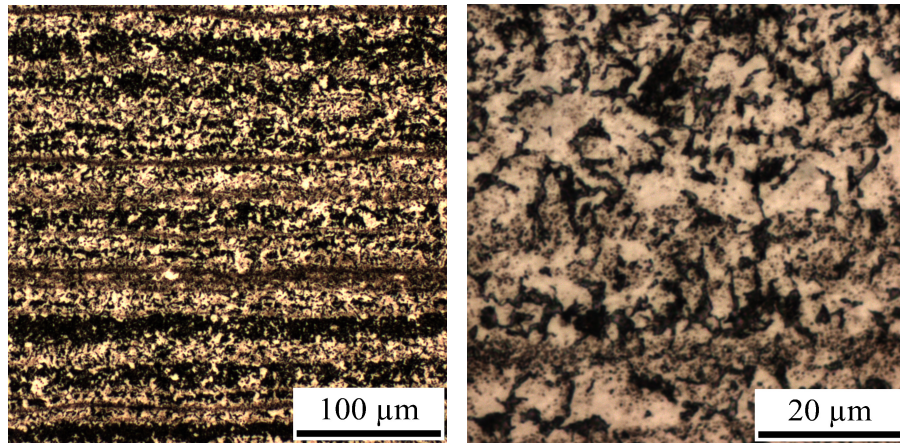
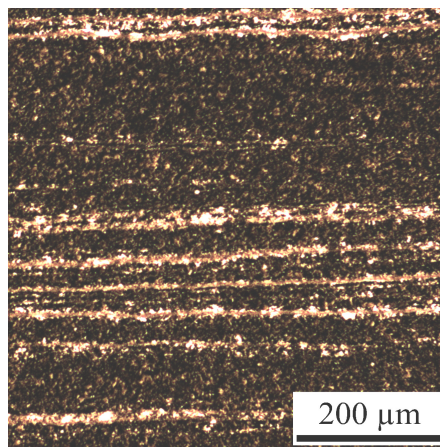


**Figure 4.28:** Dilatometric changes recorded during isothermal transformation of Alloy A at 450°C and 460°C. The curve obtained at 460°C is markedly different, suggesting that bainite is no longer the primary transformation product.



(a)

(b)



(c)

**Figure 4.29:** Optical micrographs of samples transformed in Figure 4.28. (a,b) 450°C transformation; (c) 460°C transformation.

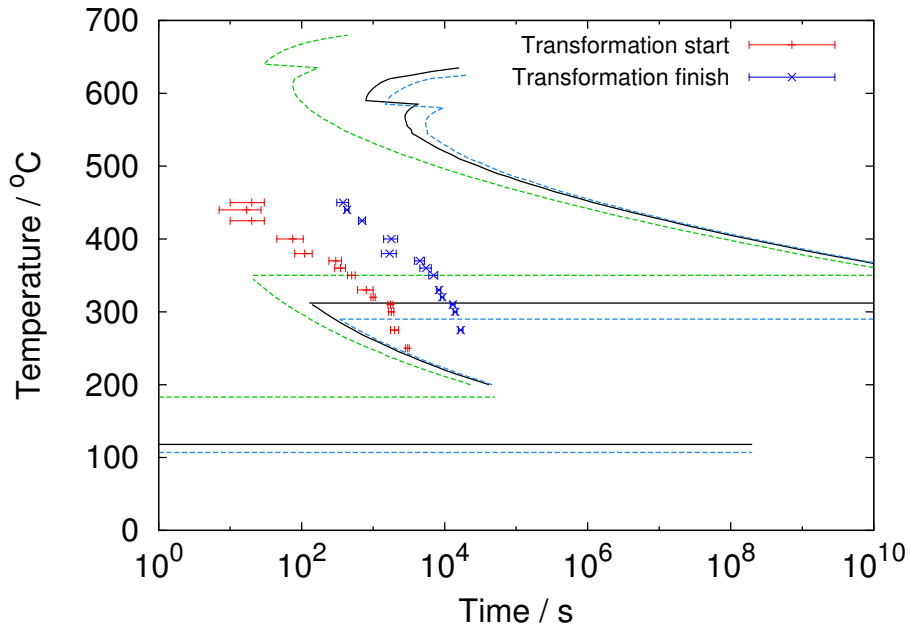


**Figure 4.30:** TTT diagram showing the effect of manganese segregation. Green represents low manganese content (1.1 wt%) and blue represents high manganese content (1.5 wt%).

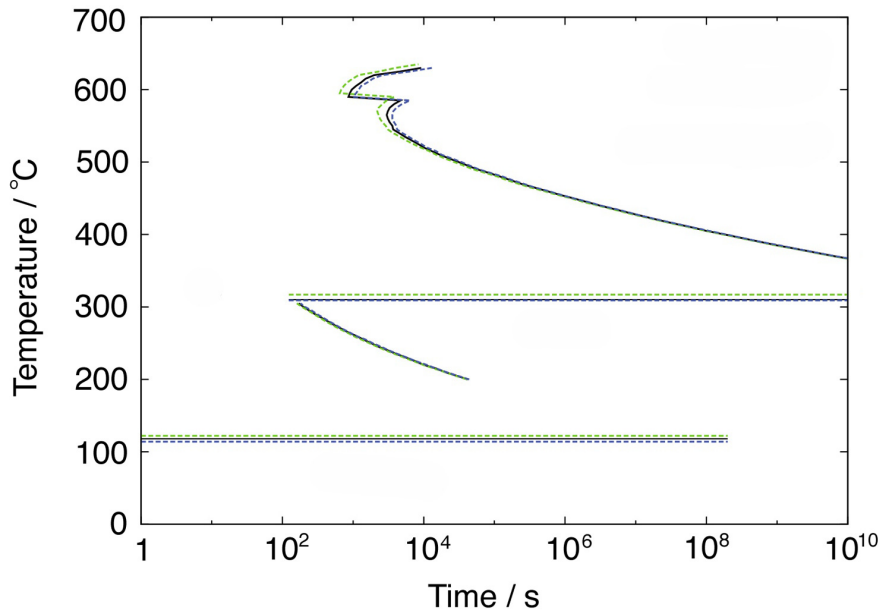


**Figure 4.31:** TTT diagram showing the effect of chromium segregation. Green represents low chromium content (0.75 wt%) and blue represents high chromium content (1.05 wt%).

## 4.4 Conclusions

A variety of characterisation techniques was used to study the isothermal transformation behaviour of a novel, fast-transforming nanostructured steel. Due to a reduced alloy content and increased austenitisation temperature, the scale of the bainitic structure is coarser than in other comparable alloys, however, hardness measurements suggest that this does not significantly affect the strength.

The low silicon content of the alloy is insufficient to prevent cementite from precipitating during bainite formation, so that the structure is not conventionally superbainitic. Electron diffraction results show that the carbides precipitate from and within the bainitic ferrite, and are present even at the lowest transformation temperatures examined (200°C). The carbides are of a fine morphology and present in small volume fractions, so that it is not possible to detect their presence using X-ray methods. Thermodynamic calculations show that cementite precipitation from the retained austenite is also possible.

Calculations and experimental evidence indicate that a proportion of the retained austenite transforms to martensite following isothermal heat treatment at 275°C or above — which may contribute to the high hardness of the alloy. Some martensite formation may also occur at lower transformation temperatures, but this was not detected in the present work. Other, high-resolution, methods may be able to positively identify martensite in the structures studied, for example by attempting to resolve a peak doublet. It would then be useful to make a quantitative assessment of the martensite volume fraction formed as a function of transformation temperature.

It is speculated that manganese segregation influences the transformation behaviour of the alloy, and results in clear banding in samples transformed at temperatures above 300°C. Ideally, additional measurements, using long-duration energy-dispersive X-ray spectroscopy or similar techniques, should be performed to confirm this quantitatively, since the current SEM data used to support this hypothesis is weak.



*Brighter than glass, and yet, as glass is, brittle;  
Softer than wax, and yet, as iron, rusty.*

William Shakespeare

## CHAPTER 5

---

# RESOLVING TOUGHNESS ANOMALIES IN NANOSTRUCTURED BAINITE

---

## 5.1 Introduction

It has been asserted that the Charpy impact toughness is much lower than might be expected from the measured  $K_{1C}$  fracture toughness in nanostructured steels [35]. For alloys of almost identical chemical composition and heat treatment, the Charpy energy reported is only 4-7 J whereas  $K_{1C}$  is some 28-32 MPa m<sup>1/2</sup> depending on the heat treatment, with all measurements conducted at ambient temperature [34, 36].<sup>1</sup> However, it remains the case that none of the published literature contains both measures of toughness on the same alloy [33, 34, 37, 38, 241–243]. In general, when comparisons are made across nanostructured bainite of different compositions, the range of Charpy energies remains from 4-7 J whereas the fracture toughness is from 28-55 MPa m<sup>1/2</sup>. For comparison, a 300M steel (consisting of a mixture of bainite and austenite) of comparable strength may have Charpy impact energy values in the range 15-30 J [244]. Meanwhile, the Aermet 100 steel has recorded impact energies of 40-70 J and  $K_{1C}$  values of 100-160 MPa m<sup>1/2</sup>, again at similar strength levels to superbainite (1.3–2 GPa) [35, 245].

---

<sup>1</sup>The relevant compositions are:

0.79C-1.56Si-1.98Mn-0.24Mo-1.01Cr-1.51Co-1.01Al-0.0V [36]

0.82C-1.55Si-2.01Mn-0.25Mo-1.01Cr-1.51Co-1.03Al-0.1V [34]

and the properties reported here are for samples transformed at 200 and 250°C.

One hypothesis states that this apparent disparity is a result of the different sample geometries required by the two tests, in one case a blunt notch and in the other an atomically sharp crack [35]. During an impact test, the stress-affected volume at the Charpy notch root is larger, as a result of the larger root radius, compared with an equivalent  $K_{1C}$  sample. It is thought that this creates a large region containing brittle martensite, prior to crack initiation. When the sample fails, it then does so in a brittle manner. Since the  $K_{1C}$  standard sample contains a sharp crack, the corresponding stress-affected region is much smaller and any martensite formed is still surrounded by plenty of retained austenite in the unstressed regions.

Understanding these mechanisms is important for assessing the relevance of the Charpy toughness results from these alloys, and for working towards controlling the toughness on the basis of phase-transformation theory and structure-property expectations. Within the context of this thesis, toughness control is relevant for the application of Alloy A (Table 3.1) to armour products, the specifications of which include a minimum required Charpy energy [193].

Accordingly, this chapter describes experiments performed on Alloys A, B and C with the purpose of better understanding the Charpy impact behaviour of nanostructured steels. The work represents the preliminary stages of an investigation of the notch root region of a Charpy sample manufactured from Alloy A, and its response to an applied stress, with the hope that this may support or invalidate the hypothesis described here.

## 5.2 Experimental methods

During a Charpy impact test, the test specimen is subject to rapid three-point-bend loading conditions. By applying a three-point-bend at low strain-rates, it is possible to recreate the loading conditions (but not the consequences of strain-rate) that exist at the notch prior to failure. Bend tests were carried out on sub-size Charpy specimens, using an Instron Mayes 100 kN servo hydraulic machine, with a gauge length of 40 mm and a displacement rate of  $0.5 \text{ mm min}^{-1}$ . Under these conditions, the failure load was found to be  $\sim 10 \text{ kN}$ . Subsequent samples were loaded to 8 kN and then unloaded, allowing the intact notch root region to be examined. Details of the Charpy specimen geometries are set out in

Sections 3.5.2 and 3.5.3.

### 5.2.1 Microhardness testing

Automatic microhardness testing of Charpy notches in Alloy A was performed using a Wilson Hardness Tukon 2500 hardness tester, according to the ASTM E384-11 standard. Samples were ground and polished as detailed in Section 3.2.

## 5.3 Results and discussion

### 5.3.1 Mechanical tests

Because of the lack of direct-comparison data between Charpy and  $K_{1C}$  results for any nanostructured steel, a set of initial experiments was performed to confirm that there is a disparity between the two in the same alloy. There is no  $K_{1C}$  data available in the literature for Alloy A, however, the fracture toughness of Alloys B and C has been measured previously [36]. Additionally, it was not possible to manufacture full-size Charpy impact specimens from the Alloy A plate. Therefore, impact energy measurements were made using Alloys B and C for the purposes of comparison. Furthermore, because all impact testing of Alloy A was performed at a much later date, the fractography observations presented in Section 5.3.2 were made on an Alloy C Charpy specimen. Aside from these practical considerations, the focus of this chapter is on Alloy A.

Table 5.1 shows the results of Charpy impact testing carried out for two different heat treatment conditions, and the corresponding  $K_{1C}$  values taken from the literature.

The impact toughness results are reasonably consistent with values reported in the literature for similar alloys [34, 38, 242]. Bhadeshia has speculated that an alloy with  $K_{1C} = 44 \text{ MPa m}^{\frac{1}{2}}$  would have a Charpy impact energy of around 5 J [35], which is roughly in agreement with the data reported here. It is interesting that the two alloys treated at 200°C exhibit identical values of  $K_{1C}$  and UTS, but somewhat different Charpy toughness values. Denting of some samples was found to occur during the test; this may have contributed to the relatively high Charpy impact energies recorded. It is noted in the literature that damaged samples such

Alloy	Transformation temperature / °C	UTS / GPa	Charpy toughness / J	$K_{1C}$ / MPa m <sup>1/2</sup>
Alloy B	200	2.2	9.0 ± 3.5	32
Alloy B	250	1.9	14.1 ± 3.1	35
Alloy C	200	2.2	3.2 ± 0.2	32
Alloy C	250	1.95	4.9 ± 0.3	38

**Table 5.1:** The results of Charpy and  $K_{1C}$  toughness measurements in three nanostructured steels. the UTS and  $K_{1C}$  data are taken from Garcia-Mateo *et al.* [36]. Compositions of alloys can be found in Table 3.1.

as these may lead to erroneous readings and should possibly be discarded [246].

Charpy tests were later performed on sub-size specimens manufactured from Alloy A. The aim was to assess whether specimen orientation has a significant influence on impact toughness. Banding due to chemical segregation was observed during the characterisation of this material in Chapter 4 and these bands could promote or inhibit crack propagation, depending upon their orientation in the specimen. Such bands have been found to reduce toughness in high-manganese bainitic steels as a result of promoting martensite formation [37]. It is possible also that the bands may deflect a crack tip if aligned perpendicular to the crack growth direction, or provide a preferential path for propagation when parallel to it. Accordingly, both transverse and longitudinal Charpy specimens (produced as described in Section 3.5.3) were tested. The results are presented in Table 5.2, and do not show any real differences between the two orientations.

Orientation	Transformation temperature / °C	Charpy toughness / J
Transverse	200	3.5 ± 0.7
Longitudinal	200	4.0 ± 1.3

**Table 5.2:** The results of Charpy impact energy measurements in Alloy A specimens machined with banding parallel (‘longitudinal’) and perpendicular (‘transverse’) to the direction of crack propagation.

The fracture load under three-point bending of an Alloy A Charpy sample treated at 200°C, and machined in the transverse orientation, was found to be  $\sim 10.4$  kN. By integrating the resulting force-deflection curve (Figure 5.1) it was possible to calculate the energy absorbed during failure to be 4.03 J, which is in accordance with the low Charpy impact energies measured in Table 5.2. Because the specimen is sub-sized, this value is not directly comparable to that from a full-sized specimen. By scaling linearly, the full-size energy absorption is estimated to be 5.4 J. However, both specimen size and strain-rate are important factors in determining the impact energy of a material and the relation between these variables is not always straightforward [246] — although the data from Table 5.2 and Figure 5.1 suggest that strain-rate does not significantly affect the measured toughness. Nevertheless, this energy absorption value should not be considered an accurate estimate, although it is reassuring that the figure obtained is within the expected range.

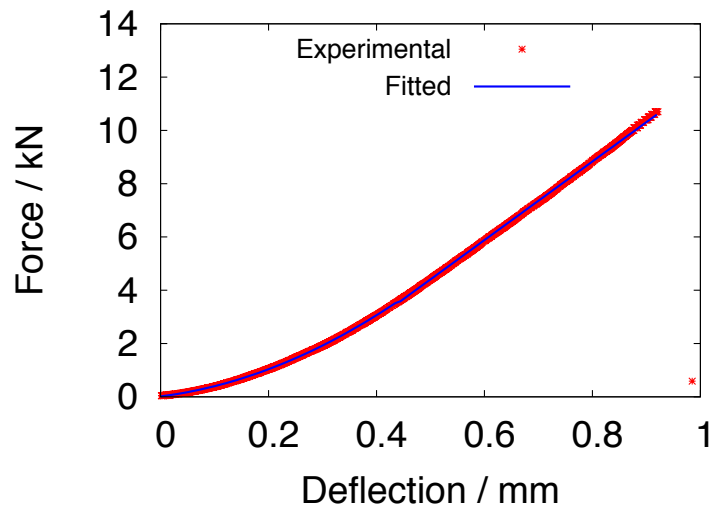


**Figure 5.1:** Force-deflection curve of a Charpy sample subjected to three-point-bending until destruction. The continuous line is an empirically-fitted function that was used to determine the area underneath the curve.

### 5.3.2 Fractography

Fractography was carried out on the Alloy C Charpy sample transformed at 200°C, using scanning electron microscopy. The fracture surface exhibited a brit-

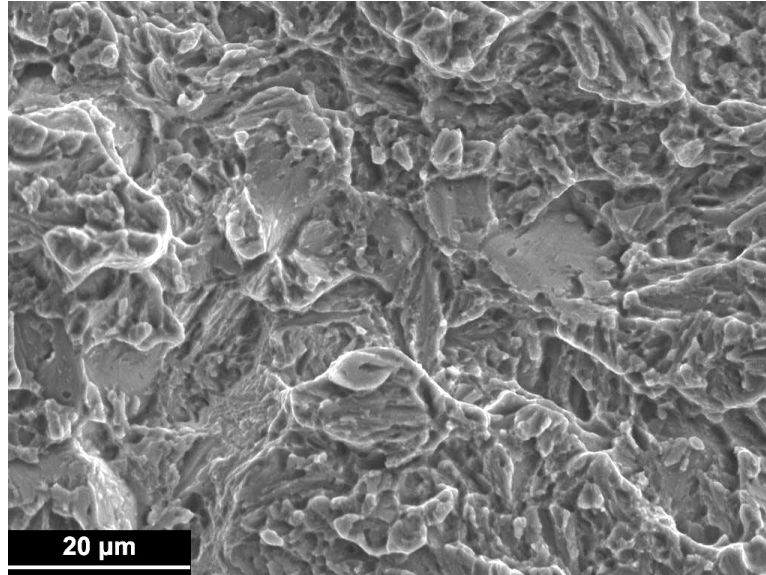
tle morphology, accompanied by a thin shear lip ( $\sim 40 \mu\text{m}$  wide). The specimen has predominantly undergone quasi-cleavage fracture, with a typical surface shown in Figure 5.2a. There were also regions of more severe cleavage, such as that presented in Figure 5.2b. Figure 5.3 additionally shows an example of intergranular fracture along prior austenite grain boundaries, close to the notch root. Of particular interest is the deformation of the microstructure at the very surface of the notch root. Figure 5.4 illustrates how the structure has undergone shear deformation — this is almost certainly a result of the machining process used to manufacture the sample. It is therefore to be expected that the material in the notch root will have undergone some hardening prior to loading. Thus, in order to demonstrate that a martensite transformation occurs during three-point-bend loading, it will be necessary to compare a stressed notch with an unstressed notch, so that the work-hardening effect of machining is accounted for.

It is informative to compare the nature of the fracture surface at the notch root, and that of the surface at the opposite end of the sample. Such a comparison is provided in Figure 5.5. It seems that the fracture surface at a distance from the notch consists predominantly of cleavage fracture, whereas the notch root region shows quasi-cleavage characteristics.

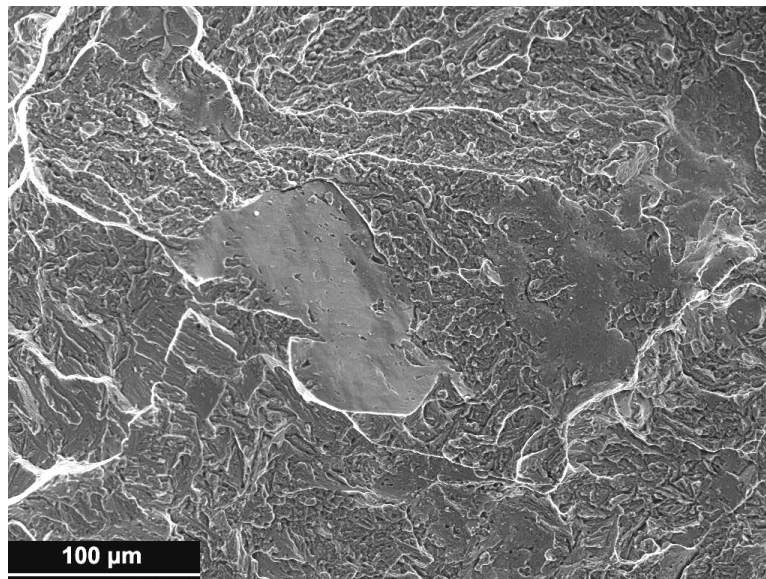
### 5.3.3 X-ray diffraction

Several approaches were taken to study the structure of the notch root region of a stressed Charpy sample, X-ray diffraction being the primary technique used. The sample was positioned with the base of the notch in the zero-displacement position. The notch itself was oriented parallel to the direction of the X-ray beam so as to guarantee irradiation in the correct place.

It was necessary to use aluminium to mask off the region around the notch, to ensure that any reflections were coming from the notch root itself and not anywhere else on the sample. To avoid any aluminium reflections interfering with the spectrum, the scanning range was limited to  $48\text{-}55^\circ$ , isolating the  $\{002\}_\gamma$  peak. By ensuring that the background level remained constant, it was possible to compare the size of the austenite peak at the notch root and at a distance from the notch. This provided a ‘before and after loading’ picture.



(a)



(b)

**Figure 5.2:** Scanning electron micrographs illustrating the fracture surface of an Alloy C Charpy specimen. (a) Typical region showing quasi-cleavage characteristics; (b) region showing large area of cleavage.

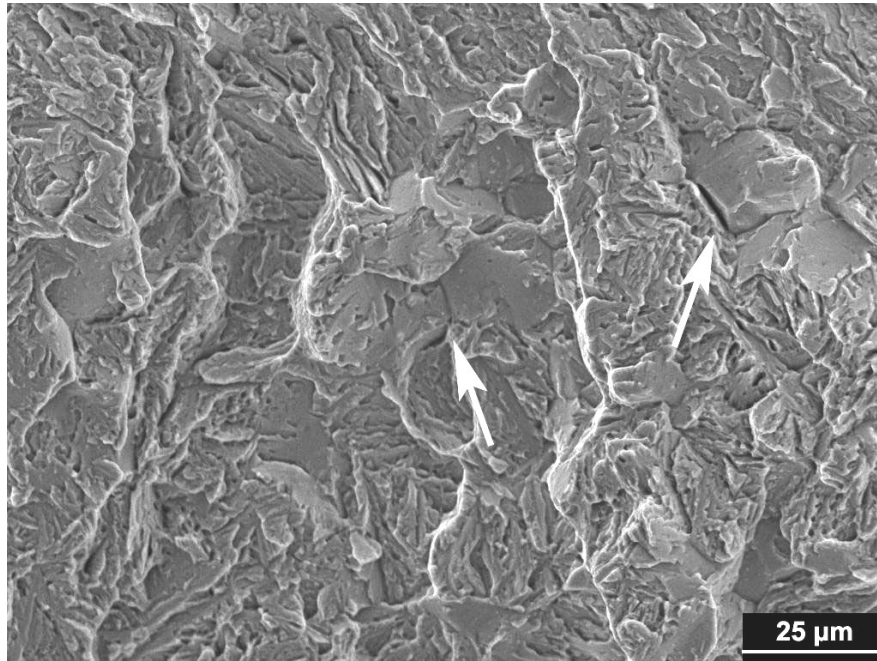


**Figure 5.3:** Scanning electron micrograph showing details of intergranular fracture occurring in the notch root region of a failed Alloy C Charpy sample.

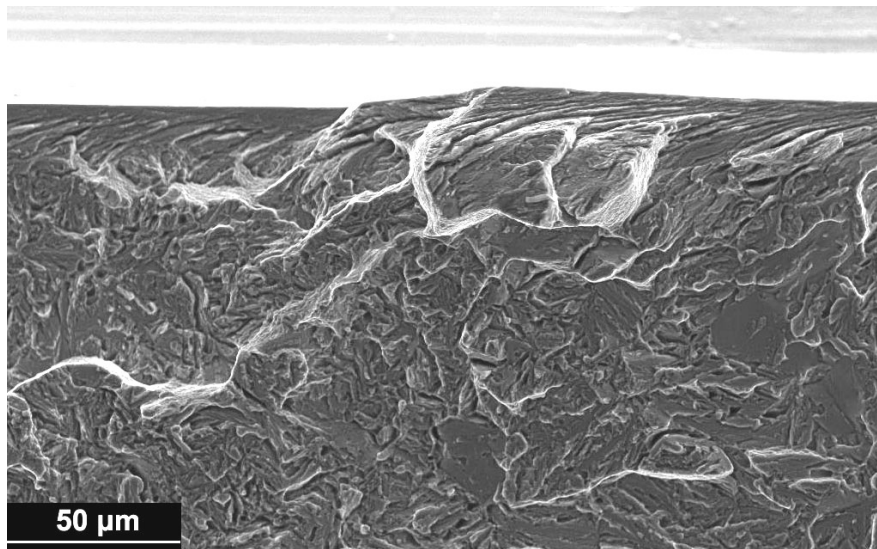
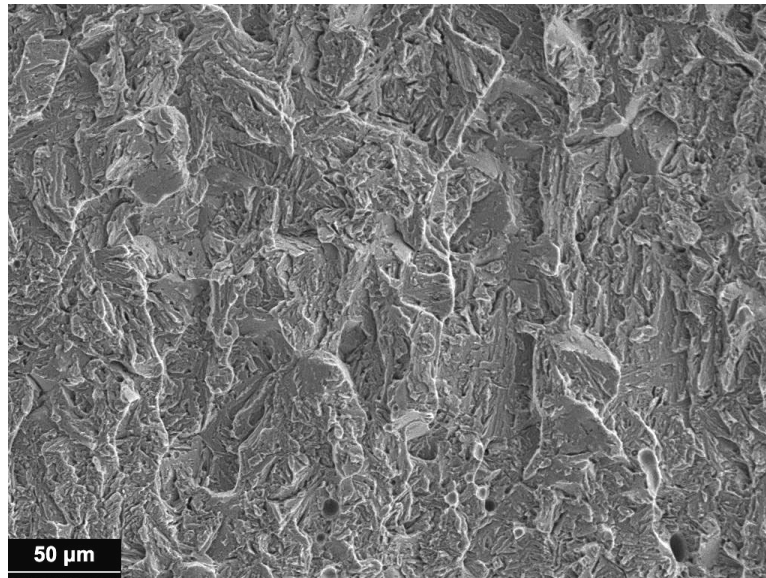
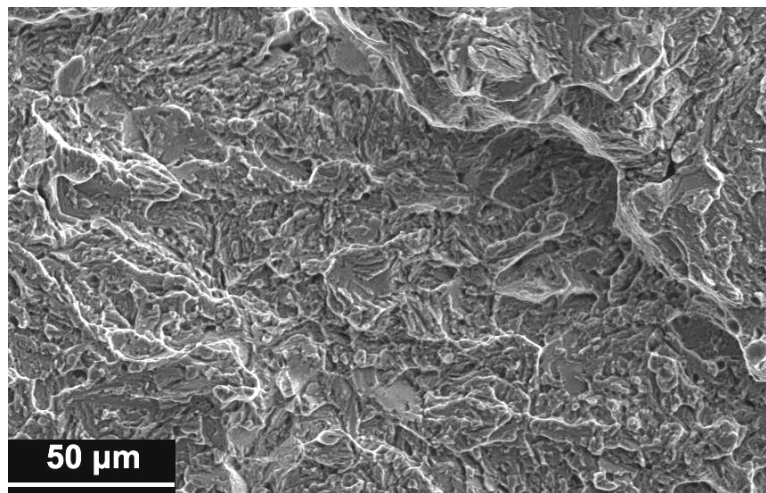


**Figure 5.4:** Scanning electron micrograph showing microstructural shear deformation at the notch root surface.



(a)



(b)

**Figure 5.5:** Scanning electron micrographs illustrating the fracture surface of an Alloy C Charpy specimen in two separate locations. (a) Base of sample (away from notch); (b) notch root region.

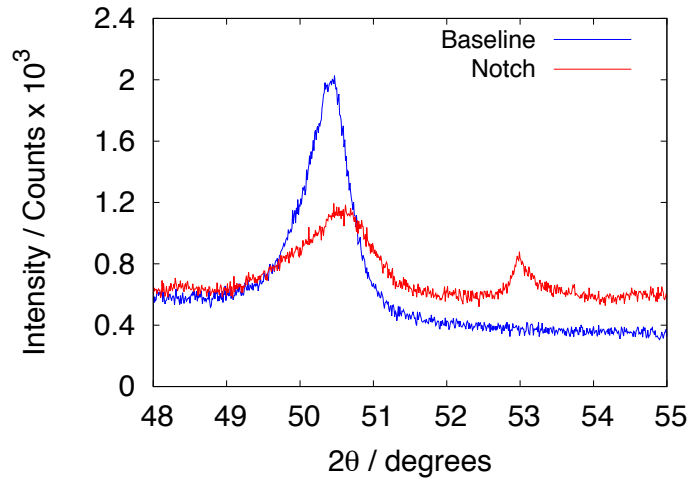


**Figure 5.6:** X-ray scans taken of the  $\{002\}_\gamma$  peak at the notch root of a stressed Charpy sample, and in an unstressed region of the same sample.

Figure 5.6 and Table 5.3 show that there is a clear reduction in integrated area of the peak at the notch root compared to that in an unstressed region of the material. At first glance this would suggest that some of the austenite has indeed undergone stress-induced transformation to martensite. However, this result is not conclusive because it is not possible to assess whether the difference in peak size is due to texture or notch effects. If the nanostructure exhibits preferred orientation, this can influence the relative intensity of diffracted peaks [200, 247]. The lower intensity peak at the notch root may then be due to this region of the sample having a different texture from that of the ‘baseline’ region, but without other austenite and ferrite peaks to use for comparison, this possibility cannot be explored. Because of the need to use a mask to isolate the notch, many of the ferrite and austenite peaks are obscured by reflections from the mask material. Aluminium, silicon and carbon masks were all tried, however, none produced a spectrum that could be accurately evaluated for texture.

The experimental set-up also neglects the influence of machining on the nanostructure below the notch, since it compares a machined region with a non-machined region.

The peak shift shown in Figure 5.6 is also unexpected. The peak from the notch root is shifted to higher  $2\theta$  values relative to the ‘unstressed’ peak. Since austenite with lower carbon content is expected to transform preferentially to martensite,

Peak location	Integrated intensity
Unstressed region	91100
Notch root	43000

**Table 5.3:** Integrated intensity of the  $\{002\}_\gamma$  peaks shown in Figure 5.6, calculated using ProFit.

any residual austenite still remaining should have a higher overall carbon content, which would manifest as a peak shift to lower  $2\theta$  values. The shift in Figure 5.6 may be a result of specimen displacement error: by setting the base of the notch to the ‘correct’ height, the material above the notch root necessarily protrudes above this level, which would cause the peak to shift to the right. The expected peak shift due to this displacement was calculated to be  $0.6^\circ$ , which is consistent with Figure 5.6.

Furthermore, the notch peak is broader — again reminiscent of a martensitic transformation, which would leave heterogeneous strains in the remaining austenite. Additionally, the preferential removal of blocky austenite (due to its lower stability) would result in a smaller overall austenite crystallite size. In theory, it is possible to separate out these contributions using a Williamson-Hall plot [248], but the analysis cannot be applied here since multiple peaks are needed.

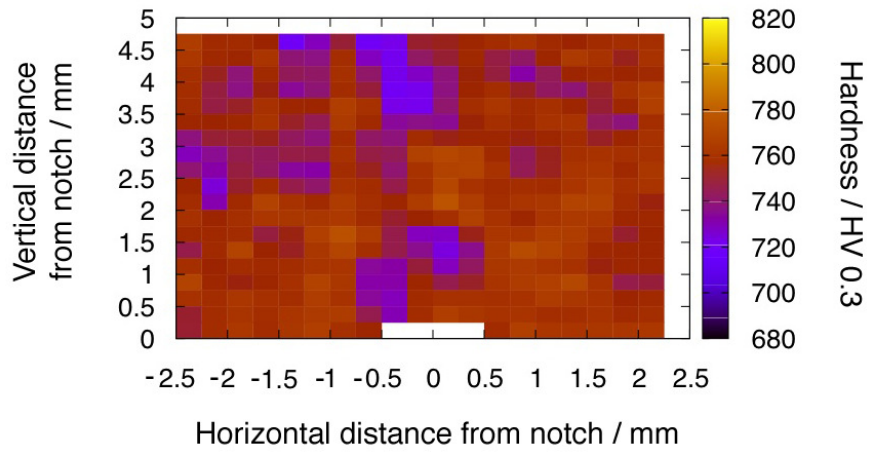
Both  $\{002\}_\gamma$  peaks show some asymmetry, possibly due to a variation in the carbon content of the austenite (which does occur in superbainitic steels [249]) and, in the case of the notch peak, an artefact of the varied specimen displacement. Reflections from material at the top of the notch will occur at higher angles than those from the notch root – in other words, diffracted beams originate from matter at different heights above the notch root (but none below) and a peak asymmetry can result.

An alternative interpretation is that the peak shift does represent a decrease in the austenite d-spacing. Although this is contrary to expectation, it may be that the volumetric expansion associated with the stress-induced martensite transformation acts to compress the remaining austenite. The shift may also be a result of strains generated at the notch root by machining.

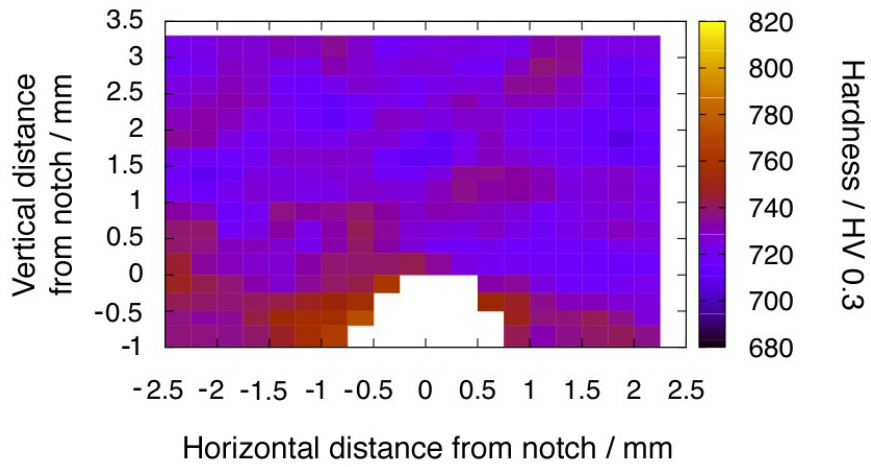
The reflection that occurs at  $53^\circ$  is currently unexplained, although some speculation as to its origin is discussed in Appendix A.1. Overall, although the X-ray evidence in support of a martensitic transformation is compelling, it is clear that additional evidence is still needed.

#### 5.3.4 Microhardness

Figure 5.7 shows the results of microhardness maps taken over the notch root regions of stressed and unstressed specimens. By taking a large number of microhardness readings in a grid around the notch, it is possible to assess the hardness in a statistical way. The difference is reasonably distinct; it seems in general that the notch root region is harder in the stressed sample than in the unstressed sample. To verify that this is a real difference, an independent t-test was applied to the data, which revealed that the difference between the two datasets is statistically significant for  $p=0.0005$ . It is unlikely, however, that this increased hardness should be attributed entirely to the formation of martensite since the area scanned is far too large to correspond to the stress-affected region, which in Chapter 6 is shown to have a size no greater than  $200\ \mu\text{m} \times 200\ \mu\text{m}$ . Because of the high hardness of the material tested, the resulting indent will be small and subject to significant measurement error. Indeed, the equipment accuracy was measured using a sample of known hardness and found to be as high as  $\pm 2\%$ , which corresponds to 15 HV0.3 and is sufficient to account for a majority of the differences.



(a)



(b)

**Figure 5.7:** Microhardness maps taken over the notch root region of (a) stressed Charpy sample; (b) unstressed Charpy sample. Zero vertical distance represents the approximate position of the notch root.

## 5.4 Conclusions

This chapter has presented a description of groundwork performed in order to understand the changes that occur at a Charpy notch root prior to crack initiation. For the first time, experiments have demonstrated the discrepancy between Charpy impact energy and  $K_{1C}$  fracture toughness measured in the same alloy. The effects of both specimen orientation (due to banding) and strain-rate were briefly considered, but neither factor was found to significantly alter the measured toughness.

Examination of failed specimens revealed that the samples undergo brittle failure, with quasi-cleavage morphology dominating the resulting fracture surface. Occasional intergranular fracture was identified close to the notch root. At a distance from the notch, the surface was characteristic of cleavage fracture. No obvious features marking the initiation of fracture were observed. However, it was found that significant shear deformation, generated during machining of the notch, was present to a depth of  $\sim 50\text{--}75\ \mu\text{m}$ .

Laboratory X-ray studies of notched samples produced strong indications that the volume fraction of retained austenite at the notch root of a stressed sample is markedly lower than the comparable value in the bulk material. However, the spectra from this investigation also contained several incongruities, speculated to be the result of residual strains, specimen displacement error and the use of an aluminium mask to isolate the notch. It is clear that a more precise technique is required to verify the measurements made, and to isolate any texture or notch effects that may be influencing the result.

On a larger scale, hardness measurements in the notch region seem to show a significant difference between stressed and unstressed samples. It is not clear why this is observed, although a likely explanation is that of error in the apparatus.

Overall, the results obtained in the course of this work show promise, however, too many uncertainties remain. With the use of more accurate and powerful techniques, it should be possible to observe, with clarity and certainty, the changes that occur at a Charpy notch root as a result of applied stress. The following

chapter details the results obtained from such a study, harnessing synchrotron techniques to resolve this difficulty.



*The real measure of success is the number of experiments that can be crowded into 24 hours.*

Thomas Edison

## CHAPTER 6

---

# TOUGHNESS ANOMALIES IN NANOSTRUCTURED BAINITE: A SYNCHROTRON STUDY

---

### 6.1 Introduction

The work described in Chapter 5 contains several indications that stress-induced phase transformations occur at the notch root of a superbainitic Charpy sample during bending. X-ray measurements reveal a reduction in the retained austenite content in this region, while SEM observations show that the notch machining process causes significant deformation in the adjacent material. Crucially, however, none of these techniques was suitable for obtaining a detailed picture of how the structure of the notch root is affected by both applied stress and machining. For example, while routine X-ray measurements are sufficient for determining phase fractions in the bulk material, a highly-focused beam is desirable to characterise the notch root region of a Charpy sample and isolate precisely the area in which any changes are concentrated.

In contrast, synchrotron X-rays allow accurate beam collimation and sample positioning. The high energies available from a synchrotron source enable spectra to be captured in transmission rather than reflection, which is beneficial since a larger total volume can be sampled. Furthermore, the use of synchrotron radiation minimises absorption and fluorescence effects, while improving resolution

and accuracy.

This chapter sets out the results from an in-depth synchrotron study of the notch root region in Charpy samples taken from Alloy A (Table 3.1). Combined with the data from Chapter 5, a clear picture is revealed of how the various phases behave when subjected to bending and machining stresses and strains.

## 6.2 Experimental methods

As well as studying stressed and unstressed samples, prepared as described in Chapter 5, a third specimen was produced. It was heated to 100°C before undergoing a similar load cycle, in order to evaluate the effect of stabilising the austenite *in situ*. In this case, the failure load was found to be 12 kN, with the intact ‘stressed’ sample being loaded to 9.7 kN (80% of the failure load).

Details of the heat treatments applied to the specimens in this chapter can be found in Section 3.4 and Table 3.2.

### 6.2.1 Synchrotron experiments

Charpy samples from Alloy A, transformed at 200°C, that had undergone three-point-bend loading (but not failure) were sliced as indicated in Figure 6.1 using electron discharge machining. Similar slices were taken from unstressed Charpy samples. The surface of each slice was prepared using the approach detailed in Section 3.2. The notch root regions of these stressed and unstressed samples were then analysed in detail using high-resolution synchrotron radiation. The sample thickness was chosen based upon calculations showing that 40% of the incident X-rays would penetrate the sample completely at a beam energy of 70 keV.

High-resolution transmission X-ray spectroscopy was performed on the I15 beamline at the Diamond Light Source in Oxford, UK, using a monochromatic X-ray beam with dimensions of  $70 \times 70 \mu\text{m}$  and a wavelength of  $0.16313 \text{ \AA}$ . Each spectrum was captured over 40 s using a flat 2-D Perkin-Elmer detector mounted perpendicular to the incident beam. A region roughly  $1 \times 1 \text{ mm}$  was mapped by taking spectra in a grid pattern with step size  $70 \mu\text{m}$  close to the notch root, and a coarser grid with step size  $100 \mu\text{m}$  further from the notch root. A lan-

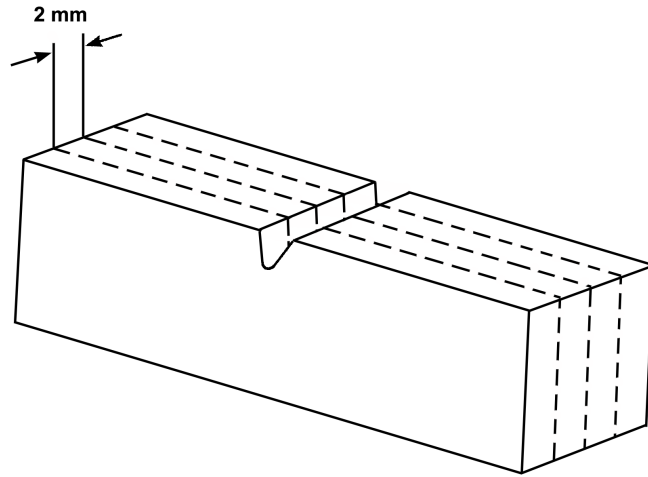


**Figure 6.1:** Figure illustrating how each Charpy specimen was sliced to produce the final synchrotron specimens.

thorium hexaboride ( $\text{LaB}_6$ ) powder standard was used as a calibrant to refine the sample-to-detector distance, beam centre, tilt and instrument parameters. Table 6.1 gives a complete summary of the synchrotron experiments, and Figure 6.2 shows a schematic of the experimental setup.

Data were recorded as 2-D images and were integrated over  $360^\circ$  and converted to  $2\theta$  data using FIT2D [250, 251]. Rietveld refinement was carried out using Bruker TOPAS v.5 software, assuming that there were two phases present: austenite and bainitic ferrite. Previous work has indicated that ferrite may be of a non-cubic nature [252, 253], so in this analysis both a cubic and a tetragonal model were used to fit the ferrite peaks. The weighted profile factor,  $R_{\text{wp}}$ , was used to judge the quality of fit. Section 3.6 contains details of the refinement process.

This refinement approach was taken as it was the most reliable method of peak fitting; the separate martensite and ferrite peaks cannot be easily resolved in these spectra. Several strategies were used to separate the martensite and ferrite phases during Rietveld refinement: modelling ferrite as cubic and martensite as tetragonal; modelling both as tetragonal; allowing lattice parameters of both to vary; assigning fixed lattice parameters to the ferrite phase (measured from the un-notched sample) and allowing the martensite lattice parameters to refine. However, in each case, the results were not reliable because the refinement was unstable, producing measured volume fractions that were not consistent between

Specimen	Location of scan	Details of scan
Stressed Charpy	Notch root	Step size: 70 $\mu\text{m}$ Scan region: 2100 $\mu\text{m} \times 1120 \mu\text{m}$ Centred on notch root
Stressed Charpy (100°C)	Notch root	Step size: 100 $\mu\text{m}$ Scan region: Horizontal linescan Scan taken over half notch region only.
Unstressed Charpy	Notch root	Fine scan at notch root Step size: 70 $\mu\text{m}$ Scan region: 560 $\mu\text{m} \times 560 \mu\text{m}$ Coarse scan further from notch Step size: 100 $\mu\text{m}$ Total scanned region: 1060 $\mu\text{m} \times 1060 \mu\text{m}$ Scan taken over half notch region only.
Unstressed Charpy	Non-machined region	Step size: 100 $\mu\text{m}$ Scan region: 1000 $\mu\text{m} \times 1000 \mu\text{m}$

**Table 6.1:** Details of synchrotron experiments carried out.

spectra. Table 6.2 shows the results generated from repeated analyses of the same spectrum, giving an indication of the variation in results. Therefore, it was decided to use a single tetragonal model ( $I\frac{4}{m}$ mm) to fit both the ferrite and martensite phases, thus obtaining reliable volume fraction measurements of the austenite, which is the key variable in this investigation.

Retained austenite content was calculated using the integrated intensities of the  $\{111\}$ ,  $\{002\}$ ,  $\{022\}$  and  $\{113\}$  austenite peaks and the  $\{011\}$ ,  $\{002\}$ ,  $\{112\}$  and  $\{022\}$  ferrite peaks. Background, scale factor, lattice parameters, peak shape, spherical harmonics and isotropic temperature factor were the refineable parameters, although a limit was placed on the tetragonal lattice to ensure  $c > a$ . Peaks present at higher angles were excluded since these represented only partial 2-D diffraction rings.

Because there was a large number of individual spectra to analyse ( $\sim 800$ ), the refinement process was automated using a MatLab script written by Matthew Blackmur, at the University of Manchester. For each data set, a manual refinement was performed in TOPAS v.5, and this refinement was then used as a

Allow $\gamma$ (cubic), $\alpha$ (cubic), $\alpha'$ (tetragonal)			
	$V_\gamma$	$V_\alpha$	$V_{\alpha'}$
Refinement 1	$11.4 \pm 0.9$	$40.6 \pm 3.8$	$48.1 \pm 4.0$
Refinement 2	$8.9 \pm 0.3$	$2.6 \pm 0.3$	$88.5 \pm 0.4$
Refinement 3	$10.5 \pm 0.3$	$2.1 \pm 0.5$	$87.3 \pm 0.5$
Refinement 4	$10.3 \pm 0.3$	$3.1 \pm 0.4$	$86.7 \pm 0.4$
Allow $\gamma$ (cubic), $\alpha$ (tetragonal), $\alpha'$ (tetragonal)			
	$V_\gamma$	$V_\alpha$	$V_{\alpha'}$
Refinement 1	$12.1 \pm 1.7$	$44.8 \pm 7.8$	$45.2 \pm 7.8$
Refinement 2	$9.9 \pm 0.3$	$88.8 \pm 1.0$	$2.3 \pm 1.0$
Refinement 3	$9.6 \pm 0.3$	$86.7 \pm 1$	$4.5 \pm 1$
Refinement 4	$11.0 \pm 1.1$	$60.6 \pm 5.07$	$28.4 \pm 5.4$
Allow $\gamma$ (cubic), $\alpha$ (tetragonal, fixed $a, c$ ), $\alpha'$ (tetragonal)			
	$V_\gamma$	$V_\alpha$	$V_{\alpha'}$
Refinement 1	$11.1 \pm 1.2$	$41.4 \pm 5.6$	$47.4 \pm 5.5$
Refinement 2	$12.0 \pm 0.5$	$11.1 \pm 2.7$	$76.9 \pm 2.4$
Refinement 3	$9.5 \pm 0.5$	$65.9 \pm 2.3$	$24.7 \pm 2.5$
Refinement 4	$11.0 \pm 0.6$	$13.0 \pm 3.19$	$76.0 \pm 2.9$
Allow $\gamma$ (cubic), $\alpha + \alpha'$ (one tetragonal phase)			
	$V_\gamma$	$V_\alpha + V_{\alpha'}$	
Refinement 1	$11.0 \pm 0.19$	$89.0 \pm 0.19$	-
Refinement 2	$11.3 \pm 0.21$	$88.7 \pm 0.21$	-
Refinement 3	$10.9 \pm 0.24$	$89.1 \pm 0.24$	-
Refinement 4	$11.1 \pm 0.21$	$88.9 \pm 0.21$	-

**Table 6.2:** Results from various refinement methods illustrating a lack of repeatability for each approach. Also included for comparison is the two-phase refinement method used in this study. Values of  $a$  and  $c$  in the third approach were taken as 2.8549 Å and 2.8785 Å respectively. These numbers were obtained from a refinement of a spectrum taken at a distance from the notch, assumed to contain only tetragonal ferrite and austenite.

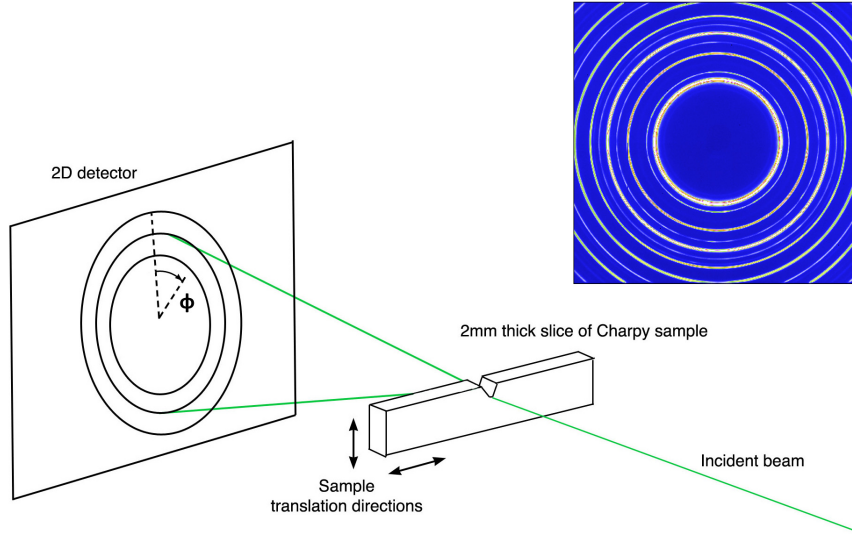


**Figure 6.2:** Schematic illustrating the experimental setup and indicating how the azimuthal angle  $\phi$  was measured. Inset is an example of Debye-Scherrer rings captured during the experiment.

‘starting point’ to refine all spectra in that dataset. The script generates a list of parameters, errors and  $R_{wp}$  values, the latter two being used to assess whether each spectrum was refined appropriately. It is then possible to identify poor refinements and carry them out manually. All automated refinement was carried out at the University of Manchester, in order to access both the appropriate software and sufficient computing power to perform rapid refinement. Consequently, it was not straightforward to repeat refinements of large datasets at later points during the work. In particular, the effect of excluding the overlapping  $\{111\}_{\gamma}$  and  $\{011\}_{\alpha}$  peaks was not initially considered. Separate calculations were subsequently performed using only non-overlapping peaks as a check, however, this did not result in a significant change in volume fraction calculations. Figure 6.3 shows two example sets of values plotted for comparison. Since the conclusions drawn in this chapter focus on trends of data only, a small systematic offset was not found to affect the interpretation of the results, as is discussed in the following section.

Residual strain was analysed using the  $\sin^2 \phi$  method [254]. In this approach, the radius of a diffraction ring is plotted as a function of  $\sin^2 \phi$ , where  $\phi$  is the azimuthal angle around the ring (Figure 6.2). This allows an assessment of the

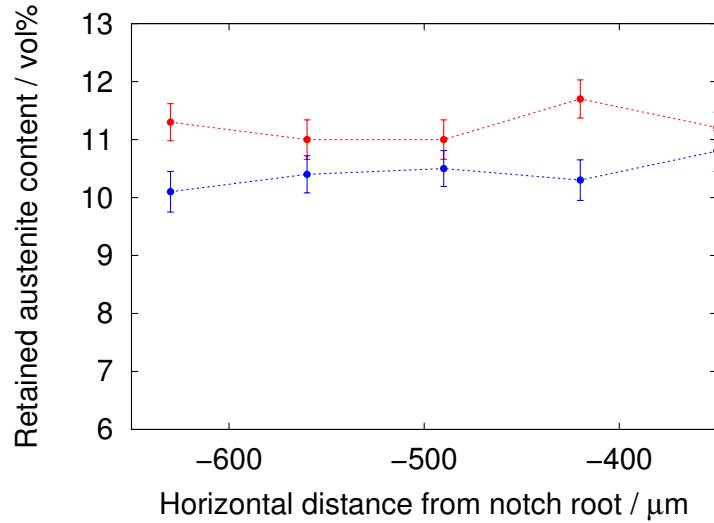


**Figure 6.3:** Retained austenite content in the stressed sample, calculated including the  $\{111\}_\gamma$  and  $\{011\}_\alpha$  peaks (red), and excluding them (blue). While there is some difference between the two datasets, the error bars in several cases suggest the discrepancy is not particularly distinct.

ellipticity of the ring: for a perfect circle (no strain anisotropy), the plot generates a horizontal line. A slope indicates that strain is present anisotropically, with the gradient of the slope representing a measure of the aspect ratio of the ellipse. Thus, the steeper the slope, the greater the anisotropy, although it must be emphasised that this is a relative measure only. It is also possible to calculate values for the lattice strain and residual stress from the data, however, this was not done for the present study since the absolute values of residual strain will have been changed as a result of cutting the samples into thin slices. The presence of strain will produce peak shifts in the X-ray spectra and, if unaccounted for, can lead to incorrect measurements of the lattice parameter, as will be shown in this chapter. The implications of strain anisotropy for the Rietveld analysis of the integrated 1-D spectra are discussed in detail in Section 6.3.1.

## 6.3 Results and discussion

The results of the notch analysis are shown in Figure 6.4. It is evident that the volume fraction of retained austenite at the notch root of a Charpy sample is greatly reduced following the application of a three-point bending load. These results are taken from a Rietveld refinement incorporating a tetragonal ferrite

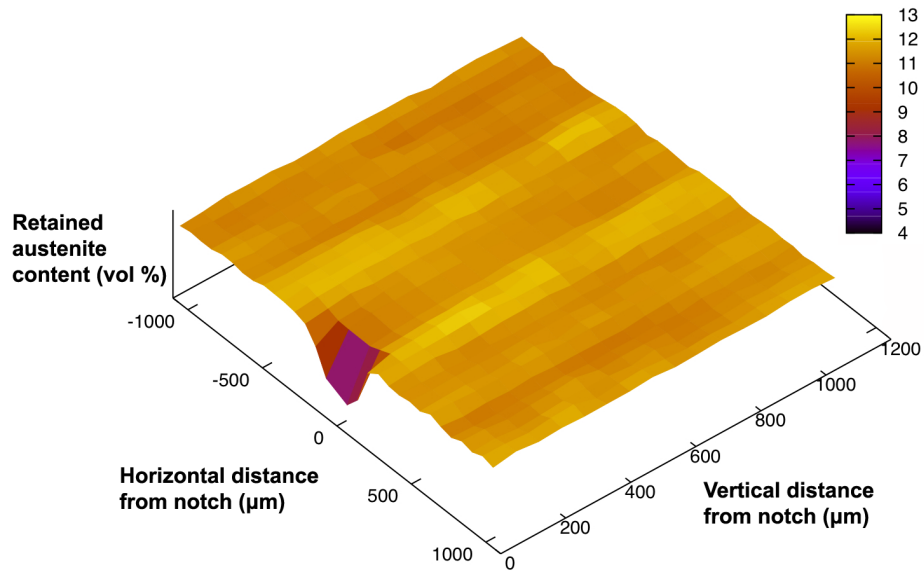
structure, since this gave improved fitting parameters, due in part to the better fitting of the tetragonal martensite peaks and recent work that suggests that the bainitic ferrite itself is not cubic [252, 253]. Figure 6.5 shows the difference in fit using a cubic ferrite model *versus* a tetragonal ferrite model. It can be seen clearly that a tetragonal lattice model provides a better refinement compared to a cubic lattice.

Figure 6.4 shows that the retained austenite content of the specimens varies only at the very base of the notch, over a vertical distance of 70  $\mu\text{m}$  (corresponding to the width of the beam). The size of the affected region below the notch is approximately 70  $\mu\text{m}$   $\times$  400  $\mu\text{m}$ . This is a fairly large area and is consistent with the expectation that stressed Charpy specimens develop a transformed region of significant size prior to crack initiation.

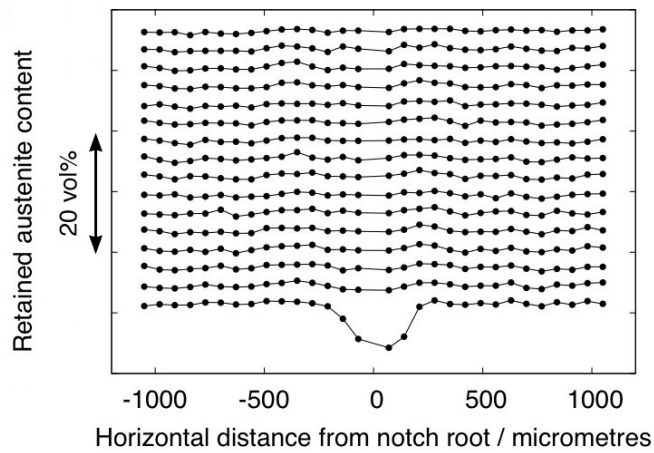
Figure 6.6 contains the combined results from three experiments and it is clear that there is a reduction in the retained austenite content even at the root of an unstressed notch, albeit to a lesser extent than in the notched and stressed sample. The effects of machining (which in this case is done after heat treatment in order to avoid decarburisation effects) are significant. This demonstrates that the microstructure of the notch root region in superbainitic Charpy samples is significantly altered and embrittled if the notch is machined after heat treatment has been carried out. It should therefore be possible to improve the results of a Charpy toughness test in this material by ensuring the notch is machined prior to heat treatment.

The effect of heating the sample during loading is illustrated in Figure 6.7. No significant differences were found between the heated sample and the unstressed sample, from which it is concluded that at this temperature, the austenite is sufficiently stable to resist further martensitic transformation.

While the use of a synchrotron has successfully shown a clear effect of both stressing and machining in these samples, the disadvantage of this approach is the lack of repeat testing. Synchrotron beamtime is limited and it was therefore not possible to take notch measurements from more than one of each kind of sample during this study, or indeed to repeat any measurements. Therefore, the results presented here lack an awareness of the variation that may exist between



(a)



(b)

**Figure 6.4:** (a) Retained austenite content in the notch root region of a stressed Charpy sample plotted as a 3-D graph. (b) 2-D representation of the data plotted in (a). Separation of individual lines corresponds to a distance of 70  $\mu\text{m}$ . The scale on the y-axis is intended as a guide to the degree of variability between data points and does not represent true, absolute values of volume percent.

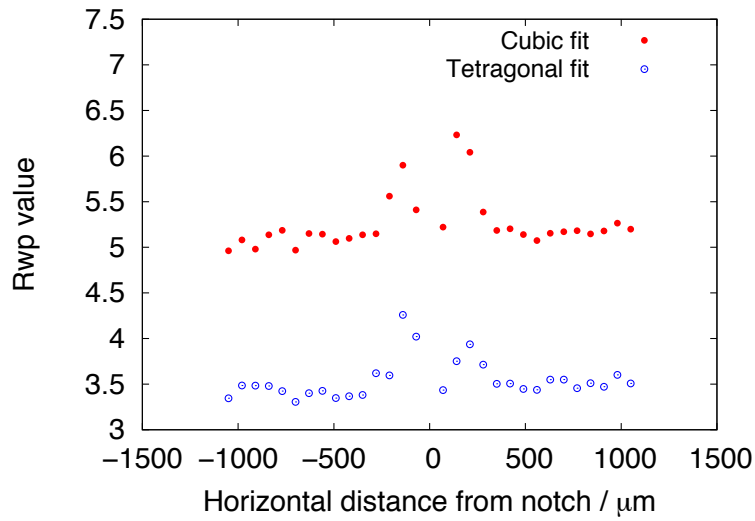


**Figure 6.5:**  $R_{\text{wp}}$  fit parameters for spectra taken during a linescan of the notch root region of a stressed Charpy sample, illustrating the improved fit from a tetragonal ferritic model. Individual lattice parameters for each fit in the tetragonal case are listed in Appendix A.2. Corresponding  $c/a$  ratios are plotted in Figure 6.14.

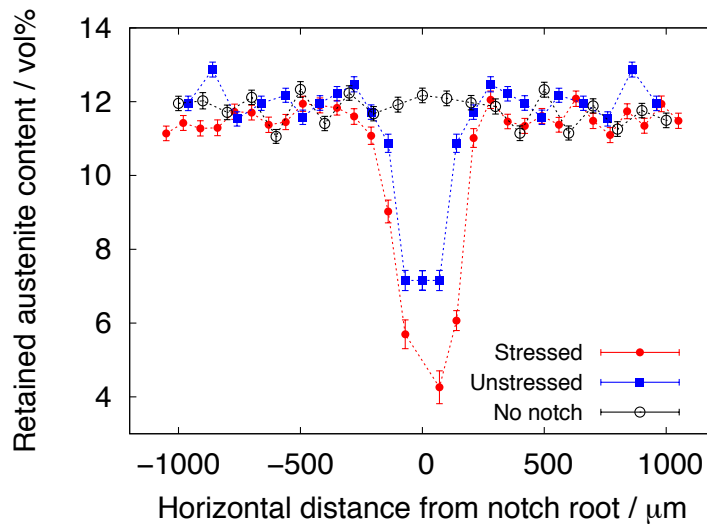


**Figure 6.6:** Retained austenite content in three different specimens: notch unstressed, notch stressed and no notch. The data represent horizontal line-scans taken directly below the notch root. Note that the data for the unstressed notch were obtained by scanning only half the notch root region; the plot of that data is therefore symmetric.

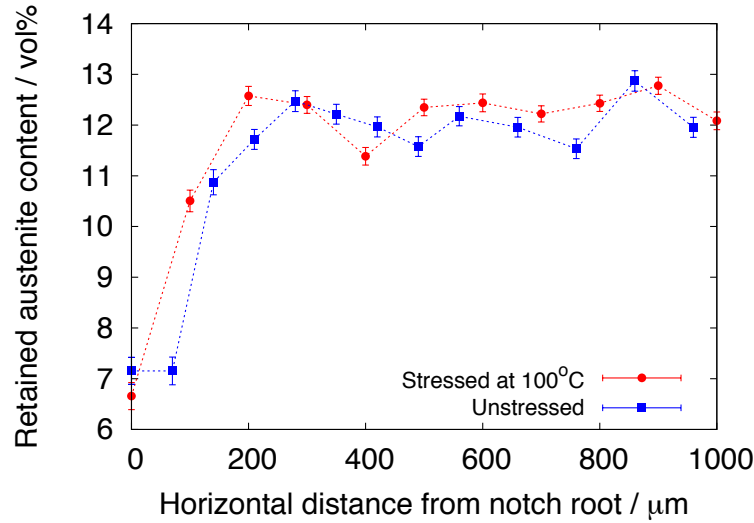


**Figure 6.7:** Retained austenite content at the notch root of a sample stressed at 100°C, with the data from an unstressed notch included for comparison. Both scans were taken over half the notch root region only.

the notches of identically-produced samples. However, it is encouraging that Figure 6.6 shows excellent agreement between the retained austenite contents measured at a distance from the notch in all three samples. For completeness, it would be desirable to measure the effect of machining on several samples to get an impression of the degree of scatter of the data.

### 6.3.1 Austenite lattice

Typically, it is expected that austenite with lower carbon contents will transform to martensite preferentially under stress. This is because dissolved carbon stabilises the austenite. Therefore, an increase in the overall austenite lattice parameter should be detected if the lower-carbon regions have transformed. The relevant data are shown in Figure 6.8.

As was also observed in the previous chapter (Figure 5.6), the austenite lattice parameter decreases in the notch region of the stressed sample. The results here show the same effect in the unstressed sample. This implies that the average austenite carbon content has fallen, rather than risen. Alternatively, it could represent residual strain in the transformed region.

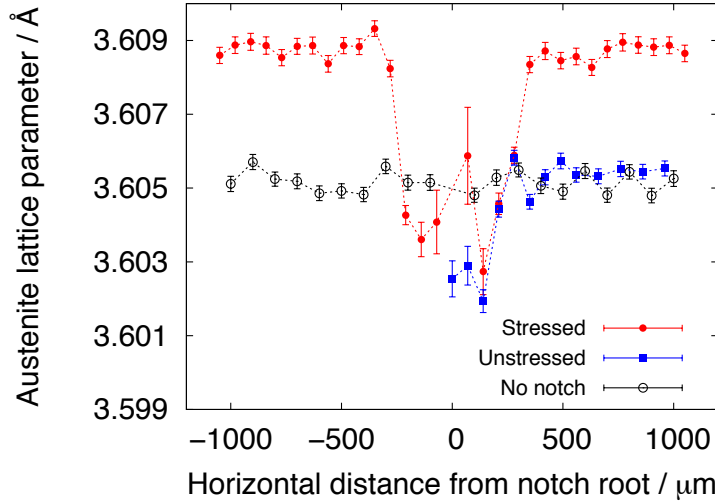


**Figure 6.8:** Plots of the lattice parameter of austenite at the notch root region of a stressed sample; an unstressed sample and in a region of no notch.

Secondly, it is notable that the lattice parameter in the ‘untransformed’ region in the stressed sample is higher than in the bulk (no notch) sample. One explanation for this is again the possibility of residual strain — although the austenite has not transformed, it will certainly have been stressed. These results may show that the stress concentration in this region is sufficient to cause plastic strain in the austenite, without inducing a martensitic transformation. Rough calculation shows that the stress at this location in an un-notched beam loaded with 8 kN is 1 GPa. This would necessitate a stress concentration factor of at least 2 in order to cause yielding when a notch is inserted, which is not unreasonable [255]. The discrepancy may also be due to chemical effects — a difference in carbon content between the two samples.

T / °C	Austenite lattice parameter / Å
200	$3.6115 \pm 0.0004$
250	$3.6218 \pm 0.001$
275	$3.6201 \pm 0.0007$
300	$3.6210 \pm 0.0007$

**Table 6.3:** Routine X-ray measurements of austenite lattice parameter.

In fact, it is unexpected that the measured lattice parameter in the bulk alloy is as low as 3.605. In laboratory X-ray tests, the lattice parameter in this alloy has been consistently measured as  $\sim 3.6\text{--}3.62$  (Table 6.3). A lattice parameter of 3.605 corresponds to an austenite carbon content of 0.75 wt%. Interestingly, this is lower than the average carbon content of the alloy.

Consider, however, that the data in Figure 6.8 are calculated from a spectrum incorporating the overlapping  $\{111\}_\gamma$  and  $\{011\}_\alpha$  peaks. If the parameters are re-calculated without these peaks, the average lattice parameter in the bulk of the stressed sample becomes  $3.6099 \pm 0.0003$  compared with the original average of  $3.6087 \pm 0.0003$ . When the overlapping peaks are incorporated, the lattice parameter is under-predicted by 0.03%, which is significant in the context of these measurements. At the notch root, the errors are much larger and there is little difference between the two methods for lattice parameter calculation (Figure 6.9). However, this does not explain the large discrepancy between the values for the bulk lattice parameter in the stressed and unstressed samples; nor does it account for the difference between the laboratory and synchrotron X-ray results, since the values listed in Table 6.3 were calculated from all complete peaks in the  $40\text{--}140^\circ 2\theta$  spectrum and therefore will also be under-predicted.

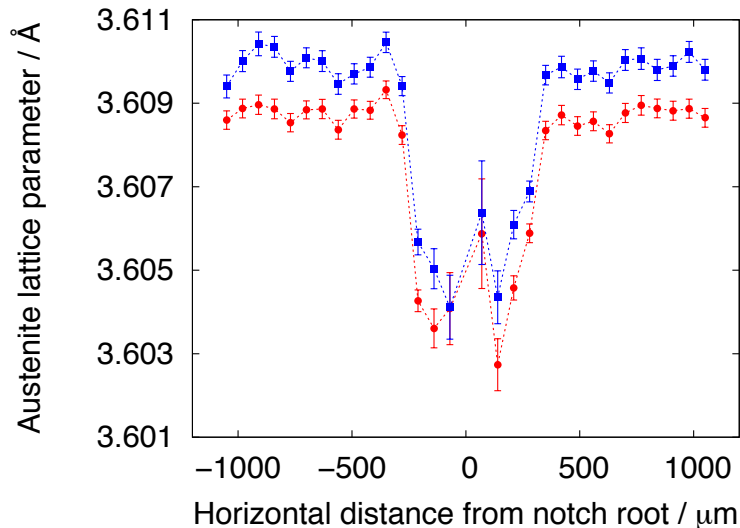


**Figure 6.9:** Retained austenite lattice parameter calculated from spectra including (red) and excluding (blue) the  $\{111\}_\gamma$  and  $\{011\}_\alpha$  peaks.

By analysing the Debye-Scherrer rings obtained during the scan, it is possible to identify regions of strain in the sample. Figure 6.10 shows the ring position plotted as a function of azimuth ( $\phi$ ) for four locations. This reveals that, although the bulk material is largely unstrained, there is residual strain present in the root region of both notches. Moreover, the positions of both austenite and ferrite reflections vary in the same manner. This strongly suggests that the strain is a result of machining rather than phase transformation. In the case of a transformation strain, the expectation is that the ferrite would show strains in the opposite direction to those observed in the austenite.

In Figures 6.10b-d, the diffraction rings show significant azimuthal intensity variation (spotting), which is due to the fact that the synchrotron beam only irradiates a small volume within the sample, containing relatively few grains, of which even fewer will conform to the required conditions for diffraction. The result is a texture-like effect. It is only the stressed notch region that displays a smoothing of the rings. In general, the degree of smoothing can be related to the grain size and lattice defect density [254], such that the region in Figure 6.10a can be interpreted as containing finer grains or increased plasticity. Both of these are expected to arise from a stress-induced martensitic transformation: the large, blocky austenite will transform preferentially and the shear strains characteristic of this transformation may cause plastic deformation and defect accumulation in the remaining austenite, although it is more common that martensite is accommodated elastically (since at room temperature the austenite strength is higher) [256].

The  $\sin^2 \phi$  analysis method was applied to the  $\{002\}_\gamma$  rings in spectra obtained from horizontal and vertical linescans in the region of both stressed and unstressed notches, in order to compare the strain in the two samples. Figure 6.11 shows the  $\sin^2 \phi$  plots corresponding to the four regions represented in Figure 6.10. The positive slope in Figures 6.11a and 6.11c indicates that the diffraction rings are widest in the horizontal direction (i.e. at  $90^\circ$  and  $270^\circ$  around the ring). In contrast, there is little variation in the y-intercept values — which represent the vertical diameter of the rings. This reveals that a compressive strain is present in the lattice, which is exactly what is seen from the austenite lattice parameter data. The direction of this strain is parallel to the notch opening direction. This raises the possibility that machining may have a small positive effect on

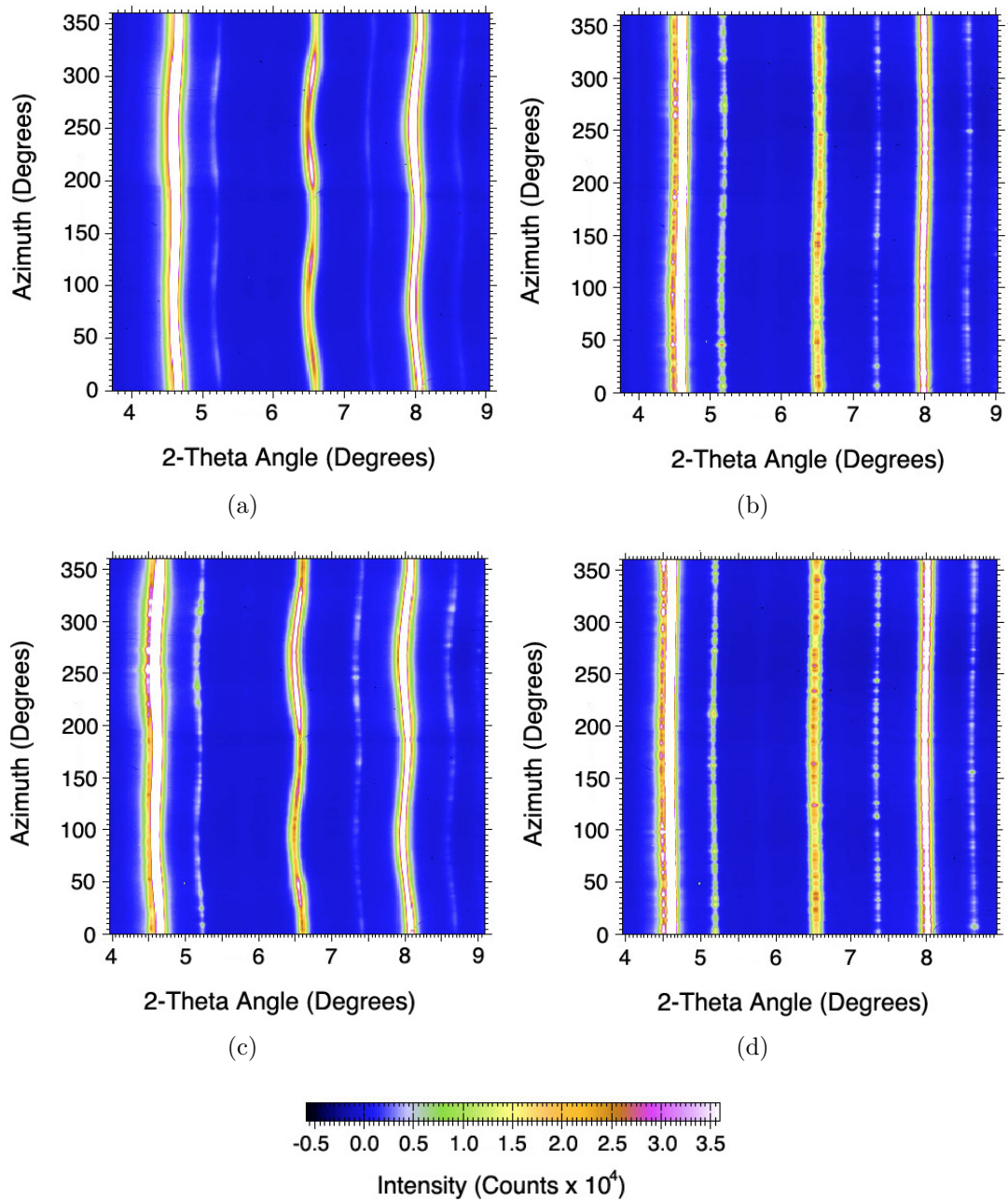


**Figure 6.10:** Azimuthal plot of Debye-Scherrer rings obtained from (a) notch root of stressed sample; (b) bulk material in stressed sample; (c) notch root of unstressed sample; (d) bulk material of unstressed sample.

toughness, by introducing a residual strain that opposes the opening of a crack tip. Practically, however, this is likely to be a minor factor relative to the loss of plasticity in the machining-affected region.

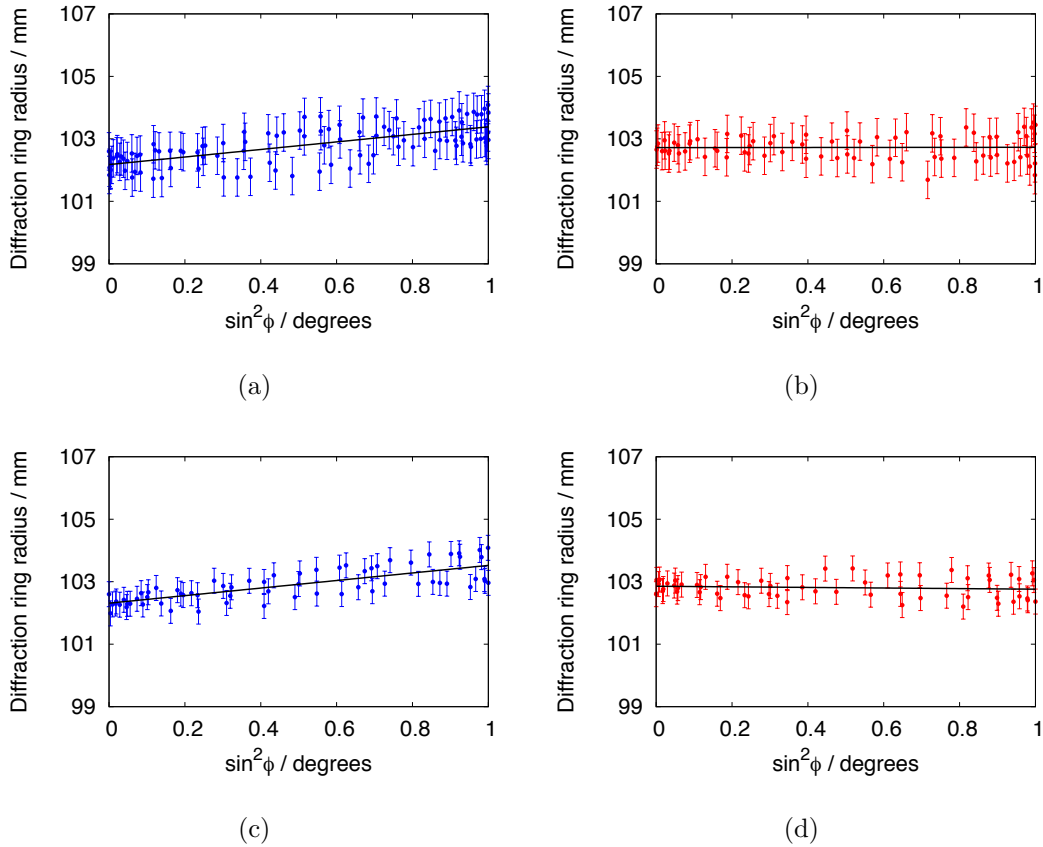


**Figure 6.11:**  $\sin^2 \phi$  plots obtained from (a) notch root of stressed sample; (b) bulk material in stressed sample; (c) notch root of unstressed sample; (d) bulk material of unstressed sample.

The slope of such a plot can be used to evaluate the degree of anisotropy of strain. Since in this case there is found to be minimal (although not zero) strain in the vertical direction, the slope of the plot gives a good guideline as to the degree of horizontal strain present. Figure 6.12 contains a summary of the variation in slope both horizontally and vertically away from the notch root in stressed and unstressed samples. These data should not be taken as an accurate measurement of strain within the samples, since the slicing of the original, thicker, specimens will have altered the strain state of the material. However, they are valuable as an illustration of the distance over which residual strain is present. In both cases,

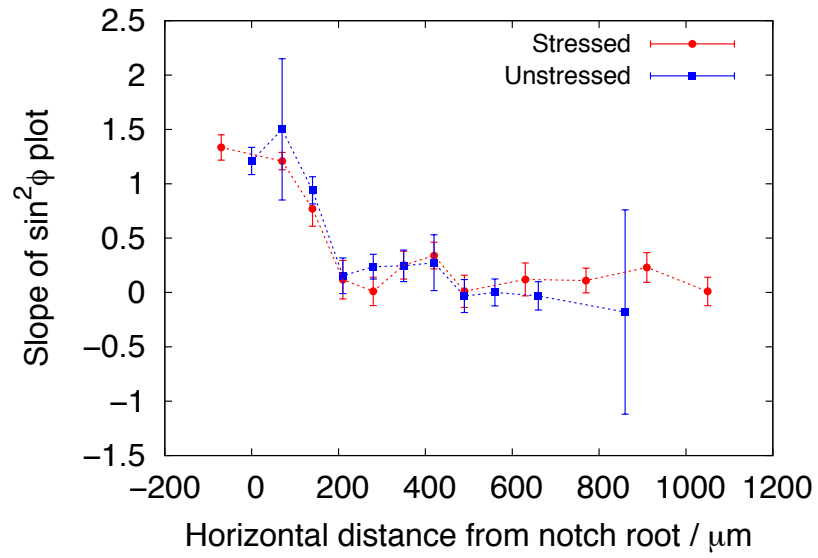
the affected area is roughly  $200 \times 200 \mu\text{m}$  at the notch root. This corresponds to the area over which the austenite appears compressed in Figure 6.8. A similar effect is observed in the vertical direction (Figure 6.13).

These results are significant because they demonstrate that machining strains dominate over transformation strains, the latter being too small to be detectable in this analysis. The data scatter obscures any differences between the strains in the stressed and unstressed notches, which would be attributable to a transformation strain present in the former. The results provide a clear justification for the unexpected reduction in austenite lattice parameter in the notch root region, which would otherwise be contrary to expectations. Because of the confounding influence of strain in the samples, it is not possible to isolate any peak shifts that are purely due to chemical effects.

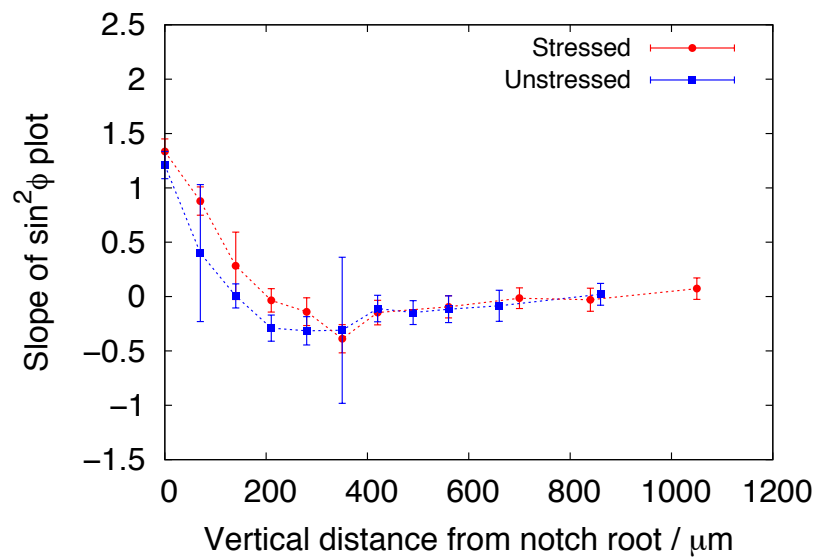
The influence of the strain-related azimuthal peak shift upon the integrated spectra used to determine volume fraction results must also be considered. Ideally, the 2-D spectrum would be caked and integrated, however, it was found that the intensity variation around the ring precluded this approach — the relative intensity and integrated intensity of the peaks varied with the azimuthal angle at which the spectrum was caked. This intensity variation was more marked among the austenite peaks and led to unreliable volume fraction calculations when using the caked spectra. Integrating over  $360^\circ$ , as was done here, is not an invalid method, since it essentially acts as an averaging process (summation followed by normalisation). The presence of strain will have produced peak broadening and, as demonstrated, peak shifts, but the calculation of integrated intensity and volume fraction may still be relied on. In particular, the fundamental result of this study — that there is a reduced quantity of austenite at the notch root — remains legitimate.

### 6.3.2 Ferrite lattice

An increase in tetragonality of the ferrite lattice can be observed by plotting the  $c/a$  ratio in the notch root region of both stressed and unstressed samples, as in Figure 6.14. There is a consistent  $c/a$  ratio of approximately 1.008 – 1.009 in the unaffected region of all three samples — a value close to that measured in a steel with similar carbon content by Smith *et al.* [253] and consistent with



(a)



(b)

**Figure 6.12:** Slope of  $\sin^2 \phi$  plots from points around the notch root in both stressed and unstressed samples.

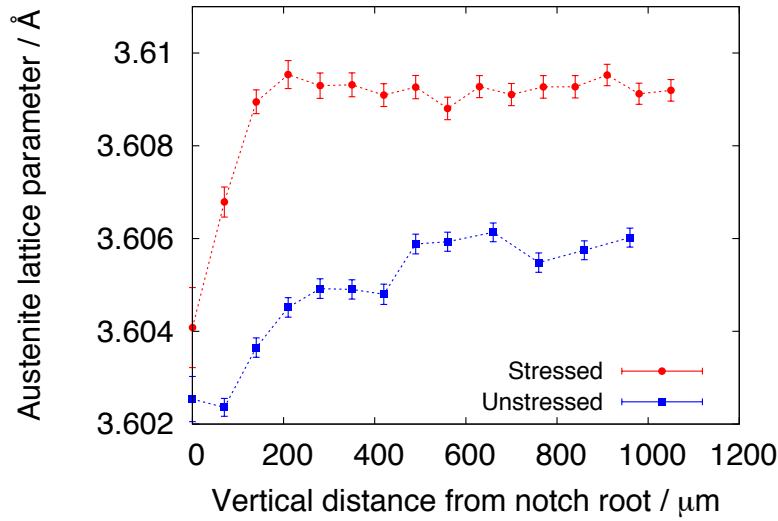


**Figure 6.13:** Plots of variation in austenite lattice parameter as a function of distance below the notch root in stressed and unstressed samples.

previous laboratory X-ray measurements of this alloy (Table 4.9). However, in the region of both notches, the  $c/a$  ratio increases, as would be expected from the presence of martensite with a larger carbon concentration than bainitic ferrite.

It is possible to calculate the expected  $c/a$  ratio for martensite at a given carbon content [253], giving  $c/a = 1.039$  (based upon an austenite carbon content of 0.86 wt%, as estimated from Figure 6.8). This is higher than the values shown in Figure 6.14 because, as described previously, in the latter graph, the  $c/a$  ratio shown is obtained by using a single tetragonal model to fit both the ferrite and martensite peaks, and so will represent a combination of the  $c/a$  ratios of the ferrite and martensite in the structure. Additionally, the value of 0.86 wt% is a measure of the average austenite carbon content, whereas the martensite will have formed primarily from austenite with below-average  $C_\gamma$ .

The negative spike in  $c/a$  at roughly  $\pm 200 \mu\text{m}$  from the notch is a consequence of the residual compressive strain present in this region, which may have reduced the overall tetragonality of the ferrite lattice. Closer to the notch root, this effect is overcome by the increase in  $c/a$  due to martensite formation. Indeed, a similar trough-peak-trough shape is present in Figure 6.8. The reason for the obvious asymmetry of the  $c/a$  peak in the stressed sample is not yet known (note that the

symmetry of the corresponding peak in the unstressed sample is a consequence of using data from a scan of half the notch).

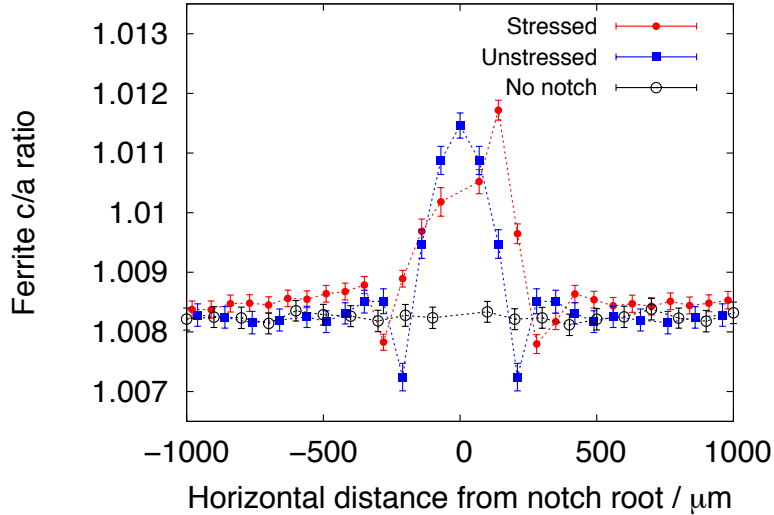


**Figure 6.14:** Plots of the  $c/a$  ratio of the ferrite at the notch root region of a stressed sample; an unstressed sample and in a region of no notch. Data from the unstressed sample was obtained from a scan of half the notch; the plot is therefore symmetric.

In addition to variations in notch root radius, there is a further difference between Charpy samples and  $K_{1C}$  samples which has not hitherto been discussed. The sharp crack required in a  $K_{1C}$  test is not machined, but rather grown downwards from the base of a machined notch. The length of the final crack is much greater than the 200  $\mu\text{m}$  over which residual strains will have an effect, such that the crack tip is located in an unstrained, untransformed region. It would be of great interest to observe whether reducing the root radius of a machined notch in a Charpy specimen has a significant toughening effect, or if the martensitic transformation and strains induced by machining dominate over those effects influenced by size of the stress-affected zone. Practically, however, it would be challenging to machine (as opposed to grow) a notch with root radius approaching atomic sharpness.

Overall, it is clear that machining induces significant changes in the structure of the notch root region of Charpy samples studied in this chapter. Experiments were performed to assess whether heat-treating Charpy samples after machining would improve toughness, however, subsequent characterisation of the samples revealed that a bainitic structure had not been achieved. The results were therefore invalid. Details of this are set out in Appendix A.3.

## 6.4 Conclusions

Synchrotron X-ray diffraction methods have been used to study quantitatively the changes experienced by residual austenite at the notch root of a nanostructured bainitic Charpy sample subjected to three-point-bend loading. The aim was to discover if the austenite undergoes a transformation to martensite due to the intensified stresses in this region, in an attempt to resolve the discrepancy between  $K_{1C}$  and Charpy toughness measurements in this and similar alloys.

It was found that there is a marked decrease in the volume fraction of residual austenite present at the notch root of a sample that had been stressed. This, along with a clear increase in the ferrite-martensite  $c/a$  ratio towards the notch root provides convincing evidence that the observed loss of austenite is due to a martensitic transformation. Furthermore, a similar (but weaker) reduction in austenite content was seen in the notch vicinity of an unstressed sample, indicating that the austenite in this alloy is susceptible to martensitic transformation during machining.

The influence of machining was further highlighted by the observation that residual compressive strains are present in a region measuring roughly  $200 \times 200 \mu\text{m}$  at the notch root of both stressed and unstressed samples. The machining strains are much greater than any transformation strains that may be present due to applied three-point-bend stresses. These latter observations have implications for the manufacture of future mechanical test specimens from these alloys, so as to avoid embrittlement. By taking steps to reverse the effect of notch machining, it may be possible to achieve large improvements in the Charpy toughness.

The key results presented in this chapter provide compelling evidence that significant quantities of martensite form at the notch root of these Charpy samples during notch machining, and during the application of a three-point-bend, prior to any crack initiation.



---

# AUSTENITE PERCOLATION IN NANOSTRUCTURED BAINITE

---

## 7.1 Introduction

The tensile behaviour of nanostructured bainite is characterised by uniform elongation accompanied by little, if any necking [33, 36, 44]. The uniform elongation therefore is usually equal to the total elongation. In general, tensile tests reveal a dependence of ductility upon transformation temperature, and an inverse correlation with strength [35, 36]. In carbide-free bainitic steels, such as superbainite, the volume fraction and morphology of austenite are controlling factors in the ductility [14, 257]. In particular, the TRIP effect comes into play – retained austenite transforms into martensite under tensile loading. This process is influenced by various factors relating to austenite stability, such as grain orientation, morphology, carbon content and scale [40, 44, 258–261].

It is possible to use standard calculation methods [42, 262, 263] to follow the variation in retained austenite during tensile tests on nanostructured bainite as a function of plastic strain, accounting for austenite composition and the temperature at which deformation occurs. It then becomes evident that the strain at the point of fracture consistently occurs when the austenite volume fraction is reduced to about 0.1, a conclusion supported by *in situ* tests in which phase fractions are monitored during tensile testing [40]. It has therefore been argued that in these steels, the failure in tension occurs when the retained austenite loses three-dimensional percolation [43]. This means that regions of austenite become

geometrically isolated from one another, to the extent that it is no longer possible for applied stresses and strains to ‘trace a path’ that passes only through the austenite phase. At this point, the stresses must additionally be borne by the more brittle martensite that results from the deformation-induced transformation of austenite, leading to fracture. Measurements of austenite volume fraction at various locations in tested tensile specimens support this idea [44].

The need to control the mechanical stability of retained austenite in automotive TRIP-assisted steels in order to ensure an optimised uniform ductility has long been recognised [39], but the important difference here is that with bulk nanostructured bainitic steel, the ductility is essentially all uniform and a different mechanism seems to govern ultimate fracture.

The goal of the work presented in this chapter was to use thermal desorption analysis (TDA) techniques on hydrogen-charged samples to test the hypothesis that the austenite in a nanostructured steel loses percolation at a volume fraction of about 0.1. A key assumption made throughout is that the gain of ferrite percolation coincides with the loss of austenite percolation.

A great deal of peripheral information on the distribution of hydrogen in the two-phase ferrite-austenite mixture is also obtained in this study. The logic of the experiments is based on the fact that the diffusivity and solubility of hydrogen is dramatically different in the two phases, with diffusion being much slower in austenite. It follows that in a percolating structure, less hydrogen should be able to penetrate the sample for a given charging time, because the hydrogen must necessarily diffuse through austenite at some stage.

### **7.1.1 Collaboration**

The work in this chapter was carried out in collaboration with Ms Eun Ju Song and Mr Do-Kyeong Han at the Graduate Institute of Ferrous Technology, POSTECH, Republic of Korea. Their contributions are included in full as they form a crucial part of the overall work. The flux model analysis in Section 7.3.4 and the permeation work in Section 7.3.5 were performed and written up by Do-Kyeong Han, and are reproduced without modification in this chapter. Eun Ju Song participated in the TDA experiments and data analysis, and carried out

the analysis described in Section 7.3.6 and Appendix A.4, regarding the oxidation effects occurring during the TDA process. Both collaborators also contributed to the description of methods in Section 7.2.

## 7.2 Experimental methods

Thermal desorption analysis is a technique normally used to study hydrogen trapping states [264, 265]. Specimens are charged electrolytically with hydrogen and then heated at a constant rate, with any desorbed hydrogen detected using gas chromatography. Strongly trapped hydrogen is released at a higher temperature and the total released can be detected by integrating the data over the time period of the experiment.

The chemical composition of the steels used in this experiment are given in Table 3.1. The vast majority of experiments reported here have been conducted on Alloy B, but because of the limited material available, some of the experiments are on Alloy D. Both can be heat-treated to produce the required nanostructure [22, 23, 30, 185]. Specimens measuring 55 mm × 12 mm × 4 mm were produced from the isothermally transformed sample of Alloy B. Samples from Alloy D were produced in 55 mm × 20 mm × 1 mm sizes because they were destined primarily for permeation experiments, and to establish the saturation concentrations of hydrogen.

In order to vary the volume fraction of austenite, the isothermally transformed samples were tempered to various extents as detailed in Table 7.1. The austenite volume fraction ( $V_\gamma$ ) was measured using quantitative X-ray analysis, with samples prepared as described in Section 3.2. Retained austenite carbon content was calculated from the measured lattice parameters as described by Dyson and Holmes [201].

The TDA samples were polished with 220-grade and 800-grade silicon carbide papers, cleaned with high-purity ethanol and electrochemically charged with hydrogen in an aqueous mixture of 3% NaCl + 0.3% NH<sub>4</sub>SCN, using a current density of 1 A m<sup>-2</sup>. The standard charging time used was 24 h, although this was varied from 1-6 h in the later stages of the experiment, in order to study the effect of charging time.

Alloy	Tempering temperature / °C	Tempering time / h	$V_\gamma$
B	Untempered	–	0.21
B	450	2.0	0.15
B	500	0.5	0.10
B	500	1.0	0.07
D	Untempered	–	0.15
D	450	2.0	0.07
D	500	0.5	0.03
D	500	1.0	0.02
E	620	24.0	0.26

**Table 7.1:** List of tempering heat-treatments used, and the retained austenite content of each sample. In the case of Alloy E, the actual mixture of austenite and ferrite is generated by annealing at the designated temperature.

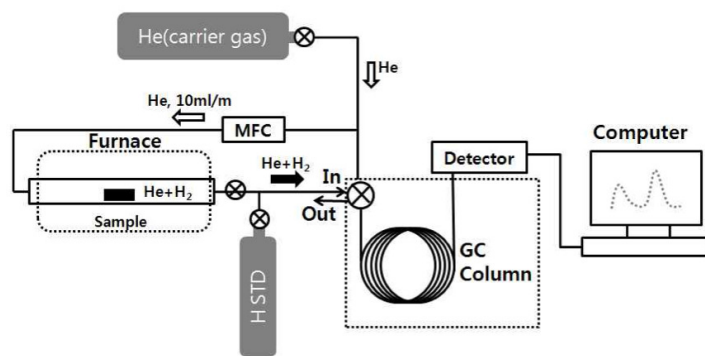
Figure 7.1a shows a schematic diagram of the TDA set-up. After charging, each sample was cleaned with ethanol, dried and placed in the furnace tube. The time interval between the completion of charging and placing the sample in the furnace was 15 min. Samples were heated to 700°C at a rate of 100°C h<sup>-1</sup>. The sample gas was analysed at 3-minute intervals using helium as a carrier gas. This transfers the desorbed hydrogen into the gas chromatograph where it is monitored by a detector. The hydrogen content was calibrated using a standard gas mixture.

The electrochemical hydrogen permeation cell used to measure the effective diffusivity of hydrogen through the variety of structures is illustrated in Figure 7.1b. The test was performed according to the ISO17081 standard. The detailed procedure is described elsewhere [266] but the test permits, in particular, the effective diffusivity and permeability to be determined by monitoring the current density through the sample as a function of time. The steady state flux of hydrogen through the sample,  $J_{ss}$ , is determined:

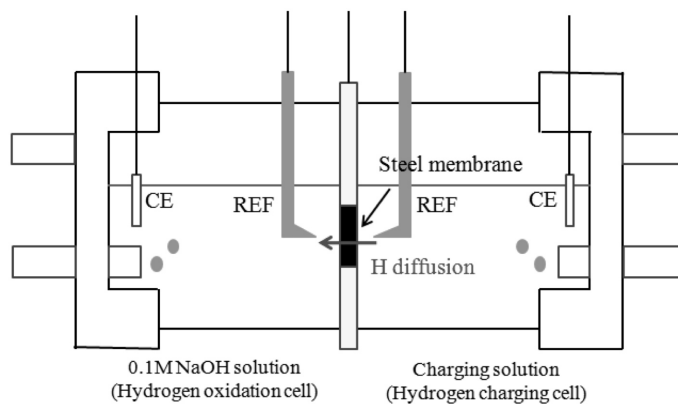
$$J_{ss} = i_{ss}/nF \quad (7.1)$$

where  $i_{ss}$  is the steady state current density,  $F$  is the Faraday constant, and  $n$  the number of electrons that participate in the electrochemical reaction.

The permeability,  $P$ , is then simply:



(a)



(b)

**Figure 7.1:** Schematic diagrams showing (a) thermal desorption and (b) Devanathan-Stachurski permeation cell used.

$$P = J_{ss}L \quad (7.2)$$

where  $L$  is the sample thickness.

A time lag  $t_l$  is defined to be that required to achieve 0.63 of the steady-state current density, and the effective diffusivity as calculated from this time lag is:

$$D_l = L^2/6t_l \quad (7.3)$$

Alternatively, both the effective diffusivity and permeability may be calculated using the break-through method, in which the time  $t_b$  is defined as that at which the current density begins to increase after beginning the experiment. The effective diffusivity calculated in this way is:

$$D_b = L^2/15.3t_b \quad (7.4)$$

## 7.3 Results and discussion

### 7.3.1 TEM characterisation

Tempering treatment	Final $V_\gamma$	Austenite carbon content / wt%	Hardness / HV30
<b>Alloy B</b>			
Untempered	0.21	$1.21 \pm 0.01$	$616 \pm 2$
400°C for 1 h	0.19		
400°C for 2 h	0.18		
450°C for 1 h	0.18		
450°C for 2 h	0.15	$0.97 \pm 0.01$	$588 \pm 2$
500°C for 30 min	0.10	$0.78 \pm 0.03$	$571 \pm 1$
500°C for 1 h	0.07	$0.75 \pm 0.03$	$569 \pm 2$
<b>Alloy D</b>			
Untempered	0.15		$626 \pm 7$
450°C for 2 h	0.07		$606 \pm 7$
500°C for 30 min	0.03		$579 \pm 8$
500°C for 1 h	0.02		$550 \pm 4$

**Table 7.2:** Hardness values for each set of samples. The retained austenite content has, in each case, an uncertainty in volume fraction of about  $\pm 0.01$ .

Both of the nanostructured alloys were characterised using transmission electron

microscopy and hardness testing. Much more detailed structural characterisation has been reported elsewhere [28, 40, 203] and so is not repeated here. The as-transformed structure of Alloy B is shown in Figure 7.2a. The alloy initially consists of two phases: bainitic ferrite and retained austenite, both of which are visible as thin plates and films in Figure 7.2a. Previous work has found that the bainite plate thickness in this alloy ranges from 12-45 nm when transformed at 200°C [28, 40]. The structure also contains some regions of fine blocky austenite; the reported ratio of film austenite to blocky austenite in this alloy, when transformed at 200°C, is approximately 3:1 by volume [28]. The as-transformed structure of Alloy D, shown in Figure 7.3a, is coarser, with an average plate thickness of 83 nm.

Bainitic steels, such as the alloys studied here, are resistant to tempering, with little reduction in hardness or austenite volume fraction below 450°C and significant softening only taking place at temperatures above 500°C [203, 204, 267]. This is reflected in the fact that the hardness remains high in both alloys, even after tempering at 500°C for one hour. However, the reduction in hardness following the tempering treatments signals the onset of austenite decomposition, as confirmed by X-ray analysis (Table 7.2). Attempts to temper Alloy B at temperatures below 450°C did not produce a particularly significant change in austenite volume fraction. Therefore, no such treatments were applied to Alloy D.

Tempering that leads to carbide precipitation from the decomposition of austenite, also hinders the coarsening of the ferrite plates since the carbides are located precisely at the plate boundaries, thus preventing significant coarsening [203]. Therefore, the plate structure is preserved after all the tempering heat treatments, as illustrated in Figures 7.2 and 7.3. All the tempering treatments listed in Table 7.2 led to carbide precipitation in Alloy B (Figures 7.2b-d). The carbides were confirmed to be cementite using electron diffraction (Figure 7.4); note that the as-transformed material is carbide-free because of the large silicon concentration in the steel. Cementite was also detected in Alloy D after all tempering treatments at 500°C (Figure 7.3d; Figure 7.4c, d). Although no carbides were found after tempering Alloy D at 450°C, it is possible that the volume fraction of any carbides is smaller than can be easily detected.

Twinning was found in all three tempered samples of Alloy B. Figure 7.5 shows

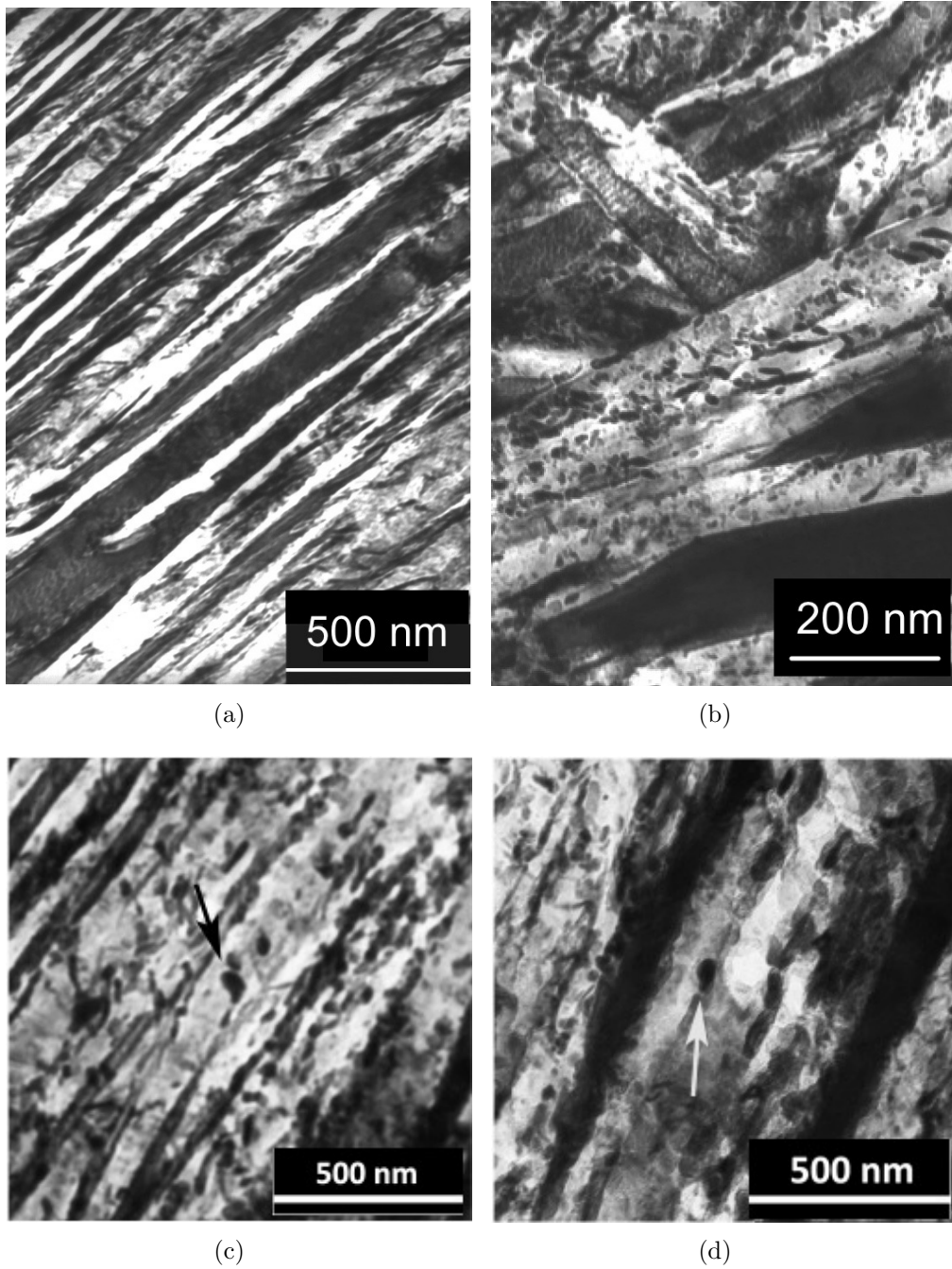


**Figure 7.2:** Alloy B. (a) As-transformed structure, with the darker regions representing retained austenite. (b) Structure containing some carbide particles, after tempering 450°C for 2 h. (c) After tempering 500°C for 0.5 h. (d) After tempering 500°C for 1 h. Carbide particles are arrowed.

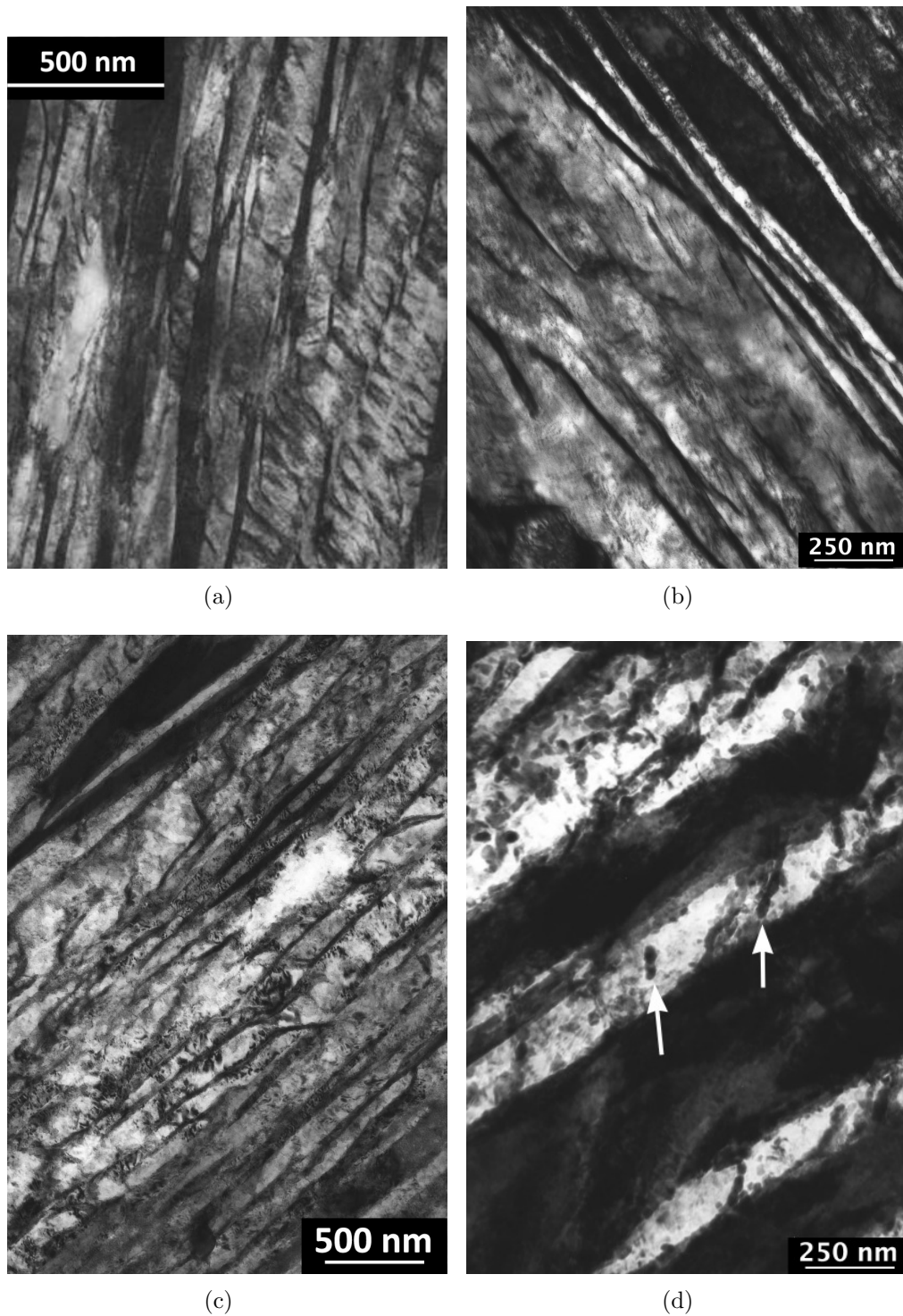


**Figure 7.3:** Alloy D. (a) As-transformed structure, with the darker regions representing retained austenite. (b) After tempering 450°C for 2 h. (c) After tempering 500°C for 0.5 h. (d) After tempering 500°C for 1 h. Carbide particles are arrowed.

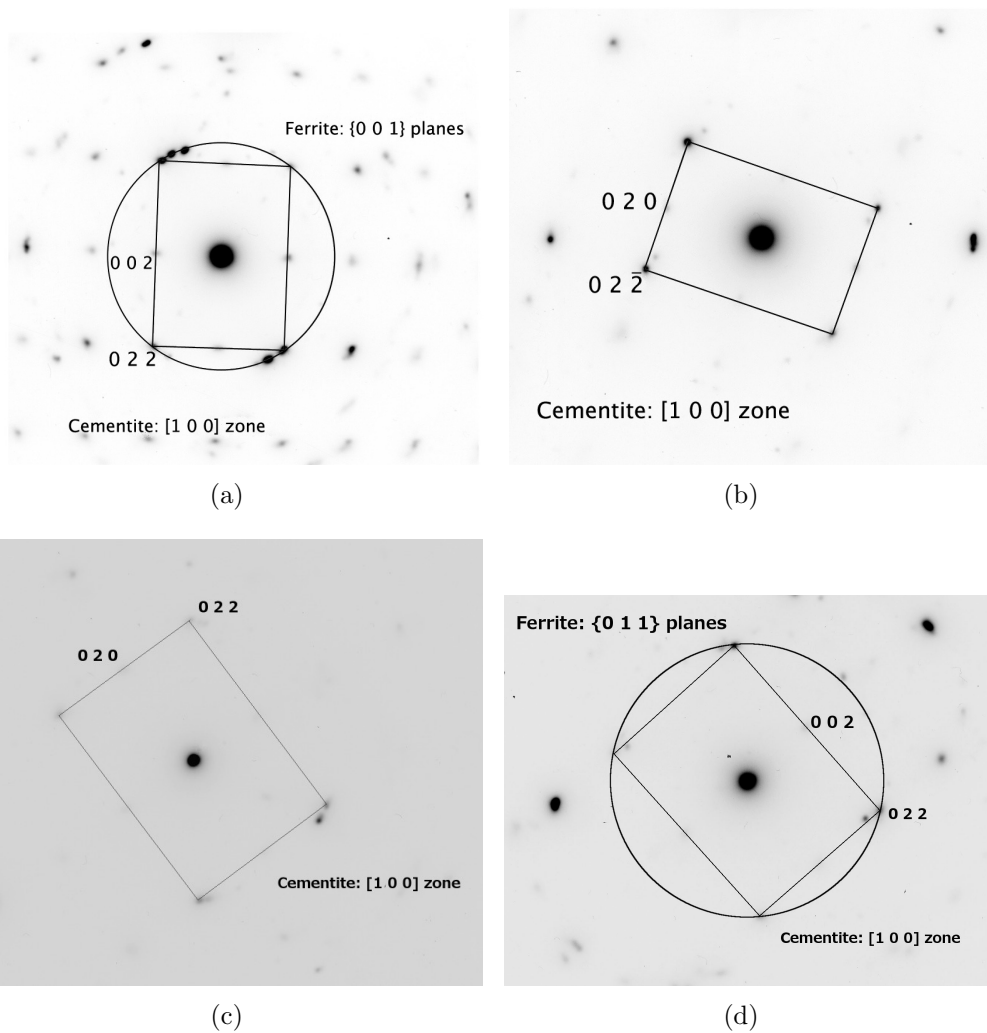


**Figure 7.4:** Electron diffraction patterns confirming the presence of cementite. (a) Alloy B, after tempering at 450°C for 2 h. (b) Alloy B, after tempering at 500°C for 1 h. (c) Alloy D, after tempering at 500°C for 30 min. (d) Alloy D, after tempering at 500°C for 1 h.

examples of twinning that has occurred in the tempered alloy. No twins were seen in the as-transformed sample although this does not rule out the possibility that they are present. From the micrographs in Figure 7.5 it is not immediately clear whether these are austenite twins or ferrite twins. The twins are present mostly in the darker regions of the micrograph, suggesting that they are austenitic twins, however, in Figures 7.5b-d the twins extend into the lighter, ferritic region. Diffraction patterns taken from the region in Figure 7.5d identify ferrite, however, there is no twinning visible on the diffraction pattern itself. It is likely that Figures 7.5b-d are ferritic twins, with the darker shade due to dislocations or other crystallographic effects. The twins in Figure 7.5a, from the sample tempered at 450°C, may be austenitic since the micrograph shows more clearly a region of retained austenite surrounded by plates of bainitic ferrite. Because this region is smaller, it was not possible to take a selected area diffraction pattern to identify the phase. It is possible that the twinned regions are martensitic, since the tempering process will have reduced the thermal stability of the retained austenite, which could then transform to martensite upon quenching to room temperature [239]. The data in Table 7.2 shows the reduction in austenite carbon content due to tempering. The formation of martensite may also contribute to the limited softening that occurs during tempering, and is consistent with the extremely high dislocation density observed in Figures 7.5c and d.

A topologically different kind of mixture of ferrite and austenite — with the latter distributed as non-percolating grains — was generated in a dual-phase steel of composition Fe-0.11C-6.17Mn-0.98Al wt%, by isothermal heat treatment at 620°C for 24 h, as illustrated in Figure 7.6. This alloy is interesting because the morphology is such that austenite grains are isolated, with continuity for any hydrogen to permeate through the ferrite (in which the hydrogen is much more mobile).

### **7.3.2 Thermal desorption analysis**

There are two essential categories of hydrogen in steel: that which is diffusible and can in principle escape from the steel; and the remainder, which is said to be trapped and is much more difficult to remove. The concept of hydrogen-trapping comes from Darken and Smith [268] who established that the passage of hydrogen through a steel is hindered by lattice imperfections (dislocations, interfaces) that

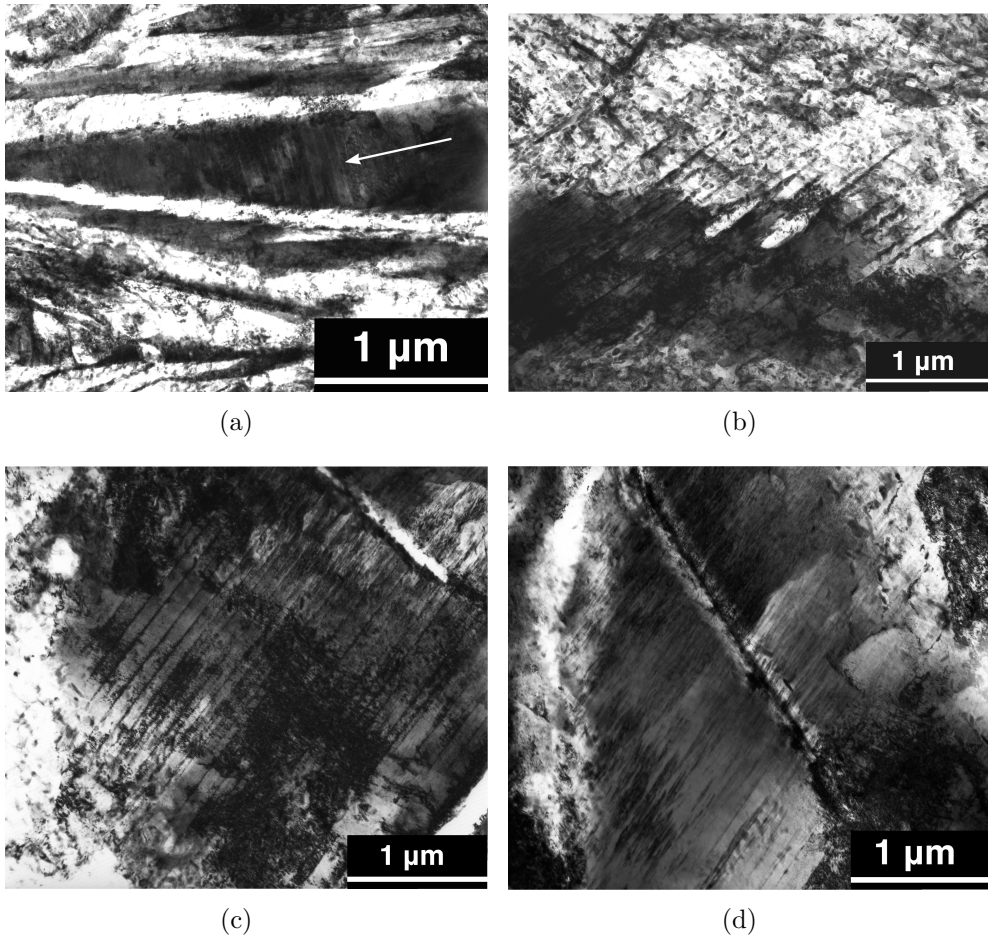


**Figure 7.5:** TEM images of twinning present in Alloy B tempered at (a) 450°C for 2 h; (b) 500°C for 30 minutes; (c) 500°C for 1 h; (d) 500°C for 1 h. The images in (c) and (d) are of the same region at different degrees of specimen tilt, showing high dislocation density.

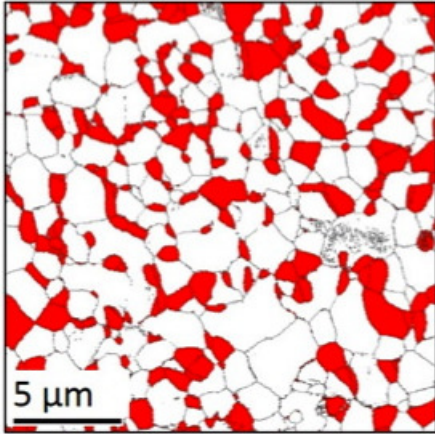


**Figure 7.6:** Alloy E. EBSD phase map with red and white regions indicating austenite ( $V_\gamma = 0.26$ ) and ferrite respectively.

tend to attract and bind it, thus rendering it immobile at temperatures where it should diffuse readily. The binding energy is defect dependent [269]. In two-phase mixtures of austenite and ferrite, of the type relevant to the present studies, the diffusivity of hydrogen in perfect austenite is far smaller than in ferrite, although its solubility in austenite is much greater than in ferrite. The austenite can, in this sense, be regarded as a macroscopic trap for hydrogen, relative to the ease with which hydrogen can diffuse in ferrite [270]. Therefore, in a thermal desorption experiment, the hydrogen in austenite is expected to be detected at a higher temperature during heating than that from ferrite, which may be released at close to ambient temperature.

Given the complexity of the problem, several experiments were carried out to understand the response of the hydrogen-charged and uncharged samples when subjected to thermal desorption analysis; these are reported first, before a discussion of the main results.

### 7.3.3 “Calibration” experiments

A sample of Alloy B was subjected to TDA before deliberate charging with hydrogen. Figure 7.7a shows the TDA output from an uncharged untempered sample with  $V_\gamma = 0.21$ , heated at  $100^\circ\text{C hr}^{-1}$ . The little hydrogen evolved does so at temperatures below  $50^\circ\text{C}$ , which means that it is not dissolved in the steel since it is easily desorbed. The origin of this low-temperature evolution is not clear, but the quantity desorbed between room temperature and  $300^\circ\text{C}$  amounts to just  $0.17 \text{ ppm g}^{-1}$  and can be neglected.

Figure 7.7b details the experiments done to assess the reproducibility of data from physically distinct samples that have been identically heat-treated and charged. The variability is likely to be due to specimen rather than instrument scatter, since the structures involved are complex.

A significant goal of the present work was to see whether the films of austenite present in the nanostructure impede the motion of hydrogen by percolating through the structure. Clearly, in order to assess this, the structure must not be saturated with hydrogen prior to the thermal desorption analysis. At the same time, sufficient hydrogen must be charged to ensure a good signal-to-noise ratio. The samples of Alloy B were therefore made 4 mm in thickness, so as to allow sufficient hydrogen to enter the specimen surface, but leaving the core with a reduced concentration. Both samples were charged using the same current density. In this way, the amount of hydrogen that effuses during TDA is a reflection of its permeation into the sample. Figure 7.7 compares the thickness effect for two samples, both transformed into nanostructured bainite at 200°C, albeit from slightly different alloys. The change in charging time from 24 h to 72 h did not alter the hydrogen content of the 1 mm thick sample, proving saturation. The total hydrogen desorbed from the 1 mm thick sample was measured to be 11.1 ppm, whereas that for the 4 mm thick sample was 19.6 ppm. The latter value should be much larger (at least 67 ppm given that the 4 mm sample is six times heavier) to match the saturation level of the thinner sample. The higher hydrogen content of the 4 mm thick sample indicates a somewhat greater penetration depth, since the penetration in the thinner sample cannot exceed 0.5 mm.

### 7.3.4 Role of retained austenite

It should be noted that heating at the rates considered here, to temperatures up to 300°C, is sufficient to detrap hydrogen that is dissolved in austenite, and that from defects such as dislocations and interfaces [271, 272]. Such hydrogen is said to be reversibly trapped and is of particular interest in embrittlement phenomena.

TDA experiments were conducted on all the samples described in Table 7.2, after charging with hydrogen for 24 h, at 100°C h<sup>-1</sup>. In Figure 7.8, the three samples that contain  $V_\gamma > 0.1$  show essentially similar behaviour; the two samples

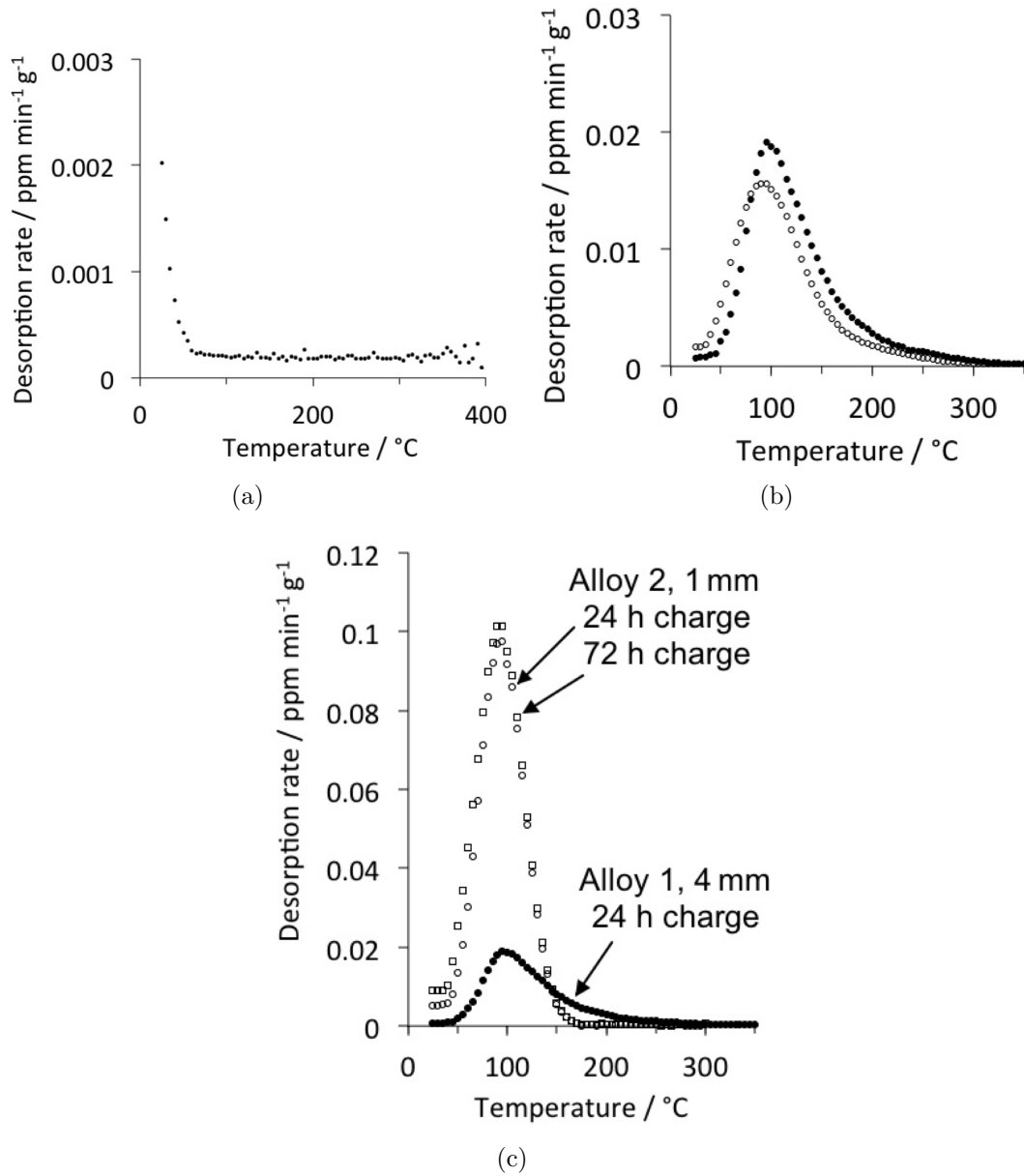


**Figure 7.7:** Thermal desorption analysis experiments at  $100^{\circ}\text{C h}^{-1}$ ,  $V_{\gamma} = 0.21$ . (a) Alloy B, behaviour of an uncharged specimen. (b) Alloy B, samples charged with hydrogen for 20 h. The two curves are from two physically different samples, identically produced before the TDA. (c) Comparison between TDA curves of 4 mm thick Alloy B samples and 1 mm thick Alloy D sample.

tested with  $V_\gamma = 0.07$  show different behaviour, with one curve replicating the larger austenite data and the other consistent with a larger quantity of hydrogen penetrated into the sample during the charging process. It follows that these data alone cannot reveal differences due to the austenite content nor phenomena associated with the percolation threshold.

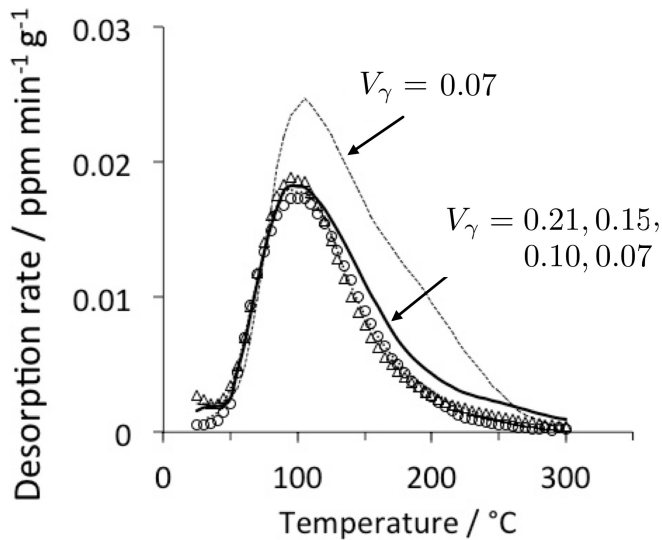


**Figure 7.8:** Alloy B. TDA data collected after charging each specimen with hydrogen for 24 h, using a heating rate of  $100^\circ\text{C h}^{-1}$ . The continuous line, triangles and circles correspond to  $V_\gamma = 0.21, 0.15, 0.10$  of retained austenite. The dashed curves are for  $V_\gamma = 0.07$ , although one of these is not easily distinguished on the diagram, but lies between the triangles and circles.

Many further experiments were conducted to verify the general impression regarding the influence of retained austenite; the data are summarised in Table 7.3. It should be noted that the amount of hydrogen desorbed during heating over an appropriate temperature range is a reflection of the amount charged into the sample, as long as saturation does not set in.

Figure 7.9a shows that the amount of hydrogen desorbed from the sample over the range  $25\text{-}300^\circ\text{C}$ , as expected, increases with the charging time. The retained austenite content has minimal influence in the early stages of charging, presumably because there is sufficient exposed ferrite at the sample surface, of the 4 mm thick specimens. However, further penetration during charging is clearly more difficult for the sample with  $V_\gamma = 0.21$  because the percolating austenite is a barrier to the diffusion of hydrogen in the sample.

Retained austenite should be a hindrance to the diffusion of hydrogen in a two-phase structure, and more so if its fraction is above a percolation threshold since there would then be no easy-diffusion paths. The data plotted in Figure 7.9b as a function of retained austenite could be argued to further support the estimate

[35] that austenite loses percolation in the bainitic sample when  $V_\gamma \lesssim 0.1$ . The desorbed hydrogen content (a reflection of the hydrogen that managed to enter the specimen) is clearly large when the percolation is lost.

However, this conclusion is not entirely established. It is not known whether there should be an abrupt change in hydrogen penetration into the sample when the percolation of austenite is lost, or whether the change should be gradual. A simple approach to this problem is illustrated in Figure 7.10, where three scenarios are illustrated.<sup>1</sup> The first is the case where percolating film-like austenite dominates the movement of hydrogen, the second where both ferrite and austenite are exposed directly to the hydrogen and the third where the austenite films have been reduced to a fraction below the percolation threshold. An estimation of the hydrogen flux  $J$  at the surface of each structure gives an impression of the relative amount of hydrogen that is able to penetrate such a sample within a given time.

Consider first the non-percolating structure (Figure 7.10b) where both  $\gamma$  and  $\alpha$  are exposed to the free surface. The net flux  $J_{os}$  per unit area into the ‘open structure’ is then

$$\begin{aligned} J_{os} &= AJ_\alpha + (1 - A)J_\gamma \\ &\equiv J_\alpha \left[ \frac{1}{\psi} + A \left( 1 - \frac{1}{\psi} \right) \right] \end{aligned} \quad (7.5)$$

where  $A$  is the fraction of the free surface occupied by ferrite,  $\psi = J_\alpha/J_\gamma$ . In contrast, the flux  $J_p$  into the structure illustrated in Figure 7.10a, where the austenite in effect is a significant barrier to the infusion of hydrogen, is simply  $J_\gamma$ , which will vary inversely with the thickness  $t$  of the austenite film because that determines the magnitude of the concentration gradient given fixed boundary conditions. The thickness is here assumed to be proportional to the volume fraction of  $V_\gamma$  of austenite as long as the latter is above the percolation threshold:

$$J_p = J_\gamma/t \approx J_\gamma/V_\gamma. \quad \text{for} \quad V_\gamma > \text{percolation threshold} \quad (7.6)$$

---

<sup>1</sup>The model presented here is somewhat simplistic but it nevertheless captures the essence of the problem. A proper treatment that includes multiple phases, multiple traps and accounts for the morphology of the phases will require a numerical approach. A start has been made on the multiple trap problem for a single phase material [272] but analysis of the more general problem incorporating morphology has not yet been achieved.

The situation illustrated in Figure 7.10c is where fraction of the film of austenite at the surface is less than unity, i.e., because the total fraction of austenite is less than the percolation threshold. For that case, the flux  $J_{np}$  is given by:

$$J_{np} = (1 - A)J_p + AJ_\alpha \quad \text{for} \quad V_\gamma < \text{percolation threshold} \quad (7.7)$$

The fluxes naturally depend on diffusion coefficients, and if it is assumed that undeformed ferrite and austenite have the diffusivities at 300 K of  $D_\alpha = 1.26 \times 10^{-8} \text{ m}^2 \text{ s}^{-1}$  [269] and  $D_\gamma = 2.65 \times 10^{-16} \text{ m}^2 \text{ s}^{-1}$  [273], then  $J_\alpha \gg J_\gamma$  and there should be an overwhelming increase in the net flux as soon as percolation is lost. This does not in fact happen (Figure 7.9). The reason is that the austenite-free structure obtained by tempering the mixture of bainitic ferrite and austenite still has a fine structure with dislocation and interface traps (the cementite itself is not a prominent trap in tempered structures [274]). Therefore, the appropriate  $D_\alpha$  is that measured using permeation experiments on this structure, reported later in this paper to be  $D_\alpha = 10^{-11} \text{ m}^2 \text{ s}^{-1}$ ; note also that this value is consistent with assessed data [275, Figure 12]. The gradient of concentration is also determined by the solubility of hydrogen in the phase as a result of charging, the atom fractions taken to be  $x_\alpha = 2.8 \times 10^{-8}$  and  $x_\gamma = 7.0 \times 10^{-5}$  [276]. Using these values, the ratio  $\psi = 15$  so equations 7.5 and 7.7 were used to calculate the variation in net flux as a function of the retained austenite content assuming  $\psi = 15$  when  $V_\gamma = 0.21$ , the largest volume fraction of austenite in the bainitic samples.

Figure 7.11 shows the results, where for the case with  $V_\gamma = 0.07$ , the area fraction  $A$  exposed to ferrite was taken to be 0.3, on the basis that no ferrite is exposed when  $V_\gamma = 0.1$  since this is at the percolation threshold. It is evident that although there will be a significant change in the passage of the hydrogen into the sample, the change is not too abrupt, consistent with the data illustrated in Figure 7.9.

### 7.3.5 Permeation experiments

The raw permeation data from experiments conducted on Alloy D samples (heat-treated as described in Table 7.1) are presented in Figure 7.12a. The derived effective-diffusivity data plotted in Figure 7.12b confirm the general expectation that the presence of the films of retained austenite reduces the effective diffusivity

**Table 7.3:** Experimental data from Alloy B, used to plot Figure 7.9. The hydrogen content listed is that evolved from the sample over the temperature range 25-300°C, using the heating rate indicated.

Number	$V_\gamma$	Charging time / h	$\dot{T}/^\circ\text{C h}^{-1}$	Desorbed H / ppm g <sup>-1</sup>
1	0.07	24	100	1.78
2	0.07	24	100	1.45
3	0.10	24	100	1.01
4	0.15	24	100	1.19
5	0.21	24	100	1.25
6	0.21	24	50	0.84
7	0.21	24	75	1.02
8	0.21	20	100	0.89
9	0.21	20	100	1.00
10	0.21	1	100	0.02
11	0.21	3	100	0.14
12	0.21	6	100	0.33
13	0.07	1	100	0.08
14	0.07	3	100	0.20
15	0.07	6	100	0.24

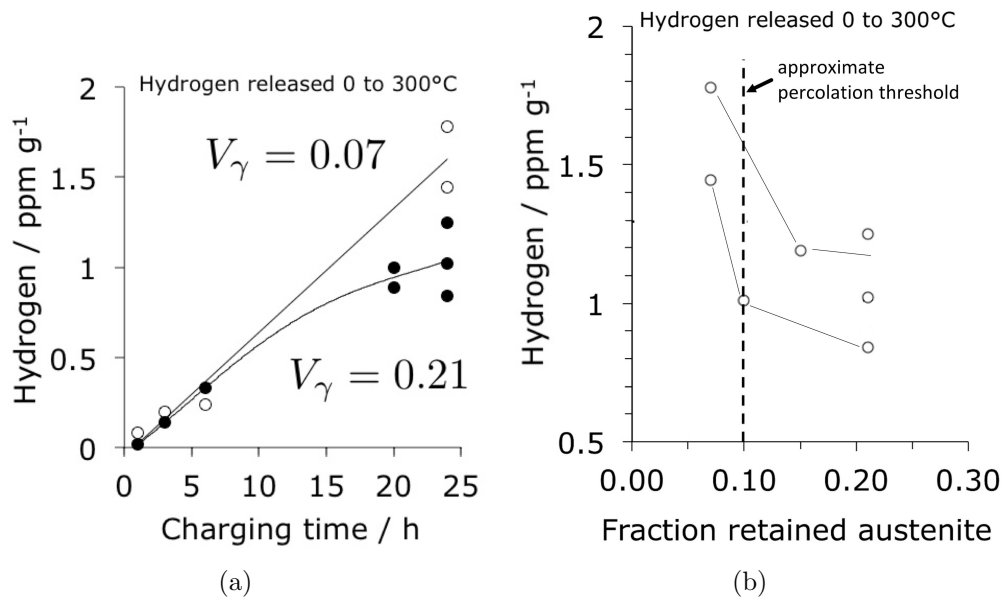


**Figure 7.9:** Alloy B. (a) Dependence of hydrogen desorbed over the temperature range 25-300°C, on the hydrogen charging time, and (b) on the volume fraction of retained austenite. The variation in samples with  $V_\gamma = 0.21$  charged for 24 h is due to the effects of different heating rates.

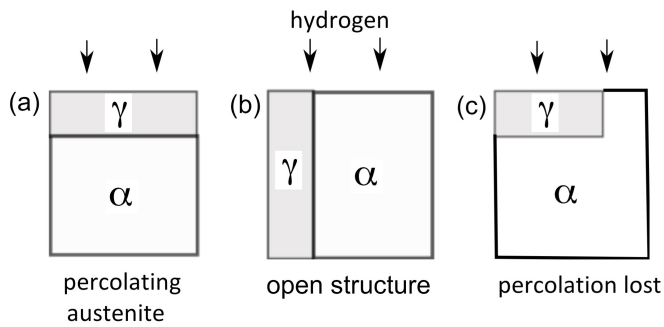


**Figure 7.10:** Different scenarios in a simplified model for the penetration of hydrogen into a two-phase mixture of ferrite and austenite.

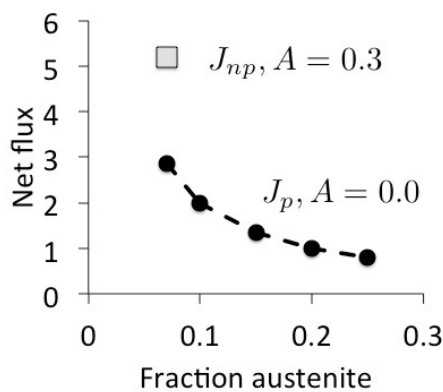
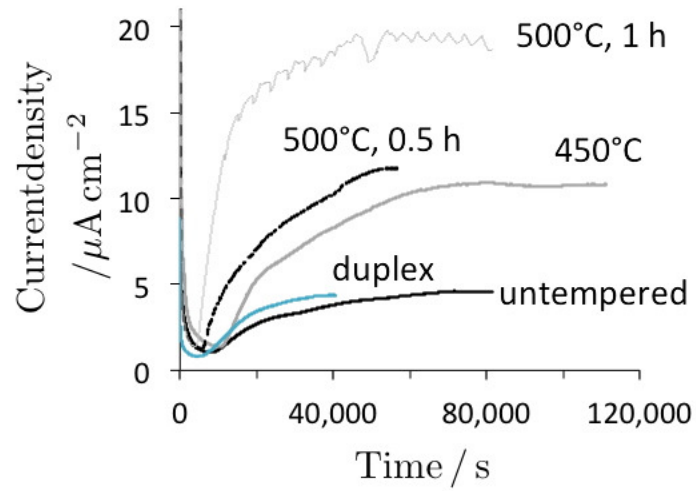


**Figure 7.11:** Calculated net flux, assuming  $J_\alpha$  has an arbitrary value equal to 15. Details in text.

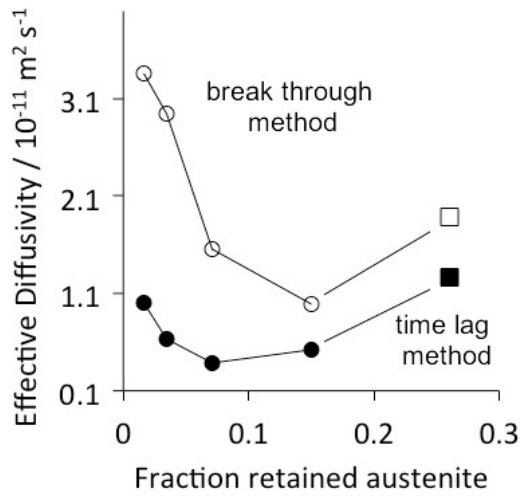
of hydrogen through the sample significantly, irrespective of the analysis method. The two methods give different answers because the time-lag method treats the problem essentially as a random walk of hydrogen through the steel, whereas the break-through technique equation is derived by considering the ability of the hydrogen to begin arriving on the other (output) side of the sample. The smaller value of the time-lag diffusivity  $D_l < D_b$  indicates that the hydrogen transport is governed by diffusion through the sheet rather than by surface kinetics.

Permeability represents the ability of a material to act as a hydrogen barrier, determined from the steady state current through the sample. This is in contrast to diffusivity, which describes the kinetics of atomic motion. The permeability increases dramatically as the retained austenite content is reduced and percolation is lost, as shown in Figure 7.12.

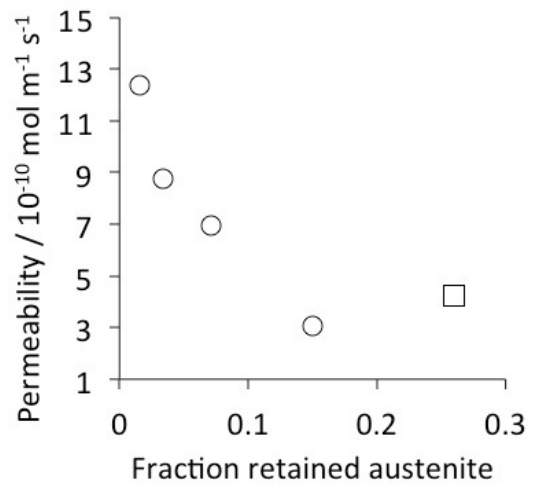
In all of the TDA experiments on charged specimens, no significant hydrogen-desorption was observed in the temperature range 300–400°C.



(a)



(b)



(c)

**Figure 7.12:** Permeation experiments on samples of Alloy D (circles) and the duplex steel (squares). (a) Current density versus time. (b) Effective diffusivities  $D_l$  and  $D_b$ . (c) permeability data.

### 7.3.6 Decomposition of retained austenite

It was also intended to study what happens to the hydrogen dissolved in the austenite, when the austenite associated with the bainitic structure decomposes into a mixture of cementite and ferrite. Previous work on nanostructured bainite has shown that the decomposition occurs during isothermal heat treatment at temperatures of 400°C or above [203, 253, 267, 277]. However, the present experiments involve continuous heating, so dilatometric experiments were done to measure the temperature range over which the substantive decomposition of austenite occurs. Given that the retained austenite is enriched in carbon to at least 1.2 wt% [37], its decomposition in the manner described was calculated to lead to a net contraction using the equations given in [239]. Figure 7.13 shows that for both heating rates studied, the austenite decomposes in a temperature range of approximately 420-530°C.

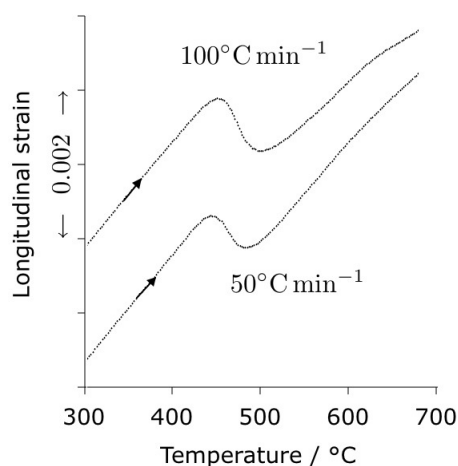


**Figure 7.13:** Alloy B. Length changes during the heating of the  $V_\gamma = 0.21$  sample. The contractions observed during heating correspond to the decomposition of the carbon-enriched retained austenite.

At the kind of heating rates used in this work, even strongly trapped hydrogen (binding energy  $\approx 50 \text{ J mol}^{-1}$ ) should escape from the sample by the point at which it reaches 300°C [271, 272]. Any hydrogen that is even more strongly trapped is unlikely to contribute to the deterioration of mechanical properties [278]. The TDA curves presented earlier show that much of the harmful hydrogen is removed by 300°C. However, to investigate whether the decomposition of austenite into a mixture of cementite and ferrite releases strongly trapped hydrogen, many of the experiments were continued to temperatures as high as 800°C.

Unfortunately, the experiments revealed rather strange results, both over the temperature range of interest from the point of view of austenite decomposition,

and beyond (Figure 7.14). It was suspected that oxidation plays a role in creating these effects. The 99.9995% pure gas contains, according to the supplier, some 2 ppm of water. The thermodynamic analysis presented in Appendix A.4 shows that with an assumed value of  $p_{\text{H}_2}/p_{\text{H}_2\text{O}} = 0.1$  given the very low concentration of water in the gas, it is possible in all the steels studied here to reduce the water into hydrogen, with the formation of Si, Al and Mn oxides (Figure 7.14b). FeO can also form but the driving force for oxidation is rather small so it is likely that the other oxides form preferentially.

To test this experimentally, a sample of the duplex steel was polished, charged and tested to generate a TDA curve, Figure 7.14c. The same sample was then polished and reheated without hydrogen charging in the TDA, and on the third occasion, the same sample was reheated without charging or polishing in the TDA. The data indicate that the high-temperature effects are associated with oxidation, and that the presence of an existing oxide film tends to diminish the effect, as seen in the third experiment (Figure 7.14c(iii)).

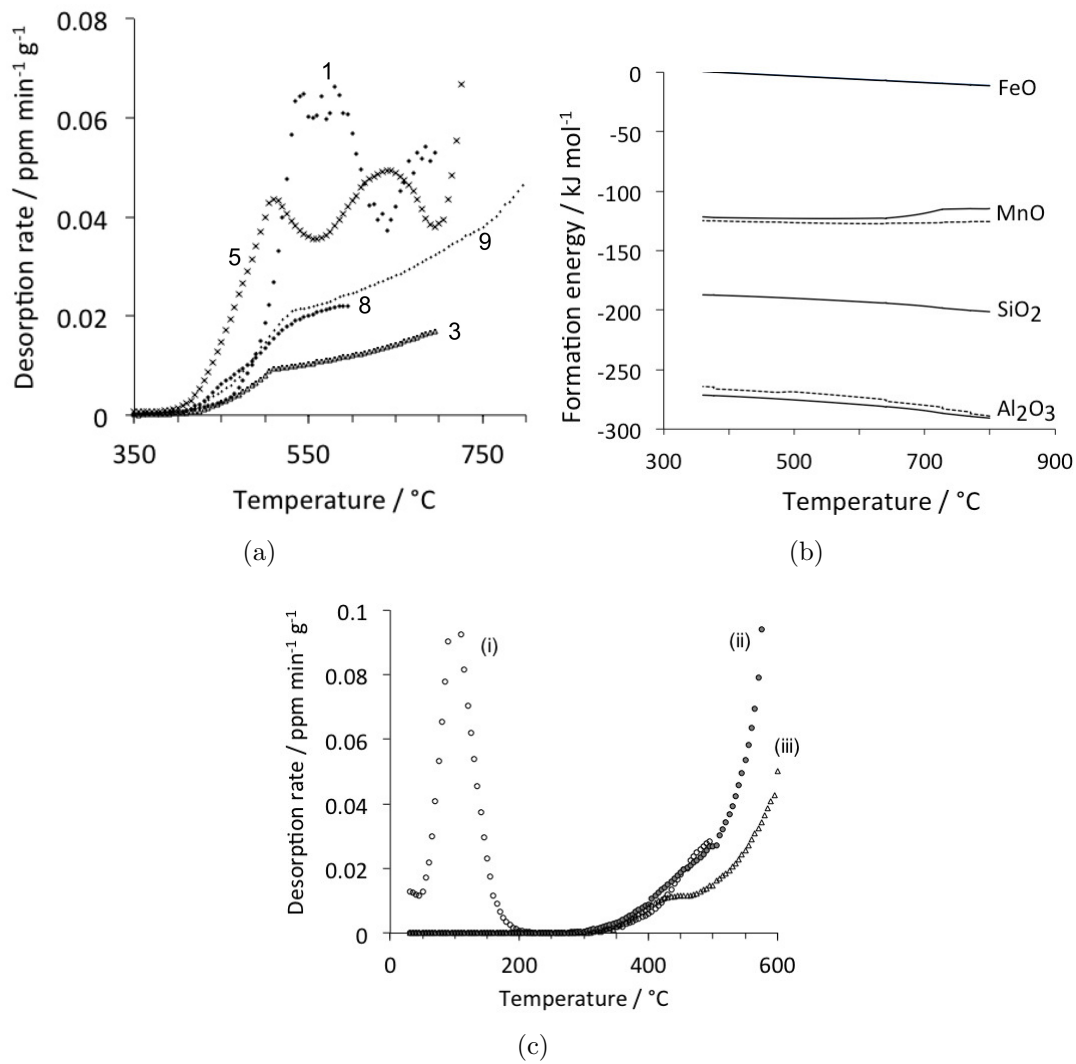


**Figure 7.14:** (a) TDA data for Alloy B; the numbers relate to those in Table 7.3. (b) Calculated free energy change for oxidation, for Alloy B (continuous lines) and Alloy E (dashed lines). (c) Data for the duplex steel sample Alloy E, 1 mm thick, hydrogen charged for 24 h, 100°C h<sup>-1</sup>. (i) Polished, charged and analysed, (ii) same sample, polished and analysed without charging, (iii) same sample, not polished or charged, analysed.

## 7.4 Conclusions

The purpose of the work in this chapter was to study the passage of hydrogen through a mixture of bainitic ferrite and films of austenite, in which the austenite fraction and morphology was such that it forms a continuous barrier between the ferrite plates, i.e., the austenite percolates through the mixture. The fraction of austenite was controlled by heat treatment so that corresponding samples in which the fraction is less than that required for percolation could be studied. Several conclusions can be reached on the basis of thermal desorption experiments, permeation experiments, theoretical analysis and comparison between samples containing radically different morphologies of austenite at approximately the same volume fraction.

The study of partially hydrogen-charged specimens of nanostructured bainite using thermal desorption shows that the amount of hydrogen absorbed by the steel, at long charging times, is smaller when the austenite fraction is beyond the percolation threshold. Indeed, the amount of hydrogen that enters the steel increases sharply when the fraction of austenite is less than the percolation threshold. Results also gave an indication of the degree of scatter obtained from identically-treated samples, due to the complexity of the structures involved.

In the nanostructured steel, the quantity of hydrogen that enters the steel during charging is not as sensitive to the austenite content as might be expected from a raw comparison of the diffusion coefficients of hydrogen in ferrite. This is because the diffusivity of hydrogen in bainitic ferrite is in fact much smaller than that for ‘perfect’ ferrite, due to trapping effects.

Consistent with experimental data, a simple flux model indicates that the increase in the hydrogen absorbed by the steel during charging is about a factor of two when the austenite in the nanostructure loses percolation.

A comparison of two steels — one with percolating austenite films ( $V_\gamma = 0.15$ ) in the nanostructure and the other in which the fraction of austenite is much larger ( $V_\gamma = 0.26$ ), but with austenite grains present in a continuous ferrite matrix — indicates a strong effect of austenite morphology on the penetration of hydrogen into the steel. The latter microstructure absorbs the hydrogen much more readily.

In summary, the nanostructured bainite containing percolating austenite is able to resist the influx of hydrogen better than in the absence of austenite, but the resistance vanishes if the austenite is present as isolated grains in a predominantly ferritic structure. In particular, this work also verifies the calculation [35] that the percolation threshold in such bainite is at approximately  $V_\gamma \approx 0.1$ , a factor important in controlling the ductility of the steel.

*The thing about iron is that you generally don't have to think fast in dealing with it.*

Terry Pratchett, *Lords and Ladies*

## CHAPTER 8

---

# SHEAR-BAND STRUCTURE IN BALLISTICALLY-TESTED BAINITIC STEELS

---

### 8.1 Introduction

Much of the work in previous chapters has focused on Alloy A: an armour concept with a steel structure consisting of nanostructured bainitic ferrite and carbon-enriched retained austenite [29]. Whereas this particular armour is for severe threats, a range of less potent projectiles can, in principle, be accommodated using coarser variants of the carbide-free mixtures of bainitic ferrite and retained austenite. It is with this in mind that bainitic alloys originally developed for use in gun barrels [22, 23] have been evaluated for their ballistic performance.

In this instance, the behaviour of interest is that which occurs during projectile penetration; in particular, the formation of adiabatic shear bands. These are narrow layers of intensely sheared material [279]. Such localisation of deformation occurs when the heat generated by the irreversible consequences of rapid deformation cannot be dissipated fast enough by diffusion. The resulting rise in temperature leads to localised softening — which cannot be compensated for by work hardening — and hence a focusing of plasticity into bands, which are typically 10-100  $\mu\text{m}$  in width [280]. The phenomenon is therefore associated with high strain-rate deformation (for example, that which occurs during machining or

ballistic impact [281, 282]) and has been speculated to be a damage mechanism in bearings [283, 284] although the evidence for this is incomplete [189]. The bands can reduce the ability of armour to resist projectiles, since plugs of material can then detach relatively easily from the armour [285].

The mechanisms responsible for shear localisation are well understood, but in steels there is an additional complication that phase transformation can occur during the adiabatic heating. Peak localised temperatures of 900°C and above have been recorded [286, 287], which is sufficient for austenitisation in many steels. This can lead to the formation of ‘transformed bands’ that are essentially fine martensite. Alternatively, the intense plasticity alone may produce ‘deformation bands’ [279]. Distinctions have been attempted on the basis of etching characteristics and hardness measurements [288] but the conclusions reached are uncertain [289, 290]. Recent work suggests that a transition from deformed to transformed bands takes place as the strain rate is increased [291]. The presence of defects, the stress state of the metal, its thermal diffusivity and its composition have also been cited as factors influencing the nature of the shear bands that are formed [282].

The purpose of the work in this chapter was, therefore, to assess the nature of the shear bands generated in these steels as a consequence of being fired at during ballistic tests. By identifying the deformation and failure mechanisms that dominate during projectile penetration, it is possible to suggest adaptations to the alloy design with a view to improving the ballistic performance.

## 8.2 Experimental methods

Alloys E and F were investigated in this study; their compositions are listed in Table 3.1. Their microstructures and mechanical properties have been reported thoroughly in the original work more than a decade ago [22, 23]. The phase fractions, consisting of bainitic ferrite ( $\alpha_b$ ), carbon-enriched retained austenite ( $\gamma$ ) and some martensite ( $\alpha'$ ) from that work are listed in Table 8.1.

The material was produced by a vacuum melting process with the ingots homogenised at 1200°C for 2 days, followed by vermiculite cooling to avoid cracking and facilitate sawing. The plate material from the top of each ingot was trimmed

	$V_{\alpha_b}$	$V_{\gamma}$	$V_{\alpha'}$	$C_{\gamma}$ / wt%
Alloy E	$0.26 \pm 0.01$	$0.07 \pm 0.01$	$0.67 \pm 0.02$	0.55
Alloy F	$0.62 \pm 0.05$	$0.12 \pm 0.01$	$0.26 \pm 0.04$	0.92

**Table 8.1:** Volume fractions of the microstructural constituents of the alloys; these figures are quoted from the original work [22, 23].  $C_{\gamma}$  refers to the carbon content of the retained austenite.

off and discarded, and the remainder was sawn in half for further processing. After heating to 1200°C, the two pieces were rolled in six passes to  $\approx 12$  mm thick plate with finish-rolling temperatures in the range 905–937°C, followed by air cooling. The ballistic testing details are confidential, but the projectiles penetrated the steel with sufficient velocity to cause the formation of shear bands; Figure 8.1 illustrates the coordinate axes.

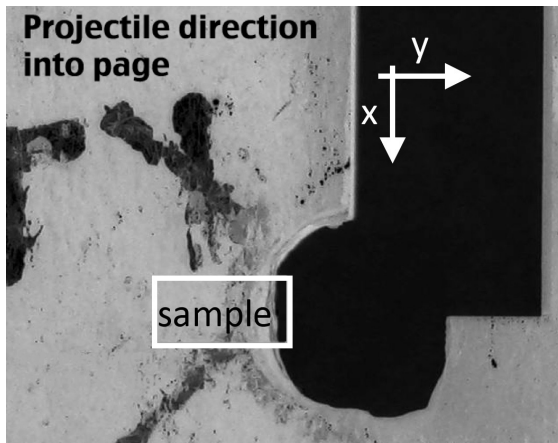


**Figure 8.1:** The hole at the bottom is created by the projectile; the location from which samples were extracted is delineated by the rectangle. The coordinates defined are used throughout the paper, with the projectile propagating along  $-z$ .

Samples for transmission electron microscopy and optical metallography were prepared from each alloy specimen as described in Sections 3.2 and 3.3.

To help understand whether the structure within the shear bands was transformed or just deformed, a set of fully martensitic samples was prepared from the alloys for comparison purposes. The specimens were austenitised for 30 min at  $A_{e3} + 10^\circ\text{C}$ ,  $A_{e3}$  being calculated using MTDATA v.4.73 with the TCFE v.5 database [195], before water quenching. Quantitative X-ray analysis was performed upon samples of the quenched material, prepared and analysed as described in Sections 3.2 and 3.6.

### 8.2.1 Convergent beam electron diffraction

Convergent beam electron diffraction (CBED) was used to obtain diffraction patterns from twinned regions within the shear band in Alloy E. This was carried out on an FEI Tecnai F20 high resolution scanning transmission electron microscope, operated at 200 kV.

This diffraction technique is distinguished from selected area diffraction (SAD) by the nature of the incident beam. Whereas in selected area diffraction, the electron beam is parallel, CBED uses a conical beam of electrons incident on the specimen surface. The benefit of using CBED over SAD (relevant to this work) is the ability to obtain conventional diffraction patterns from much smaller specimen regions. Typically, the smallest region that can be studied using SAD is of the order of  $0.1\ \mu\text{m}$  in diameter [292, 293]. Spherical aberration effects within the objective lens produce inaccuracies in selecting a specific area from which to obtain a diffraction pattern; for apertures smaller than  $5\ \mu\text{m}$  this uncertainty becomes problematic [294]. Therefore, when it is necessary to make observations of a small, specific region in a sample, CBED is preferred, since the location can be more accurately pinpointed.

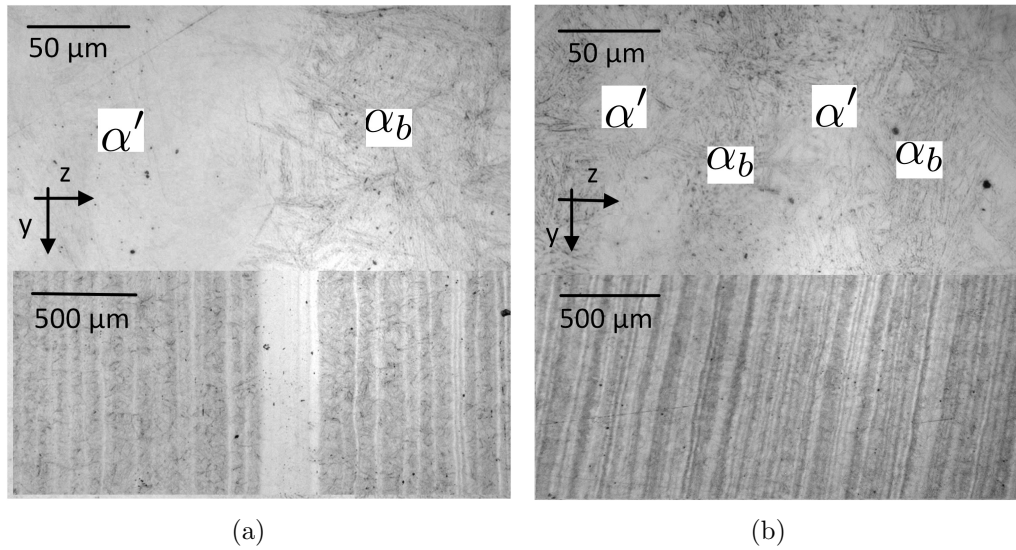
## 8.3 Results and discussion

In the discussion that follows, the term *uniform-shear strain* is used to distinguish ordinary deformation — which is fairly homogeneously distributed over macroscopic dimensions — from the highly localised strain *inside* a shear band.

### 8.3.1 Metallography

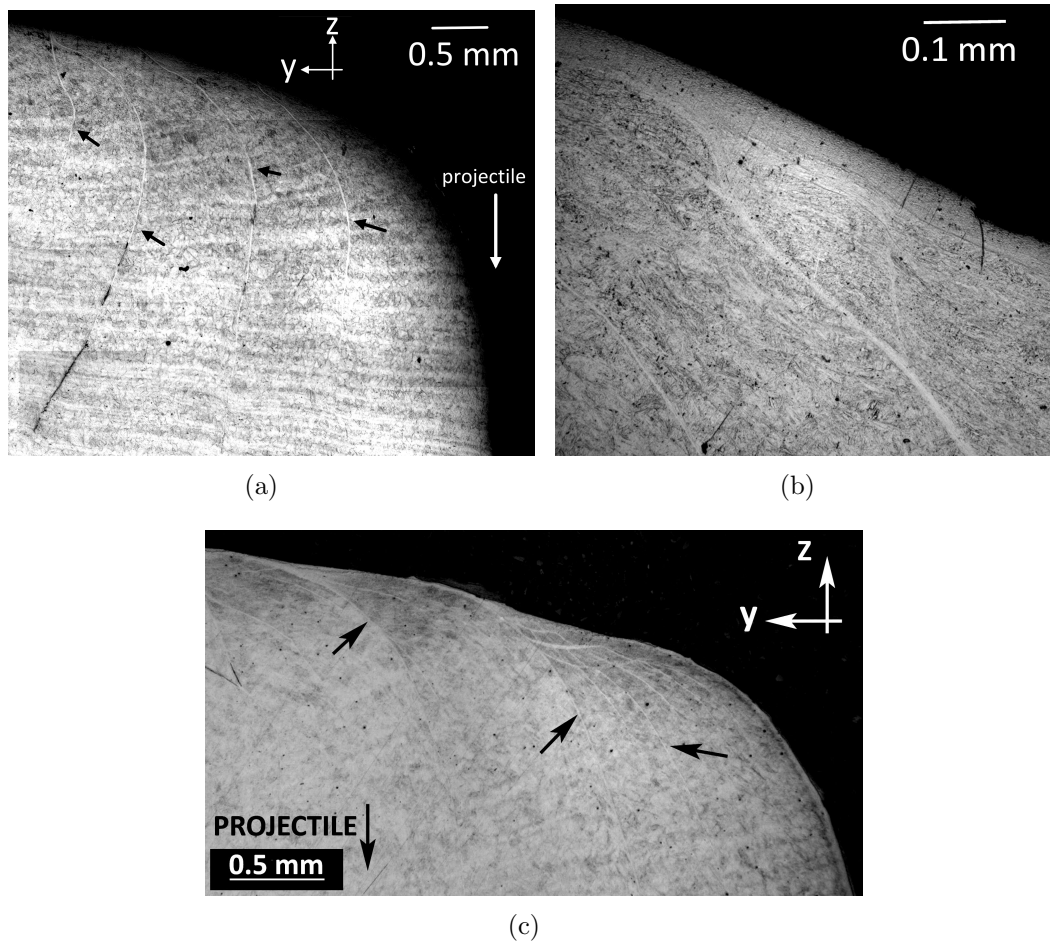
Figure 8.2 shows chemical segregation-induced bands that are more prominent in the manganese-rich alloy, because this solute is well-known to partition during solidification. The depleted regions transform into a predominantly bainitic structure, whereas the light-etching regions contain untempered martensite. The bands lie in the  $x - y$  plane with  $y$  corresponding to the rolling direction of the plates. They are useful in this study as markers of strains caused by impact.

Figure 8.3 shows extensive shear banding at the entry-point of the projectile, extending to some 6 mm along  $y$  from the hole. The bands are thicker towards the surface of the plate where the deformation of the region in the immediate

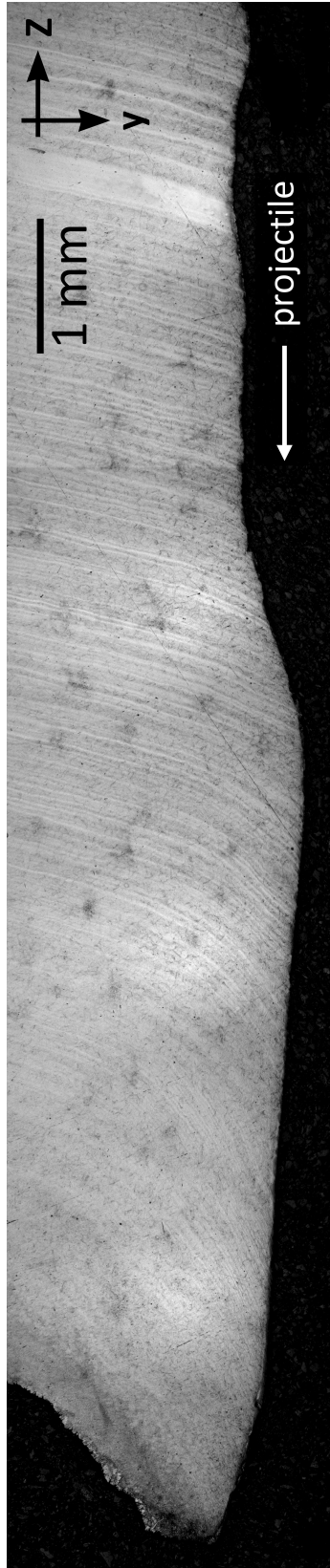


**Figure 8.2:** Micrographs illustrating banding, as a function of depth within the steel plate. (a) Alloy E; (b) Alloy F. The terms  $\alpha_b$  and  $\alpha'$  refer to regions that are predominantly bainitic or martensitic.

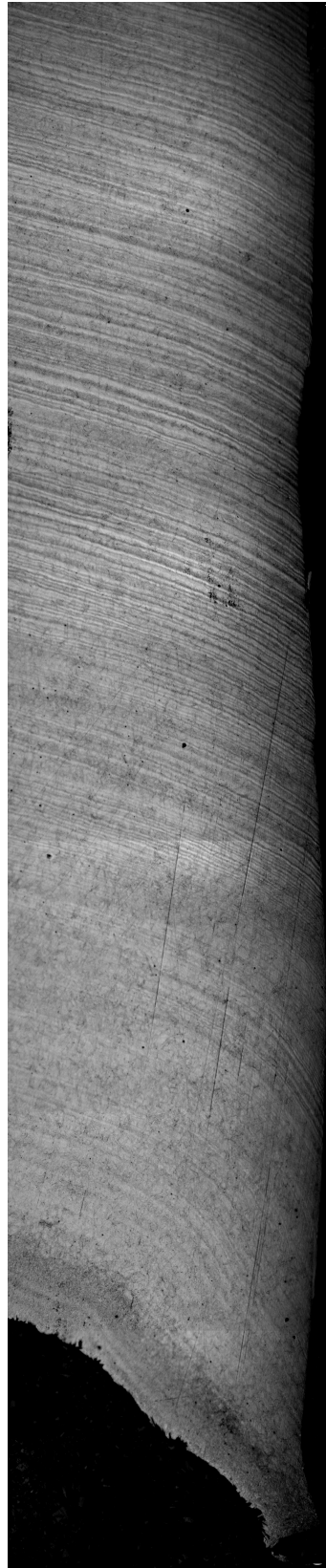
vicinity of the projectile is intense, as shown in Figure 8.3b. Indeed, the segregation bands in that region appear discontinuous as a result of the severe strains accommodated in the shear bands. The pattern formed by the segregation bands shows that in both samples, the extent of plastic deformation of the material beyond the hole increases with depth of penetration, consistent with the expected reduction of the projectile velocity (Figure 8.4). Accordingly, the amount of shear banding also decreased with the depth of penetration. The projectile creates a plug that eventually is detached from the armour; these observations indicate that adiabatic shear has the greatest role in the vicinity of the impact, followed by less localised deformation as the kinetic energy is dissipated during the process of penetration.



**Figure 8.3:** Fine shear bands due to ballistic impact, some of which are indicated by the black arrows. (a,b) Alloy E; (c) Alloy F.



(a)



(b)

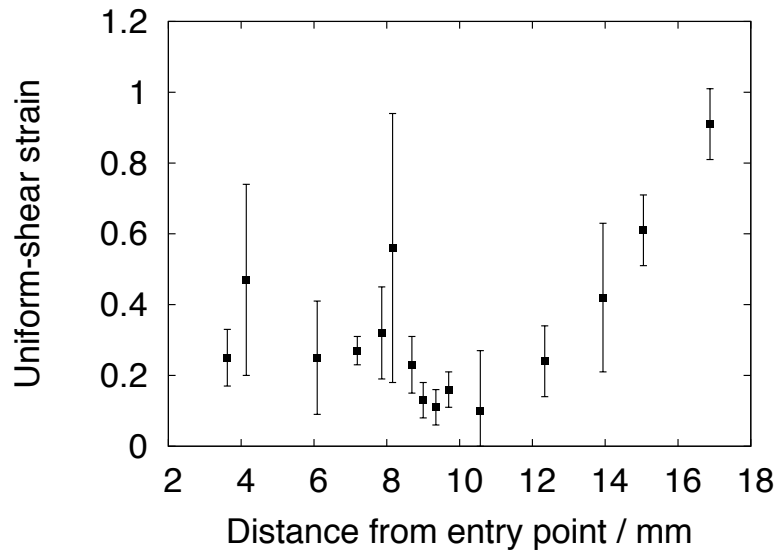
**Figure 8.4:** Bullet hole through the depth of the plate, with segregation bands showing the pattern of deformation. (a) Alloy E; (b) Alloy F.

Using the segregation bands as guides, it was possible to obtain quantitative measurements for the shear strain along the inner surface of the hole. The results are presented in Figure 8.5. In both cases, the shear strain at the surface remains roughly constant for most of the penetration — what changes is the extent of material that undergoes uniform shear. While shear bands are visible reaching a penetration depth of 6 mm, the region of constant uniform-strain extends twice as far as this. Towards the entry point of the material, the segregation bands are less clear and so it is difficult to assess the uniform-shear strain early on in penetration. In Alloy E, which has clearer segregation bands, there appears to be hardly any measurable uniform-shear strain at the surface in the early stages of penetration. This indicates that virtually all of the initial deformation is accommodated in the shear bands. The increase in uniform-shear strain towards the exit region in both alloys may be due to this section of material not being constrained. These results indicate that the projectile slows down with penetration, and it is expected that adiabatic shear is most intense at the initial entry point. As the projectile penetrates and slows, ordinary deformation, spread out over a larger region, occurs.

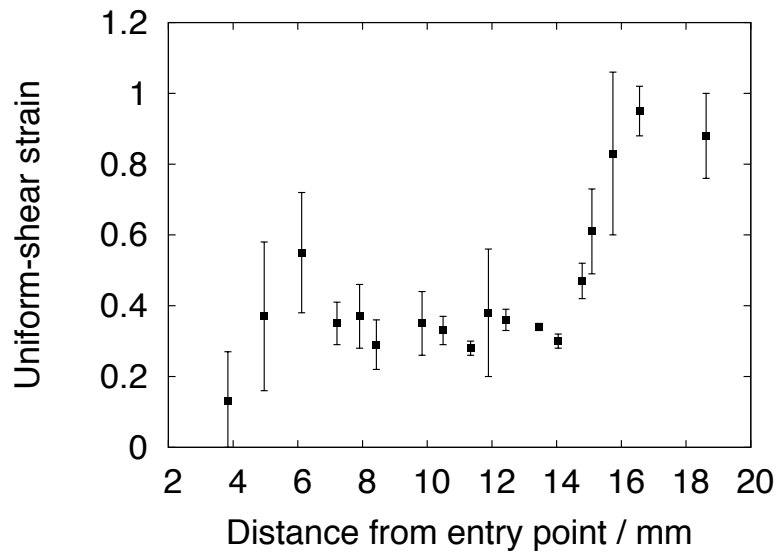
Measurements of the shear strain within a shear band in Alloy E (Figure 8.6) are consistent with the assumption of high adiabatic shear in the early stages of penetration. Due to the large shear strains involved, the accuracy of the results is limited, however, the data indicate that there is an extremely high degree of shear strain within the shear band. Nevertheless, the values obtained are consistent with measured shear strains quoted in the literature [295].

### **8.3.2 Transmission electron microscopy**

Consistent with previous work [22, 23] and the quantitative details listed in Table 8.1, the structure of the as-received material in both alloys consisted predominantly of bainitic ferrite and retained austenite, with some twinned martensite observed in Alloy E, as illustrated in Figure 8.7. Electron diffraction analysis occasionally revealed faint reflections from cementite (Figure 8.8), but the volume fraction must be sufficiently small to make the particles difficult to detect amongst the contrast from dislocations and other features within the microstructure.



(a)



(b)

**Figure 8.5:** Graphs showing the degree of uniform-shear strain at the surface of the hole as a function of depth of penetration. (a) Alloy E; (b) Alloy F.

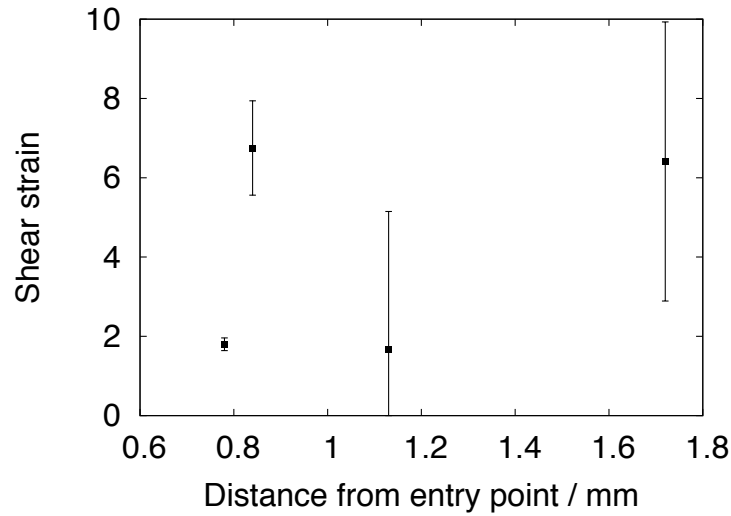
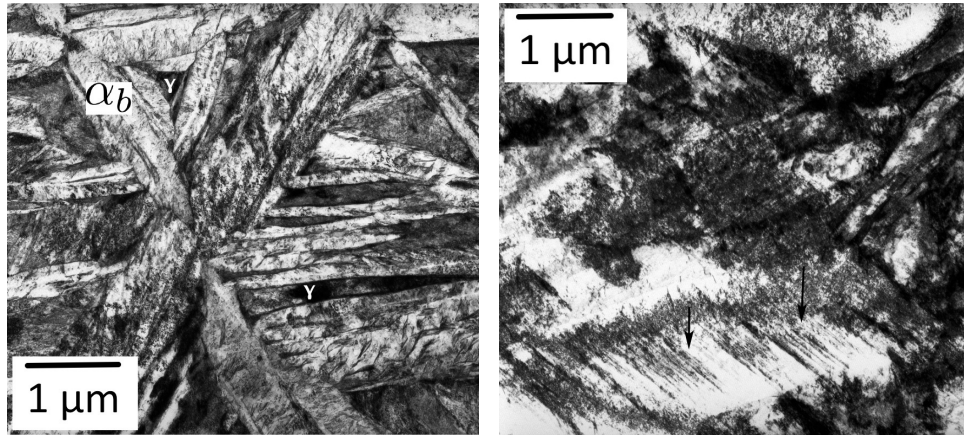


**Figure 8.6:** Graph showing the degree of shear strain within a shear band present in Alloy E, as a function of depth of penetration.

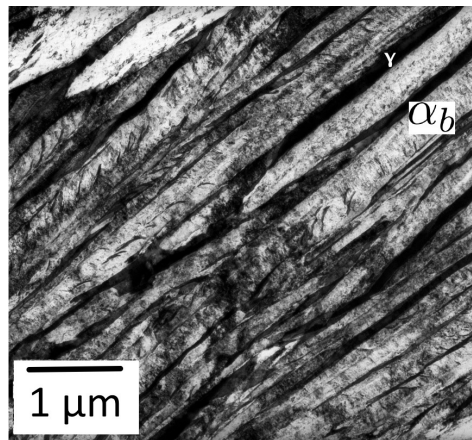
In contrast, the structure within the shear bands (Figures 8.9, 8.10) shows deformation leading to the formation of irregular, cell-like structures, although electron diffraction shows that the cells do not represent a large spread in orientation. The images are not reminiscent of a structure that has been austenitised due to adiabatic heating followed by quenching to martensite, where neat plates or laths of martensite would be expected. Electron diffraction again indicates that cementite is present (Figure 8.11). While this may suggest that the microstructure has not undergone reaustenitisation, it is likely that any carbides would nevertheless be retained during the austenitisation process, since the timescales in question are too brief to permit carbide dissolution.

Several examples of twins or twin-like structures were observed in the shear bands of both alloys (Figures 8.12, 8.13). The long, thin nature of the structures identifies them as mechanical twins rather than annealing twins. Convergent beam electron diffraction analysis reveals that these are ferritic twins (Figure 8.14), most likely from regions of martensite. However, it cannot be determined if this martensite is a remnant of the as-transformed structure, or has been newly formed in the shear band. On closer examination, the twins in Figure 8.12 appear to be bent, as though they have been deformed, which would indicate that this is the original martensite. These observations are speculative, however, and it is therefore useful to make a comparison with structures that have undergone martensitic



(a)

(b)



(c)

**Figure 8.7:** The microstructure in the as-received condition. (a,b) Alloy E; (b) Alloy F.

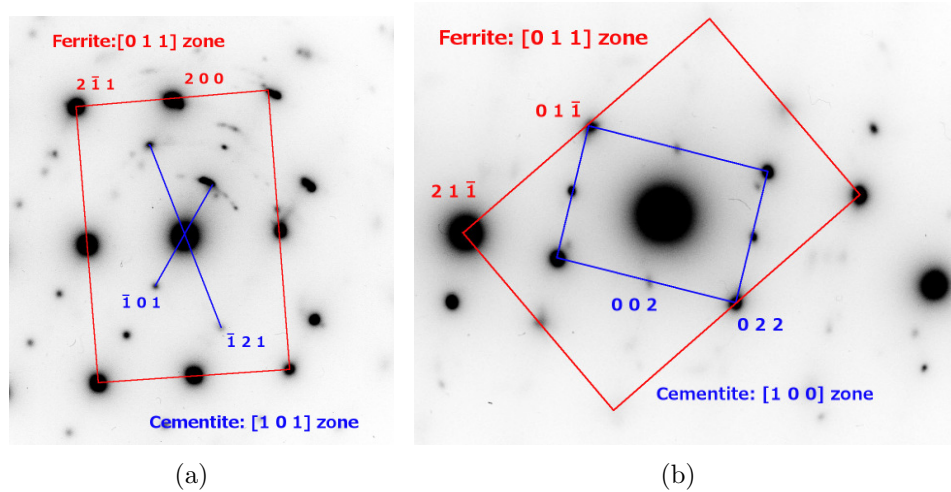


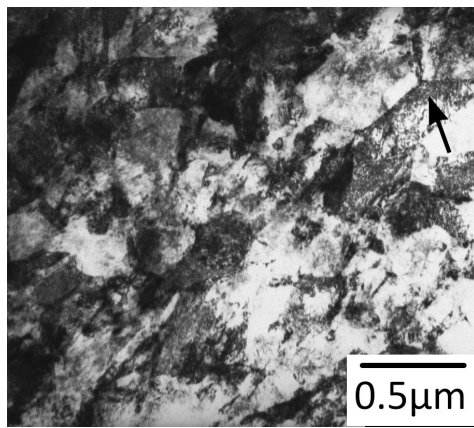
**Figure 8.8:** Electron diffraction patterns showing reflections of cementite in the as-received alloys. (a) Alloy E; (b) Alloy F.

transformation with certainty.

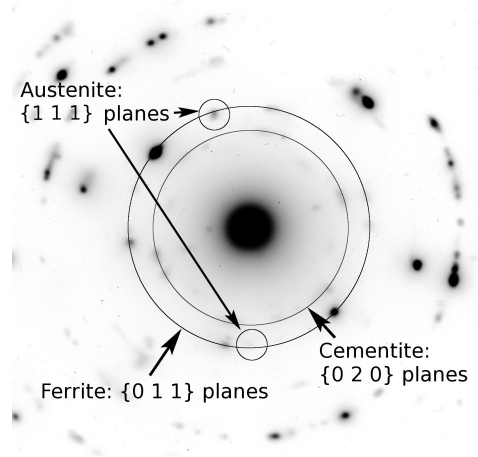
The mere plastic deformation of the plate-like structure of bainite or martensite on its own does not seem to produce the kinds of structures illustrated in Figure 8.9. Ordinary deformation experiments either by tensile testing or using rolling deformation indicate that for significant strains, the plate-like features remain easily discernible after deformation; however, annealing after such cold-deformation leads to micrographs similar to those illustrated in Figure 8.9 [5, 296, 297]. It might therefore be concluded that the structures illustrated here are generated by warm deformation during the adiabatic heating.

Notice also the presence of retained austenite within the bands, as detected using electron diffraction. This retained austenite is probably a vestige of the carbon-enriched austenite that is stabilised by the bainite reaction and, although some of it is expected to decompose into martensite during deformation, the remainder will be mechanically stabilised [298–303].

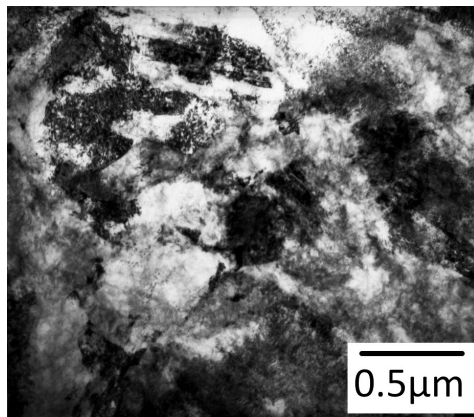
These ideas were tested further in two respects. First, a sample from Alloy E was austenitised at  $810^{\circ}\text{C}$  and from Alloy F at  $775^{\circ}\text{C}$ , for 30 min periods; both these temperatures are just  $10^{\circ}\text{C}$  above the respective calculated  $Ae_3$  temperatures. The goal was to produce as small an austenite grain size as possible because it is assumed that during adiabatic heating, any austenite grains would have a small



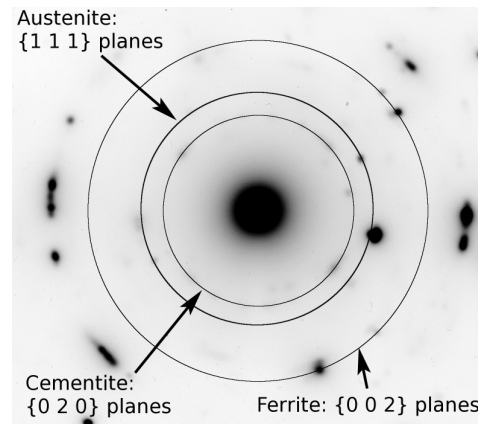
(a)



(b)



(c)



(d)

**Figure 8.9:** Micrographs of samples extracted from shear bands using focused ion beam milling. (a,b) Alloy E; (c,d) Alloy F.

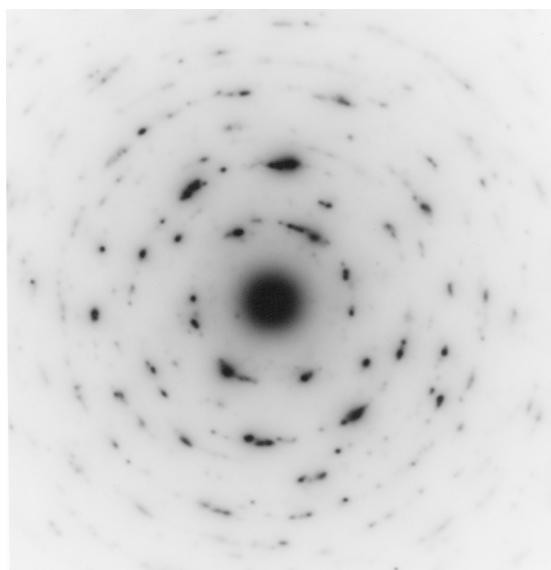


**Figure 8.10:** Electron diffraction pattern taken with wide aperture, showing the limited spread of orientations found in the shear band.

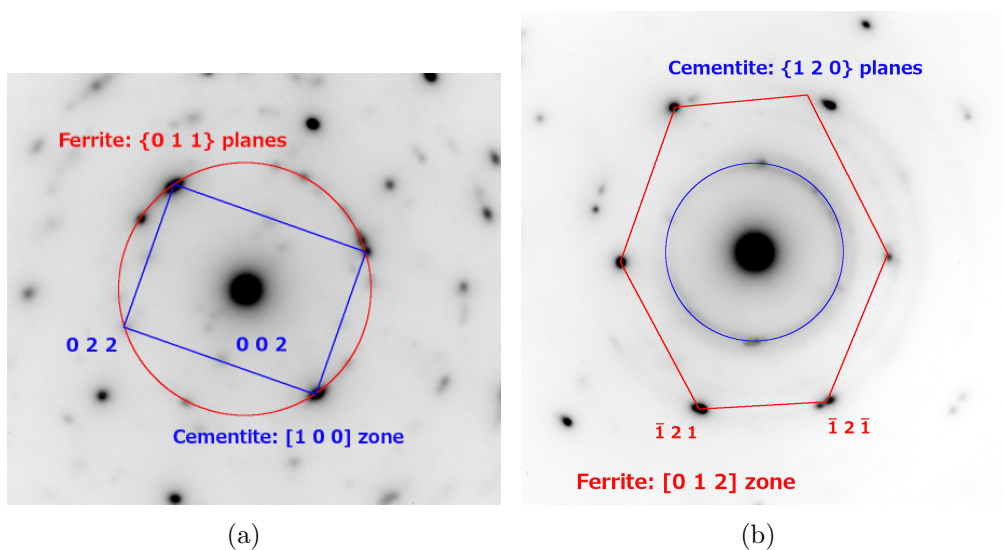


**Figure 8.11:** Electron diffraction patterns showing cementite in the shear bands. (a) Alloy E; (b) Alloy F.

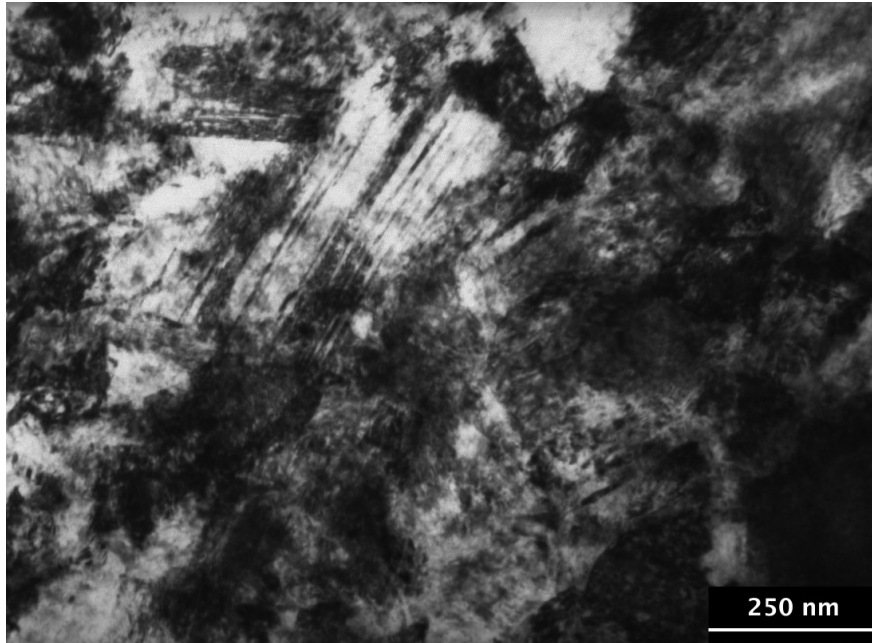


**Figure 8.12:** Detail of twin structures observed in shear band of Alloy E.

grain size due to the rapidity of the process and the high defect density. X-ray analysis (Figure 8.15) showed that both alloys contain negligible quantities of austenite upon quenching, so that they are effectively 100% martensitic. The presence of austenite in the shear bands therefore seems to contradict the idea of these being ‘transformed bands’. Secondly, the structure illustrated in Figure 8.16 has clear martensite plates and extensive twinning, inconsistent with the transmission electron micrographs of the shear bands. Although a transformed band would not be expected to be morphologically identical to a conventional quenched structure, it is notable that there is no sign of any lath-like features in the shear band.

A final consideration should be given to the effect of the carbon enrichment and subsequent deformation of austenite. The  $M_S$  of enriched, deformed austenite will be lower than that of the bulk alloy used to obtain the structures in Figure 8.16. Because of the combined heating and deformation processes undergone by the austenite in the shear band, it is difficult to estimate quantitatively how the austenite-martensite transformation will be affected. It is possible — although unlikely — that some regions of austenite could be sufficiently chemically and mechanically stabilised to avoid forming martensite altogether, despite the conditions being adequate to transform the bulk of the shear band. In this case,

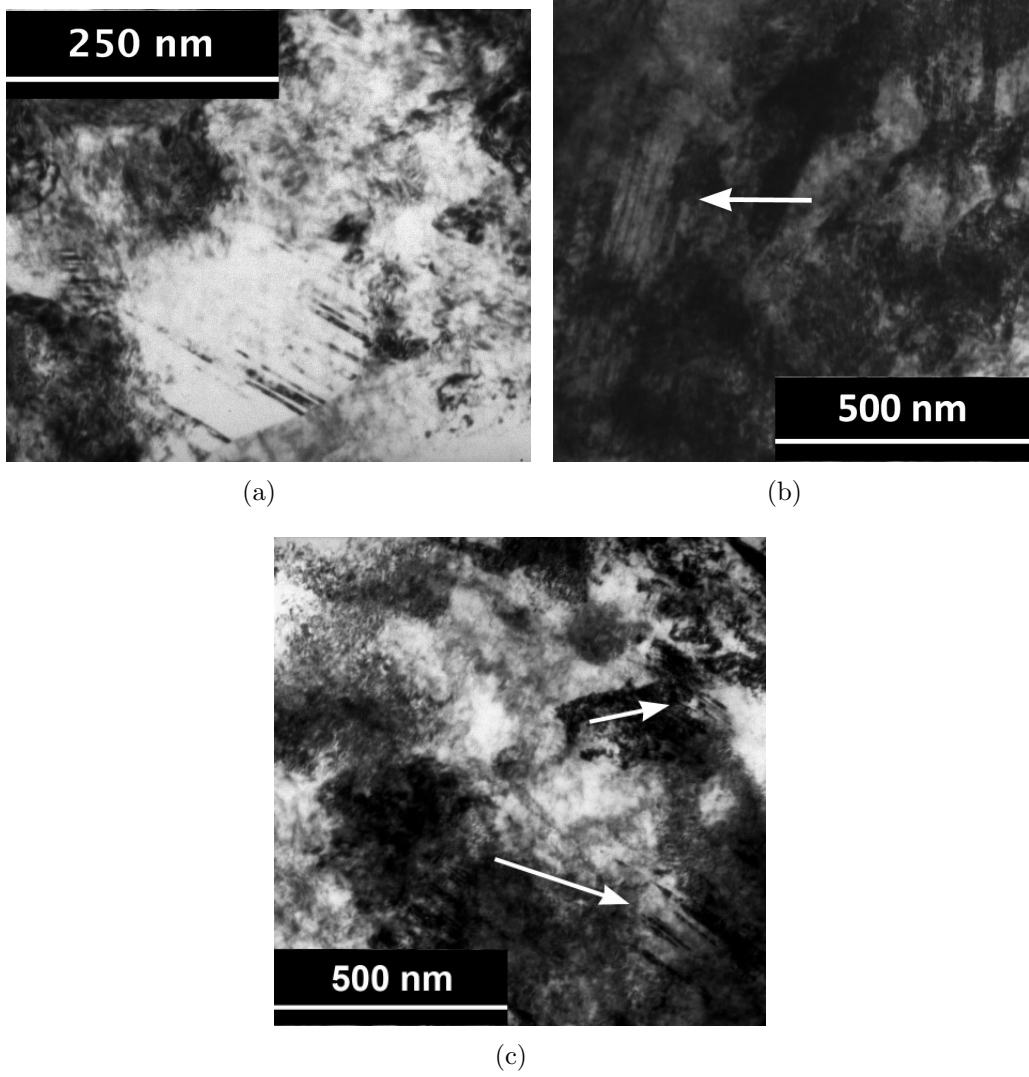


**Figure 8.13:** Details of twin structures observed in the shear bands. (a,b) Alloy E; (c) Alloy F.

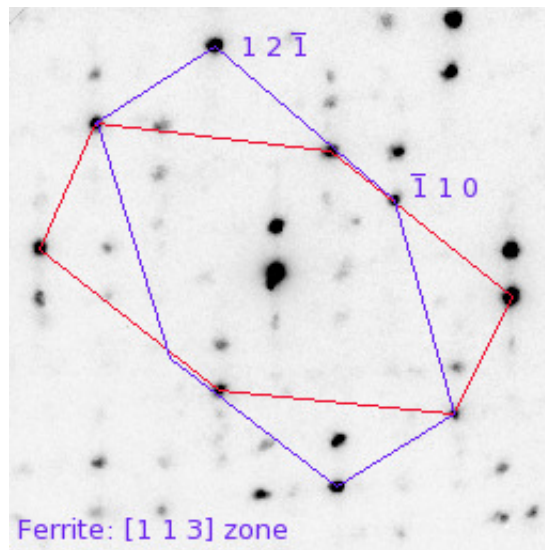


**Figure 8.14:** Convergent beam electron diffraction pattern taken from the region in Figure 8.12, showing ferrite twins reflected about the  $\{112\}$  planes. Also visible are several additional spots generated by double diffraction.

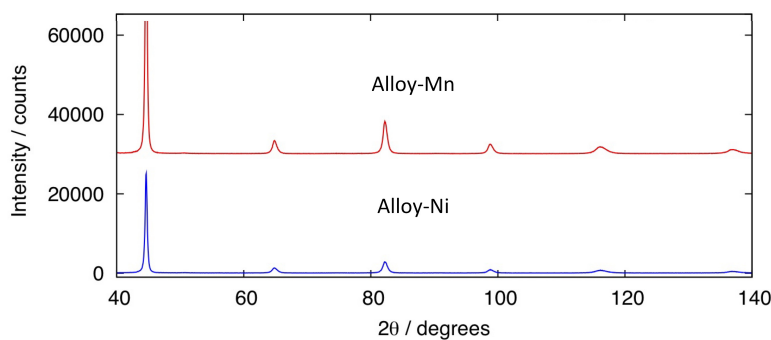
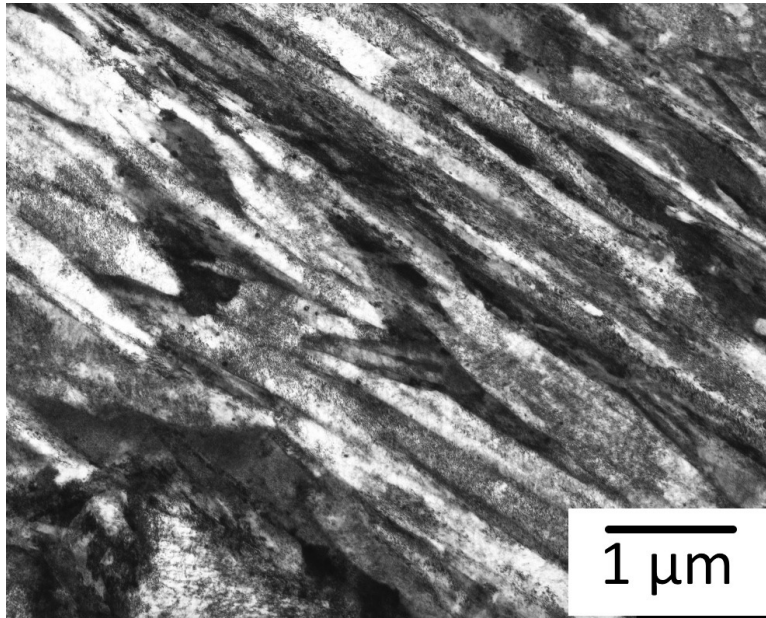


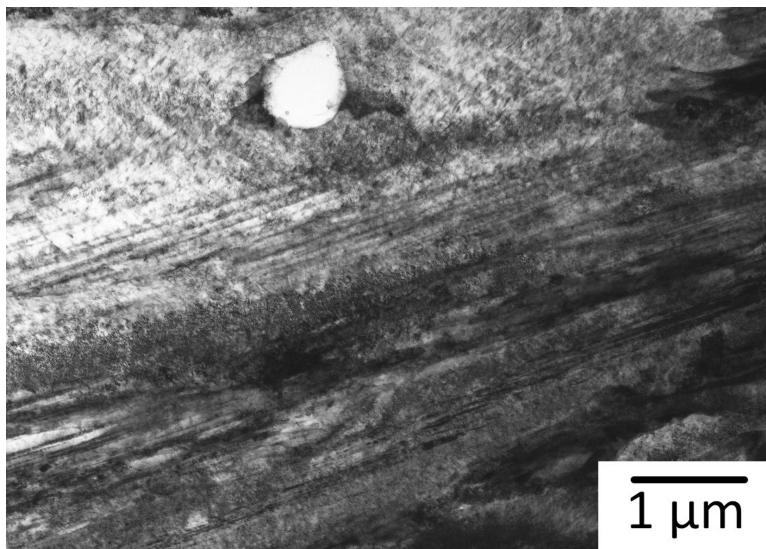
**Figure 8.15:** X-ray diffraction spectra of austenitised and quenched martensitic samples, with diffraction peaks visible only from the martensite.

the presence of austenite in the shear band would not rule out the possibility of transformation having occurred.

It is necessary to perform additional experiments and calculations to assess whether this idea is reasonable. However, because of the high strain rates and cooling rates involved, this is a difficult scenario to simulate experimentally. It is possible to account for austenite grain size and prior deformation using the method of Yang and Bhadeshia [220], although this model considers only uniaxial deformation rather than shear deformation. Without knowing more about the stress and strain state of the shear band material during impact, the results from a calculation are unlikely to be particularly meaningful.



(a)



(b)

**Figure 8.16:** Alloy E in an austenitised and quenched condition showing (a) fine plates of martensite; (b) twinning.

Although it is acknowledged that austenite may still be present in a transformed band, the morphological evidence remains in contradiction to that scenario. Thus, the totality of the evidence seems to suggest that for the circumstances of the present work, the shear bands represent plastically warm-deformed regions of the original mixtures of bainitic ferrite, retained austenite and untempered martensite. It is speculated, therefore, that shear banding as a phenomenon could be mitigated by introducing a high density of precipitate particles that would resist the softening of the allotropic lattices of iron.

## 8.4 Conclusions

Shear bands that form during the ballistic testing of microstructures consisting of a mixture of bainitic ferrite, carbon-enriched retained austenite and untempered martensite have been characterised using a variety of metallographic and X-ray diffraction techniques. It appears from these observations that the bands consist of deformed layers in which the original structure becomes mechanically mixed, and resembles a warm-worked microstructure that is still in an unrecrystallised state. The results show that for the circumstances of the present work, the bands are unlikely to represent phase transformation from austenite that forms during adiabatic heating and transforms subsequently into martensite.

By measuring the deflection of segregation bands as a function of the depth below the impact surface, it is found that the plasticity spreads laterally as the projectile penetrates, thus reducing the possibility of shear bands. The shear strain within the shear-bands is estimated to be between 2 and 6.

Finally, it is speculated that the introduction of a large density of fine carbide particles may help reduce the tendency to localise plastic deformation by making the structure more resistant to softening at high temperatures.

*Once again science saves the day. The end.*

Professor Farnsworth, *Futurama*

## CHAPTER 9

---

# GENERAL CONCLUSIONS AND FUTURE WORK

---

This thesis contains an account of several novel concepts that reinforce the primary goal of understanding the mechanisms that govern properties such as toughness, ductility and ballistic resistance in nanostructured steels. Much of the research has focused on examining the retained austenite within the mixed structures in question, and determining its response to various loading conditions. The results reveal new ways in which the stability and morphology of the retained austenite in these alloys influence their mechanical behaviour, generating key experimental evidence in support of existing theories, while providing additional scope for improvement of properties.

Detailed characterisation of a commercial, fast-transforming nanostructured steel has shown that both cementite precipitation and martensite transformation occur during the heat treatment process. This produces an alloy that is not carbide-free, but contains a nanoscaled mixture of bainitic ferrite plates, retained austenite and some cementite. A reduction in the silicon content to 0.71 wt% is responsible for the cementite formation, which was only seen to occur within plates of bainitic ferrite, although thermodynamic calculations indicate that precipitation should also occur from retained austenite. The removal of carbon from solution has negative implications for the stability of the retained austenite; X-ray observations indicate that the carbon content of this phase is below that predicted by the  $T'_0$  curve. In fact, the martensite is produced during the final quench to room temperature, from austenite that is not sufficiently stabilised, despite becoming

enriched in carbon during isothermal holding. The presence of martensite in the structure may contribute to the high hardness measured in the alloy, even though the structure is coarse when compared with other superbainitic steels.

The quantity of retained austenite at the notch root of superbainitic Charpy impact test pieces decreases as a result of both applied stress and notch machining. Along with observations of increased ferritic tetragonality in the same region, this demonstrates that such specimens are susceptible to notch embrittlement due to stress-induced martensitic transformation, which may explain the noted discrepancy between Charpy impact toughness and  $K_{1C}$  fracture toughness in this alloy. Furthermore, it was found that machining imparts significant changes to the structure and crystal lattice in the notch root region, in the form of surface shear deformation and residual compressive strains. By carefully choosing a sample manufacturing process that avoids some effects of notch machining and surface decarburisation, it may be possible to improve the Charpy impact toughness of a nanostructured bainitic steel.

It is well-known that retained austenite morphology can affect the ductility of a mixed-microstructure steel: there are stark differences between films of austenite and blocks, both of which may be present in nanostructured bainite. However, what may be termed the ‘macro-morphology’ of the austenite phase in these steels can also influence their tensile behaviour. Austenite percolation — three-dimensional connectivity — was studied in a series of hydrogen desorption and permeation experiments. Combined with a theoretical analysis, it can be concluded that nanostructured steels are able to absorb hydrogen much more readily (by roughly a factor of two) following loss of percolation, when the austenite no longer presents an unavoidable barrier to the passage of hydrogen. Experimental observations indicate that this percolation threshold is reached when the volume fraction of austenite drops below approximately 0.1, which is consistent with previous theory [43].

The critical importance of austenite morphology was highlighted further by comparison with a dual-phase steel consisting of isolated austenite grains. Despite a greater volume fraction of austenite being present in the latter alloy, it was more amenable to the diffusion and absorption of hydrogen, since the austenite no longer presented an effective barrier.

The damage mechanisms that operate during the ballistic penetration of steel plate armour containing a mixture of bainitic ferrite, carbon-enriched retained austenite and untempered martensite were studied using metallographic and electron diffraction techniques. Adiabatic shear bands form close to the surface of the plate, but are not present in deeper regions because the plasticity of the steel spreads laterally with the depth of penetration of the projectile. The structure within the shear bands remains unrecrystallised during adiabatic heating, resembling instead a warm-worked microstructure. It is estimated that the shear bands are subject to a strain of between 2 and 6 during this process. The introduction of a large density of fine carbide particles may help reduce the tendency to localise plastic deformation by making the structure more resistant to softening at high temperatures.

## 9.1 Scope for future work

The research summarised in this thesis has contributed to an improved understanding of how the complex and fine structures in steels respond to mechanical stimuli. This has significant implications for the manner in which future measurements should be performed. Furthermore, these results can now be applied to the design of new nanostructured bainitic steels, and improvement of the existing alloys. Some suggestions for future approaches are outlined below:

- It would be valuable to further investigate the contributions of residual strain due to machining, martensitic transformation due to machining, and that due to applied stress, to the embrittlement of material at Charpy notches. It is presumed that heat-treatment after machining is sufficient to eliminate any adverse effects, but ideally this needs to be verified experimentally. More accurate measurements of the residual strain can be made by using high-energy synchrotron X-rays to penetrate a full-sized specimen.
- More complete Charpy data is desirable to gain a fuller picture of the toughness of nanostructured bainite. It should be possible to relate the ductile-brittle transition curve to the temperatures at which austenite at the notch root is fully stabilised against martensitic transformation during impact.
- Using a combination of finite element methods and accurate strain measurements during *in-situ* bending of a Charpy sample, it would be useful

to map quantitatively the triaxial stress state of the notch root material, alongside the degree of stress-induced transformation. Modelling the transformation with the use of this data would enable the influence of the stress state on the martensite-start temperature to be calculated. If the loading is known to increase  $M_S$  by a given amount, it should be possible to create an alloy with a depressed  $M_S$ , to compensate. In this way, the alloy can better resist this specific case of embrittlement. It would be necessary to examine whether the amount of alloying additions required to achieve this was reasonable.

- The influence of strain-rate upon the austenite-martensite stress-induced transformation has been broadly neglected throughout this thesis, but it may be important. An *in-situ* synchrotron study of both Charpy and tensile test specimens subject to varying strain-rates would provide a quantitative understanding of how martensitic transformation depends on this factor. This is particularly important where toughness results are concerned, however, it would be interesting to see if there is much change in the behaviour of a tensile specimen with strain-rate. Since it is not practical to perform such experiments at the high strain-rates experienced during an impact test, it may be useful to combine the detailed *in-situ* results with a split-Hopkinson bar test or similar, to understand whether any relationship identified at lower strain-rates is also valid at higher strain-rates.
- In the case of tensile and toughness testing, the austenite-martensite transformation plays a key role. In the context of relating Charpy impact toughness to ballistic performance, the contribution of stress-induced martensite formation should be considered. Specifically, whether such a transformation occurs before or after any crack initiation, and the area over which it extends.

---

# BIBLIOGRAPHY

---

- [1] M. F. Ashby and D. R. H. Jones. *Engineering Materials 1: An Introduction to Properties, Applications and Design*. Butterworth-Heinemann, Oxford, UK, 3rd edition, 2005.
- [2] M. F. Ashby and D. R. H. Jones. *Engineering Materials 2: An Introduction to Microstructures, Processing and Design*. Butterworth-Heinemann, Oxford, UK, 3rd edition, 2006.
- [3] M. F. Ashby. *Materials Selection in Mechanical Design*. Butterworth-Heinemann, Oxford, UK, 3rd edition, 2005.
- [4] G. E. Dieter. Introduction to ductility. In *Ductility: Papers presented at a seminar of the American Society for Metals*, pages 1–30, Metals Park, Ohio, October 1968. American Society for Metals.
- [5] N. Tsuji, Y. Ito, Y. Saito, and Y. Minamino. Strength and ductility of ultrafine grained aluminium and iron produced by ARB and annealing. *Scripta Materialia*, 47:893–899, 2002.
- [6] E. S. Davenport and E. C. Bain. Transformation of austenite at constant subcritical temperatures. *Metallurgical Transactions*, 90:117–154, 1930.
- [7] K. J. Irvine and F. B. Pickering. Low-carbon bainitic steels. *Journal of the Iron and Steel Institute*, 187:292–309, 1957.
- [8] K. J. Irvine and F. B. Pickering. The metallography of low-carbon bainitic steels. *Journal of the Iron and Steel Institute*, 188:101–122, 1958.
- [9] H. K. D. H. Bhadeshia. *Bainite in Steels, 2nd edition*. Institute of Materials, London, 2001.

- [10] S. J. Matas and R. F. Hehemann. The structure of bainite in hypoeutectoid steels. *TMS-AIME*, 221:179–185, 1961.
- [11] R. Entin. The elementary reactions in the austenite-pearlite and austenite-bainite transformations. In V.F. Zackay and H.I. Aaronson, editors, *Decomposition of Austenite by Diffusional Processes*, pages 295–311, New York, 1962. Interscience.
- [12] V. F. Zackay, E. R. Parker, D. Fahr, and R. Bush. The enhancement of ductility in high-strength steels. *Transactions ASM*, 60:252–259, 1967.
- [13] S. Chatterjee and H. K. D. H. Bhadeshia. Transformation induced plasticity assisted steels: stress or strain affected martensitic transformation? *Materials Science and Technology*, 23:1101–1104, 2007.
- [14] H. K. D. H. Bhadeshia and D. V. Edmonds. Bainite in silicon steels: a new composition-property approach, part 1. *Metal Science*, 17:411–419, 1983.
- [15] H. K. D. H. Bhadeshia and D. V. Edmonds. Bainite in silicon steels: a new composition-property approach, part 2. *Metal Science*, 17:420–425, 1983.
- [16] C. H. Young and H. K. D. H. Bhadeshia. Strength of mixtures of bainite and martensite. *Materials Science and Technology*, 10:209–214, 1994.
- [17] M. J. Leap and J. C. Wingert. The effects of grain-refining precipitates on the development of toughness in 4340 steel. *Metallurgical and Materials Transactions A*, 30:93–114, 1999.
- [18] Y. Tomita and K. Okabayashi. Improvement in lower temperature mechanical properties of 0.40% C-Ni-Cr-Mo ultrahigh strength steel with second phase lower bainite. *Metallurgical Transactions A*, 14:485–492, 1983.
- [19] Y. Tomita and K. Okabayashi. Heat treatment for improvement in lower temperature mechanical properties of 0.40% C-Cr-Mo ultrahigh strength steel. *Metallurgical and Materials Transactions A*, 14:2387–2393, 1983.
- [20] T. V. L. Narasimha Rao, S. N. Dikshit, G. Malakondalah, and P. Rama Rao. On mixed upper bainite-martensite in an AISI 4330 steel exhibiting an uncommonly improved strength-toughness combination. *Scripta Metallurgica et Materialia*, 24:1323–1328, 1990.

- [21] A. Saha Podder, D. Bhattacharjee, and R. K. Ray. Effect of martensite on the mechanical behavior of ferrite-bainite dual phase steels. *ISIJ International*, 47:1058–1064, 2007.
- [22] F. G. Caballero, H. K. D. H. Bhadeshia, K. J. A. Mawella, D. G. Jones, and P. Brown. Design of novel high strength bainitic steels: Part 1. *Materials Science and Technology*, 17:512–516, 2001.
- [23] F. G. Caballero, H. K. D. H. Bhadeshia, K. J. A. Mawella, D. G. Jones, and P. Brown. Design of novel high strength bainitic steels: Part 2. *Materials Science and Technology*, 17:517–522, 2001.
- [24] H. Matsuda and H. K. D. H. Bhadeshia. Kinetics of the bainite transformation. *Proceedings of the Royal Society A*, 460:1707–1722, 2004.
- [25] H. K. D. H. Bhadeshia. A rationalisation of shear transformations in steels. *Acta Metallurgica*, 29:1117–1130, 1981.
- [26] H. K. D. H. Bhadeshia and A. R. Waugh. Bainite: an atom probe study of the incomplete reaction phenomenon. *Acta Metallurgica*, 30:775–784, 1982.
- [27] A. Ali and H. K. D. H. Bhadeshia. Nucleation of Widmanstätten ferrite. *Materials Science and Technology*, 6:781–784, 1990.
- [28] C. Garcia-Mateo and F. G. Caballero. The role of retained austenite on tensile properties of steels with bainitic microstructures. *Materials Transactions*, 46:1839–1846, 2005.
- [29] H. K. D. H. Bhadeshia. The first bulk nanostructured metal. *Science and Technology of Advanced Materials*, 14:014202, 2013.
- [30] F. G. Caballero, H. K. D. H. Bhadeshia, K. J. A. Mawella, D. G. Jones, and P. Brown. Very strong low temperature bainite. *Materials Science and Technology*, 18:279–284, 2002.
- [31] C. Garcia-Mateo, F. G. Caballero, and H. K. D. H. Bhadeshia. Development of hard bainite. *ISIJ International*, 43:1238–1243, 2003.
- [32] C. Garcia-Mateo and H. K. D. H. Bhadeshia. Nucleation theory for high-carbon bainite. *Materials Science and Engineering A*, 378:289–292, 2004.

- [33] C. Garcia-Mateo, F. G. Caballero, and H. K. D. H. Bhadeshia. Mechanical properties of low-temperature bainite. *Materials Science Forum*, 500-501:495–502, 2005.
- [34] P. M. Brown and D. P. Baxter. Hyper-strength bainitic steels. In *Proc. Conf. MS&T 2004*, pages 433–438, New Orleans, LA, USA, 2004. TMS/ASM.
- [35] H. K. D. H. Bhadeshia. Nanostructured bainite. *Proceedings of the Royal Society A*, 466:3–18, 2010.
- [36] C. Garcia-Mateo and F. G. Caballero. Ultra-high-strength bainitic steels. *ISIJ International*, 45:1736–1740, 2005.
- [37] F. G. Caballero, J. Chao, J. Cornide, C. Garcia-Mateo, M. J. Santofimia, and C. Capdevila. Toughness deterioration in advanced high strength bainitic steels. *Materials Science and Engineering A*, 525:87–95, 2009.
- [38] M. N. Yoozbashi, S. Yazdani, and T. S. Wang. Design of a new nanostructured, high-Si bainitic steel with lower cost production. *Materials and Design*, 32:3248–3253, 2011.
- [39] P. Jacques, Q. Furnémont, T. Pardoen, and F. Delannay. On the role of martensitic transformation on damage and cracking resistance in TRIP-assisted multiphase steels. *Acta Materialia*, 49:139–152, 2001.
- [40] M. Y. Sherif. *Characterisation and development of nanostructured, ultrahigh strength and ductile bainitic steels*. PhD thesis, University of Cambridge, 2006.
- [41] P. Jacques, Q. Furnémont, A. Mertens, and F. Delannay. On the sources of work hardening in multiphase steels assisted by transformation-induced plasticity. *Philosophical Magazine A*, 81:1789–1812, 2001.
- [42] M. Y. Sherif, C. Garcia-Mateo, T. Sourmail, and H. K. D. H. Bhadeshia. Stability of retained austenite in TRIP-assisted steels. *Materials Science and Technology*, 20:319–322, 2004.
- [43] H. K. D. H. Bhadeshia. Properties of fine-grained steels generated by displacive transformation. *Materials Science and Engineering A*, 481-482:36–39, 2008.

- [44] C. Garcia-Mateo, F. G. Caballero, T. Sourmail, M. Kuntz, J. Cornide, V. Smanio, and R. Elvira. Tensile behaviour of a nanocrystalline bainitic steel containing 3 wt% silicon. *Materials Science and Engineering A*, 549:185–192, 2012.
- [45] H. I. Aaronson. On the problem of the definitions and the mechanisms of the bainite reaction. In *The Mechanisms of Phase Transformations in Crystalline Solids*, volume 33 of *Monograph and Report Series No. 33*, pages 207–281, London, U.K., 1969. Institute of Metals.
- [46] R. F. Hehemann, K. R. Kinsman, and H. I. Aaronson. A debate on the bainite reaction. *Metallurgical Transactions*, 3:1077–1094, 1972.
- [47] H. I. Aaronson, G. Spanos, and W. T. Reynolds Jr. A progress report on the definitions of bainite. *Scripta Materialia*, 47:139–144, 2002.
- [48] H. I. Aaronson. Reply to a discussion by J. W. Christian and D. V. Edmonds of papers by Aaronson and co-workers on the proeutectoid ferrite and bainite reactions. *Scripta Metallurgica*, 22:567–572, 1988.
- [49] P. G. Boswell, K. R. Kinsman, G. J. Shiflet, and H. I. Aaronson. Ferrite morphology and allotriomorph thickening kinetics round the bay region mainly in Fe-C-2 wt% Mo alloys, and the three definitions of bainite. In *Mechanical Properties and Phase Transformation in Engineering Materials*, page 445, Warrendale, Pennsylvania, 1986. TMS.
- [50] L. J. Habraken and M. Economopolous. Bainitic microstructures in low-carbon alloy steels and their mechanical properties. In *Transformation and Hardenability in Steels*, pages 69–108, Ann Arbor, Michigan, 1967. Climax Molybdenum.
- [51] J. R. Vilella. Discussion on crystallography of austenite decomposition. *Transactions AIME*, 140:332, 1940.
- [52] M. Hillert. The role of interfacial energy during solid state phase transformations. *Jernkontorets Annaler*, 141:757, 1957.
- [53] B. L. Bramfitt and J. G. Speer. A perspective on the morphology of bainite. *Metallurgical and Materials Transactions A*, 21:817–829, 1990.

- [54] B. A. Leont'ev and G. V. Kovalevskaya. Mechanism of the bainitic transformation of austenite. *Fizika Metallov i Metallovedenie*, 38:1050, 1974.
- [55] R. W. K. Honeycombe and H. K. D. H. Bhadeshia. *Steels: Microstructure and Properties, 2nd edition*. Edward Arnold, 1995.
- [56] A. Borgenstam, P. Hedström, M. Hillert, P. Kolmskog, A. Stormvinter, and J. Ågren. On the symmetry among the diffusional transformation products of austenite. *Metallurgical and Materials Transactions A*, 42:1558–1574, 2011.
- [57] Z. G. Yang and H. S. Fang. An overview on bainite formation in steels. *Current Opinion in Solid State and Materials Science*, 9:277–286, 2005.
- [58] L. E. Samuels. *Light Microscopy of Carbon Steels*. ASM International, 1999.
- [59] J. M. Robertson. The microstructure of rapidly cooled steel. *Journal of the Iron and Steel Institute*, 119:391–424, 1929.
- [60] R. F. Mehl. Mechanism and rate of decomposition from austenite. In *Hardenability of Alloy Steels*, pages 1–65. ASM, 1939.
- [61] L. C. Chang and H. K. D. H. Bhadeshia. Microstructure of lower bainite formed at large undercoolings below bainite start temperature. *Materials Science and Technology*, 12:233–236, 1996.
- [62] R. F. Hehemann. The bainite transformation. In H.I. Aaronson and V.F. Zackay, editors, *Phase transformations*, pages 397–432. ASM, 1970.
- [63] A. R. Troiano. Transformation and retention of austenite in SAE 5140, 2340 and T1340 steels of comparable hardenability. *Transactions ASM*, 41:1093–1112, 1949.
- [64] E. P. Klier and T. Lyman. The bainite reaction in hypoeutectoid steels. *Transactions AIMME*, pages 395–422, 1944.
- [65] T. Lyman and A. R. Troiano. Influence of carbon content upon the transformations in 3% chromium steel. *Transactions ASM*, 37:402–448, 1946.
- [66] A. Hultgren. *Journal of the Iron and Steel Institute*, 114:421–422, 1926.

- [67] M. Hillert. The growth of ferrite, bainite and martensite. Internal report, Swedish Institute for Metals Research, Stockholm, Sweden, 1960.
- [68] A. Borgenstam, M. Hillert, and J. Ågren. Metallographic evidence of carbon diffusion in the growth of bainite. *Acta Materialia*, 57:3242–3252, 2009.
- [69] F. Wever and W. Jellinghaus. Transformation kinetics of austenite II: Dilatometry investigations of austenite decomposition. *Mitt. Kaiser-Wilhelm-Institute Eisenforsch*, 14:85, 1932.
- [70] A. Portevin and P. Chevenard. The transformations during the cooling of steels. *Comptes Rendus Physique*, 204:772, 1937.
- [71] C. Zener. Kinetics of the decomposition of austenite. *Transactions AIMME*, 167:550–595, 1946.
- [72] J. R. Vilella, G. E. Guellich, and E. C. Bain. On naming the aggregate constituents in steel. *Transactions ASM*, 24:225–261, 1936.
- [73] E. C. Bain. *Functions of the Alloying Elements in Steel*. American Society for Metals, Cleveland, Ohio, USA, 1939.
- [74] A. Hultgren. Isothermal transformation of austenite. *Transactions ASM*, 39:915–989, 1947.
- [75] M. Hillert. Paraequilibrium. Technical report, Swedish Institute for Metals Research, Stockholm, Sweden, 1953.
- [76] P. Bowman. The partition of molybdenum in steel and its relation to hardenability. *Transactions ASM*, 35:112, 1945.
- [77] E. S. Davenport. Isothermal transformation in steels. *Transactions ASM*, 27:837–886, 1939.
- [78] T. Murakami and Y. Imai. An investigation on isothermal transformation in steels. 1: The cause of modification of S-curves of some alloy steels. *Science Reports RITU*, 1,2:87–92, 1949.
- [79] F. Wever and H. Lange. The transformation kinetics of austenite I: Magnetic investigations of the decomposition of austenite. *Mitt. Kaiser-Wilhelm-Institute Eisenforsch*, 14:71–83, 1932.

- [80] A. R. Troiano. in discussion with C. Zener. *Transactions AIMME*, 167:550–595, 1946.
- [81] C. Zener. Equilibrium relations in medium-alloy steels. *Transactions AIME*, 167:513–534, 1946.
- [82] A. R. Troiano. in discussion with A. Hultgren. *Transactions ASM*, 39:915–989, 1947.
- [83] G. V. Smith and R. F. Mehl. Lattice relationships in decomposition of austenite to pearlite, bainite and martensite. *Transactions AIME*, 150:210–226, 1942.
- [84] F. C. Hull and R. F. Mehl. The structure of pearlite. *Transactions ASM*, 30:381–424, 1942.
- [85] A. Dubé and B. H. Alexander. in discussion with A. Hultgren. *Transactions ASM*, 39:915–989, 1947.
- [86] T. Ko and S. A. Cottrell. The formation of bainite. *Journal of the Iron and Steel Institute*, 172:307–313, 1952.
- [87] G. R. Speich and M. Cohen. The growth rate of bainite. *TMS-AIME*, 218:1050–1059, December 1960.
- [88] R. H. Goodenow, S. J. Matas, and R. F. Hehemann. Growth kinetics and the mechanism of the bainite transformation. *TMS-AIME*, 227:651–658, June 1963.
- [89] L. Kaufman, S. V. Radcliffe, and M. Cohen. Thermodynamics of the bainite reaction. In V. F. Zackay and H.I. Aaronson, editors, *The Decomposition of Austenite by Diffusional Processes*, pages 313–352, New York, 1962. Interscience.
- [90] R. Trivedi. The role of interfacial free energy and interface kinetics during the bainite reaction. *Metallurgical Transactions*, 1:921–927, 1970.
- [91] R.D. Townsend and J.S. Kirkaldy. Widmanstätten ferrite formation in Fe-C alloys. *Transactions ASM*, 61:605, 1968.
- [92] E. P. Simonen, H. I. Aaronson, and R. Trivedi. Lengthening kinetics of ferrite and bainite sideplates. *Metallurgical Transactions*, 4:1239–1245, 1973.

- [93] A. P. Miodownik. The mechanism of phase transformations in metals. *Institute of metals monograph and report*, 18:319, 1956.
- [94] J. M. Oblak and R. F. Hehemann. Structure and growth of Widmanstätten ferrite and bainite. In *Transformations and hardenability in steels*, pages 15–30, Ann Arbor, Michigan, 1967. Climax Molybdenum.
- [95] J. Deliry. Nouveau carbure de fer transformation bainitique dans les aciers au carbone silicium. *Memoires Scientifiques de la Revue de Metallurgie*, 62:527–550, 1965.
- [96] K. J. Irvine and F. B. Pickering. High carbon bainitic steels. In *Physical Properties of Martensite and Bainite, Special Report 93*, pages 110–125, London, 1965. Iron and Steel Institute.
- [97] D. N. Shackleton and P. M. Kelly. Morphology of bainite. In *Physical Properties of Martensite and Bainite, Special Report 93*, pages 126–134, London, 1965. Iron and Steel Institute.
- [98] J. W. Christian. The origin of surface relief effects in phase transformations. In V.F.Zackay and H.I. Aaronson, editors, *Decomposition of Austenite by Diffusional Processes*, pages 371–386. AIME, Interscience, 1962.
- [99] J. S. Bowles and J. K. Mackenzie. The crystallography of martensite transformations, part I. *Acta Metallurgica*, 2:129–138, 1954.
- [100] D. N. Shackleton and P. M. Kelly. The crystallography of cementite precipitation in the bainite transformation. *Acta Metallurgica*, 15:979–992, 1967.
- [101] G. R. Srinivasan and C. M. Wayman. The crystallography of the bainite transformation. *Acta Metallurgica*, 16:621–636, 1968.
- [102] G. R. Srinivasan and C. M. Wayman. Transmission electron microscope studies of the bainite transformation in iron-chromium-carbon alloys. *Acta Metallurgica*, 16:609–620, 1968.
- [103] N. F. Kennon and R. H. Edwards. Isothermal transformation of austenite at temperatures near  $M_S$  I: Transformation products. *Journal of the Australian Insitute of Metals*, 15:195, 1970.

- [104] H. I. Aaronson. The proeutectoid ferrite and the proeutectoid cementite reaction. In V. F. Zackay and H. I. Aaronson, editors, *Decomposition of Austenite by Diffusional Processes*, page 387, New York, 1962. Interscience.
- [105] C. Laird and H. I. Aaronson. Mechanisms of formation of  $\theta$  and dissolution of  $\theta'$  precipitates in an Al-4% Cu alloy. *Acta Metallurgica*, 14:171–185, 1966.
- [106] C. Laird and H. I. Aaronson. The growth of  $\gamma$  plates in an Al-15% Ag alloy. *Acta Metallurgica*, 17:505–519, 1969.
- [107] M. Nemoto. Growth of bainite in an iron-nickel-carbon alloy. In P. R. Swann, C. J. Humphrey, and M. J. Goringe, editors, *High Voltage Electron Microscopy*, pages 230–234, New York, 1974. Academic Press.
- [108] J. D. Watson and P. G. McDougall. The crystallography of Widmanstätten ferrite. *Acta Metallurgica*, 21:961–973, 1973.
- [109] H. I. Aaronson, M. G. Hall, D. M. Barnett, and K. R. Kinsman. The Watson-McDougall shear: proof that Widmanstätten ferrite cannot grow martensitically. *Scripta Metallurgica*, pages 705–712, 1975.
- [110] P. G. McDougall. Comment on “the Watson-McDougall shear: proof that Widmanstätten ferrite cannot grow martensitically”. *Scripta Metallurgica*, 9:713–715, July 1975.
- [111] H. K. D. H. Bhadeshia. BCC-BCC orientation relationships, surface relief and displacive phase transformations in steels. *Scripta Metallurgica*, 14:821–824, 1980.
- [112] J. S. Bowles and C. M. Wayman. The growth mechanism of AuCu II plates. *Acta Metallurgica*, 22:833–839, 1979.
- [113] J. W. Christian. Martensitic transformations: A current assessment. In *The Mechanisms of Phase Transformations in Crystalline Solids*, volume 33 of *Monograph and Report Series No. 33*, page 129, London, 1969. Institute of Metals.
- [114] H. K. D. H. Bhadeshia and D. V. Edmonds. The bainite transformation in a silicon steel. *Metallurgical Transactions A*, 10:895–907, 1979.
- [115] H. K. D. H. Bhadeshia and D. V. Edmonds. The mechanism of bainite formation in steels. *Acta Metallurgica*, 28:1265–1273, 1980.

- [116] R. Le Houillier, G. Bégin, and A. Dubé. A study of the peculiarities of austenite during the formation of bainite. *Metallurgical Transactions*, 2:2645–2653, 1971.
- [117] M. Takahashi and H. K. D. H. Bhadeshia. A model for the microstructure of some advanced bainitic steels. *Materials Transactions JIM*, 32:689–696, 1991.
- [118] M. Hillert, L. Höglund, and J. Ågren. Role of carbon and alloying elements in the formation of bainitic ferrite. *Metallurgical and Materials Transactions A*, 35:3693–3700, 2004.
- [119] H. K. D. H. Bhadeshia. Bainite: Overall transformation kinetics. *Journal de Physique Colloque*, C4 43:443–448, 1982.
- [120] G. I. Rees and H. K. D. H. Bhadeshia. Bainite transformation kinetics, part I, modified model. *Materials Science and Technology*, 8:985–993, 1992.
- [121] G. I. Rees and H. K. D. H. Bhadeshia. Bainite transformation kinetics, part II, non-uniform distribution of carbon. *Materials Science and Technology*, 8:994–996, 1992.
- [122] S. B. Singh and H. K. D. H. Bhadeshia. Estimation of bainite plate thickness in low-alloy steels. *Materials Science and Engineering A*, 245:72–79, 1998.
- [123] N. Chester and H. K. D. H. Bhadeshia. Mathematical modelling of bainite transformation kinetics. *Journal de Physique IV*, C5 7:41–46, 1997.
- [124] J. E. Burke. Grain growth in alpha brass. *Journal of Applied Physics*, 18:1208, 1947.
- [125] K. Lucke, G. Masing, and P. Nolting. Einfluss von kleinen beimengen auf des rekristallisation-overhalten reinstaluminium. *Zeitschrift für Metallkunde*, 47:64, 1956.
- [126] G. F. Bolling and W. C. Winegard. Grain growth in zone-refined lead. *Acta Metallurgica*, 6:283–287, 1958.
- [127] K. T. Aust and J. W. Rutter. Grain boundary migration in high purity Pb and dilute Pb-Sn alloys. *TMS-AIME*, 215:119–127, 1959.

- [128] E. L. Holmes and W. C. Winegard. Effects of lead, bismuth, silver and antimony in grain growth in zone-refined tin. *Journal of the Institute of Metals*, 88:468, 1960.
- [129] K. Lücke and K. Detert. A quantitative theory of grain-boundary motion and recrystallization in metals in the presence of impurities. *Acta Metallurgica*, 5:628–637, 1957.
- [130] H. K. D. H. Bhadeshia. Considerations of solute-drag in relation to transformations in steels. *Journal of Materials Science*, 18:1473–1481, 1983.
- [131] K. R. Kinsman and H. I. Aaronson. Influence of molybdenum and manganese on the kinetics of the proeutectoid ferrite reaction. In *Transformation and Hardenability in Steels*, pages 39–53, Ann Arbor, Michigan, 1967. Climax Molybdenum.
- [132] D. E. Coates. Diffusional growth limitations to hardenability. *Metallurgical Transactions*, 4:2313–2325, 1973.
- [133] H. K. D. H. Bhadeshia. Solute-drag, kinetics and the mechanism of the bainite transformation. In A.R. Marder and J.I. Goldstein, editors, *Phase Transformation in Ferrous Alloys*, pages 335–340, Ohio, USA, 1984. TMS-AIME.
- [134] I. Stark, G. D. W. Smith, and H. K. D. H. Bhadeshia. The element redistribution associated with the ‘incomplete reaction phenomenon’ in bainitic steels: an atom-probe investigation. In *Proceedings of an International Conference: Phase Transformations ’87*, pages 211–215. Institute of Metals, 1988.
- [135] I. Stark, G. D. W. Smith, and H. K. D. H. Bhadeshia. The distribution of substitutional alloying elements during the bainite transformation. *Metallurgical Transactions A*, 21:837–845, 1990.
- [136] F. G. Caballero, M. K. Miller, S. S. Babu, and C. Garcia Mateo. Atomic scale observations of bainite transformation in a high carbon high silicon steel. *Acta Materialia*, 55:381–390, 2007.
- [137] J. W. Christian. *Theory of Transformations in Metal and Alloys, Part I*. Pergamon Press, Oxford, 2nd edition, 1975.

- [138] M. Takahashi. Recent progress: kinetics of the bainite transformation in steels. *Current Opinion in Solid State and Materials Science*, 8:213–217, 2004.
- [139] M. Hillert. Diffusion in growth of bainite. *Metallurgical and Materials Transactions A*, 25:1957–1966, 1994.
- [140] Y. Ohmori and T. Maki. Bainitic transformation in view of displacive mechanism. *Materials Transactions JIM*, 22:631–641, 1991.
- [141] W. Steven and A. G. Haynes. The temperature of formation of martensite and bainite in low-alloy steels. *Journal of the Iron and Steel Institute*, 183:349–359, 1956.
- [142] J. W. Christian. Thermodynamics and kinetics of martensite. In *Proc. Int. Conf. on Martensite Transformations*, pages 220–234, Cambridge, MA, 1979. ICOMAT-79, MIT Press.
- [143] M. Oka and H. Okamoto. Variation of transition temperatures from upper to lower bainites in plain carbon steels. *Journal de Physique IV*, C8:503–508, 1995.
- [144] M. Takahashi and H. K. D. H. Bhadeshia. Model for transition from upper to lower bainite. *Materials Science and Technology*, 6:592–603, 1990.
- [145] M. Oka and H. Okamoto. Isothermal transformations in hypereutectoid steels. In *Proceedings of the International Conference on Martensitic Transformations*, pages 271–275. ICOMAT-86, Japan Institute of Metals, 1986.
- [146] G. R. Srinivasan and C. M. Wayman. Isothermal transformations in an Fe-7.9 Cr-1.1 C alloy. *Transactions AIME*, 242:79–82, 1968.
- [147] Y. Ohmori and R. W. K. Honeycombe. The isothermal transformation of plain carbon austenite. *ICSTIS Supplementary Transactions ISIJ*, 11:1160–1164, 1971.
- [148] A. A. B. Sugden and H. K. D. H. Bhadeshia. Lower acicular ferrite. *Metallurgical Transactions A*, 20:1811–1818, 1989.
- [149] W. T. Reynolds Jr., F. Z. Li, C. K. Shui, and H. I. Aaronson. The incomplete transformation phenomenon in Fe-C-Mo alloys. *Metallurgical Transactions A*, 21:1433–1463, 1990.

- [150] W. T. Reynolds Jr., S. K. Liu, F. Z. Li, S. Hartfield, and H. I. Aaronson. An investigation of the generality of incomplete transformation to bainite in Fe-C-X alloys. *Metallurgical Transactions A*, 21:1479–1491, 1990.
- [151] G. J. Shiflet and H. I. Aaronson. Growth and overall transformation kinetics above the bay temperature in Fe-C-Mo alloys. *Metallurgical Transactions A*, 21:1413–1432, 1990.
- [152] G. Spanos. The fine structure and formation mechanism of lower bainite. *Metallurgical and Materials Transactions A*, 25:1967–1980, 1994.
- [153] D. H. Huang and G. Thomas. Metallography of bainitic transformation in silicon containing steels. *Metallurgical Transactions A*, 8:1661–1674, 1977.
- [154] H. K. D. H. Bhadeshia. Rail steels. In J.A. Charles, G.W. Greenwood, and G.C. Smith, editors, *Future Developments of Metals and Ceramics*, page 25, London, 1992. Institute of Materials.
- [155] J. K. Yates. Innovation in rail steel. *Science in Parliament*, 53:2–3, 1996.
- [156] E. Swallow and H. K. D. H. Bhadeshia. High resolution observations of displacements caused by bainitic transformation. *Materials Science and Technology*, 12:121–125, 1996.
- [157] G. R. Speich. Growth kinetics of bainite in a three per cent chromium steel. In H.I. Aaronson and V.F. Zackay, editors, *Decomposition of Austenite by Diffusional Processes*, pages 353–369, New York, 1962. AIME, Interscience.
- [158] Y. Ohmori. The crystallography of the lower bainite transformation in a plain carbon steel. *Trans. ISIJ*, 11:95–101, 1971.
- [159] B. P. J. Sandvik. The bainite reaction in Fe-Si-C alloys: the primary stage. *Metallurgical Transactions A*, 13:777–787, 1982.
- [160] H. K. D. H. Bhadeshia. The bainite transformation: unresolved issues. *Materials Science and Engineering A*, 273-275:58–66, 1999.
- [161] M. Hillert. Paradigm shift for bainite. *Scripta Materialia*, 47:175–180, 2002.
- [162] D. Quidort and Y. J. M. Bréchet. Isothermal growth kinetics of bainite in 0.5% C steels. *Acta Materialia*, 49:4161–4170, 2001.

- [163] T. C. Tszeng. Autocatalysis in bainite transformations. *Materials Science and Engineering A*, 293:185–190, 2000.
- [164] H. S. Fang, J. J. Wang, Z. G. Yang, C. M. Li, X. Z. Bo, and Y. K. Zheng. *Bainite Phase Transformation*. Science Press, Beijing, 1999.
- [165] T. Y. Hsu. On bainite formation. *Metallurgical and Materials Transactions A*, 21:811–816, 1990.
- [166] H. Fang, J. Yang, Z. Yang, and B. Bai. The mechanism of bainite transformation in steels. *Scripta Materialia*, 47:157–162, 2002.
- [167] Z. Yang, C. Zhang, H. Fang, J. Yang, B. Bai, and J. Wang. A rationalisation of sympathetic nucleation-ledgewise growth theory of bainite transformation in Fe-C alloys. *Journal of Materials Science and Technology*, 17:433–438, 2001.
- [168] D. Quidort and Y. Bréchet. The role of carbon on the kinetics of bainite transformation in steels. *Scripta Materialia*, 47:151–156, 2002.
- [169] K. M. Wu, M. Kagayama, and M. Enomoto. Kinetics of ferrite transformation in an Fe-0.28 mass% C-3 mass% Mo alloy. *Materials Science and Engineering*, A343:143–150, 2003.
- [170] H. I. Aaronson, W. T. Reynolds, and G. R. Purdy. Coupled-solute drag effects on ferrite formation in Fe-C-X systems. *Metallurgical and Materials Transactions A*, 35A:1187–1210, 2004.
- [171] M. Peet, S. S. Babu, M. K. Miller, and H. K. D. H. Bhadeshia. Three-dimensional atom probe analysis of carbon distribution in low-temperature bainite. *Scripta Materialia*, 50:1277–1281, 2004.
- [172] E. S. Humphreys, H. A. Fletcher, J. D. Hutchins, A. J. Garrat-Reed, W. T. Reynolds Jr., H. I. Aaronson, G. R. Purdy, and G. D. W. Smith. Molybdenum accumulation at ferrite:austenite interfaces during isothermal transformation of an Fe-0.24% C-0.93% Mo alloy. *Metallurgical and Materials Transactions A*, 35:1223–1235, 2004.
- [173] S. M. C. Van Bohemen, M. J. M. Hermans, and G. Den Ouden. Acoustic emission monitoring of bainitic and martensitic transformation in medium

- carbon steel during continuous cooling. *Materials Science and Technology*, 18:1524–1528, 2002.
- [174] C. Garcia-Mateo, F. G. Caballero, and H. K. D. H. Bhadeshia. Low temperature bainite. *Journal de Physique IV*, 112:285–288, 2003.
- [175] M. X. Zhang and P. M. Kelly. Determination of carbon content in bainitic ferrite and carbon distribution in austenite by using CBKLD. *Mater. Charact.*, 40:159–168, 1998.
- [176] C. N. Hulme-Smith, I. Lonardelli, A. C. Dippel, and H. K. D. H. Bhadeshia. Experimental evidence for non-cubic bainitic ferrite. *Scripta Materialia*, 69:409–412, 2013.
- [177] S. J. Matas and R. F. Hehemann. Structure of bainite in hypoeutectoid steels. *Transactions AIME*, 221:179, 1968.
- [178] H. J. Stone, M. J. Peet, H. K. D. H. Bhadeshia, and P. J. Withers. Synchrotron X-ray studies of austenite and bainitic ferrite. *Proceedings of the Royal Society A*, 464:1009–1027, 2008.
- [179] S. S. Babu, E. D. Specht, S. A. David, E. Karapetrova, P. Zschack, M. J. Peet, and H. K. D. H. Bhadeshia. In-situ observations of lattice parameter fluctuations in austenite and transformation to bainite. *Metallurgical and Materials Transactions A*, 36:3281–3289, 2005.
- [180] K. Rakha, H. Beladi, I. Timokhina, X. Y. Xiong, S. Kabra, K.-D. Liss, and P. Hodgson. On low temperature bainite transformation characteristics using in-situ neutron diffraction and atom probe tomography. *Materials Science and Engineering A*, 589:303–309, 2014.
- [181] F. G. Caballero, M. K. Miller, and C. Garcia-Mateo. Carbon supersaturation of ferrite in a nanocrystalline bainitic steel. *Acta Materialia*, 58:2338–2343, 2010.
- [182] F. G. Caballero, M. K. Miller, C. Garcia-Mateo, and J. Cornide. New experimental evidence of the diffusionless transformation nature of bainite. *Journal of Alloys and Compounds*, 577S:626–630, 2013.
- [183] H. K. D. H. Bhadeshia. Steels for rails. In K. Buschow, R. W. Cahn, M. C. Flemings, B. Iischer, E. J. Kramer, and S. Mahajan, editors, *Encyclopedia*

- of Materials Science: Science and Technology*, pages 1–7. Pergamon Press, Elsevier Science, 2002.
- [184] F. G. Caballero and H. K. D. H. Bhadeshia. Very strong bainite. *Current Opinion in Solid State and Materials Science*, 8:251–257, 2004.
- [185] C. Garcia-Mateo, F. G. Caballero, and H. K. D. H. Bhadeshia. Acceleration of low-temperature bainite. *ISIJ International*, 43:1821–1825, 2003.
- [186] V. Sista, P. Nash, and S. S. Sahay. Accelerated bainitic transformation during cyclic austempering. *Journal of Materials Science*, 42:9112–9115, 2007.
- [187] G. Gomez, T. Pérez, and H. K. D. H. Bhadeshia. Air cooled bainitic steels for strong, seamless pipes. Part 1 - alloy design, kinetics and microstructure. *Materials Science and Technology*, 25:1501–1507, 2009.
- [188] G. Gomez, T. Pérez, and H. K. D. H. Bhadeshia. Air cooled bainitic steels for strong, seamless pipes. Part 2 - Properties and microstructure of rolled material. *Materials Science and Technology*, 25:1508–1512, 2009.
- [189] H. K. D. H. Bhadeshia. Steels for Bearings. *Progress in Materials Science*, 57:268–435, 2012.
- [190] J. R. Yang, C. Y. Huang, and S. C. Wang. The development of ultra-low-carbon bainitic steels. *Materials and Design*, 13:355–338, 1992.
- [191] G. Frommeyer, U. Brück, and P. Neumann. Supra-ductile and high-strength manganese-TRIP/TWIP steels for high energy absorption purposes. *ISIJ International*, 43:438–446, 2003.
- [192] H. I. Aaronson, W. T. Reynolds Jr., G. J. Shiflet, and G. Spanos. Bainite viewed three different ways. *Metallurgical Transactions A*, 21:1343–1380, 1990.
- [193] A. J. Rose, F. Mohammed, A. W. F. Smith, P. A. Davies, and R. D. Clarke. Superbainite: laboratory concept to commercial product. *Materials Science and Technology*, IN PRESS, 2014.
- [194] L. C. Chang and H. K. D. H. Bhadeshia. Austenite films in bainitic microstructures. *Materials Science and Technology*, 11:874–881, 1995.

- [195] S. M. Hodson. *MTDATA — Metallurgical and Thermomechanical Database*. National Physical Laboratory, Teddington, U.K., 1989.
- [196] NPL. *MTDATA*. Software, National Physical Laboratory, Teddington, U.K., 2006.
- [197] C. N. Hulme-Smith. Personal communication. 2012.
- [198] M. N. Shetty. *Dislocations and Mechanical Behaviour of Materials*. PHI Learning Pvt. Ltd., 2013.
- [199] G. E. Dieter. *Mechanical Metallurgy*. McGraw-Hill, UK, 1988.
- [200] M. J. Dickson. The significance of texture parameters in phase analysis by X-ray diffraction. *Journal of Applied Crystallography*, 2:176–180, 1969.
- [201] D. J. Dyson and B. Holmes. Effect of alloying additions on the lattice parameters of austenite. *Journal of the Iron and Steel Institute*, pages 469–474, 1970.
- [202] H. K. D. H. Bhadeshia, S. A. David, J. M. Vitek, and R. W. Reed. Stress-induced transformation to bainite in Fe-Cr-Mo-C pressure vessel steel. *Materials Science and Technology*, 7:686–698, 1991.
- [203] C. Garcia-Mateo, M. Peet, F. G. Caballero, and H. K. D. H. Bhadeshia. Tempering of a hard mixture of bainitic ferrite and austenite. *Materials Science and Technology*, 20:814–818, 2004.
- [204] M. J. Peet. *Transformation and tempering of low-temperature bainite*. PhD thesis, University of Cambridge, 2010.
- [205] R. Jenkins and R.L. Snyder. *Introduction to X-ray powder diffractometry*. John Wiley and Sons, New York, USA, 1996.
- [206] L. B. McCusker, R. B. von Dreele, D. E. Cox, D. Louër, and P. Scardi. Rietveld refinement guidelines. *Journal of Applied Crystallography*, 32:36–50, 1999.
- [207] H. Amel-Farzad, H. R. Faridi, F. Rajabpour, A. Abolhasani, Sh. Kazemi, and Y. Khaledzadeh. Developing very hard nanostructured bainitic steel. *Materials Science and Engineering A*, 559:68–73, 2013.

- [208] H. Huang, M. Y. Sherif, and P. E. J. Rivera-Diaz del Castillo. Combinatorial optimization of carbide-free bainitic nanostructures. *Acta Materialia*, 61:1639–1647, 2013.
- [209] H. S. Yang and H. K. D. H. Bhadeshia. Uncertainties in dilatometric determination of the martensite start temperature. *Materials Science and Technology*, 23:556–560, 2007.
- [210] J. H. Pak, H. K. D. H. Bhadeshia, L. Karlsson, and E. Keehan. Coalesced bainite by isothermal transformation of reheated weld metal. *Science and Technology of Welding and Joining*, 13:593–597, 2008.
- [211] C. García de Andrés, F. G. Caballero, C. Capdevila, and D. San Martín. Revealing austenite grain boundaries by thermal etching: advantages and disadvantages. *Materials Characterization*, 49:121–127, 2002.
- [212] R. T. DeHoff. Quantitative microstructural analysis. In *Fifty Years of Progress in Metallographic Techniques*, pages 63–95, Philadelphia, 1968. ASTM, American Society for Testing and Materials.
- [213] M. J. Peet and H. K. D. H. Bhadeshia. Program MAP STEEL MUCG83, <http://www.msm.cam.ac.uk/map/steel/programs/mucg83.html>.
- [214] H. K. D. H. Bhadeshia. Thermodynamic analysis of isothermal transformation diagrams. *Metal Science*, 16:159–165, 1982.
- [215] T. Okumura. MAP\_STEEL\_MTTTDDATA, <http://www.msm.cam.ac.uk/map/steel/programs/MTTTDDATA.html>.
- [216] E. Kozeschnik and B. Buchmayr. MatCalc — a simulation tool for multi-component thermodynamics, diffusion and phase transformation kinetics. In *Mathematical Modelling of Weld Phenomena*, volume 5, pages 349–361. London Institute of Materials, 2001.
- [217] P. Payson and C. H. Savage. Martensite reactions in alloy steels. *Transactions ASM*, 33:261–280, 1944.
- [218] R. A. Grange and H. M. Stewart. The temperature range of martensite formation. *Transactions AIME*, 167:467–494, 1946.
- [219] G. Ghosh and G. B. Olson. Kinetics of FCC-BCC heterogeneous martensitic nucleation. *Acta Metallurgica et Materialia*, 42:3361–3370, 1994.

- [220] H. S. Yang, D. W. Suh, and H. K. D. H. Bhadeshia. More complete theory for the calculation of the martensite-start temperature in steels. *ISIJ International*, 52:162–164, 2012.
- [221] T. Sourmail and C. Garcia-Mateo. Critical assessment of models for predicting the Ms temperature of steels. *Computational Materials Science*, 34:323–334, 2005.
- [222] W. G. Vermeulen, P. F. Morris, A. P. de Weijer, and S. van der Zwaag. Prediction of martensite start temperature using artificial neural networks. *Ironmaking and Steelmaking*, 23:433–437, 1996.
- [223] H. K. D. H. Bhadeshia. Neural networks in materials science. *ISIJ International*, 39:966–979, 1999.
- [224] C. Capdevila, F. G. Caballero, and C. Garcia de Andrés. Determination of martensite-start temperature in steels: Bayesian neural network model. *ISIJ International*, 42:894–902, 2002.
- [225] D. J. C. MacKay. Practical bayesian framework of backpropagation networks. *Neural Computation*, 4:448–472, 1992.
- [226] D. J. C. MacKay. Bayesian interpolation. *Neural Computation*, 4:415–447, 1992.
- [227] T. Sourmail and H. K. D. H. Bhadeshia. Neural networks. In Z. Barber, editor, *Introduction to Materials Modelling*, London, 2005. Institute of Materials.
- [228] H. K. D. H. Bhadeshia, R. C. Dimitriu, S. Forsik, J. H. Pak, and J. H. Ryu. Performance of neural networks in materials science. *Materials Science and Technology*, 25:504–510, 2009.
- [229] T. Sourmail and C. Garcia-Mateo. A model for predicting the martensite-start temperature of steels. *Computational Materials Science*, 34:213–218, 2005.
- [230] D. P. Koistinen and R. E. Marburger. A general equation prescribing the extent of the austenite-martensite transformation in pure iron-carbon alloys and plain carbon steels. *Acta Metallurgica*, 7:59–60, 1959.

- [231] S. A. Khan and H. K. D. H. Bhadeshia. Kinetics of martensitic transformation in partially bainitic 300M steel. *Materials Science and Engineering A*, 129:257–272, 1990.
- [232] H. K. D. H. Bhadeshia. The lower bainite transformation and the significance of carbide precipitation. *Acta Metallurgica*, 28:1103–1114, 1980.
- [233] H. Okamoto and M. Oka. Lower bainite with midrib in hypereutectoid steels. *Metallurgical Transactions A*, 17:1113–1120, 1986.
- [234] T. Sourmail, F. G. Caballero, C. Garcia-Mateo, V. Smanio, C. Ziegler, M. Kuntz, R. Elvira, A. Leiro, E. Vuorinen, and T. Teeri. Evaluation of potential of high Si high C steel nanostructured bainite for wear and fatigue applications. *Materials Science and Technology*, 29:1166–1173, 2013.
- [235] E. Keehan, L. Karlsson, H.-O. Andrén, and H. K. D. H. Bhadeshia. Influence of carbon, manganese and nickel on microstructure and properties of strong steel weld metals part 2 – impact toughness gain resulting from manganese reductions. *Science and Technology of Welding and Joining*, 11:9–18, 2006.
- [236] E. Keehan, L. Karlsson, H. O. Andrén, and H. K. D. H. Bhadeshia. New developments with C-Mn-Ni high strength steel weld metals, Part A - Microstructure. *Welding Journal*, 85:200–210s, 2006.
- [237] S. K. Putatunda, A. V. Singar, R. Tackett, and G. Lawes. Development of a high strength high toughness ausferritic steel. *Materials Science and Engineering A*, 513:329–339, 2009.
- [238] Q. Furnémont, M. Kempf, P. J. Jacques, M. Göken, and F. Delannay. On the measurement of the nanohardness of the constitutive phases of TRIP-assisted multiphase steels. *Materials Science and Engineering A*, 328:26–32, 2002.
- [239] A. Saha Podder and H. K. D. H. Bhadeshia. Thermal stability of austenite retained in bainitic steels. *Materials Science and Engineering*, 527:2121–2128, 2010.
- [240] F. G. Caballero, M. K. Miller, and C. Garcia-Mateo. Opening previously impossible avenues for phase transformation in innovative steels by atom probe tomography. *Materials Science and Technology*, IN PRESS, 2014.

- [241] M. R. Zhang and H. C. Gu. Microstructure and properties of carbide free bainite railway wheels produced by programmed quenching. *Materials Science and Technology*, 23:970–974, 2007.
- [242] T. S. Wang, J. Yang, C. J. Shang, X. Y. Li, B. Zhang, and F. C. Zhang. Microstructures and impact toughness of low-alloy high-carbon steel austempered at low temperature. *Scripta Materialia*, 61:434–437, 2009.
- [243] S. K. Putatunda, C. Martis, and J. Boileau. Influence of austempering temperature on the mechanical properties of a low carbon low alloy steel. *Materials Science and Engineering A*, 528:5053–5059, 2011.
- [244] Y. Tomita and T. Okawa. Effect of microstructure on mechanical properties of isothermally bainite-transformed 300M steel. *Materials Science and Engineering*, 172:145–151, 1993.
- [245] P. M. Novotny. Fundamentals of aging and tempering in bainitic and martensitic steel products. In G. R. Speich, editor, *Symp. 34th Mechanical Working and Steel Processing*, pages 215–236, Warrendale, PA, 1992. Iron and Steel Society of AIME.
- [246] American Society for Testing and Materials. Standard test method and definitions for mechanical testing of steel products. ASTM A370, 1980.
- [247] B. D. Cullity. *Elements of X-ray Diffraction*. Addison–Wesley Publishing Company, Reading, Massachusetts, USA, 1959.
- [248] G. K. Williamson and W. H. Hall. X-ray line broadening from filed aluminium and wolfram. *Acta Metallurgica*, 1:22–31, 1953.
- [249] C. Garcia-Mateo, F. G. Caballero, M. K. Miller, and J. A. Jimenez. On measurement of carbon content in retained austenite in a nanostructured bainitic steel. *Journal of Materials Science*, 47:1004–1010, 2012.
- [250] A. P. Hammersley. Fit2d: An introduction and overview. Internal report, ESRF, 1997.
- [251] A. P. Hammersley. Fit2d v9.129 reference manual v3.1. Internal report, ESRF, 1998.

- [252] J. H. Jang, H. K. D. H. Bhadeshia, and D. W. Suh. Solubility of carbon in tetragonal ferrite in equilibrium with austenite. *Scripta Materialia*, 68:195–198, 2012.
- [253] C. N. Hulme-Smith, I. Lonardelli, M. J. Peet, A. C. Dippel, and H. K. D. H. Bhadeshia. Enhanced thermal stability in nanostructured bainitic steel. *Scripta Materialia*, 69:191–194, 2013.
- [254] A. Wanner and D. C. Dunand. Synchrotron X-ray study of bulk lattice strains in externally loaded Cu-Mo composites. *Metallurgical and Materials Transactions A*, 31:2949–2962, 2000.
- [255] W. D. Pilkey and D. F. Pilkey. *Peterson's Stress Concentration Factors*. John Wiley and Sons, 2008.
- [256] N. M. Zhang and P. M. Kelly. Crystallographic features of phase transformations in solids. *Progress in Materials Science*, 54:1101–1170, 2009.
- [257] B. P. J. Sandvik and H. P. Nevalainen. Structure-property relationships in commercial low-alloy bainitic-austenitic steel with high strength, ductility and toughness. *Metals Technology*, 8:213, 1981.
- [258] J. R. Patel and M. Cohen. Criterion for the action of applied stress in the martensitic transformation. *Acta Metallurgica*, 1:531–538, 1953.
- [259] N. K. Balliger and T. Gladman. Work hardening of dual-phase steels. *Metal Science*, 15:95–108, March 1981.
- [260] C. A. N. Lanzillotto and F. B. Pickering. Structure-property relationships in dual-phase steel. *Metal Science*, 16:371–382, 1982.
- [261] K. Hase, C. Garcia-Mateo, and H. K. D. H. Bhadeshia. Bimodal size distribution of bainite plates. *Materials Science and Engineering A*, 438-440:145–148, 2006.
- [262] G. B. Olson and M. Cohen. Kinetics of strain-induced martensitic transformation. *Metallurgical Transactions A*, 6A:791–795, 1975.
- [263] K. Sugimoto, N. Usui, M. Kobayashi, and S. Hashimoto. Effects of volume fraction and stability of retained austenite on ductility of TRIP-aided dual-phase steels. *ISIJ International*, 32:1311–1318, 1992.

- [264] W. Y. Choo and J. Y. Lee. Thermal analysis of trapped hydrogen in pure iron. *Metallurgical Transactions A*, 13A:135–140, 1982.
- [265] K. Ono and M. Meshi. Hydrogen detrapping from grain boundaries and dislocations in high purity iron. *Acta Metallurgica et Materialia*, 40:1357–1364, 1992.
- [266] D. K. Han. Hydrogen assisted cracking of ferritic linepipe steel and corrosion behaviour of austenitic TWIP steel. Master’s thesis, Pohang University of Science and Technology, Pohang, Republic of Korea, 2013.
- [267] H. S. Hasan, M. J. Peet, and H. K. D. H. Bhadeshia. Severe tempering of bainite generated at low transformation temperatures. *International Journal of Materials Research*, 103, 2012.
- [268] L. S. Darken. Diffusion of carbon in austenite with a discontinuity of composition. *Transactions AIME*, 180:430–438, 1949.
- [269] J. P. Hirth. Effects of hydrogen on the properties of iron and steel. *Metallurgical and Materials Transactions A*, 11:861–890, 1980.
- [270] Y. D. Park, I. S. Maroef, A. Landau, and D. L. Olson. Retained austenite as a hydrogen trap in steel welds. *Welding Journal, Research Supplement*, 81:27S–35S, 2002.
- [271] J. H. Ryu, Y. S. Chun, C. S. Lee, H. K. D. H. Bhadeshia, and D. W. Suh. Effect of deformation on hydrogen trapping and effusion in TRIP-assisted steel. *Acta Materialia*, 60:4085–4092, 2012.
- [272] E. J. Song, D. W. Suh, and H. K. D. H. Bhadeshia. Theory for hydrogen desorption in ferritic steel. *Computational Materials Science*, 79:36–44, 2013.
- [273] X. Sun, J. Xu, and Y. Li. Hydrogen permeation behaviour in austenitic stainless steels. *Materials Science and Engineering A*, 114:179–187, 1989.
- [274] B. D. Craig. On the elastic interaction of hydrogen with precipitates in lath martensite. *Acta Metallurgica*, 25:1027–1030, 1977.
- [275] N. Yurioka and H. Suzuki. Hydrogen-assisted cracking in C-Mn and low alloy steel weldments. *International Materials Reviews*, 35:217–249, 1990.

- [276] A. Turnbull and R. B. Hutchings. Analysis of hydrogen diffusion in a two-phase alloy. *Materials Science and Engineering A*, 177:161–171, 1994.
- [277] F. G. Caballero, M. K. Miller, and C. Garcia-Mateo. Atom probe tomography analysis of precipitation during tempering of a nanostructured bainitic steel. *Metallurgical and Materials Transactions A*, 42:3660–3668, 2011.
- [278] K. Takai and R. Watanuki. Hydrogen in trapping states innocuous to environmental degradation of high-strength steels. *ISIJ International*, 43:520–526, 2003.
- [279] T. W. Wright. *The physics and mathematics of adiabatic shear bands*. Cambridge University Press, Cambridge, U. K., 2002.
- [280] S. M. Walley. Shear localization: a historical overview. *Metallurgical and Materials Transactions A*, 38:2629–2653, 2007.
- [281] H. C. Rogers. Adiabatic plastic deformation. *Annual Review of Materials Science*, 9:283–311, 1979.
- [282] S. P. Timothy. The structure of adiabatic shear bands in metals: a critical review. *Acta Metallurgica*, 35:301–306, 1987.
- [283] W. J. Davies. Surface fatigue in ball bearings, roller bearings, and gears in aircraft engines. In *Fatigue in Rolling Contact*, pages 23–40, London, U.K., 1963. Institution of Mechanical Engineers.
- [284] H. Schlicht. About adiabatic shear bands and the generation of “high-angle white bands” in roller bearings. *Materialwissenschaft und Werkstofftechnik*, 39:217–226, 2008.
- [285] H. Nahme and E. Lach. Dynamic behaviour of high strength armour steel. *Journal de Physique IV*, 7, Colloque C3:373–378, 1997.
- [286] J. L. Derep. Microstructure transformation induced by adiabatic shearing in armour steel. *Acta Metallurgica*, 35:1245–1249, 1987.
- [287] A. Marchand and J. Duffy. An experimental study of the formation process of adiabatic shear bands in a structural steel. *Journal of the Mechanics and Physics of Solids*, 36:251–283, 1988.

- [288] H. C. Rogers and C. V. Shastri. Material factors in adiabatic shear bands in steels. In M. A. Meyers and L. E. Murr, editors, *Shock Waves and High-Strain-Rate Phenomena in Metals*, pages 285–298, New York, USA, 1981. Plenum Press.
- [289] C. L. Wittman, M. A. Meyers, and H.-R. Pak. Observation of an adiabatic shear band in AISI 4340 steel by high-voltage transmission electron microscopy. *Metallurgical Transactions A*, 21:707–716, 1990.
- [290] J. H. Beatty, L. W. Meyer, M. A. Meyers, and S. Nemat-Nasser. *Formation of controlled adiabatic shear bands in AISI 4340 high strength steel*, pages 645–656. Marcel Dekker, New York, 1992.
- [291] M. N. Bassim, A. G. Odeshi, and M. Bolduc. Deformation and failure of a rolled homogeneous armour steel under dynamic mechanical loading in compression. In *12th International Conference on Fracture*, pages 3464–3473, New York, USA, 2009. Curran Associates Inc.
- [292] P. E. Champness. Convergent beam electron diffraction. *Mineralogical Magazine*, 51:33–48, 1987.
- [293] A. Saha Podder. *Tempering of a mixture of bainite and retained austenite*. PhD thesis, University of Cambridge, 2011.
- [294] J. J. Bozzola and L. D. Russell. *Electron Microscopy: Principles and Techniques for Biologists*. Jones & Bartlett Learning, London, U.K., 2nd edition, 1999.
- [295] D. R. Lesuer, C. K. Syn, and O. D. Sherby. Severe plastic deformation through adiabatic shear banding in Fe-C steels. *Materials Science and Engineering A*, 410-411:222–225, 2005.
- [296] R. Ueji, N. Tsuji, Y. Minamino, and Y. Koizumi. Ultragrain refinement of plain low carbon steel by cold-rolling and annealing of martensite. *Acta Materialia*, 50:4177–4189, 2002.
- [297] X. Zhao, T. F. Jing, Y. W. Gao, G. Y. Qiao, J. F. Zhou, and W. Wang. Annealing behavior of nano-layered steel produced by heavy cold-rolling of lath martensite. *Materials Science and Engineering A*, 397:117–121, 2005.

- [298] E. S. Machlin and M. Cohen. Burst phenomenon in the martensitic transformation. *TMS-AIME*, 191:746–754, 1951.
- [299] H. C. Fiedler, B. L. Averbach, and M. Cohen. The effect of deformation on the martensitic transformation. *Transactions ASM*, 47:267–290, 1955.
- [300] K. Tsuzaki, S. Fukasaku, Y. Tomota, and T. Maki. Effect of prior deformation of austenite on the gamma-epsilon martensitic transformation in Fe-Mn alloys. *Transactions JIM*, 32:222–228, 1991.
- [301] P. H. Shipway and H. K. D. H. Bhadeshia. Mechanical stabilisation of bainite. *Materials Science and Technology*, 11:1116–1128, 1995.
- [302] S. Chatterjee and H. K. D. H. Bhadeshia. TRIP-assisted steels: cracking of high carbon martensite. *Materials Science and Technology*, 22:645–649, 2006.
- [303] M. Maalekian, E. Kozeschnik, S. Chatterjee, and H. K. D. H. Bhadeshia. Mechanical stabilisation of eutectoid steel. *Materials Science and Technology*, 23:610–612, 2007.
- [304] J. O. Andersson, T. Helander, L. Hoglund, P. Shi, and B. Sundman. ThermoCalc & DICTRA, computational tools for materials science. *CALPHAD*, 26:273–312, 2002.
- [305] D. R. Stull and H. Prophet. Janaf thermochemical tables. Technical Report NSRDS-NBS-37, National Bureau of Standards, Washington, D. C., USA, 1981.
- [306] E. T. Turkdogan. *Physical Chemistry of High Temperature Technology*, volume 5. Academic Press, New York, USA, 1980.



## APPENDIX

**A.1 Laboratory X-ray analysis of Charpy notch**

The additional peak occurring at  $53^\circ$  in the notch scan shown in Figure 5.6 is believed to be an aluminium peak, although no peak for aluminium exists at this point according to the literature. Specimen displacement error cannot explain why it may have shifted to this position, however, the peak occurs whenever an aluminium mask is used on this sample, and disappears when it is taken away. Figure A.1 shows a scan taken of only the mask material, which verifies this.

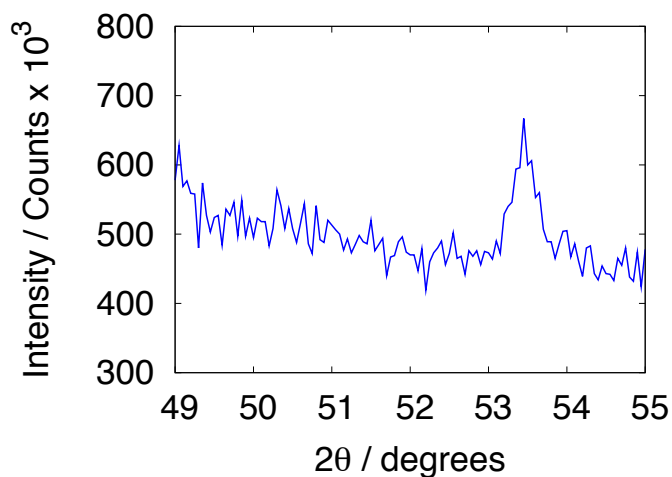


**Figure A.1:** X-ray scan taken of the aluminium mask material (foil) between 49 and 55 degrees  $2\theta$ . Note that the peak has shifted to higher angles relative to the peak in Figure 5.6, due to specimen displacement effects.

## A.2 Tetragonality of ferrite

This section contains a list of the individual ferrite lattice parameters generated from fitting the synchrotron data in Chapter 6 with a tetragonal ferrite model. The list corresponds to the data points plotted in Figure 6.4b.

$a / \text{\AA}$	$c / \text{\AA}$
2.8549	2.8786
2.8585	2.8826
2.8547	2.8781
2.8553	2.8790
2.8553	2.8785
2.8545	2.8779
2.8553	2.8788
2.8549	2.8784
2.8543	2.8775
2.8548	2.8787
2.8549	2.8786
2.8548	2.8783
2.8548	2.8781
2.8549	2.8786
2.8547	2.8782
2.8547	2.8785
2.8550	2.8784
2.8551	2.8787
2.8547	2.8779
2.8544	2.8779
2.8549	2.8784
2.8546	2.8785
2.8545	2.8780
2.8545	2.8779
2.8552	2.8790
2.8548	2.8783
2.8546	2.8780
2.8549	2.8785
2.8551	2.8788
2.8546	2.8778

**Table A.1:** List of ferrite lattice parameters corresponding to the data in Figure 6.4b, assuming tetragonal ferrite. The error in each case is approximately  $\pm 0.0004$ .

### A.3 Effects of machining upon Charpy tests

In order to understand what contribution the effects of machining have upon the measured Charpy toughness of nanostructured steels studied in Chapter 6, a set of Charpy impact tests was performed using two groups of samples. The first group was produced by heat-treating before machining, and should therefore contain regions of residual strain and martensite. The samples in the second group were machined to shape, sealed inside quartz tubes containing argon gas, and then heat-treated. This was expected to eliminate the effects of machining that have been observed in this work.

	Transformation temperature / °C	Charpy toughness / J	Hardness / HV30
HTM	200	3.4	634 ± 3
HTM	200	2.9	637 ± 2
HTM	250	4.6	567 ± 2
HTM	250	5.4	580 ± 3
HTM	250	4.7	564 ± 4
MHT	200	6.0	387 ± 3
MHT	200	4.9	624 ± 3

**Table A.2:** The results of Charpy toughness measurements in a superbainitic alloy (Alloy C), with specimens heat-treated prior to machining (HTM), and heat-treated after machining (MHT).

Table A.2 contains the results of the tests. Unfortunately, the hardness of the MHT sample with 6 J toughness was found to be highly irregular. Optical characterisation shows that both MHT samples contain notable inhomogeneities in structure, likely due to chemical segregation (Figure A.2). The micrographs show that the MHT samples are unlikely to have been fully austenitised, and are not bainitic. All samples listed in Table A.2 were machined from the same piece of material, however, it is possible that it is an end-piece offcut from a larger casting, in which such compositional variation would be possible. These tests should be repeated with homogeneous samples, to confirm the hypothesis proposed. As the data stand, a comparison of toughness values is not legitimate. Note also that there appear to be regions of pearlite in Figure A.2b, indicating that the cooling rate from austenitisation temperature was not high enough to avoid other

transformations taking place.

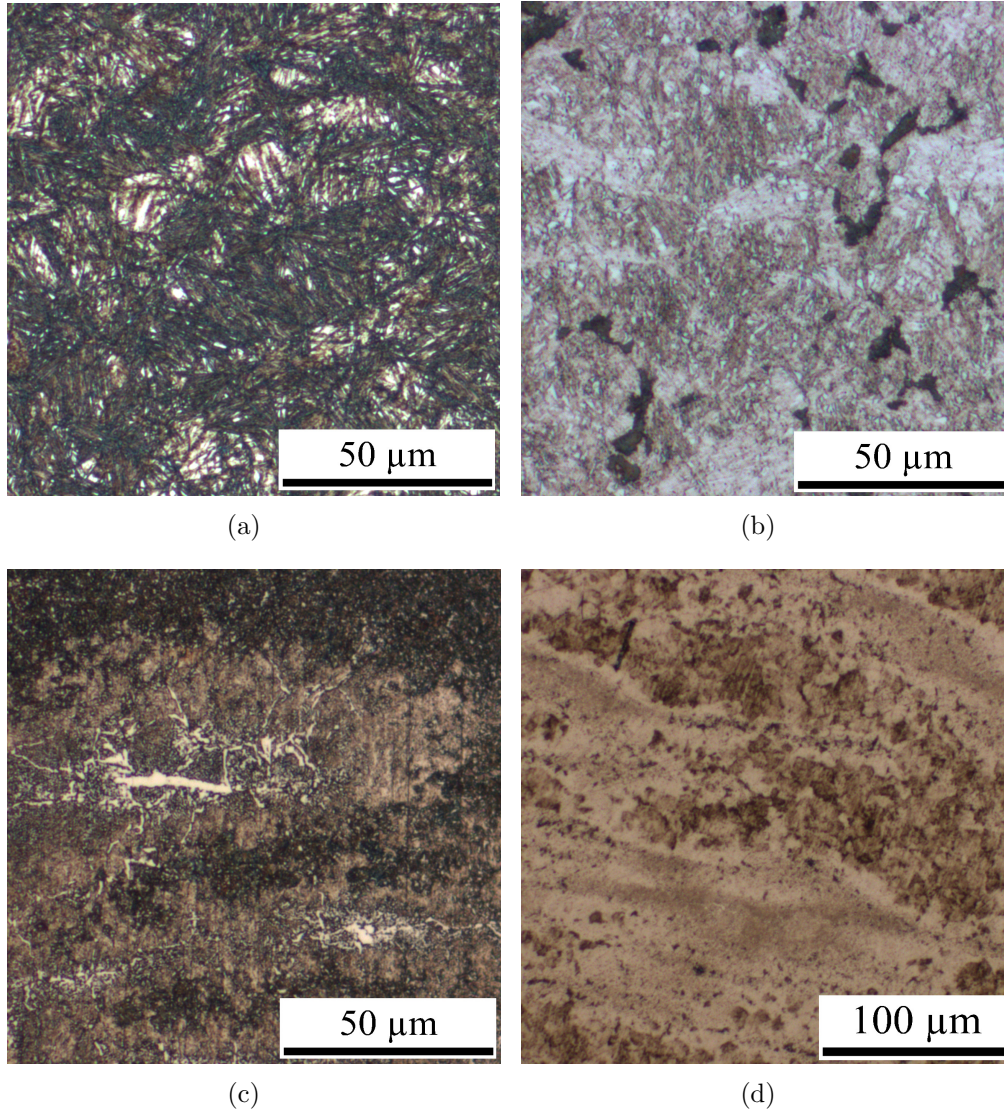


**Figure A.2:** Optical micrographs of Charpy specimens listed in Table A.2. (a) HTM, 200°C; (b) HTM, 250°C; (c,d) MHT, 200°C. The latter two structures show evidence of significant chemical inhomogeneities.

## A.4 Thermodynamics of oxidation

Assuming the manufacturer's statement that the gas used in the thermal desorption analysis contains about 2 ppm of water, and that the evolved hydrogen is typically one tenth of this value at any instant of time, the ratio of partial pressures  $p_{\text{H}_2}/p_{\text{H}_2\text{O}} \approx 0.1$ , the oxidation of elements within the steel may be represented by the following equation:

$$\text{H}_2\text{O} + \frac{x}{y}\text{Me} = \frac{1}{y}\text{Me}_x\text{O}_y + \text{H}_2$$

$$\Delta G = \Delta G_{\text{Me}_x\text{O}_y}^\circ - \Delta G_{\text{H}_2\text{O}}^\circ + RT \ln \frac{a_{\text{Me}_x\text{O}_y}^{\frac{1}{y}} p_{\text{H}_2}}{p_{\text{H}_2\text{O}} a_{\text{Me}}^{\frac{x}{y}}} \quad (\text{A.1})$$

where 'Me' represents the metal,  $x$  and  $y$  depend on the type of oxide as listed in Table A.3,  $a$  represents the activity of the material identified by the subscript, and  $R$  is the gas constant. The activity of the pure oxide was always taken to be unity, and those of the metallic elements in the steel concerned calculated using ThermoCalc [304].

**Table A.3:** Thermodynamic data for oxidation

Reaction	Standard free energy change / $\text{kJ mol}^{-1}$	Reference
$\text{H}_2 + \frac{1}{2}\text{O}_2 = \text{H}_2\text{O}$	$\Delta G_{\text{H}_2\text{O}}^\circ = -247.70 + 0.0558T$	[305]
$\text{Fe} + \frac{1}{2}\text{O}_2 = \text{FeO}$	$\Delta G_{\text{FeO}}^\circ = -264.00 + 0.0646T$	[305]
$\text{Mn} + \frac{1}{2}\text{O}_2 = \text{MnO}$	$\Delta G_{\text{MnO}}^\circ = -388.90 + 0.0763T$	[306]
$\frac{1}{2}\text{Si} + \frac{1}{2}\text{O}_2 = \frac{1}{2}\text{SiO}_2$	$\Delta G_{\text{SiO}_2}^\circ = -473.15 + 0.0988T$	[305]
$\frac{2}{3}\text{Al} + \frac{1}{2}\text{O}_2 = \frac{1}{3}\text{Al}_2\text{O}_3$	$\Delta G_{\text{Al}_2\text{O}_3}^\circ = -561.00 + 0.1077T$	[305]

